1983

Response Of Cable Roofs To Wind

Ismail Deeb El-ashkar

CANADIAN THESES ON MICROFICHE

I.S.B.N.

THESES CANADIENNES SUR MICROFICHE

National Library of Canada
Collections Development Branch

Canadian Theses on
Microfiche Service

Ottawa, Canada
K1A 0N4

Bibliothèque nationale du Canada
Direction du développement des collections

Service des thèses canadiennes
sur microfiche

NOTICE

The quality of this microfiche is heavily dependent upon the quality of the original thesis submitted for microfilming. Every effort has been made to ensure the highest quality of reproduction possible.

If pages are missing, contact the university which granted the degree.

Some pages may have indistinct print especially if the original pages were typed with a poor typewriter ribbon or if the university sent us a poor photocopy.

Previously copyrighted materials (journal articles, published tests, etc.) are not filmed.

Reproduction in full or in part of this film is governed by the Canadian Copyright Act, R.S.C. 1970, c. C-30. Please read the authorization forms which accompany this thesis.

AVIS

La qualité de cette microfiche dépend grandement de la qualité de la thèse soumise au microfilmage. Nous avons tout fait pour assurer une qualité supérieure de reproduction.

S'il manque des pages, veuillez communiquer avec l'université qui a conféré le grade.

La qualité d'impression de certaines pages peut laisser à désirer, surtout si les pages originales ont été dactylographiées à l'aide d'un ruban usé ou si l'université nous a fait parvenir une photocopie de mauvaise qualité.

Les documents qui font déjà l'objet d'un droit d'auteur (articles de revue, examens publiés, etc.) ne sont pas microfilmés.

La reproduction, même partielle, de ce microfilm est soumise à la Loi canadienne sur le droit d'auteur, SRC 1970, c. C-30. Veuillez prendre connaissance des formules d'autorisation qui accompagnent cette thèse.

THIS DISSERTATION
HAS BEEN MICROFILMED
EXACTLY AS RECEIVED

LA THÈSE A ÉTÉ
MICROFILMÉE TELLE QUE
NOUS L'AVONS REÇUE

NL-339 (r. 82/08)

Canada

RESPONSE OF CABLE ROOFS TO WIND

by

Ismail D. El-ashkar

Faculty of Engineering Science

Submitted in partial fulfillment

of the requirements for the degree of

Doctor of Philosophy

Faculty of Graduate Studies

The University of Western Ontario

London, Ontario

May, 1983

ABSTRACT

A nonlinear solution is formulated for a single hanging cable and flat rectangular and circular cable roofs under the effect of the initial tension and the applied loads. The solution is based on a small strain large displacement theory.

The linear deflection of a curved tension roof under additional static loads is studied using the assumption that the deflection under these additional loads is small with respect to that under the initial loads. Approximate analytical solutions for the initial and additional deflections are obtained.

The linear undamped free vibration problem of a flat cable tension roof with any boundary is considered using the assumption that an orthogonal, isotropic network can be replaced by an equivalent membrane found by energy considerations. Free vibration is solved for rectangular, circular and elliptical boundaries. For the elliptical flat cable roof, a simplified solution, very well suited for practical applications, is derived.

The partial differential equation of free undamped vibration of a general curved membrane surface is

formulated and solved, with some simplifications, for a rectangular hyperbolic paraboloid cable roof. The general solution outlined above is extended to include the case of the circular hyperbolic paraboloid cable roof.

The problem of a free vibrating membrane backed by a cavity with openings is theoretically studied and complemented by experimental verification of the theory. Theoretical and experimental values for frequency reduction due to inertia are given.

The statistical theory of wind forces is reviewed and applied to determine the dynamic response of cable roofs to wind loading. The problem of air-structure interaction is outlined and parameters for the aerodynamic and acoustical damping ratio are described. The behaviour of cable roofs in turbulent wind is studied in the wind tunnel using two aeroelastic models. The similarity requirements for modelling are reviewed with special attention being paid to the effect of the air enclosed under the roof. A similarity law for the modelling of this enclosure is presented and its role in free vibration as well as wind induced vibration is investigated. A wind tunnel study of a large tension roof is described.

The design implications of cable tension roof behaviour under turbulent wind load are discussed.

ACKNOWLEDGEMENTS

The author would like to thank the Faculty of Engineering Science of The University of Western Ontario for the opportunity to carry out this study.

The author would like to express his sincere appreciation to Professor M. Novak for the very capable assistance, guidance and encouragement extended to him throughout his graduate study.

The author would like to thank Professor A.G. Davenport and the staff of the Boundary Layer Wind Tunnel for the use of the laboratory facilities and the valuable assistance given him during the experimental portion of this study.

Finally, the author would like to express his deepest appreciation and love to his wife Almaza and his son and daughter, who have sacrificed so much and have offered so much enthusiasm in order for him to finish this study.

Financial support from the Natural Science and Engineering Research Council of Canada for the project is gratefully acknowledged.

TABLE OF CONTENTS

LIST OF PHOTOGRAPHIC PLATES

LIST OF TABLES

LIST OF FIGURES

NOMENCLATURE

A = cross-sectional area of cable; cable roof plan area

A_o = a single area of cavity openings

A_c = total area of cavity wall ($2\pi a \bar{H}$)

A_{nm} = amplitude of vibration in mode nm

A_r = area ratio

a = radius of cable roof

a_o = radius of a single cavity opening

$\bar{a}$ = dimensionless parameter

$1/a$ = scale wind speed (the dispersion)

C = damping constant

C^2 = dimensionless parameter

C_m = coefficient of virtual mass

C_{nm} = generalized damping of the nmth natural mode

C_q = wind pressure coefficient

$C_{\bar{q}}$ = mean pressure coefficient

$C_{q_{max}}$ = maximum pressure coefficient

$C_{q_{min}}$ = minimum pressure coefficient

C_{σ_q} = rms pressure coefficient

$C_{\bar{q}_\ell}$ = the internal mean pressure coefficient

$C_{q_{\sigma_\ell}}$ = the internal rms pressure coefficient

$C_v(r,s:\omega)$ = Real, co-spectrum

ce_m = a cosine type Mathieu function of the first kind and of order m

Ce_m = a cosine type modified Mathieu function of the first kind and of order m

$\bar{c}$ = dimensionless parameter

c_o = speed of sound in air

D = diameter of circular tension roof; domain

D_{ol} = structural damping ratio of natural mode ol

d = the semi-interfocal of ellipse

ds = arc length

E = modulus of elasticity

e = eccentricity of ellipse

F = central sag; stress function

$F(x,y,z,t)$ = fluctuating force

$\bar{F}(x,y,z)$ = static force of wind

F_{nm} = the symmetric generalized force of the nmth natural mode

F'_{nm} = the asymmetric generalized force of the nmth natural mode

$F_{r_{ol}}$ = the generalized force due to radiated pressure for the natural mode ol

$F_{\ell_{ol}}$ = the generalized force due to change in internal pressure for the natural mode ol

$F_{\bar{V}_{ol}}$ = the generalized wind force for the natural mode ol

$F_{\dot{w}_{ol}}$ = the generalized force due to the relative movement of the roof with respect to wind for the natural mode ol

f = frequency in cycles per second cps (Hz)

$\bar{f}$ = reduced frequency ($\frac{fL}{\bar{V}_{10}}$, L ≃ 1200 m)

$\hat{f}$ = reduced frequency ($fz/\bar{V}(z)$)

f_n = natural frequency of cable in C.P.S. (Hz)

f_{nm} = natural frequency of the nmth mode in C.P.S. (Hz)

f^*_{o1} = fundamental frequency in vacuo

f^* = integrand

f_x, f_y = the drop along the x axis and the y axis in Cartesian coordinates

f_1, f_2 = the drop and the sag of circular H.P. at $\theta=0, \pi$ and $\theta=\pi/2, 3\pi/2$ respectively in polar coordinates

$f_{c,j}$ = the coincidence frequency

g = gravitational acceleration (32.2 ft/sec^2, 9.81 m/sec^2): peak factor

H = the total horizontal tension per unit length, under initial applied loads

H_o = the initial horizontal component of applied tension

ΔH = the increment in the horizontal component of cable tension

$\Delta H_{ox}, \Delta H_{oy}$ = the initial additional horizontal components of tension per unit length in the x,y directions

$\Delta H_x, \Delta H_y$ = the additional horizontal component of tension per unit length due to the additional applied loads in the x,y directions

$\bar{H}$ = average height of cavity

H_o, H_1 = the Struve functions of zero order and first order

$|H_{nm}(\omega)|^2$ = the mechanical admittance function of the nmth mode

h = roof thickness

$\bar{h}$ = dimensionless tension increment parameter

I^* = Hamilton's integral

$I(v)$ = turbulence intensity ($= \sigma_v/\bar{V}_{10}$)

$|I_{nm}(\omega)|$ = the symmetric joint acceptance function of the nmth mode

$|I'_{nm}(\omega)|$ = the asymmetric joint acceptance function of the nmth mode

J_k = Bessel function of the first kind and kth order

j_{nm} = roots of Bessel function J_n with argument of order m

k = surface drag coefficient; subscript

K^2 = frequency argument in the ellipse free vibration problem ($= \omega^2 d^2 m/4T$)

K = air bulk modulus

K_{nm} = the generalized stiffness of the nmth mode

L = length scale of turbulence

L_x, L_y, L_z = length scale of turbulence in the longitudinal, lateral and vertical direction of wind

L_s = length scale associated with characteristic frequency f_s ($= \bar{V}(z)/f_s$)

L_o = the unextended length of the cable

L_e = the extended length of the cable

ΔL_o = extension in cable length

ℓ = cable span

$\Delta\ell$ = spatial separation ($= \sqrt{\Delta x^2+\Delta y^2+\Delta z^2}$)

ℓ' = the effective length of the air mass in Helmholtz Resonator.

m = mass per unit length of cable; mass per unit area of roof material; integer

m_r = mass per unit area ratio

m_t = sum of the mass per unit area of the roof material and the air attached to the roof surface during vibration

M_{nm} = generalized mass of the nmth mode

N = number of wall openings; life time of structure in years

N_r, N_t = stress resultants in radial and tangential directions

n = integer

$P(>V)$ = cumulative probability distribution

$p(V)$ = probability distribution

p = acoustic pressure; point load

Δp = change in acoustic pressure

$\bar{P}$ = dimensionless load parameter

$Q(r,s;\omega)$ = imaginary, quadrature spectrum

q = uniformly distributed static load

$\bar{q}$ = dimensionless load parameter.

q_o = initial permanent uniformly distributed static load

$q(x,y,z,t)$ = wind pressure at point (x,y,z) and time t

$\bar{q}(x,y,z)$ = mean wind pressure at point (x,y,z)

$q_d(x,y,z)$ = dynamic head pressure $(= 1/2\ \rho\ \bar{V}^2(x,y,z))$

$\hat{q}$ = maximum and minimum pressure field

q_s = net static pressure

q_u = external pressure

q_r = radiated pressure due to roof movement

q_ℓ = internal pressure in the enclosed volume

q_i = the incident wind pressure

R = dimensionless radius; return period

R_{or}, R_{ot} = radii of curvature in the radial and tangential directions

$R(r)$ = shape function in polar coordinate r

$R_v(r,s;\tau)$ = cross-correlation function of wind velocity at points r,s with time lag τ

$R_{q_r q_s}$ = cross-correlation of wind pressure at points r,s

r = polar coordinate

S = plan area of H.P. roof

$S_v(f)$ = longitudinal power spectral density of wind fluctuations at frequency f C.P.S. (Hz)

$S_w(f)$ = vertical power spectral density of wind fluctuations

$S_v(r,s;\omega)$ = cross-spectrum of longitudinal wind velocity between points r,s at frequency ω (rad/sec)

$S^n(r,s;\omega)$ = normalized cross-spectrum

$S_{v_i v_j}(r,s;\omega)$ = cross-spectrum between the ith and jth components of the wind at points r,s

$S_F(f)$ = power spectrum of the fluctuating force F

S_q = pressure spectrum

$S_{z_{nm}}$ = the spectrum of the generalized coordinate z_{nm}

$S_{w_{nm}}$ = the spectrum of response in the nmth mode

S_w = the spectrum of response due to all modes

se_m = a sine type of Mathieu function of the first kind and of order m

Se_m = a sine type of modified Mathieu function of the first kind and of order m

T = tension in cable; tension per unit arc length in cable roof; time scale

$T(t)$ = time function

T^* = kinetic energy

t = time

U = dimensionless radial displacement; modal wind speed (the mode of extreme data)

U_o = dimensionless initial radial strain

u = radial displacement

V_o = original volume of the enclosure

ΔV = change in the air volume within the enclosure

V^* = friction velocity; potential energy

$V(z,t)$ = wind velocity at height z and time t

$\bar{V}(z)$ = mean wind velocity at height z above ground

$\bar{V}_G$ = gradient wind velocity

$\bar{V}_{10}$ = reference wind velocity at height 10 m (in m/sec)

V_c = the convection velocity

V_r = relative velocity

$\hat{V}(z)$ = the maximum peak wind velocity

$v'(z,t)$ = fluctuating component of wind velocity at height z and time t

$\bar{W}$ = dimensionless transverse displacement of cable

W_o = dimensionless transverse displacement of circular roof

W_{oc} = dimensionless centre displacement of circular roof

w = transverse displacement due to additional loads

w_o = initial transverse displacement

w_x, w_y, w_t = first derivatives of transverse displacement with respect to coordinates x,y and time t

w_{nm} = mode shape nm

$\bar{w}_{nm}$ = the average amplitude of displacement of the membrane surface in the nmth mode

$\hat{w}_t$ = the total peak response

$w_{q,st}$ = the quasi-static deflection

$\dot{w}$ = the velocity of vibrating membrane

x,y,z = system Cartesian coordinate axes

$X(x)$ = shape function in direction x

$Y(y)$ = shape function in direction y

$\bar{X}, \bar{Z}$ = dimensionless coordinates

Y_k = Bessel function of the second kind and the kth order

$\Delta x, \Delta y, \Delta z$ = separation in directions x,y,z

z_G = gradient height

z_o = roughness length (height)

z_d = zero plane displacement

z_{nm} = the symmetric generalized coordinate

z'_{nm} = the asymmetric generalized coordinate

α = power law exponent; characteristic number

α_o = dimensionless parameter

α_c = volume of air ratio

β_c = cavity parameter (additional mass parameter)

β_r = the acoustic damping ratio

β_v = the aerodynamic damping ratio

γ = apparent frequency; air specific heat ratio

$\gamma^2(r,s;\omega)$ = coherence function

δ = boundary layer thickness

δ_s = logarithmic decrement

δ_v = bandwidth

$\varepsilon_r, \varepsilon_t$ = strain in radial and tangential directions

η = the extension factor for cables; elliptical coordinate

θ = polar coordinate; angle in degrees

θ^* = constant; angle in degrees between spatial separation and direction of flow

κ = Von Karman constant ($\simeq 0.4$)

λ = wave length ($= \bar{V}(z)/f$)

$\lambda^2, \bar{\lambda}^2$ = dimensionless load parameters

λ_L = length scale

λ_M = mass scale

λ_m = mass per unit area scale

λ_T = time scale

λ_{T_o} = tension per unit length scale

λ_V = wind velocity scale

λ_{V_o} = dynamic stiffness scale (internal volume scale)

μ_o = dynamic viscosity of air

ν = Poisson's ratio

ν^2 = tension/mass per unit area ratio

ξ = elliptical coordinate; inward displacement of the air in the Helmholtz Resonator

ξ_o = elliptical coordinate at the ellipse boundaries

ρ = mass density of air

σ = density of structure material

σ_r, σ_t = stresses in radial and tangential directions

σ_v = the rms of wind fluctuations $(= \sqrt{\sigma_{\bar{v}}^2 + \sigma_{\bar{u}}^2 + \sigma_{\bar{w}}^2})$

$\sigma_{\bar{v}}, \sigma_{\bar{u}}, \sigma_{\bar{w}}$ = the rms of wind fluctuations in x,y,z directions

σ_q = the rms of wind pressure

τ = time lag; sampling period

$\phi(\theta)$ = shape function in polar coordinate θ

$\phi(\eta)$ = shape function in elliptical coordinate η

$\phi(x,y)$ = shape function in Cartesian coordinates x,y

$\phi_{nm}(r)$ = shape function in polar coordinate r, for the nmth mode

χ = the aerodynamic admittance function

$\psi(\xi)$ = shape function in the elliptical coordinate ξ

ω = frequency in Rad/sec

ω_{nm} = circular frequency of mode nm in Rad/sec

ω_R = frequency of the Helmholtz Resonator in Rad/sec

Γ = the Gamma function; life expectancy of the turbulent eddies

∇^2 = the two-dimensional Laplacian operator

CHAPTER I

INTRODUCTION

1.1 GENERAL

The aesthetic appeal and small weight of cable systems has led to their increased popularity in recent years. Their ability to span large distances and to adapt to a wide variety of shapes has fostered this appeal.

Of course, the idea of suspended structures is not a new one; it goes back to the Arabs with their big tents, even to Biblical times and probably long before that. In nature, the spider's web is an example of these systems.

The available historical evidence suggests that natural ropes were the first materials used and that the earliest version of tension roofs was a tent. With the availability of iron and steel as structural materials, the first forms of modern suspension structures, in which high tension steel cables are used, began to take shape. The real developments in the analysis, design and construction of cable roofs occurred only after the Rayleigh arena was built in the United States in 1953. This progress has indeed been rapid. To date, Saudi Arabia is the site of the world's largest roof, a five million square foot tent roof, under construction [1].

The economic expediency of cable roofs is well known from the practice of their application within the last thirty years in different buildings and constructions. The substantial advantages of these systems, especially for covering of large spans, are universally recognized at present. Under the existing trend of further considerable increase of spans for public as well as for special industrial buildings and constructions, the suspended systems will remain for a long period of time as the most expedient and in many cases as the only possible decision in this field.

1.2 AIM AND SCOPE OF STUDY

The general aim of this work is to give a unified account of cable tension roofs from the point of view of a structural engineer as well as researcher who has interests in both the theoretical and practical aspects of the subject. The purpose of this research work is to identify the main problems of dynamic behaviour of tension roofs and to contribute to their solution. Therefore, the work in this thesis includes the following:

1. The description of suspension roof structures and the review of the development of their analysis and design within the last 30 years.

2. The review of the classical theories of statics and dynamics of a single cable; this is necessary because the cable is the main element in cable roofs and some configurations of cable roofs are similar to the single cable.
3. The study of static analysis of cable tension roofs and formulation of a theory for the linear and non-linear response under static loading for two of the most common shapes, the rectangular and circular type.
4. The review of recent developments in statistical theory of turbulent wind.
5. The study of free vibration analysis of cable tension roofs and development of a theory for the free vibration of the two common shapes, i.e., the rectangular and circular hyperbolic paraboloid tension roofs.
6. Development of a theory for the free vibration of cable roofs backed by a cavity with openings and study the effect of the enclosure under the roof on its frequency characteristics.
7. The theoretical study of static and dynamic response of cable tension roofs due to wind loading.
8. The study of air-roof interaction and its effect on the roof frequency response functions.
9. Experimental study to verify the theories developed.
10. Additional goal of the experimental study is to estimate damping of the cable roof structures from all sources

and to measure the internal pressure fluctuations within the enclosure under the roof.

In this thesis, these objectives have been pursued and the results of the investigation are presented here, based on an analytical approach for all the problems involved.

1.3 DESCRIPTION AND DESIGN OF SUSPENSION ROOFS

A suspension structure may be defined as a structure whose principal supporting elements are tension members draped between anchorages, as defined by ASCE Committee State-of-the-Art [2], Butler [3] and Roland [Frei Otto Tension Structures, 4].

A cable-suspended roof is a suspension structure in which twisted wire strands, or ropes, usually of steel, serve as the primary tension members. Those members consist of sagging cables having little flexural rigidity, carrying downward vertical loading and other cables being provided for ancillary purposes, such as to provide damping and/or additional stiffness.

1.3.1 Types of Suspension Roofs

Suspension roofs may be classified according to their shape and method of carrying the decking. The shape may be categorized according to the number of layers of cables in the system and the curvature of the surface formed by the cables. Suspension roofs may consist of single or double

layer cable systems. When viewed in plan, the cables in a layer may be arranged in parallel, radially or as a mesh. The mesh arrangement, Figure 1.1, is often referred to as double, triple and quadruple threaded cable nets, as well as nets of hexagonal mesh patterns.

The surface formed by a real or imaginary membrane stretched over a cable layer may be synclastic which has curvatures of the same sign in principal directions or anti-clastic, which has opposite curvatures in these directions. Examples of possible shapes of suspension roofs are shown in Figure 1.2.

For many suspension roofs, the decking is placed directly over the cables, Figure 1.3a, while other hanging roofs have been constructed with the roof decking attached to a framework which is, in turn, supported by a cable system, Figure 1.3b [7].

1.3.2 Materials and Structural Elements

The construction materials particularly suitable for suspension structures loaded in tension with the least possible material are those having the highest possible ratio of strength to bulk density. Structural steel strands and structural steel ropes, because with their tensile strength of 1275 to 2137 N/mm^2 (185,000 to 310,000 psi), they have the highest strengths of all commercially available

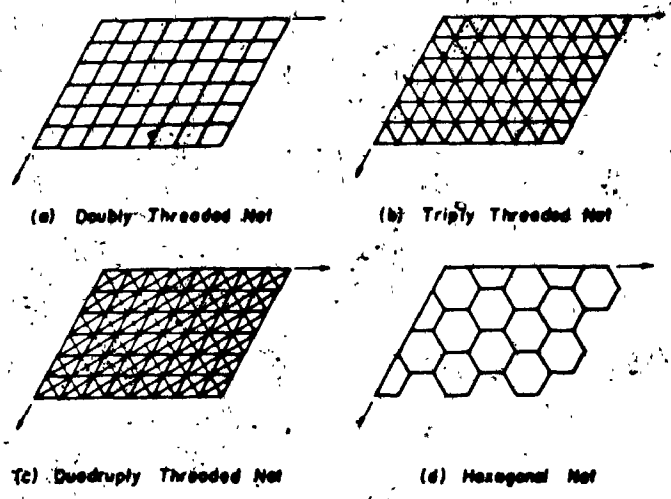

FIGURE (1.1) Cable Net Mesh Patterns.

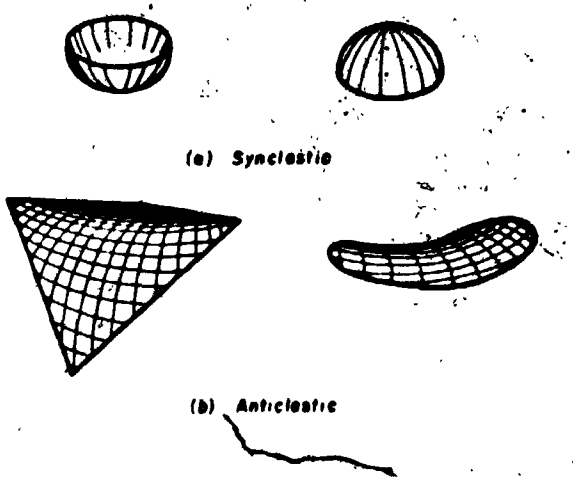

FIGURE (1.2) Examples of Suspension Roof Surfaces.

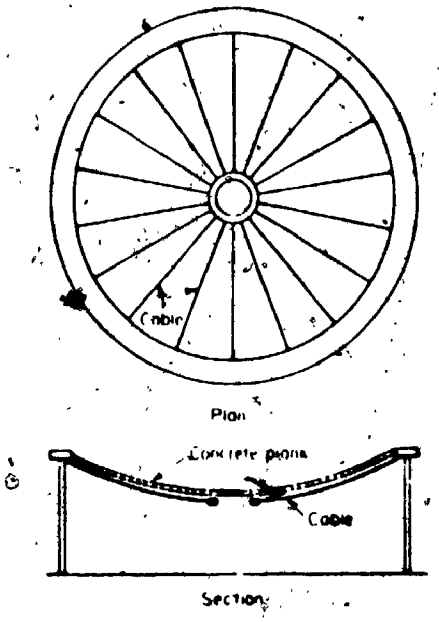

FIGURE (1.3a) Circular Tension Roof, Decking Placed Over Cables, [5].

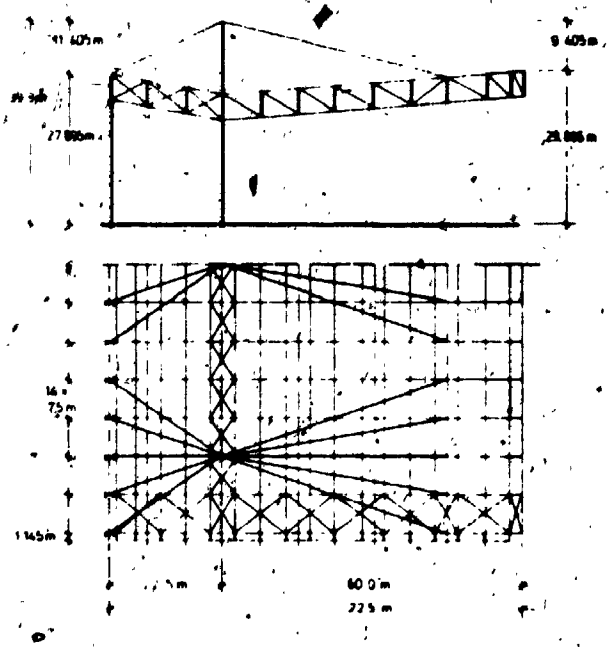

FIGURE (1.3b) Cable-stayed Roof, Decking Attached to a Framework, [7].

structural materials and are generally more economical for tension members than, for example, solid round bars of mild steel or medium-tensile steel. A strand is an assembly of steel wires wrapped helically around a centre wire in one or more symmetrical layers and has the cross-sections and schematic arrangement shown in Figures 1.4a and 1.4b.

A rope is composed of a plurality of strands wrapped helically around a core, as shown in Figure 1.4c. A typical minimum breaking load being 240 t for 50 mm (265 t for 2 inches) diameter and 530 t for 75 mm (585 t for 3 inches) diameter ropes. As protection against corrosion, steel cables are galvanized and can additionally be sheathed with plastic.

Tension members (cables) which form open networks and lattice works are primary structures and have to be covered with continuous membrane or be infilled with panels. Isotropic membranes, such as plastic sheets, lattice sheets, metal membranes (steel or aluminum) sheets and rubber membranes may be used as a continuous membrane covering attached to the supporting cables, Figure 1.5. Materials which may be used as filling panels are fine mesh netting (to fill large meshes in very coarse mesh work), flexurally rigid slabs or plates of sheet metal, plywood hard-board, gypsum, insulating materials, lightweight concrete,

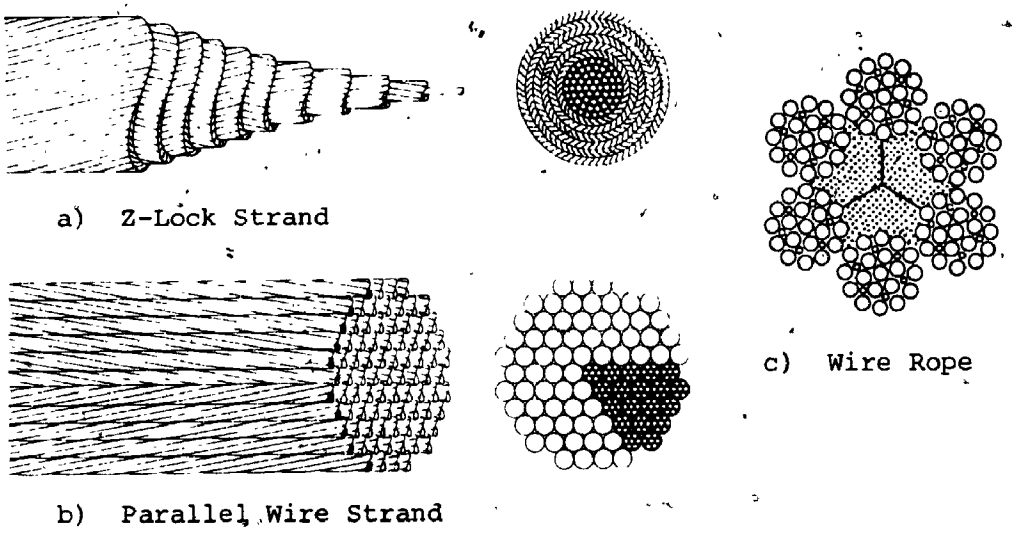

a) Z-Lock Strand

c) Wire Rope

b) Parallel Wire Strand

FIGURE 1.4 Types of Cables

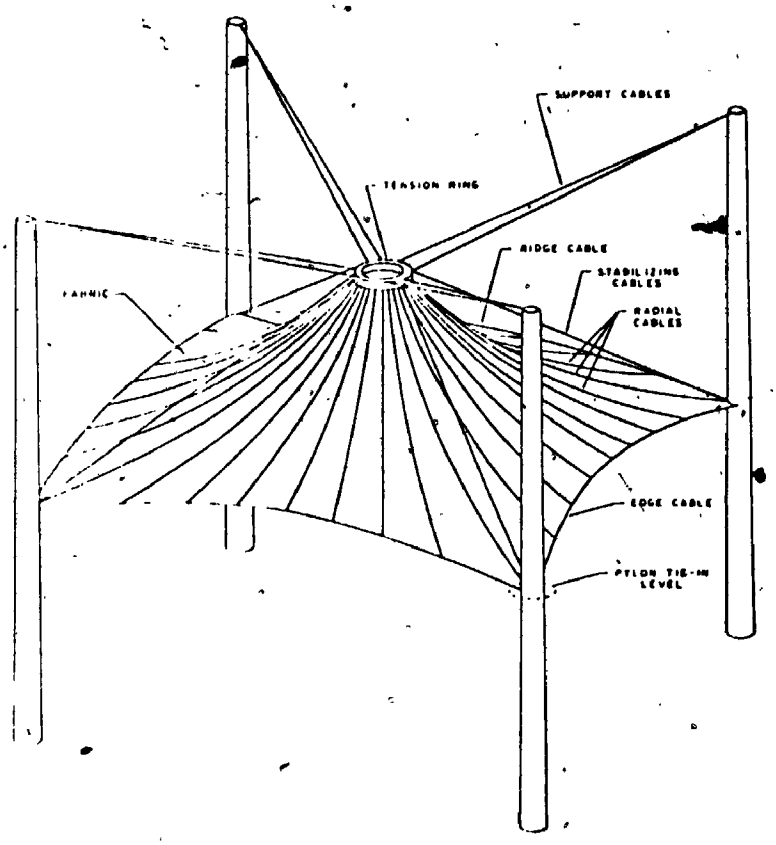

FIGURE 1.5 Isotropic Continuous Membrane Covering [116]

plastics, thin corrugated or folded plates and sandwich slabs with foamed plastic insulating layers.

The slabs or plates are either suspended between the meshes, Figure 1.6a, or are installed as long panels between parallel cables, Figure 1.6b, or they may be mounted over or under the network. In cable-suspension roofs it is sometimes uneconomical to space the cables too closely and secondary members may be used to break down the space of the infilling. These members are usually of conventional steel work. Both secondary members and infilling must be capable of accepting the large deflection movements which occur in cable-suspension roofs.

There are two ways of transmitting the forces in the cables to the ground: by a reinforced concrete ring supported by vertical columns at close spacing, Figure 1.6a, or by steel anchorages and accompanied fittings, Figure 1.6b. In general, fittings should be capable of developing at least the breaking strength of the cables to which they are attached. In double-layer suspension roofs, the strut and/or ties may be made of steel tubes.

A knowledge of the limitations of building materials and construction systems is an important prerequisite for assessing the effect of the free span of a structure upon its shape.

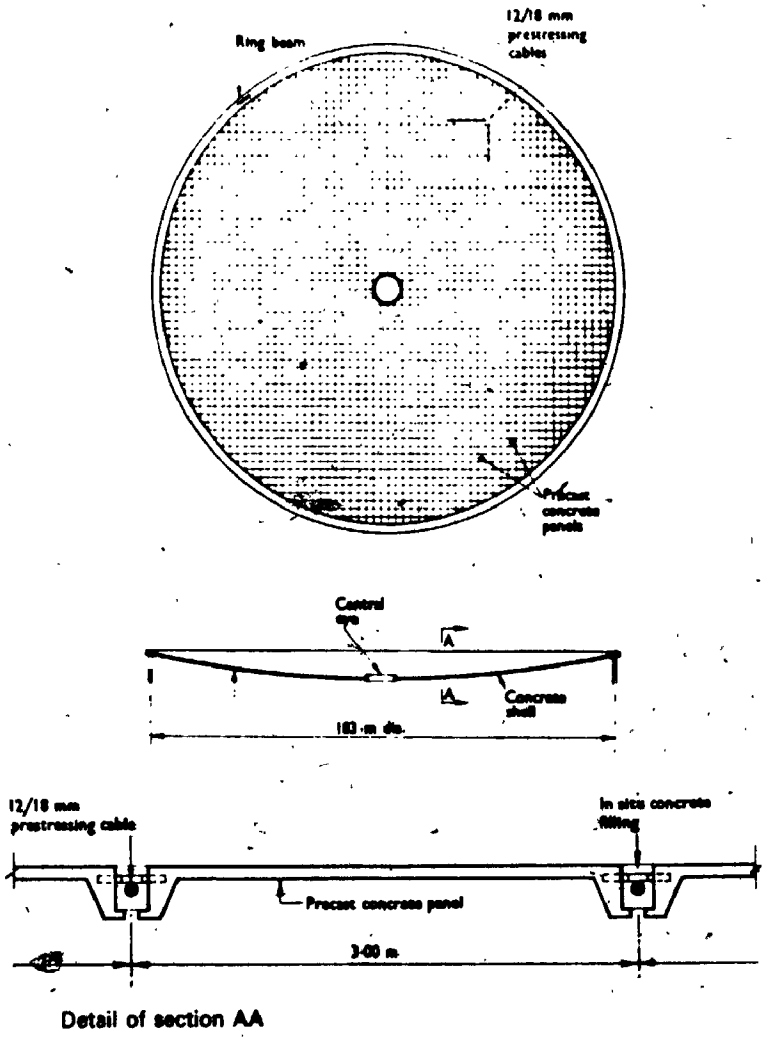

FIGURE (1.6a) Concrete Panels Suspended Between Cables

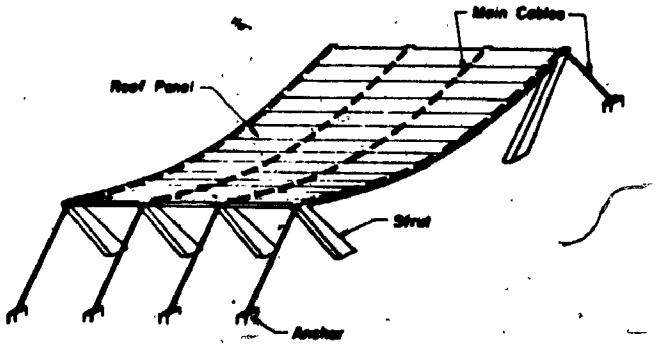

FIGURE (1.6b) Roof Panels Installed Along Parallel Cables

These relationships play a decisive part in the structural and architectural mastery of suspension roofs.

1.3.3 Structural and Architectural Considerations

Many forms of suspension roofs are possible and there is a variety of configurations of cable roofs that can be used. If adequately treated, structural suspension systems offer numerous forms, not only for roofs but for the entire building.

The type of suspension system selected, whether single or double layer, anticlastic or synclastic, stiffened by flexural members or unstiffened, self-anchored or externally anchored, is largely dependent on structural considerations and architectural requirements. The configuration of the cable system is influenced to a great extent by structural considerations such as, for example, foundation conditions which may determine whether the system is self-anchored or externally anchored, the method of stabilizing the roof against undesirable response to dynamic loading, and the choice of dimensional parameters such as clearance, sag, and inclination of anchor stays so as to minimize the forces in the cables.

1.3.4 Method of Design

The most common methods of design for single layer

systems, stated by Zetlin [5], are:

a. Catenaries

This is the most elementary structural suspension system and it requires end towers and abutments to resist the tension in the catenary. It also requires a stiff structure to eliminate flutter of cables.

b. Tents

This system consists basically of parallel cables or cables radiating from one support point to abutments with the roofing material spanning the cables. It may require vertical posts within the covered space. The cables are essentially sloping catenaries designed by statics only, so that there is no attempt to solve the flutter problem.

c. Prestressed Catenaries

Where a clear span unobstructed by central supports is required, suspension roofs consisting of radial cables with central tension ring and external compression ring can be used, Figure 1.3a. As decking, precast or poured-in-place concrete panels may be used.

d. Grid Meshes

To avoid flutter in prestressed catenaries, without adding heavy weight, meshes of interlacing cables are often

used. In some cases, these surfaces have reverse curves created by cables having opposite curvatures, Figure 1.7a. Usually, the convex cables have an initial tension and pull against the concave cables. Other examples of this type are the saddle-shaped and diamond-shaped cable-suspension roofs, Figures 1.7b and 1.7c.

As compared to simply suspended cable roofs, a much stiffer design makes use of cables in two layers. In order to achieve the necessary stability, the cables in two layer systems are prestressed. This results in increased horizontal peripheral forces together with an increased downward loading on the sagging cables in the form of a reaction transmitted from the hogging cables. The two-layer systems fall into two principal categories [3]:

a. Lens-shaped systems which are circular or elliptical in plan.

b. Systems which are rectangular in plan.

In lens-shaped systems, the peripheral horizontal forces are usually resisted by a ring beam which is stressed primarily in compression. The cable layout can be either radial as in the case of a 'bicycle wheel' system, Figure 1.8a, or rectilinear in the form of a square grid, Figure 1.8b. In either case, the average resultant peripheral forces under uniform loading are primarily radial. The

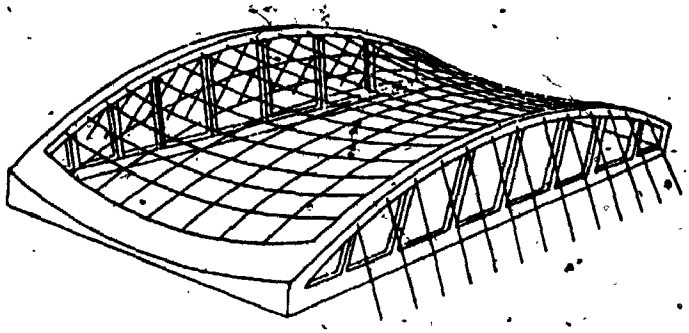

FIGURE (1.7a) Double Curvature Cable Net

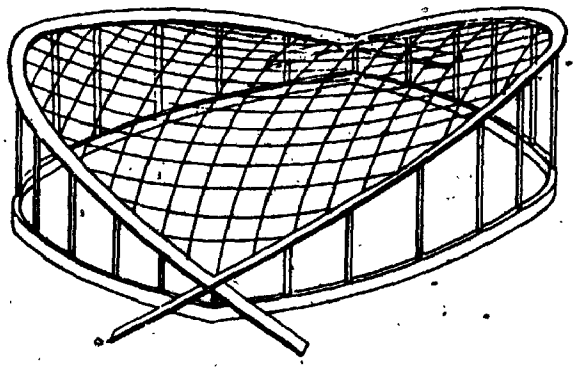

FIGURE (1.7b) Saddle-shaped Cable Net

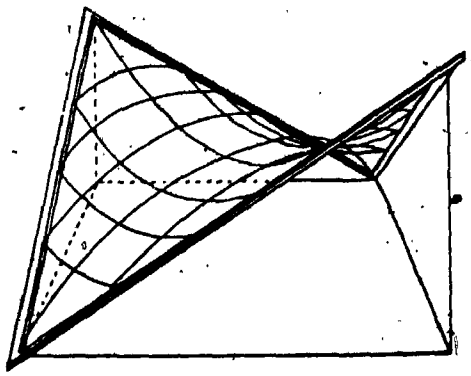

FIGURE (1.7c) Diamond-shaped Cable Net

cables can be arranged in the form of a convex lens, a concave lens, or an intermediate shape (a double ring beam being required in the latter two instances), Figures 1.8c and 1.8d. The upper and lower layers are linked structurally by means of struts in the convex design and ties in the concave design.

For systems which are rectangular in plan, a ring beam solution is not often feasible and anchorages must be provided to resist the horizontal peripheral forces. The cable layout usually differs from that of lens-shaped systems in that the cables are arranged in parallel trusses spanning in one direction only, as shown in Figure 1,8e. However, in the two-layer systems, either of the two layers can be used to pretension the other through the web members. The cladding can be placed directly on the upper or the lower cables. The cables carrying the cladding are often called the carrying cables and the others are the damping and/or pretensioning cables, Figure 1.9. In general, the double-layer systems are primarily used to dampen the suspension roofs against flutter and to produce a high degree of rigidity.

1.3.5 Method of Erection

The sequence of erection of cable-suspension roofs is fairly uniform for all types of structures.

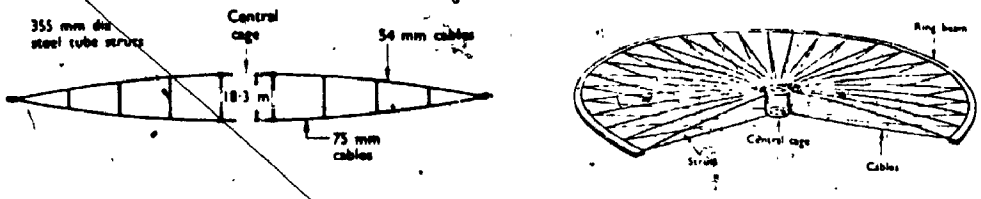

FIGURE 1.8a Cross-section of Bicycle Wheel-shaped Roof, (Circular in Plan)

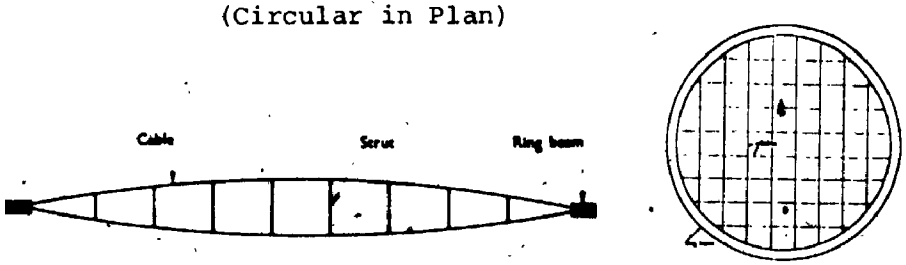

FIGURE 1.8b Cross-section of Convex Type Lens-shaped Roof

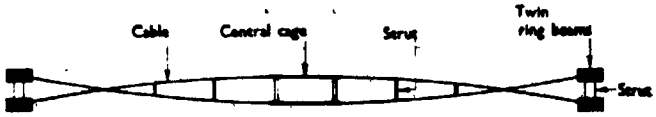

FIGURE 1.8c Cross-section of Intermediate Type Lens-shaped Roof

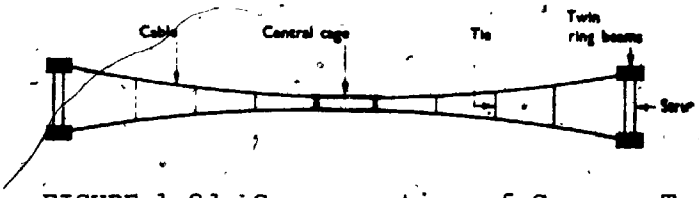

FIGURE 1.8d Cross-section of Concave Type Lens-shaped Roof

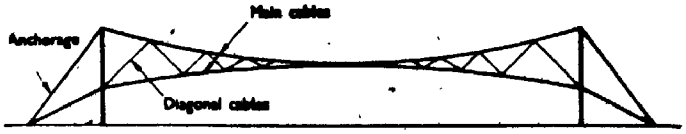

FIGURE 1.8e Cross-section of Truss-shaped Roof

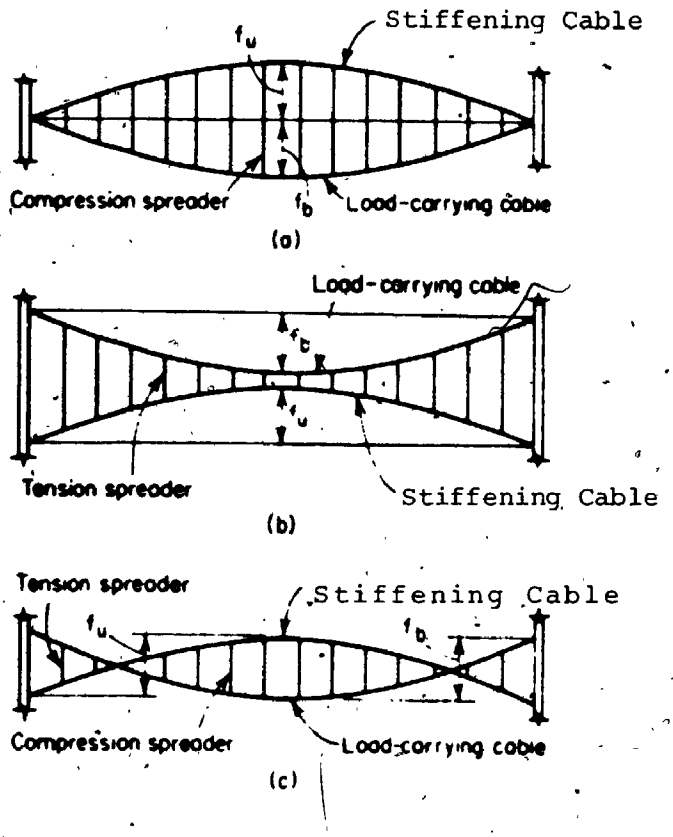

FIGURE 1.9 Stiffening Systems in Cable Roof Structures

Construction begins with cable supports which include anchorages, buttresses, rings, masts, etc. Next, the cables are placed and adjusted to some preliminary position. Roofing and other dead loads to be supported by the cable system are then placed on the structure without tight interlocking. The cables are then given a final adjustment before proceeding with tightening the supported structure and finishing the roof surface.

In net systems, the main cables are placed and adjusted for position. After the system of cross cables is placed, the net is prestressed by jacking a tension force into the cross cables. The tension in the main cables is usually not measured or directly controlled. An alternative to net systems placement, the cables are partially or wholly preassembled on the ground and then lifted into position together.

In radial systems, the load-carrying cables reach maximum tension prior to live load application under full dead load. The scaffolding under the tension ring is generally set low enough that the ring rises off the scaffolding as the latter part of dead load is applied.

In double-layer systems, only the preload or stiffening cables reach maximum tension when the struts or ties are inserted. As dead load is applied, the tension in the load-

carrying cables increases and the tension in the preload cables decreases.

Practice appears to vary as to whether another adjustment of individual cables is made after the dead load is in place. In radial systems, where uniform loading on the rings is important, a final cable adjustment is common.

Precast concrete panels may be used as infilling in prestressed catenaries and grid mesh systems, forming dished shell roofs of circular or elliptical shape in plan. After the cables are placed and adjusted to some preliminary position, the panels are hung on the cables; then the cables are stressed in predetermined sequences until the weight of the panels is fully balanced by the upward component of the cable, as described by Lin and Young [6]. Grout is placed between the panels. This is done in several stages, each stage being balanced by additional post-tensioning in the cables. Finally, the cables receive final stressing to provide for live load.

1.3.6 Difference Between Cable Systems and Shells

A distinguishing difference in behaviour between pure cable systems (catenaries) and shell systems is that the former are prone to much higher deflection. This difference is due to the fact that in pure cable structures, deflection under load is related to the cross-sectional area of the

cables and Young's modulus for steel.

In a prestressed concrete shell structure, however, deflection is related to the cross-sectional area of concrete and Young's modulus for concrete. Because the ratio of concrete/steel cross-sectional area is usually much larger than the ratio of the two values of Young's modulus, the deflections experienced by concrete shells are of the order 1/10 of those for a corresponding pure cable structure.

1.3.7 Design Principles

It is a significant feature of cable-suspension roofs that they cannot be designed in the conventional sense (i.e., as typical rigid buildings) [2,4,5]. As there are no flexurally rigid elements which permit a certain amount of freedom of shape, but only non-rigid elements (cables), therefore the shape of cable-suspension roofs is determined by loading, span and sag.

The main supporting elements in suspension roofs are the cables, which must be designed to withstand their own weight, infilling and the superimposed loading.

The principal causes of superimposed loading are: snow, hail or ice in cold climates, sand or dust in arid climates, rainwater buildup on dished roofs, wind forces, suspended services (such as rain drainage services),

maintenance loads, erection loads including prestress forces, and such effects as temperature changes, cable stretch and the creep and elastic deformation of reinforced concrete supporting elements.

Regarding the effect of wind loads, this can be assessed by wind tunnel tests especially in the case of large roofs. However, it is probable that the majority of existing structures with up to 80 m (270 ft) span have been designed only on the basis of code of practice values for both downward and upward static wind loading.

The design process for pure double-cable systems (catenaries) for symmetrical loading is as follows [3]:

1. A depth-span ratio is chosen.
2. The size and number of the top and bottom cables are chosen.
3. A prestress for the top and bottom cables is assumed. The geometry of the cable-suspension roof is determined under the prestressing only.
4. The dead load is applied, and the alteration in cable stress and consequent change in geometry is evaluated.
5. The superimposed load then is applied, and the changes in cable stress and geometry are again evaluated.
6. A check is to be made that the allowable stresses are not exceeded and that the geometry of the system is

adequate for practical purposes at each stage. If the result is unsatisfactory, the process is repeated until all the criteria are satisfied.

In a circular roof with a symmetrical cable layout in plan, the calculation for symmetrical loading can be carried out for a single truss in isolation. For nonsymmetrical layouts, or for asymmetrical loading arrangements, it is necessary to consider the whole roof structure, including the ring beams as an interrelated structural system.

The design process for a double-curvature net is basically similar to that for a two-layer system.

The design of a shell-type cable structure is subjected to two entirely different structural states. During the construction of the concrete shell, the system behaves as a pure cable structure. After the completion of the shell erection and application of prestress, it acts as a prestressed concrete shell structure.

The design and construction process for typical dished shell systems is as follows:

1. A construction system is chosen having regard for the economic and other factors prevailing at the site.
2. The thickness of the shell and all dimensions of any ribbing are assumed.

3. A sag-span ratio is assumed and the structure is designed as a normal shell subject to the required loading conditions.
4. The ring beam is designed as part of the shell structure.
5. The size and number of cables necessary to give the prestress required to neutralize shell tension stresses are evaluated.
6. The exact construction sequence is determined.
7. The cable network, including the ring beam, is analyzed sequentially for every loading combination during construction.
8. A check is made on the cable stresses and geometry at each stage and the process repeated until all the criteria are satisfied.

1.3.8 Other Design Considerations

The flexibility and light weight of very large suspension roofs make wind tunnel tests on aerodynamic models desirable, if not essential, to establish wind loading and to assess the dynamic behaviour of the roof.

In design practice, the current approach to the design of suspension roofs for dynamic loading is to choose cable parameters such that the frequencies of anticipated exciting forces will never occur in the vicinity of a cable natural

frequency, and if it occurs the amplitude of vibrations is to be reduced. Zetlin [5] stated that one way to avoid having a frequency ω in the vicinity of the natural frequency, ω_n, is to increase the mass supported by the cable. To increase mass on a cable (catenary) is to increase geometrical stiffness, thereby increasing the frequency.

The amplitude of vibration decreases for a given forcing function and damping coefficient as the cable stiffness increases. Therefore, for a given cable tension, the greater the dead load, the greater the cable tension, the stiffer the cable and thus the amplitude of vibration is reduced.

If the cable is damped, the increase in amplitude at resonance is lowered.

The current practice indicates that, by providing damping, the unpredictability of the forcing frequency and the natural frequency of the entire suspension roof need not be a concern to the designer, provided that the damping is adequate to restrict the amplitude of vibration to an acceptable value.

An efficient method for increasing the stiffness of suspension roofs is to use two interconnected curved cables, Figure 1.9.

The current design practice is to utilize a configuration

of a double layer system consisting of primary and secondary cables [5,16,17]. Primary and secondary cables are usually erected in pairs, one below the other, separated by struts or ties which are inserted in a manner such as to prestress the primary and secondary cables of the pair against each other. This method of construction will increase the natural frequency of the cable system due to the increase in its stiffness.

Other effects that should be considered in design include cable stretch and support displacements. Cable stretch influences the configuration of the cable system and thereby the force in it. The displacements of the supporting structural members should be considered in the design of the suspension system, including the long term displacements resulting from creep and shrinkage of reinforced concrete members.

1.3.9 Economics

Architects and engineers have a strong interest in utilizing suspension systems for supporting roofs covering large areas. This interest results primarily from two factors: The first is aesthetic: the variety of roof forms and building shapes possible with suspension systems presents many opportunities for architectural expression, the second is economic.

For large roofs, the cost per unit area of a roof structure rises very approximately in a linear fashion. In terms of the direct structural costs, therefore, long-span roofs may not prove more economical than shorter spans but their construction may well affect the usefulness of the covered space. For example, in countries with severely hot or cold conditions, uncovered sports stadia cannot be used during the severe seasons. If these stadia are covered, it could lead to greater interest in sports as well as increased economic gain. Furthermore, suspension systems may be less expensive than other structural systems for supporting large span roofs when high-strength cables are used. The high-strength cable is approximately six times as strong as structural steel, which results in less weight of structural material but costs only about twice as much per kilogram. Furthermore, it is as easy to string a 100 m cable as a 10 m one.

In a suspension roof, the cables themselves and their erection represent the smaller portion of their cost; the larger portion is in the fitting, their connections, and the anchorage members. Because of this, suspension roofs are not likely to be economical for spans less than about 122 m, Table 1.1, [8], unless the design and method of erection eliminate fittings and anchorage at the end of each cable, as when a ring beam system is used instead of

cable truss system or when a continuous cable is used to transverse (across) a smaller span several times. With large spans, however, cables become extremely economical since the cost of fittings per unit area covered is reduced. This emphasizes an important potential of long-span suspension roofs: their cost per unit covered area tends to decrease, if truss cables are used, and increase slowly if ring beam systems are used. On the other hand, the cost of conventional framing increases more.

The variation of the quantities of materials in cables and ring beams as well as the overall cost of roof per unit area with spans are shown in Figures 1.10 to 1.12. These quantities were collected by Butler [3]. The cost is based on prices in England in the 1970s. It should be noted that the cost per unit area of many of the major elements such as cladding, waterproofing, finishing, fire protection, pumps and foundations remains roughly constant.

Because of the relatively low cost of the cables as a proportion of the whole, the overall cost increases slowly in relation to the span. In the cable truss systems, the cost of anchorages and foundations is much higher than the column and foundation cost for ring beam systems. This fact has to be borne in mind when considering the unit weights shown in Figure 1.11.

TABLE 1.1 Comparison of Costs of Various Roof Systems [8]

Span	Cable	Arch	Truss	Plate Girder
30·5 m (100 ft)	100%	82%	92%	118
61 m (200 ft)	100%	82%	100%	—
91·5 m (300 ft)	100%	94%	—	—
122 m (400 ft)	100%	—	—	—

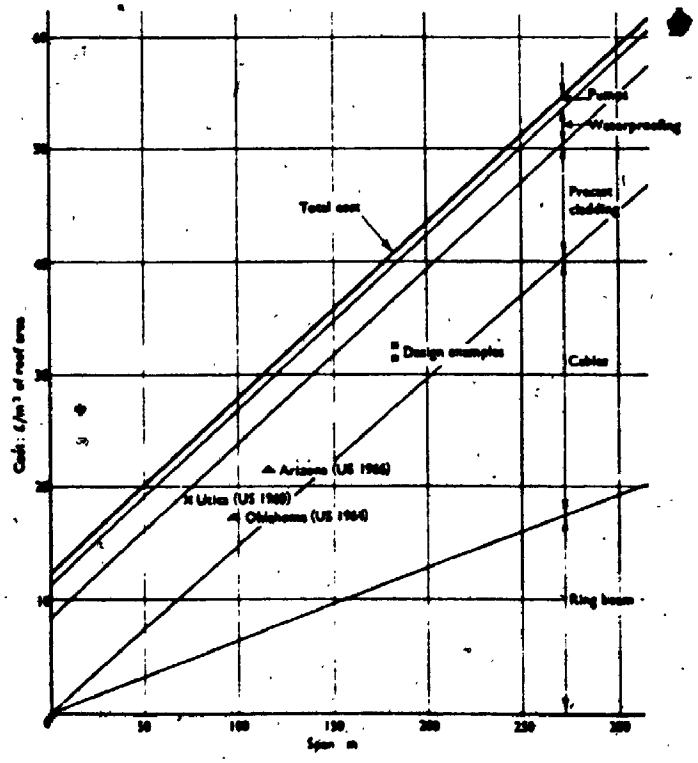

FIGURE 1.10 Estimated Cost of Dished Shell Roof in Relation to Span [3]

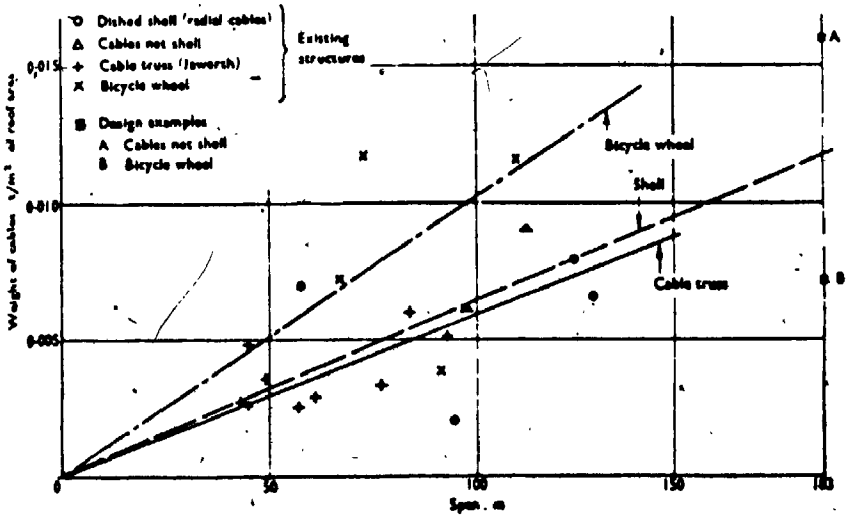

FIGURE 1.11 Weight of Steel in Cables in Relation to Span [3]

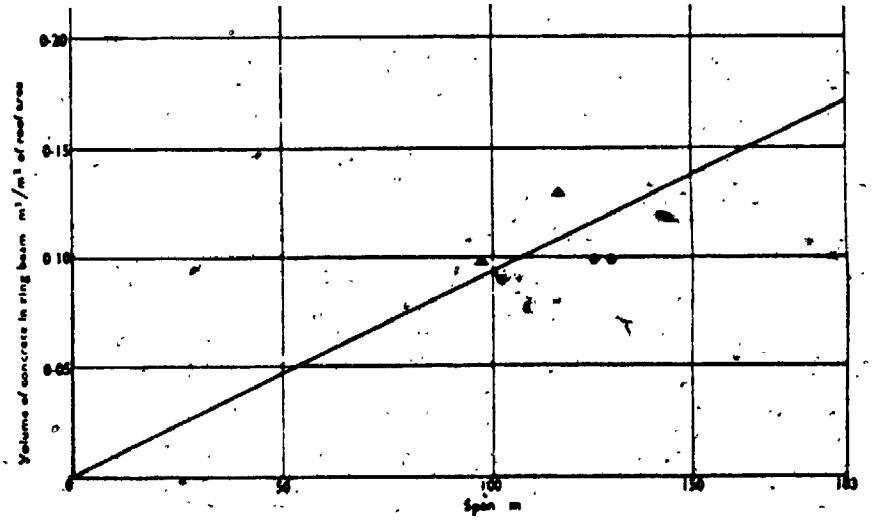

FIGURE 1.12 Volume of Concrete in Ring Beam in Relation to Span [3]

The cost of ventilation, heat and air conditioning, essential in sports stadia, must be considered and sometimes it is relatively high compared to the cost of the roof structure.

The cost information available indicates that cable roofs are strikingly economical for spans of 120 m to 170 m. Extensions made from existing data show that this economy is likely to continue up to spans of 300 m and more.

1.3.10 Advantages and Disadvantages

Suspension systems may have aesthetic and economic advantages for long span roofs. However, because of their flexibility and light weight, some factors must be considered in design which may be neglected for roofs having more conventional framing.

Erection times are quite short in cable roof construction. A roof of about 7,000 square metres area was completed in four weeks [2]. The time required to place the decking was the major portion of the total, while actual cable placement time was much less.

Another great advantage in erecting cable roofs is the small amount of scaffolding required. Cantilevers,

parallel systems and nets can be constructed with no temporary support for the roof. Radial systems require temporary support only for the tension ring.

In light roof structures, especially those with low inherent stiffness, gusts and turbulence may cause vibration or flutter of a local portion of the roof or of the roof as a whole. This tendency is common in cable-suspension roofs and in some cases the resulting oscillations may be destructive.

A qualitative analysis can be conducted on relatively simple models using rather crude equipment to investigate tendencies to flutter. If flutter is anticipated, it is usually possible, for very little added initial cost, to provide a stiffening system which will damp such oscillations.

In large covered stadia, a high degree of natural lighting can be achieved by using a pure cable structure and by substituting transparent roof cladding for the more usual opaque type.

With shell systems, partial natural lighting can be achieved by providing a large central opening which is roofed by a pure cable structure incorporating transparent roof cladding or by being left uncovered.

The type of roof cladding can have an important effect on the heat gain or loss in a building. For example, the use of large areas of transparent cladding can lead to a substantial buildup of heat within the building.

By providing an opaque roofing material having reasonable insulation properties, a standard of spectator comfort appropriate to sports activities can be achieved at low services cost.

1.4 DEVELOPMENTS IN CABLE-ROOF ANALYSIS

Most of the developments in the analysis of cable-roof systems have taken place after 1950, although some work on the subject was reported earlier as well. Two points most relevant to theoretical analysis are to be emphasized.

A cable exhibits a marked nonlinear behaviour when loaded and the degree of nonlinearity varies with the type of cable structure as well as loading. It is necessary to distinguish this nonlinearity, which may be called geometric nonlinearity, from possible material nonlinearity. In order to sustain loads, a cable has to follow the funicular curve of the loads and undergo large geometric adjustments, particularly when the loading is concentrated or asymmetric. Geometric nonlinearity will therefore occur in cable behaviour irrespective of whether the cable

material has a linear or nonlinear stress-strain curve. Nonlinearity is more pronounced in roofs where cables are not pretensioned. The other problem that demands analytical skill is the generally high degree of indeterminacy of these systems.

The problem of analyzing cable systems can prove to be quite complex in general but simplifying assumptions can be made to reduce the effort required, particularly for preliminary design work. There are two broad categories into which the development of cable-roof analysis can be placed, depending upon whether the network is treated as a continuous membrane, or a discrete system. In almost all analytical procedures published for cable roofs the contribution of the cladding to the stiffness of the network is disregarded. That being the case, the bare network is in fact a discrete system and its treatment as a continuum is an approximation. Analytical procedures on the basis of the continuum approach have been used to produce simplified approximate formulae for computations of cable systems.

If the structure is treated as a discrete system, any method of analysis must basically lend itself to the solution of stiffness or flexibility matrices set up for the structure. The continuous approach leads to a set of

nonlinear differential equations. The use of iterative procedures becomes imperative for the solution of this nonlinear problem.

Most of the analytical studies on cable systems have assumed the supporting structure of the roof to be rigid. However, evaluation of the effect of the support flexibility, which can be considered, has engaged the attention of researchers also [9,10,11]. A better understanding of the cable roof and the supporting structure, in relation to each other, is leading to a gradual departure from the early practice of making massive supporting beams.

It can be said in general that the problem of analyzing cable networks for static effects has been adequately met during the 30 years of their development after the 1950s but there is only a meager amount of information available on the dynamic analysis of suspension roofs.

Cable roofs are flexible long-span structures and as such are prone to significant aerodynamic excitation. Some existing roofs of this type have shown a tendency to flutter, but there is little work reported on the assessment of aerodynamic behaviour of cable roofs [12,13,14].

Cable roof structures belong to the class of light and flexible structural systems which are sensitive to

vibrations. Therefore, the design and construction of these structures require an examination of the dynamic behaviour. An examination of the dynamic behaviour of cable roof structures is necessary to ensure a safe and serviceable structure design. The examination can be separated into two parts:

a. the determination of the actual forces
b. the analysis of the structure for the acting forces

Today, the development of computing methods has made possible calculations of great accuracy. Nevertheless, there is a lack of information about the load condition and there is a need to examine the assumptions under which the calculations are made. An interaction between theoretical and experimental methods is, therefore, of importance. A possible way to examine the dynamic problems of cable roof structures is shown in Figure 1.13. Theoretical research includes the development of analytical and numerical methods to analyze cable structures. On the other hand, the experimental work has to prove the assumption on which a theoretical calculation is based, and to verify theoretical considerations.

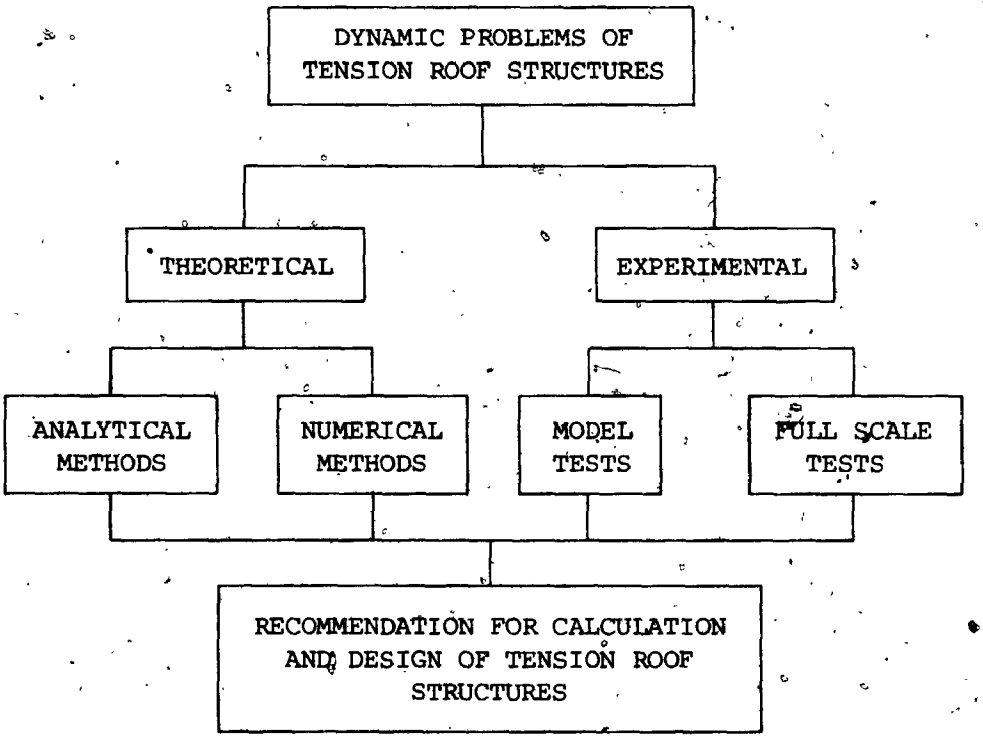

FIGURE 1.13 Researching Themes of Dynamic Problems of Cable Roof Structures

CHAPTER 2

STATIC ANALYSIS

2.1 STATIC ANALYSIS OF A SINGLE CABLE

2.1.1 Introduction

Cable roofs are by their definition composed of cables having different shapes in plane and many possible arrangements. The main element in the system is the single cable.

Galileo in "Discourses On Two New Sciences", published in 1638, muses on the shape of a hanging chain and concludes that it is parabolic. Bernoullis (James and his brother John), Leibnitz and Huygens more or less jointly discovered the catenary [18], the word coming from the Latin for chain and meaning universally the form of a chain hanging between two points.

In the discovery of the catenary different approaches were employed, with Huygens relying on geometrical principles and Leibnitz and the Bernoullis using the calculus, then a comparatively recent invention.

The nature and applications of the exact and approximate classical solutions for the static response of a single cable are explored first.

2.1.2 The Catenary

A uniform inextensible cable, or chain, that hangs between two fixed points that are at the same level assumes the shape of a catenary.

The elements of the cable are assumed to be perfectly flexible, with no flexural rigidity: the cable can sustain only tensile forces. An elegant way of describing this pure cable behaviour is that attributed to James Bernoulli [18], "The action of any part of the line upon its neighbour is purely tangential".

By applying the second law of Newtonian mechanics to an isolated segment of the cable, located at (x,z) in Figure 2.1, and recalling that the downward force for each segment of length is proportional to the arc length ds, given by the geometrical constraint

$$(\frac{dx}{ds})^2 + (\frac{dz}{ds})^2 = 1 \qquad (2.1)$$

the vertical equilibrium of the segment yields

$$mg\Delta s + T\frac{dz}{ds} + \frac{d}{ds}(T\frac{dz}{ds})\Delta s - T\frac{dz}{ds} = 0$$

This equation reduces to

$$\frac{d}{ds}(T\frac{dz}{ds}) = -mg \qquad (2.2)$$

where T is the tension in the cable, $\frac{dz}{ds}$ is the sine of the

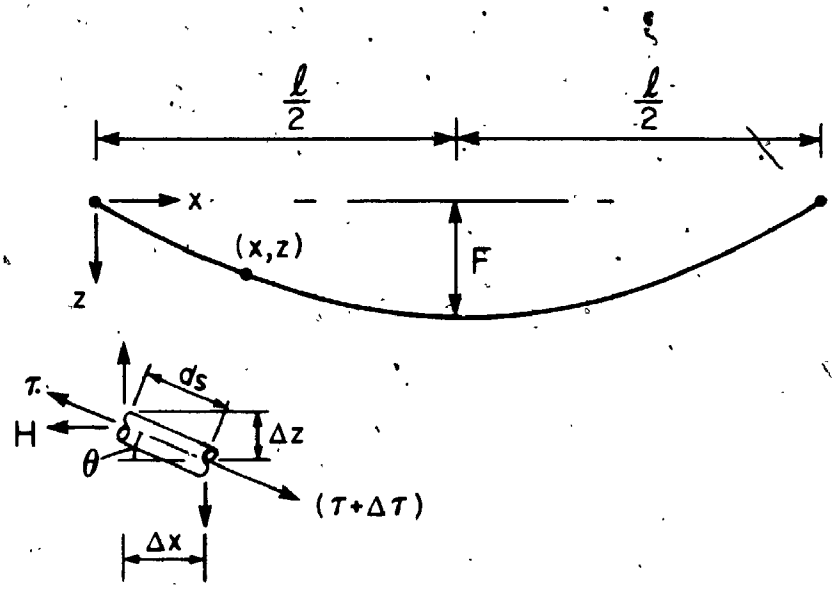

FIGURE 2.1 STATIC EQUILIBRIUM OF CATENARY

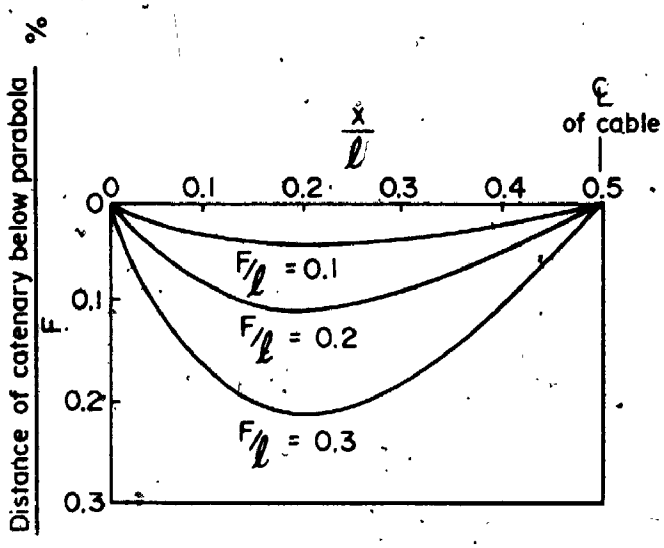

FIGURE 2.2 DIFFERENCE BETWEEN THE ORDINATES OF A PARABOLIC CABLE ARC AND A CATENARY HAVING THE SAME SPAN AS WELL AS CENTRAL SAG (FROM [20])

angle (θ) subtended to the horizontal by the tangent to the curve, and mg is the self-weight of the cable per unit length. Horizontal equilibrium of the segment yields

$$T \frac{dx}{ds} = T \frac{dx}{ds} + \frac{d}{ds} \left(T \frac{dx}{ds}\right) \Delta s$$

which reduces to

$$\frac{d}{ds} \left(T \frac{dx}{ds}\right) = 0 \quad \text{since } \Delta s \neq 0 \tag{2.3}$$

where $\frac{dx}{ds}$ is the cosine of the angle of inclination θ.

Equation 2.3 may be integrated directly to give

$$T \frac{dx}{ds} = T \cos\theta = \text{const} = H_o \tag{2.4}$$

where H_o is the horizontal component of cable tension which is constant everywhere, since no longitudinal loads are acting; substitute Eq. 2.4 into Eq. 2.2 and rearrange. We get

$$H_o \frac{d^2z}{dx^2} = - mg \frac{ds}{dx} \tag{2.5}$$

Substitute Eq. 2.1 into Eq. 2.5, giving

$$H_o \frac{d^2z}{dx^2} = -mg \sqrt{1 + \left(\frac{dz}{dx}\right)^2} \tag{2.6}$$

This is the governing differential equation for the cable hanging under its own weight; the same equation applies

for any permanent superimposed load uniformly distributed along the whole arc length with mg replaced by (mg + q), where q is the permanent uniformly distributed load per unit length of arc.

Equation 2.6 could be obtained directly if Newton's second law is applied for the whole cable in the vertical direction and differentiated twice with respect to x.

Integrate Eq. 2.6 twice, substituting the boundary conditions

$$z = 0 \quad \text{at } x = 0 \tag{2.7a}$$

and

$$z = 0 \quad \text{at } x = \ell \tag{2.7b}$$

It can be seen that a solution that satisfies Eq. 2.6 and the boundary conditions (2.7) gives the equation

$$z = \frac{H_o}{mg} \left\{ \cosh \left(\frac{mg\ell}{2H_o} \right) - \cosh \frac{mg}{H_o} \left(\frac{\ell}{2} - x \right) \right\} \tag{2.8}$$

as the response of the cable for uniformly distributed load, along its arc.

This equation also could be obtained directly by applying the energy approach, by minimizing the potential energy consistent with its constraints [19].

From equations 2.1 and 2.8, the length of a portion

of the cable is given by

$$s = \int_0^x \sqrt{1 + \left(\frac{dz}{dx}\right)^2}\, dx$$

$$= \frac{H_o}{mg} \left\{ \sinh \frac{mg\ell}{2H_o} - \sinh \frac{mg}{H_o} \left(\frac{\ell}{2} - x\right) \right\} \qquad (2.9)$$

For $x = \ell$,

$$L_o = \frac{2H_o}{mg} \sinh \left(\frac{mg\ell}{2H_o}\right) \qquad (2.10)$$

where L_o is the length of the cable. If a cable of length L_o is used to span between two fixed points at a distance ℓ, the horizontal component of cable tension may be found by solving Eq. 2.10. The tension T in the cable at any point with abscissa x, is determined from Eqs. 2.2 and 2.9 as

$$T = H_o \cosh \frac{mg}{H_o} \left(\frac{\ell}{2} - x\right) \qquad (2.11)$$

Also, the maximum sag F is determined for $x = \ell/2$ in Eq. 2.8 as

$$F = \frac{H_o}{mg} \left[\cos \left(\frac{mg\ell}{2H_o}\right) - 1\right] \qquad (2.12)$$

2.1.3 The Parabola

When the sag/span ratio of the cable is small (1:8 or less), simplifications can be made; this often corresponds to the situation where cables with relatively low sag are used for cable roofs.

The weight of a freely hanging cable of constant cross section is, in fact, distributed uniformly along its length. As stated in the previous analysis, the catenary is the exact solution to the differential equation for response due to self weight. However, the approximation is to assume the weight mg to be distributed uniformly along the horizontal length of span between two supports.

This approximate theory provides explicit, consistent methods for finding static response accurate to the third order of small quantities. By following a similar treatment to that in the analysis of the catenary, the differential equation governing equilibrium of a segment of the cable in the vertical is accurately specified by

$$H_o \frac{d^2z}{dx^2} = -mg \qquad (2.13)$$

and in the horizontal direction by

$$T \frac{dx}{ds} = H_o \qquad (2.14)$$

The exact equation for the vertical direction is

$$H_o \frac{d^2z}{dx^2} = -mg \{1 + (\frac{dz}{dx})^2\}^{1/2}$$

so, in assuming the profile is almost flat, we are choosing to ignore $(dz/dx)^2$ in comparison to unity, or in other

words, we assume ds $\simeq$ dx in Eq. 2.5, as the load acting on the cable is projected along its horizontal span.

Integrating Eq. 2.13 twice and applying the boundary condition from Eq. 2.7, the geometry of the cable reached is

$$z = -\frac{mg}{H_o}\frac{x^2}{2} + C_1 x + C_2$$

where C_1 and C_2 are integration constants to be determined from the boundary conditions,

$$\text{for } z = 0 \quad \text{at } x = 0 \quad C_2 = 0$$

$$\text{for } z = 0 \quad \text{at } x = \ell \quad C_1 = \frac{mg\ell}{2H_o}$$

gives

$$z = \frac{mg\ell}{2H_o} x - \frac{mg}{2H_o} x^2 \qquad (2.15a)$$

In nondimensional form

$$Z = \frac{1}{2} X(1-X) \qquad (2.15b)$$

where $X = \frac{x}{\ell}$, $Z = \frac{z}{(\frac{mg\ell^2}{H_o})}$

The complete geometry of the cable can be defined if the value of H_o is specified or the coordinates of any point on the parabolic curve are known.

The horizontal component of cable tension is easily obtained by considering half of the cable span as a free body. Taking moments about one of the supports,

$$H_o = \frac{mg\ell^2}{8F} \tag{2.16}$$

where F is the sag. The cable length is

$$L_o = \int_o^{\ell} [1 + (\frac{dz}{dx})^2]^{1/2} \, dx \tag{2.17}$$

Substituting the value of Z from Eq. 2.15, expanding the expression binomially and integrating the expression for the length L_o, we obtain

$$L_o = \ell[1 + \frac{8}{3} (\frac{F}{\ell})^2 + \frac{32}{5} (\frac{F}{\ell})^4 + \ldots] \tag{2.18}$$

In these calculations, the effect of cable stretch can be assumed to have been accounted for.

The difference between the catenary and the parabola for different values of F/ℓ is shown in Figure 2.2, [20]. The difference in geometry is almost negligible for F/ℓ ratios within practical range. It is sufficiently accurate, therefore, to treat the curve of a freely hanging cable as parabolic in order to ascertain its geometry.

2.1.4 Cable Deformation

If the two ends of a cable are fixed in space with

span ℓ and sag F, and it hangs under its own weight, the cable length L_o, between those two points, can be changed for the following reasons: [20],

1. cable extension due to its tension
2. temperature change
3. slip of the cable at a support.

In any case, if the change in the sag of a cable due to change in the length can be computed, it is possible to set up the new geometry of the cable.

From Eq. 2.14, the tension in the cable at any point is

$$T = H_o\left(1 + \frac{64F^2x^2}{\ell^4}\right)^{1/2} \qquad (2.19)$$

and the change in length ΔL_o, due to elastic stretching, is given by

$$\Delta L_o = \int_o^{L_o} \frac{T dL_o}{AE} \qquad (2.20)$$

By integrating Eq. 2.20, we get

$$\Delta L_o = \frac{H_o L_o}{EA}\left(1 + \frac{16}{3}\frac{F^2}{\ell^2}\right) \qquad (2.21)$$

where, A = cable cross section and E = its modulus of elasticity. Similar treatment could be followed for temperature change and slip of the cable at the support.

2.1.5 Nonlinear Response of Cable to Vertical Load

Around the middle of the nineteenth century, theories were developed proposing approximate analyses for the behaviour of a heavy parabolic cable under various types of applied loading, partly by Rankine in 1858 but mainly by anonymous writers in 1860 and 1862. It was realized at this time that the response of the cable was nonlinear.

The problem of analyzing a freely suspended cable with level supports has been treated in numerous papers [18,20,21,22] but a simplified solution can be developed as follows. We will consider the case of single load to understand the behaviour of the cable; this will be needed later in the understanding of the behaviour of cable roofs under static loading.

The equations of equilibrium were solved in this work in a straightforward manner and compatibility of displacements was satisfied by cable equations in which all important terms were retained.

Simplifications can then be made to the general result. The solutions may be linearized or adapted to apply to cables that are initially taut and flat. In either case, the results are considerably simplified.

The cable AB, shown in Figure 2.3, has a dead weight

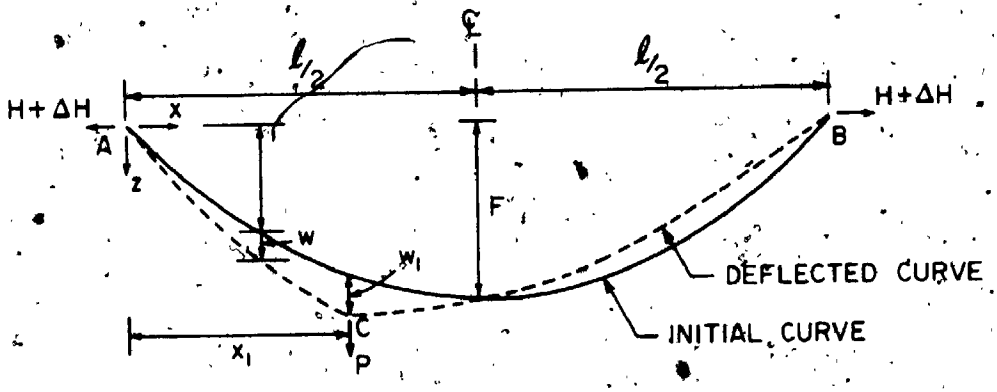

FIGURE 2.3 CABLE SUBJECTED TO A CONCENTRATED LOAD

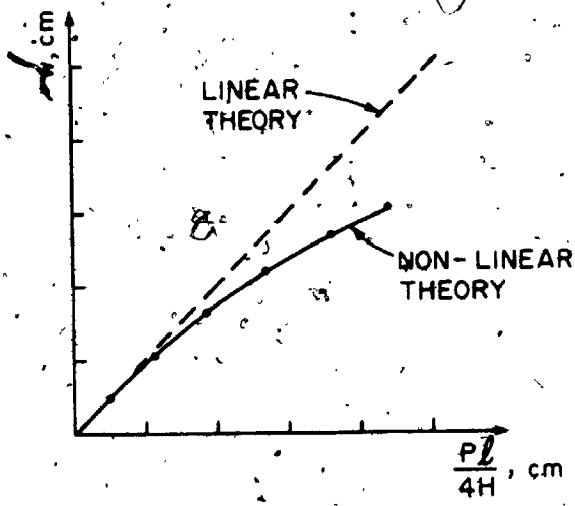

FIGURE 2.4 COMPARISON OF LINEAR & NON-LINEAR RESPONSE OF SINGLE CABLE DUE TO CONCENTRATED LOAD [FROM 18]

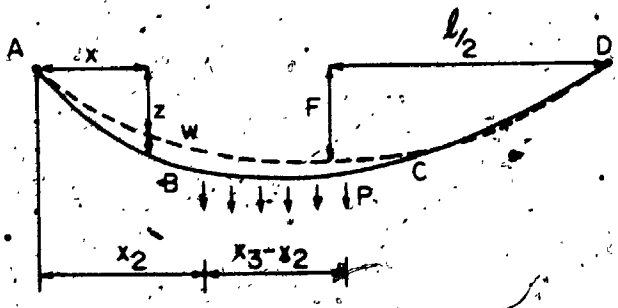

FIGURE 2.5 CABLE SUBJECTED TO UNIFORMLY DISTRIBUTED LOAD

(mg + q) per unit length of span and is hanging initially in the shape of a parabola. The geometry of the cable is described by Eq. 2.15 and the horizontal component of cable tension H_o is given by Eq. 2.16. A point load P is applied at a distance x_1 from the left hand support. Provided that additional movements of the cable are small, and the profile remains relatively shallow and in the deflected position, the cable can be considered to consist of two parts, curves AC and CB, with first derivative discontinuity at C. Vertical equilibrium of a free body at a cross-section x, of the cable requires that

$$(H_o+\Delta H)\frac{d}{dx}(z+w) = P\left(1 - \frac{x_1}{\ell}\right) + \frac{mg\ell}{2}\left(1 - \frac{2x}{\ell}\right) \qquad (2.22)$$

$$\text{for } 0 \leq X \leq x_1$$

where w is the additional vertical cable deflection and ΔH is the increment in the horizontal component of cable tension, owing to the point load.

The right-hand side of Eq. 2.22 is analogous to the shear force in a simply supported beam of uniform weight under the action of a point load.

Rearranging Eq. 2.22 gives

$$(H_o+\Delta H)\frac{dz}{dx} + (H_o+\Delta H)\frac{dw}{dx} = P\left(1 - \frac{x_1}{\ell}\right) + \frac{mg\ell}{2}\left(1 - \frac{2x}{\ell}\right)$$

Since

$$H_o \frac{dz}{dx} = V = \frac{mg\ell}{2} - mgx = \text{shear at C}$$

in which $\frac{mg\ell}{2}$ = Reaction at A, mgx = load up to x.

Therefore,

$$(H_o+\Delta H)\frac{dw}{dx} = P(1 - \frac{x_1}{\ell}) - \Delta H \frac{dz}{dx} \qquad (2.23)$$

Similarly, for $x_1 < x < \ell$

$$(H_o+\Delta H)\frac{dw}{dx} = - \frac{Px_1}{\ell} - \Delta H \frac{dz}{dx} \qquad (2.24)$$

Integrating Eq. 2.23 and satisfying the boundary conditions, w = 0 at x = 0, for $0 \leq x \leq x_1$, the dimensionless equations for the additional vertical deflection are

$$W = \frac{1}{1+\bar{h}} [(1 - X_1)X - \frac{\bar{h}}{2\bar{P}} X(1-X)] \qquad (2.25)$$

for $0 \leq X \leq X_1$, and

$$W = \frac{1}{1+\bar{h}} [(1-X)X_1 - \frac{\bar{h}}{2\bar{P}} X(1-X)] \qquad (2.26)$$

for $X_1 \leq X \leq 1$

where: $W = w/(P\ell/H_o)$, $X = \frac{x}{\ell}$

$\bar{h} = \Delta H/H_o$, $X_1 = \frac{x_1}{\ell}$

$\bar{P} = P/mg\ell$

Equations 2.25 and 2.26 give the same value for the

vertical deflection under the point load, at $x = x_1$. To complete the solution, $\bar{h}$ must be evaluated. As in static response under self weight, the horizontal component of the tension increment may be calculated using geometry, as a condition of compatibility as

$$L_o + \Delta L_o = L_{AC}' + L_{CB} \tag{2.27}$$

where L_o = the original length of cable

ΔL_o = extension of the cable due to increment in tension H_o

L_{AC} and L_{CB} are the extended lengths under the point applied load.

From Eq. 2.18

$$L_o = \ell\left[1 + \frac{8}{3}\left(\frac{F}{\ell}\right)^2\right] \tag{2.28}$$

From Eq. 2.21 and due to ΔH

$$\Delta L_o = \frac{\Delta H L_o}{AE}\left[1 + \frac{16}{3}\left(\frac{F}{\ell}\right)^2\right] \tag{2.29}$$

From Eq. 2.17 and Eq. 2.25

$$L_{AC} = \ell\left[1 + \frac{(mg)^2 \ell^2}{24(H_o+\Delta H)^2}(1-3X_1+3X_1^2)\right] \tag{2.30}$$

From Eqs. 2.17 and 2.26

$$L_{BC} = \ell\left[1 + \frac{(mg)^2}{8(H_o+\Delta H)^2} X_1(1-X_1)(1+2\bar{P})^2\right] \tag{2.31}$$

Substituting Eqs. 2.28, 2.29, 2.30 and 2.31 into the compatibility equation (2.27) gives

$$\bar{h}^3 + \{2 + [\frac{\frac{8}{3}(\frac{F}{\ell})^2}{\bar{a}}]\}\ \bar{h}^2 + \{1 + \frac{\frac{16}{3}(\frac{F}{\ell})^2}{\bar{a}}\}\ \bar{h} - [\frac{\bar{C}}{\bar{a}} - \frac{\frac{8}{3}(\frac{F}{\ell})^2}{\bar{a}}] = 0 \qquad (2.32)$$

where, $\bar{a} = \frac{H_o}{EA}\frac{L_e}{\ell}$ (2.33)

$$\bar{C} = (\frac{mg\ell}{H_o})^2[\frac{1}{24} + \frac{1}{2}X_1(1-X_1)\bar{P}(1+\bar{P})] \qquad (2.34)$$

L_e is the extended length of cable (= L_o x η, where L_o is the original unextended length of the cable and η is the extension factor).

To evaluate $\frac{8}{3}(\frac{F}{\ell})^2/\bar{a}$, substitute for $\bar{a}$ from Eq. 2.33 and for F from Eq. 2.16 for the parabola, giving

$\frac{8}{3}(\frac{F}{\ell})^2/\bar{a} = \frac{1}{24}\lambda^2$, where

$$\lambda^2 = (\frac{mg\ell}{H_o})^2\ \ell/(\frac{H_o L_e}{EA}) \qquad (2.35)$$

Substitution for $\bar{C}$ and $\bar{a}$ from Eqs. 2.34 and 2.33 gives

$$\frac{\bar{C}}{\bar{a}} = \lambda^2[\frac{1}{24} + \frac{1}{2}X_1(1-X_1)\bar{P}\ (1+\bar{P})]$$

Substituting for $\frac{8}{3}(\frac{F}{\ell})^2/\bar{a}$ and $\bar{C}/\bar{a}$ into Eq. 2.32, gives the final equation of horizontal tension increment in the cable due to applied concentrated load as

$$\bar{h}^3 + (2+\lambda^2/24)\bar{h}^2 + (1+\lambda^2/12)\bar{h} - \frac{1}{2}\lambda^2 X_1(1-X_1)\bar{P}(1+\bar{P}) = 0 \tag{2.36}$$

The same equation was obtained by Irvine [18] using a completely different approach in which he realized the importance of the nondimensional parameter λ^2. Basically, this parameter accounts for geometric and elastic effects and is of fundamental importance in the static and also dynamic response of suspended cables.

From the theory of polynomials with real coefficients, the cubic equation for $\bar{h}$ has only one real positive root. Irvine [18] presented in table form the solution for the case of midspan loading for different values of λ^2 and $\bar{P}$.

2.1.5.1 Taut Flat Cable

When a cable is initially flat, or very shallow, we may set $z(x)$ in equations of parabolic cable response (2.25) and (2.26) to zero and the equation for additional displacement reduces to

$$W = \frac{1}{1+\bar{h}}(1-X_1)X \tag{2.37}$$

for $0 \leq X \leq X_1$ and

$$W = \frac{1}{1+\bar{h}}(1-X)X_1 \tag{2.38}$$

for $X_1 \leq X \leq 1$.

The compatibility equation (2.27) reduces to

$$\ell + \Delta\ell = \ell_{AC} + \ell_{CB} \tag{2.39}$$

Substitute for ℓ and $\Delta\ell$ from Eqs. 2.18 and 2.21 and put $F/\ell \cong 0$ for the taut cable. The following equation is obtained:

$$(1+\bar{h})^2\bar{h} = \frac{1}{2}\lambda^2 X_1(1-X_1)\bar{P}(1+\bar{P}) \tag{2.40}$$

The same equation can be extracted from the general cubic equation (2.36) when λ^2 is very small and then $\frac{\lambda^2}{24}$ and $\frac{\lambda_o^2}{12}$ can be neglected.

For a massless taut string loaded at its mid-span, a very illustrative force-deflection relation can be derived from the consideration of equilibrium. Using the Taylor's series this relation becomes (e.g. Novak [58])

$$P = \frac{2H_o}{\ell} w_c + \frac{EA}{\ell^3} w_c^3 - \frac{3}{4}\frac{EA}{\ell^5} w_c^5 + \ldots \tag{2.41}$$

in which P = the concentrated applied force, H_o = original tension in the string, ℓ = original span and w_c = string deflection at mid-span. It is clear from Eq. 2.41, that the nonlinear terms of response are dependent on the string properties (A,E), while the linear term does not and that the greater the pretension H_o, the smaller

nonlinearity of the cable.

The mid-span response under point load is presented in Figure 2.4, which shows the extent to which geometric nonlinearity can affect response even when the loaded profile is still relatively shallow.

2.1.5.2 Linearized Solutions

The point load problem is linearized by neglecting all second-order terms which appear in the differential equations of equilibrium and in the compatibility equation. This necessitates the removal of the term $\Delta H \frac{dw}{dx}$ from Eq. 2.23 and Eq. 2.24 and ΔL_o from Eq. 2.29. This reduces Eq. 2.25 to

$$W = (1-X_1)X - \frac{\bar{h}}{2\bar{P}} X(1-X) \qquad (2.41a)$$

for $0 \leq X \leq X_1$, and Eq. 2.26 to

$$W = (1-X)X_1 - \frac{\bar{h}}{2\bar{P}} X(1-X) \qquad (2.41b)$$

for $X_1 \leq X \leq 1$.

Substituting this into the reduced compatibility equation yields

$$\bar{h} = \frac{6\bar{P}}{(1+12/\lambda^2)} X_1(1-X_1) \qquad (2.42)$$

For taut flat cables, $\lambda^2 << 1$ and $\bar{h} \to 0$. Hence, the classical linear theory of the taut string is recovered. When $\lambda^2 >> 1$, $\bar{h} \to 6\bar{P}\, X_1(1-X_1)$, which is a result typical for bridge cables. This result was produced in the mid-nineteenth century for just that purpose [18].

2.1.6 Nonlinear Cable Response to a Uniformly Distributed Load

A parabolic cable is fixed between two supports at the same level and loaded by a uniformly distributed load of intensity q per unit length, applied from $x = x_2$ to $x = x_3$ (Figure 2.5). By exploring the analogy that exists with simply supported beams, expressions may be written for the vertical equilibrium in the three different regions of the span.

After integration and adjustment for the required boundary conditions, the following dimensionless equations are obtained for the additional vertical cable response:

$$W = \frac{1}{(1+\bar{h})} \left\{ \left[(X_3 - X_2) - \frac{1}{2}(X_3^2 - X_2^2) \right] X - \frac{\bar{h}}{2\bar{q}} X(1-\bar{q}) \right\} \tag{2.43}$$

for $0 \leq X \leq X_2$;

$$W = \frac{1}{1+\bar{h}} \left\{ \left[-\frac{1}{2} X_2^2 + X_3 X - \frac{1}{2} X^2 - \frac{1}{2}(X_3^2 - X_2^2) X \right] - \frac{\bar{h}}{2\bar{q}} X(1-X) \right\} \tag{2.44}$$

for $X_2 \leq X \leq X_3$ and

$$\bar{w} = \frac{1}{(1+\bar{h})} \left[\frac{1}{2}(X_3^2-X_2^2)(1-X) - \frac{\bar{h}}{2\bar{q}} X(1-X)\right] \qquad (2.45)$$

for $X_3 \leq X \leq 1$.

Here

$$W = \frac{w}{(q\ell^2/H_o)}, \qquad \bar{h} = \frac{\Delta H}{H_o}$$

$$X = \frac{x}{\ell}, \qquad \bar{q} = q/mg$$

The increment in the horizontal component of cable tension is found from the compatibility equation

$$L_o + \Delta L_o = L_{AB} + L_{BC} + L_{CD} \qquad (2.46)$$

The resulting dimensionless cubic equation in $\bar{h}$ is

$$\bar{h}^3 + (2 + \frac{\lambda^2}{24})\bar{h}^2 + (1 + \frac{\lambda}{12})\bar{h} - \frac{\lambda^2}{2}[\frac{1}{2}(X_3^2-X_2^2)-\frac{1}{3}(X_3^3-X_2^3)]\bar{q}$$

$$-\frac{\lambda^2}{2}[\frac{1}{3}(X_3^3-X_2^3)-X_2^2(X_3-X_2)-\frac{1}{4}(X_3^2-X_2^2)^2]\bar{q}^2 = 0 \qquad (2.47)$$

When $\bar{q}$ is positive, there is just one positive real root, which is what is required.

When the load is extended over the whole span, the response and the increment in tension are given by these expressions:

$$W = \frac{1}{2(1+\bar{h})}\left(1 - \frac{\bar{h}}{\bar{q}}\right)X(1-X)$$

$$\bar{h}^3+\left(2 + \frac{\lambda^2}{24}\right)\bar{h}^2+\left(1 + \frac{\lambda^2}{12}\right)\bar{h} - \frac{\lambda^2}{12}\,\bar{q}\left(1 + \frac{\bar{q}}{2}\right) = 0 \qquad (2.48)$$

Different cases between $\bar{h}$ and $\bar{q}$ are discussed by Irvine [18] who presented tabulated solutions for different cases of uniformly distributed load.

2.2 STATIC ANALYSIS OF CABLE ROOFS

2.2.1 Introduction

A suspension structure may be defined as a structure whose principal supporting elements are members draped between anchorages. A cable-suspended structure is a suspension structure in network form in which twisted wire strands or ropes, usually of steel, serve as the primary members. The cables have little flexural rigidity and exhibit a marked nonlinear behaviour when loaded; the degree of nonlinearity varies with the type of cable structure as well as the loading. It is necessary to distinguish this nonlinearity which may be called geometric nonlinearity from possible material nonlinearity also present due to cable twist.

In general, the static response of cable roofs is difficult to predict due to this geometric nonlinearity. The nonlinearity in cable roofs arises because, for

equilibrium to be satisfied, the cable network must deflect under applied load, and in deflecting, the lengths of the cables change sufficiently for the cable tensions to change appreciably. Therefore, in its new position of equilibrium, both the geometry of the surface and the network tensions have changed. If the networks are pretensioned, and the pretensions are large and the applied load is small, the additional tensions are negligibly small and the deflection is linearly related to the load. For large values of applied load, the additional tensions begin to become important and the load-deflection relation is no longer linear. Such a change in the load-deflection characteristics represents a nonlinear stiffening effect due to the large increase in the cable tension. Therefore, the structural analysis of cable roofs under static loading may be considered as comprised essentially of two steps:

1. Determining the shape of the network under the initial loading, with regard to the nonlinear load-displacement relation.
2. Computing the linear response of the curved surface that results from change of loading, temperature or support position, based on the assumption that the deflections under these additional loads or effects are small with respect to that under the initial loads.

Cable roofs may be treated mathematically as discrete or continuous systems. In the discrete approach, the real structure is represented by an assemblage of elements interconnecting a finite number of nodal points at which the loading is assumed concentrated. At each node, equilibrium of forces and compatibility of displacements must be satisfied. Mathematically, this model may be represented by a set of difference equations. When expanded, these yield a set of simultaneous algebraic equations.

In the continuous approach, simultaneous ordinary or partial differential equations are utilized to represent the real structure, assuming that the structural properties may be adequately represented as uniform or slightly varying.

2.2.2 Review of Existing Approaches

Numerous studies of the behaviour of cable networks have been published with the vast majority of the theoretical work being computer oriented.

A review report by the ASCE subcommittee on cable-suspended structures [2], cites many references to numerical work published up to 1971. More recent numerical studies are those by Clark [23], Mollmann [24], West and Kar [25].

There have been very few analytical studies published. Because of the mathematical difficulties that arise, numerical methods are by far the most popular. However, some analytical work was published by Shore and Bathish [26], Trostel [27], Schleyer [28], Dean and Ugarte [29], and recently by Irvine [18,30].

Analytically, Dean and Ugarte [29] obtained a closed form mathematical solution for the deflection of structural nets loaded by a single concentrated nodal load or a uniform nodal load. Their solution was based on the nodal equilibrium equation developed and solved numerically by Siev and Eidelman [3]]. Dean and Ugarte's solution is valid only for a net which has constant elevation around its boundary.

Shore and Bathish [26] utilized double Fourier series to transform the integro-differential equations into a set of nonlinear algebraic equations. They described experimental work in their paper and verified their numerical results based on nonlinear theory.

Irvine [18,30] presented analytical solutions for the response of certain pretensioned networks, based on the same assumption made by Shore and Bathish [26], by replacing the networks by equivalent membranes. In Irvine's work, the governing equations are rearranged to be simple and

yield accurate expressions for the static response of some types of networks.

Most of the previous work is based on the assumption that the relationship between the displacement and applied static loading is nonlinear. This nonlinear behaviour is typical of cable-supported structures although for most practical suspension structures, the behaviour is not so strongly nonlinear.

The governing equations for displacements of cable roofs can be derived utilizing either a discrete or continuous mathematical representation of the structure.

If a discrete approach is utilized, the formulation results in a set of nonlinear algebraic equations. The simpler discrete problem can be solved by numerical procedures. A continuous approach leads to a set of nonlinear differential equations.

2.2.3 Idealization of Suspension-Cable Roof By a Continuous Membrane

Fabric membranes, from the point of view of structural design, can be treated as very fine-meshed networks. Hence, there is no fundamental qualitative difference between fabric membranes and cable networks, only a quantitative difference with regard to mesh size [4]. In a

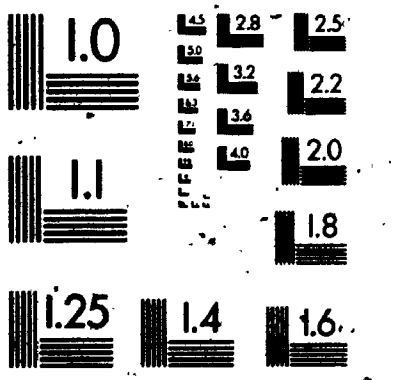
1.0
1.1
1.25
1.4
1.6
2.8
3.2
3.6
4.0
2.5
2.2
2.0
1.8

few very recent cable roofs under design [32], a membrane analogy is realized by forming a concrete membrane by grouting the lightweight concrete panels to the pretensioned suspended cables to form a monolithic membrane.

The approach used in this work for the computation of the initial and final shape of suspension cable roofs is to treat the structure as a continuous system by replacing the cable network by equivalent thin elastic membrane without shear rigidity.

2.2.4 Static Loading

The static loads used in the determination of the initial shape of the structure are: self weight of cables, initial tension in cables, weight of continuous membrane or weight of concrete panels, used as filling, thermal insulation and waterproofing, if any.

The static loads used in the determination of the final shape are static external and internal wind pressure, rainwater, snow or hail, sand or dust and maintenance loadings as well as dynamic wind loading and ground motion due to earthquake excitation.

A nonlinear theory is used herein for determining the response of practically shaped cable roofs, subject to static loading and the applied initial tension which

$$B = 0 \tag{4.54}$$

Finally, since w and hence R(r) must vanish on the boundaries r = a,

$$J_n\left(\frac{\omega_n a}{\nu}\right) = 0 \tag{4.55}$$

Denoting the mth positive solution of this equation by ω_{nm}, gives

$$J_n\left(\frac{\omega_{nm} a}{\nu}\right) = 0 \quad (m = 1,2,3,\ldots) \tag{4.56}$$

The roots of J_n, designated by $j_{nm} = \frac{\omega_{nm} a}{\nu}$ are given in Table 2.1, and the natural circular frequencies of the circular membrane follow as

$$\omega_{nm} = j_{nm} \sqrt{\frac{T}{ma^2}} \tag{4.57}$$

Substituting all the results obtained and making the necessary notation adjustment in Eq. 4.47, we get the mode shape of the displacement w at (r,θ) and time t for the mode of order n and rank m, given as

$$w_{nm}(r,\theta,t) = J_n\left(\frac{\omega_{nm} r}{\nu}\right)[(a_{nm}\cos n\theta + b_{nm}\sin n\theta)\cos\omega_{nm}t + (C_{nm}\cos n\theta + D_{nm}\sin n\theta)\sin\omega_{nm}t] \tag{4.58}$$

The order of Bessel function determines the number of nodal diameters in the mode of vibration, while the rank of the Bessel function zeroes determines the number of nodal circles in the mode, including the edge circle.

TABLE 4.1 Roots of Bessel Functions, j_{nm}

n/m.	0	1	2	3
1	2.404	3.832	5.135	6.379
2	5.520	7.016	8.417	9.760
3	8.654	10.173	11.620	13.017
4	11.792	13.323	14.796	16.224

Typical mode shapes are shown in Figure 4.6.

From the general expansion theorem [74] the different modes give the displacement as

$$w(r, \theta, t) = \sum_n \sum_m J_n\left(\frac{\omega_{nm} r}{v}\right)\left[\left(a_{nm}\cos n\theta + b_{nm}\sin n\theta\right)\cos\omega_{nm} t + \left(C_{nm}\cos n\theta + D_{nm}\sin n\theta\right)\sin\omega_{nm} t\right] \quad (4.59)$$

$$n = 0,1,2,3,\ldots \; ; \; m = 1,2,3,\ldots$$

The amplitude of vibration, as stated before, may be obtained from the initial conditions where the eigenvalues (4.57) and eigenfunctions (4.58) are obtained from the boundary conditions. Let us assume that, in addition to the boundary conditions (4.46), we may be given two initial conditions which prescribe the deflection w and the velocity $\frac{\partial w}{\partial t}$ as functions of r and θ at an initial time t = 0

$$w(r,\theta,o) = f_1(r,\theta) \quad (4.60a)$$

$$\frac{\partial w(r,\theta,o)}{\partial t} = f_2(r,\theta) \quad (4.60b)$$

Substituting Eq. 4.60a into Eq. 4.59 gives

$$f_1(r,\theta) = \sum_n \sum_m \left(a_{nm}\cos n\theta + b_{nm}\sin n\theta\right) J_n\left(\frac{\omega_{nm} r}{v}\right) \quad (4.61a)$$

$$f_2(r,\theta) = \sum_n \sum_m \omega_{nm}\left(C_{nm}\cos n\theta + D_{nm}\sin n\theta\right) J_{nm}\left(\frac{\omega_{nm} r}{v}\right) \quad (4.61b)$$

where $0 < r < a$, $0 < \theta \leq 2\pi$, $n = 0,1,2,\ldots$, $m = 1,2,3,\ldots$.

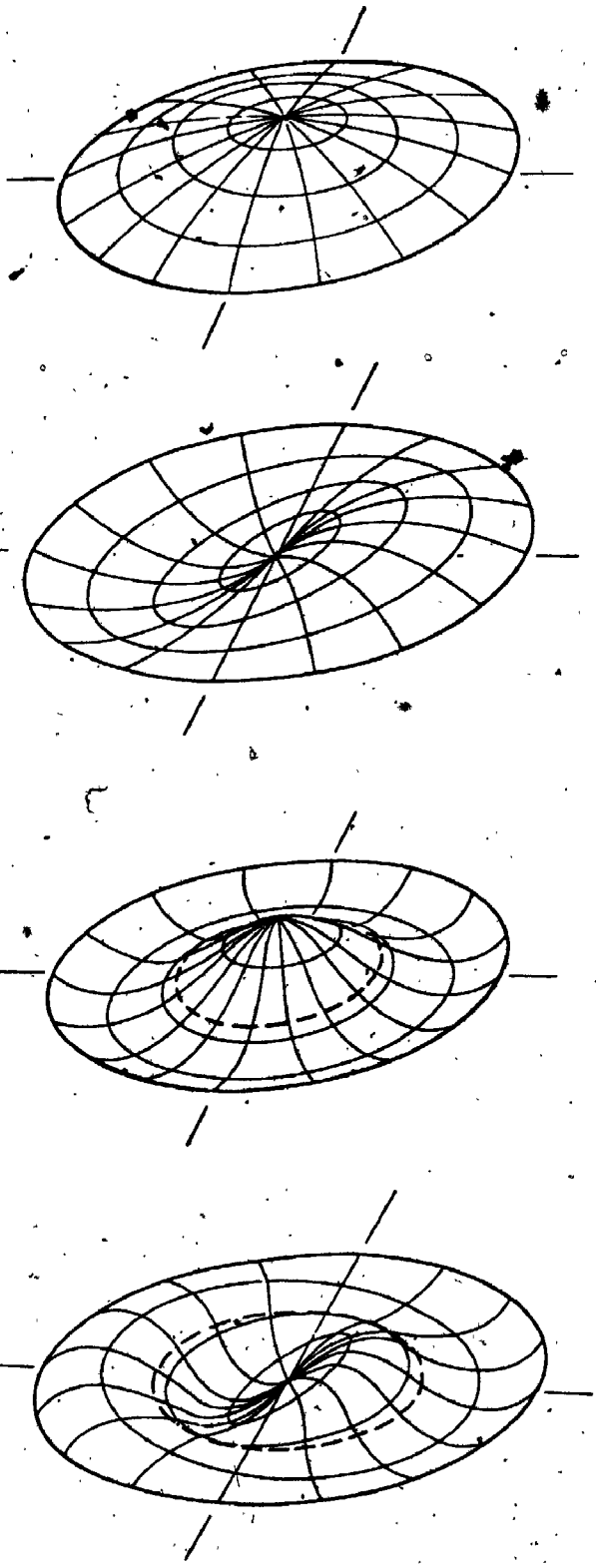

$$\omega_{01} = \frac{2.405}{a}\sqrt{\frac{T}{m}}$$

$$\omega_{11} = \frac{3.832}{a}\sqrt{\frac{T}{m}}$$

$$\omega_{02} = \frac{5.520}{a}\sqrt{\frac{T}{m}}$$

$$\omega_{12} = \frac{7.016}{a}\sqrt{\frac{T}{m}}$$

FIGURE 4.6 Modes shape of Circular Membrane w_{nm} [36]

The determination of the constants a_{nm}, b_{nm}, C_{nm} and D_{nm} is explained in detail elsewhere [74]. For simplicity, let us consider only the special case where f_1 is independent of θ and $f_2 = 0$; that is, we assume that initially the membrane is deflected into a radially symmetrical form and is released from rest. In this case, only symmetrical modes independent of θ occur, for which $n = 0$. Furthermore, the initial velocities of all the points in the membrane vanish (4.61b), if the constants C_{nm} and D_{nm} are set equal to zero. Hence, Eq. 4.59 reduces to the form

$$w(r,t) = \sum_m A_{om} J_o(\frac{\omega_{om} r}{\nu}) \cdot \cos\omega_{om} t \qquad (4.62)$$

where ω_{om} is the mth positive solution of

$$J_o(\frac{\omega_{om} r}{\nu}) = 0 \quad (m=1,2,3,\ldots) \qquad (4.63)$$

and Eq. 4.61a reduces to

$$f(r) = \sum_m A_{om} J_o(\frac{\omega_{om} r}{\nu}) \;,\; 0<r<a \;;\; m=1,2,3\ldots \qquad (4.64)$$

Reference to procedures detailed in [65,74] and similar to those for the rectangular membrane leads to the determination of A_{om} as,

$$A_{om} = \frac{2}{a^2 [J_1(\frac{\omega_{om} a}{\nu})]^2} \int_o^a r\, f(r)\, J_o(\frac{\omega_{om} r}{\nu}) dr \qquad (4.65)$$

The frequency of vibration ω_{nm} is obtained from Eq. 4.57, the mode shapes, determined by the boundary conditions,

from Eq. 4.58, and the constants A,B,C,D which determine the amplitude of vibration, from the initial conditions. The displacement at any location (r,θ) on the vibrating circular membrane, at any time t, is completely described by Eq. 4.59.

4.2.2.4 Free Vibration of an Elliptical Membrane

Consider an elliptical membrane, stretched over a plane elliptical frame under an all-round tension, with fixed edge and having the major and minor semi-axes a, b respectively, Figure 4.7. Let m be its mass per unit area and T the uniform tension per unit arc length applied to the membrane.

The solution of the two-dimensional general equation of vibrating membrane (4.32), for elliptical region is most easily obtained by expressing the problem in elliptical coordinates, Appendix A, [75,81].

In transforming the coordinates in Eq. 4.32, to elliptical coordinates ξ, η, the following relations are applied:

$$x = d \cosh\xi \cos\eta, \quad y = d \sinh\xi \sin\eta \qquad (4.66)$$

The Laplacian operator is given by, Appendix A,

$$\nabla^2 = \left(\frac{\partial^2}{\partial\xi^2} + \frac{\partial^2}{\partial\eta^2}\right) \frac{2}{d^2(\cosh 2\xi - \cos 2\eta)} \qquad (4.67)$$

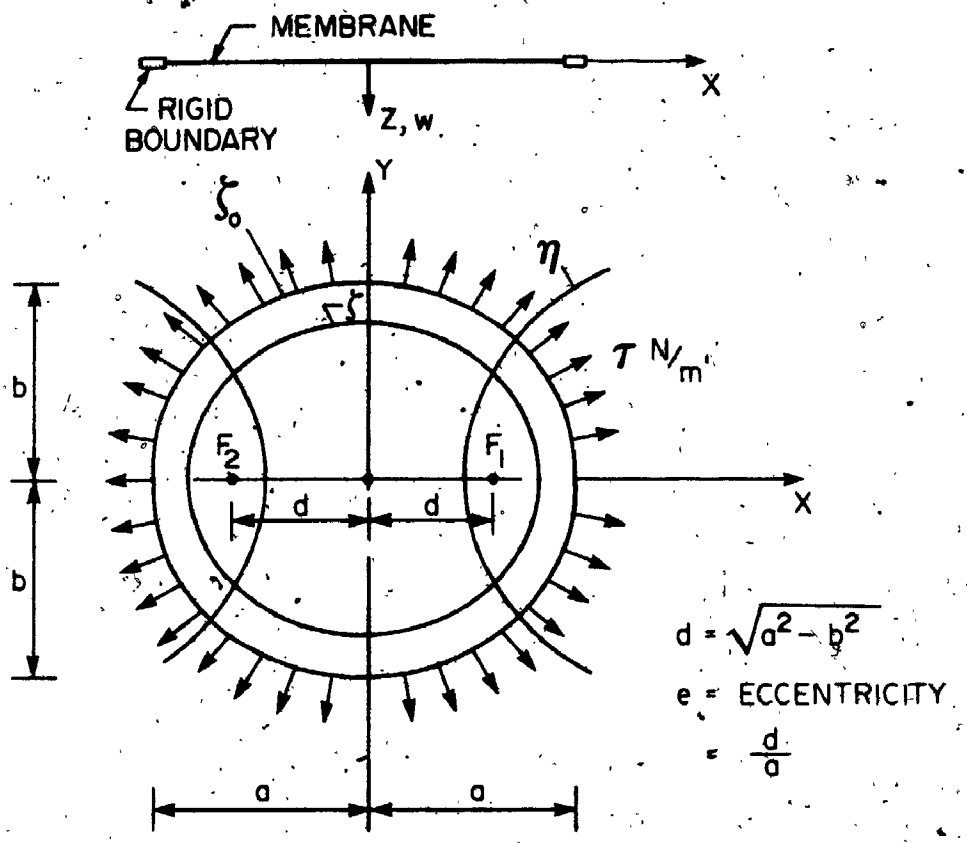

FIGURE 4.7 ELLIPTICAL STRETCHED MEMBRANE AND ELLIPTIC NOTATION.

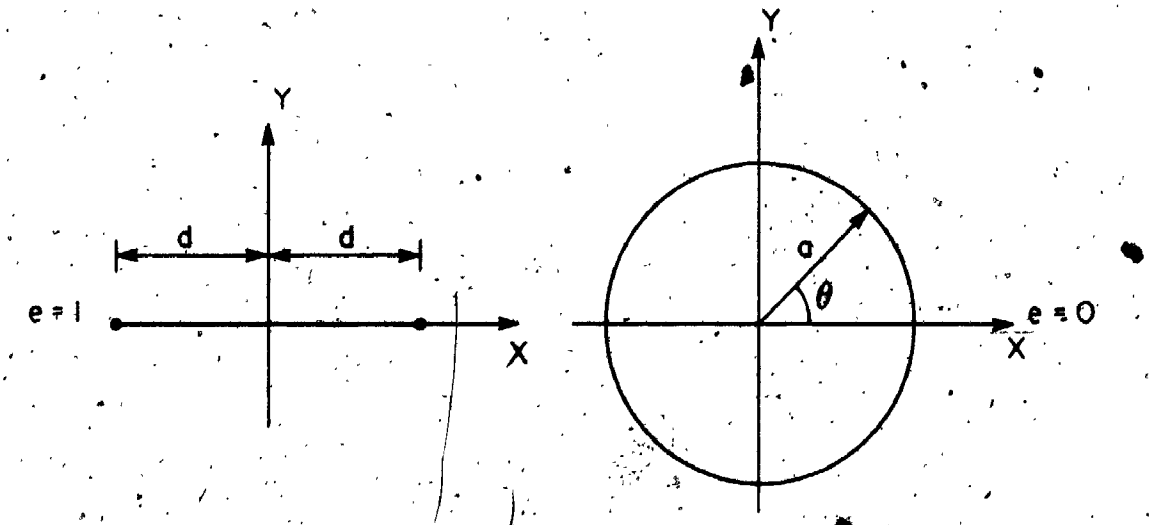

FIGURE 4.8 ELLIPSE REDUCED TO CIRCLE WHEN ITS ECCENTRICITY $e \rightarrow 0$, AND TO A LINE WHEN $e \rightarrow 1$.

in which d is the semi-interfocal distance of the ellipse $= \sqrt{a^2-b^2}$. Equation 4.32 becomes

$$\left(\frac{\partial^2 w}{\partial \xi^2} + \frac{\partial^2 w}{\partial \eta^2}\right) \frac{2}{d^2(\cosh 2\xi - \cos 2\eta)} = \frac{1}{v^2}\frac{\partial^2 w}{\partial t^2} \qquad (4.68)$$

in which $v^2 = \frac{T}{m}$. If $w(\xi,\eta,t)$ varies sinusoidally with time t, we may take

$$w(\xi,\eta,t) = w(\xi,\eta)e^{i\omega t} \qquad (4.69)$$

Substituting Eq. 4.69 into Eq. 4.68 and the equation of free vibration in elliptical coordinates becomes

$$\frac{\partial^2 w}{\partial \xi^2} + \frac{\partial^2 w}{\partial \eta^2} + 2k^2(\cosh 2\xi - \cos 2\eta)w = 0 \qquad (4.70)$$

in which $k = \frac{\omega d}{2v}$.

Applying separation of variables,

$$w(\xi,\eta) = \psi(\xi)\phi(\eta) \qquad (4.71)$$

where ψ is a function of ξ alone, and ϕ a function of η alone. Substituting Eq. 4.71 into Eq. 4.70 we obtain,

$$\phi\frac{d^2\psi}{d\xi^2} + \psi\frac{d^2\phi}{d\eta^2} + 2k^2(\cosh 2\xi - \cos 2\eta)\psi\phi = 0 \qquad (4.72)$$

Dividing by $\psi\phi$ and rearranging leads to

$$\frac{1}{\psi}\frac{d^2\psi}{d\xi^2} + 2k^2\cosh 2\xi = -\frac{1}{\phi}\frac{d^2\phi}{d\eta^2} + 2k^2\cos 2\eta \qquad (4.73)$$

Since the left-hand side of Eq. 4.73 is independent of η

and the right-hand side is independent of ξ, each side must be a constant. Denoting this constant by α, and substituting into Eq. 4.73, we obtain the following two differential equations:

$$\frac{d^2\phi}{d\eta^2} + (\alpha - 2k^2\cos 2\eta)\phi = 0 \qquad (4.74)$$

and

$$\frac{d^2\psi}{d\xi^2} - (\alpha - 2k^2\cosh 2\xi)\psi = 0 \qquad (4.75)$$

Equations 4.74 and 4.75 are the canonical forms of Mathieu's equation and called the Mathieu and modified Mathieu equations respectively. These equations are linear and of the second order with periodic coefficients. Their solutions take different forms according to the values of α and k.

The solution for Eq. 4.70 comprises the product of two functions which are solutions of Eqs. 4.74 and 4.75 respectively for the same values of α and k. Since α, the separation constant, may have any value, the number of solutions is unlimited.

For the free vibration of the elliptical membrane under investigation, the displacement from the equilibrium position is a periodic function of one of the coordinates. This is similar to a circular membrane, for which the displacement at any radius depends upon $\cos m\theta$ and $\sin m\theta$

which are periodic functions of the polar coordinate θ. The displacement of an elliptical membrane is periodic in the elliptical coordinate η. Thus, if k is assigned, the displacement w will have period π or 2π in η, provided α has one of an infinite sequence of particular numbers. Those particular numbers are called characteristic numbers, and in order for the solution of Eq. 4.74 to be periodic with period π or 2π, α and k must be interrelated: α is a function of k such as

$$\alpha = m^2 + \alpha_1 k + \alpha_2 k^2 + \alpha_3 k^3 + \ldots . \qquad (4.76)$$

in which m is an integral and the α's are constants to be determined. The desired form $\alpha = m^2$ for the circular membrane is obtained when $k = 0$ and the periodic solutions $\cos m\theta$, $\sin m\theta$ are achieved.

The solutions of Eq. 4.74 are called (ordinary) Mathieu functions, being periodic in η with period π or 2π; the corresponding solutions of Eq. 4.75, for the same α as in Eq. 4.74, are known as modified Mathieu functions. In practical applications, the appropriate solutions are usually given by ordinary and modified Mathieu functions of integral order. By assuming the amplitude of displacement is unity, the solutions of Eq. 4.74 are, [75],

$$\phi(\eta) = ce_m(\eta,k) \text{ or } se_m(\eta,k) \qquad (4.77)$$

for m = 0,1,2...

and for Eq. 4.75

$$\psi(\xi) = Ce_m(\xi,k) \text{ or } Se_m(\xi,k) \qquad (4.78)$$

for m = 1,2,3...

Here,

ce_m = a cosine type Mathieu function of the first kind and order of integral m, k > 0

se_m = a sine type Mathieu function of the first kind and order of integral m, for k > 0

Ce_m = a cosine type modified Mathieu function of the first kind and order of integral m, for k > 0

Se_m = a sine type modified Mathieu function of the first kind and order of integral m, for k > 0

The notation ce_m, se_m is an abbreviation of cosine-elliptic and sine-elliptic respectively. Those functions reduce to a multiple of cosmη and sinmη when k = 0, as stated briefly earlier. Since m may be any positive integer, there is an infinite number of solutions. The functions ce_m are even in η, and the functions se_m are odd in η.

The modified Mathieu functions Ce_m, Se_m are periodic in ξ with period πi and 2πi respectively, and these reduce to coshmξ or sinhmξ when k = 0. The series of these

functions and their properties are presented in [75].

The type of solution which will be chosen for Eq. 4.70 in terms of ce_m Ce_m or se_m Se_m depends on m, chosen in Eq. 4.76, being even or odd.

The permissible forms of solution for Eq. 4.70 [75] are

$$w_m(\xi,\eta,t) = C_m Ce_m(\xi,k)\, ce_m(\eta,k)\cos(\omega_m t + \varepsilon_m) \quad (4.79a)$$

and

$$w_m(\xi,\eta,t) = S_m Se_m(\xi,k)\, se_m(\eta,k)\cos(\omega_m t + \varepsilon_m) \quad (4.79b)$$

in which C_m and S_m are arbitrary constants determinable from the conditions specified for the configuration of velocity distribution over the membrane at $t = 0$. ω_m is the natural frequency of the mth free mode of vibration and ε_m its relative phase-shift. Since each integral value of m gives a separate solution of the differential equation, the complete solution of Eq. 4.70, expressed in elliptic coordinates, is

$$w(\xi,\eta,t) = \sum_{m=0} C_m Ce_m(\xi,k)\, ce_m(\eta,k)\cos(\omega_m t + \varepsilon_m) + \sum_{m=1} S_m Se_m(\xi,k)\, se_m(\eta,k)\cos(\omega_m t + \varepsilon_m) \quad (4.80)$$

This solution satisfies the continuity of displacement as well as the continuity of gradient (slope) conditions at any interfocal line. These two conditions imply

continuity of displacement and gradient in crossing the interfocal line orthogonally. In Eq. 4.80, any product pair of solutions Ce or Se are constant on any confocal ellipse. Hence, the symmetry is governed by ce or se. Since,

$$ce_m(\eta,k) = ce_m(\pi+\eta,k) = ce_m(2\pi-\eta,k)$$

$$m = 0,2,4,\ldots$$

it follows that the displacement expressed by

$$Ce_m(\xi,k)\,ce_m(\eta,k) \quad \text{(for m even)}$$

is symmetrical about both the major and minor axes of the ellipse. Since

$$ce_m(\eta,k) = -ce_m(\pi\pm\eta,k) = ce_m(2\pi-\eta,k)$$

$$m = 1,3,5,\ldots$$

it follows that the displacement, expressed by

$$Ce_m(\xi,k)\,ce_m(\eta,k) \quad \text{(for m odd)}$$

is symmetrical about the major axis but antisymmetrical about the minor axis.

Similarly, since

$$se_m(\eta,k) = \mp\, se_m(\pi\pm\eta,k) = -se_m(2\pi-\eta,q)$$

$$m = 1,3,5,\ldots$$

it follows that the displacement expressed by

$Se_m(\xi,k)se_m(\eta,k)$ (m odd)

corresponds to a displacement antisymmetrical about the major axis but symmetrical about the minor axis. Finally, since

$$se_m(\eta,k) = \pm se_m(\pi\pm\eta,k) = -se_m(2\pi-\eta,k)$$

$$m = 2,4,6,\ldots$$

so

$Se(\xi,k)se(\eta,k)$ (m even)

corresponds to a displacement antisymmetrical about both axes.

The symmetry or antisymmetry about the major and minor axes is the same as that for the degenerate forms $\cos m\theta$, $\sin m\theta$ about $\theta = 0, \frac{\pi}{2}$ respectively. It is also remarkable that when $k = 0$, the Mathieu functions $ce_m(\eta,0)$ and $se_m(\eta,0)$ are reduced to $\cos m\eta$ and $\sin m\eta$ respectively, in which η is to be replaced by θ of the polar coordinate system.

Each individual solution in Eq. 4.80 for $m=0,1,2,\ldots$ corresponds to a different mode of vibration, Fig. 4.8a. When k has its appropriate value, the dynamic deformation surface of the membrane and the natural frequency differ for each m. "Any mode may exist separately, or they may all be present." The maximum displacement of the surface for

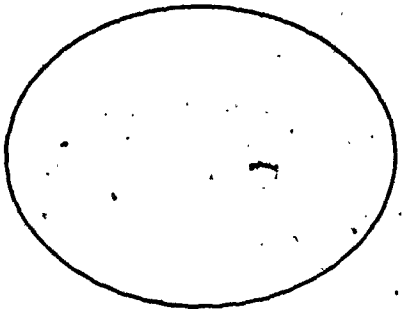

MODE w_{01}

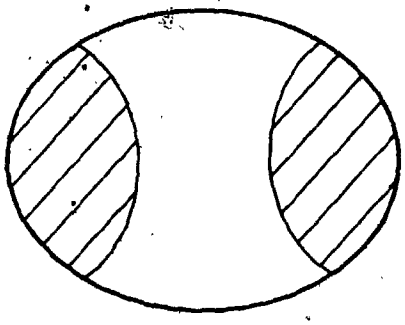

MODE w_{21}

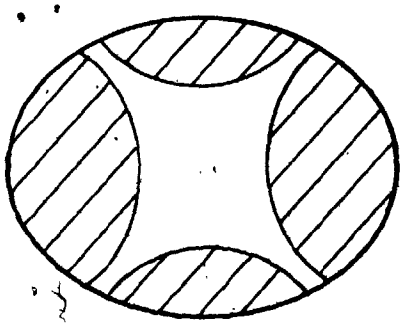

MODE w_{41}

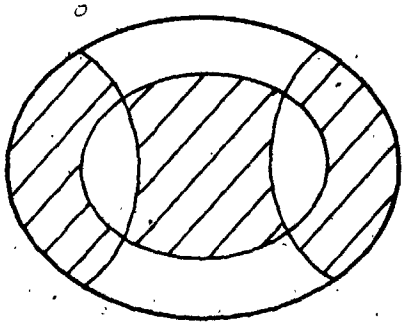

MODE w_{22}

FIGURE 4.8 a POSSIBLE VIBRATION MODES OF A FLAT ELLIPTICAL TENSION ROOF.

a particular mode depends upon the value of C_m or S_m. These in turn are governed by the configuration of and the normal velocity distribution over the membrane at time t = 0.

The boundary condition for all η is that w = 0 at the clamping ring where $\xi = \xi_o$. Since $ce_m(\eta,k)$, $se_m(\eta,k)$ are independent of ξ, we must have

$$Ce_m(\xi_o,k) = 0 \quad \text{for } m = 0,1,2,... \tag{4.81a}$$

$$Se_m(\xi_o,k) = 0 \quad \text{for } m = 1,2,3,... \tag{4.81b}$$

Now ξ_o is fixed, so we need those positive values of k, say $k_{m,n}$ for which the respective functions in Eq. 4.81 vanish. These may be regarded as the positive parametric zeroes of the functions. They define a series of confocal nodal ellipses. There is an infinity of zeroes for each m, i.e. one for each n = 1,2,3,.... Hence, for Ce_m there are (n-1) nodal ellipses within the clamping ring, or n nodal ellipses including the clamping ring, and likewise for Se_m, but their locations differ.

Equations 4.81 are known as the natural frequencies equations of the elliptical membrane, since their roots are used to calculate the natural frequencies of the modes of the membrane.

Also the functions $ce_m(\eta,k)$, $se_m(\eta,k)$ for $m \geq 1$ have zeroes in η. Hence, w vanishes if η satisfies the respective equations:

$$ce_m(\eta,k_{m,n}) = 0 \qquad (4.82a)$$

and

$$se_m(\eta,k_{m,n}) = 0 \qquad (4.82b)$$

The roots of Eqs. 4.82 define a series of confocal nodal hyperbolas.

Since $ce_m(\eta,k_{m,n})$, $se_m(\eta,k_{m,n})$ each have m zeroes in $0 \leq \eta < \pi$, therefore for a given m each function gives rise to m nodal hyperbolas.

From physical consideration, and since $w(\xi,\eta,t)$ must be a continuous function of ξ,η within the ellipse, which vanishes at its periphery, we may expand the solution in Eq. 4.80, at any point of the membrane in the form of a double series, namely [75]:

$$w(\xi,\eta,t) = \sum_{m=0}\left[\sum_{n=1} C_{m,n}Ce_m(\xi,k_{m,n})ce_m(\eta,k_{m,n})\cos(\omega_{m,n}t + \varepsilon_{m,n})\right] + \sum_{m=1}\left[\sum_{n=1} S_{m,n}Se_m(\xi,k_{m,n})se_m(\eta,k_{m,n})\cos(\omega_{m,n}t + \varepsilon_{m,n})\right] \qquad (4.83)$$

in which $C_{m,n}$, $S_{m,n}$ are arbitrary constants to be determined from the initial conditions, $\omega_{m,n}$ is the frequency

of mode mn, having n nodal ellipses and m nodal hyperbolas, and $\epsilon_{m,n}$ its relative phase shift. The displacement $w(\xi,\eta,t)$ is a continuous function and vanishes at the boundaries of the membrane at $\xi = \xi_o$. Multiplying both sides of Eq. 4.83 by

$$(\cosh 2\xi - \cos 2\eta)\,Ce_m(\xi,k_{m,n})\,ce_m(\eta,k_{m,n})$$

and integrating with respect to η from 0 to 2π, and with respect to ξ from 0 to ξ_o. All the terms vanish except at m,n, hence,

$$C_{m,n} = \frac{\int_0^{\xi_o}\int_0^{2\pi} Ce_m(\xi,k_{m,n})\,ce_m(\eta,k_{m,n})\,w(\xi,\eta)\,(\cosh 2\xi - \cos 2\eta)\,d\xi d\eta}{\pi \int_0^{\xi_o} Ce_m^2(\xi,k_{m,n})\,[\cosh 2\xi - I_{m,n}]\,d\xi} \tag{4.84}$$

where

$$I_{m,n} = \frac{1}{\pi}\int_0^{2\pi} ce_m^2(\eta,k_{m,n})\cos 2\eta\, d\eta \tag{4.85}$$

In a similar manner it can be shown that

$$S_{m,n} = \frac{\int_0^{\xi_o}\int_0^{\pi} Se_m(\xi,k_{m,n})\,se_m(\eta,k_{m,n})\,w(\xi,\eta)\,(\cosh 2\xi - \cos 2\eta)\,d\xi d\eta}{\pi \int_0^{\xi_o} Se_m^2(\xi,k_{m,n})\,[\cosh 2\xi - \Psi_{m,n}]\,d\xi} \tag{4.86}$$

where

$$\Psi_{m,n} = \frac{1}{\pi}\int_0^{2\pi} se_m^2(\eta,k_{m,n})\cos 2\eta\, d\eta \tag{4.87}$$

The denominators of Eqs. 4.83 and 4.85 may be evaluated numerically.

By this the problem of free vibration of elliptical membrane clamped at its boundaries is completed. The above solution was formulated by McLachlan [75]. From this general solution, the author derives a simplified solution very well suited for practical applications as described below.

When the fundamental ellipse tends to a circle, the semifocus $d \to 0$ and since $k = 1/2\ \frac{\omega}{\nu}d$, $k \to 0$, and the series for $ce_m(\eta,k)$ tend to $\cos m\eta = \cos m\theta$ for $(m \geq 1)$, where the confocal hyperbolae becoming radii of the circle with $\eta = \theta$; Figure 4.8.

In the same way as $d \to 0$, $e \to 0$ and $k \to 0$ and

$se_m(\eta,k) \to \sin m\eta = \sin m\theta$ for $(m \geq 1)$.

Similarly as $d \to 0$, $\xi \to \infty$ and $d\cosh\xi \to d\sinh\xi \to a$. Hence,

$Ce_m(\xi,k) \to J_m(\frac{\omega}{\nu}r)$ and $Se_m(\xi,k) \to J_m(\frac{\omega}{\nu}r)$. And Eq. 4.80 reduces to

$$w(r,\theta) = \sum_{m=0}^{\infty} A_m J_m(\frac{\omega_m}{\nu}r)\cos m\theta + \sum_{m=1}^{\infty} B_m J_m(\frac{\omega_m}{\nu}r)\sin m\theta \quad (4.88)$$

where A_m and B_m are arbitrary constants to be determined

from the initial conditions and related to C_m and S_m. The frequency equation is obtained from the vanishing of w at the boundaries, giving,

$$J_m(\frac{\omega}{\nu}a) = 0 \tag{4.89}$$

The roots define the nodal circles, instead of nodal ellipses, while the nodal diameters are defined by the roots of

$$\cos m\theta = 0 \text{ and } \sin m\theta = 0 \tag{4.90}$$

Hence, the theory of free vibration of the circular membrane is obtained.

In structural engineering considerations $k << 1$, and the frequency equation is given approximately for this case as

$$k_{on}^2 \simeq \frac{1}{16}(4n-1)\pi^2 e^{-2\xi_o} \tag{4.91}$$

Substitute for $k^2 = \frac{\omega_{on}^2 d^2}{4\nu^2}$, $\nu^2 = \frac{T}{m}$, and the frequency equation for the free vibration of cable roof in elliptical boundaries may be written as

$$\omega_{on}^2 \simeq \frac{1}{4}\frac{T}{m}\frac{\pi^2}{d^2}(4n-1)^2 e^{-2\xi_o} \tag{4.92}$$

in which n indicates the number of nodal ellipses for the roof under investigation, and ξ_o its elliptical coordinate

at the boundaries.

4.2.2.5 Free Vibration of Rectangular Hyperbolic Paraboloid Membrane

Consider a hyperbolic paraboloid membrane, rectangular in plan (saddle shape), as shown in Figure 4.9, whose surface under static equilibrium is defined by

$$w_o(x,y) = \frac{f_x}{a^2} x^2 - \frac{f_y}{b^2} y^2 \qquad (4.93)$$

where f_x, f_y are the drop along the x axes and the sag along the y axes respectively, and 2a, 2b its horizontal dimensions.

In free vibrations, we will assume the membrane will vibrate about the equilibrium configuration and restrict the analysis to small amplitude oscillations about this static equilibrium position.

Let xyz be a right-handed Cartesian coordinate system with the origin at the saddle point 0, and consider a differential element dx dy, cut from the deformed membrane by two pairs of parallel planes normal to the x and y axes as shown in Figure 4.10.

Assume the membrane is given initial displacement at t = 0, described as

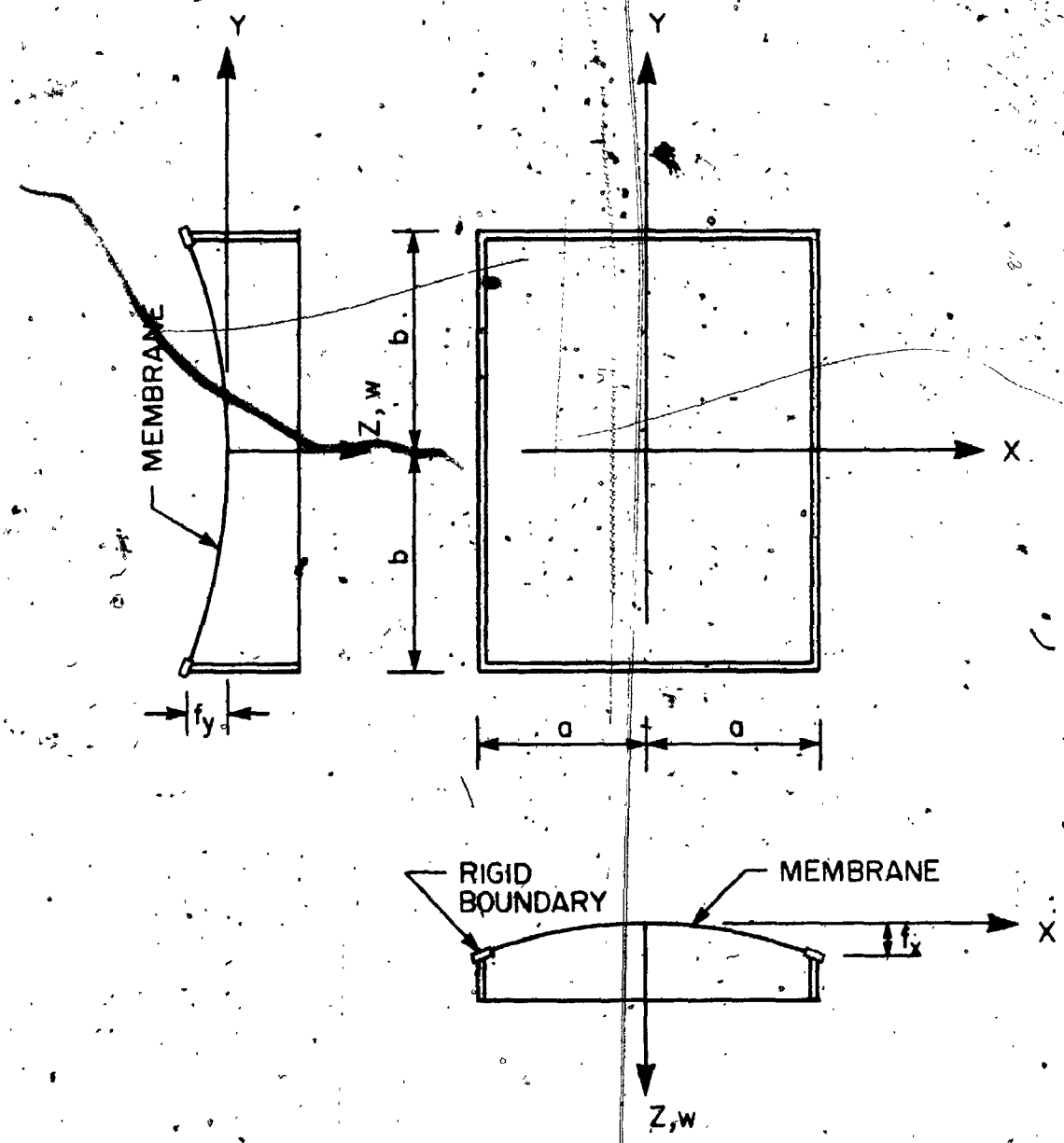

FIGURE 4.9 RECTANGULAR HYPERABOLIC PARABOLOID COORDINATES AND DEFINITION.

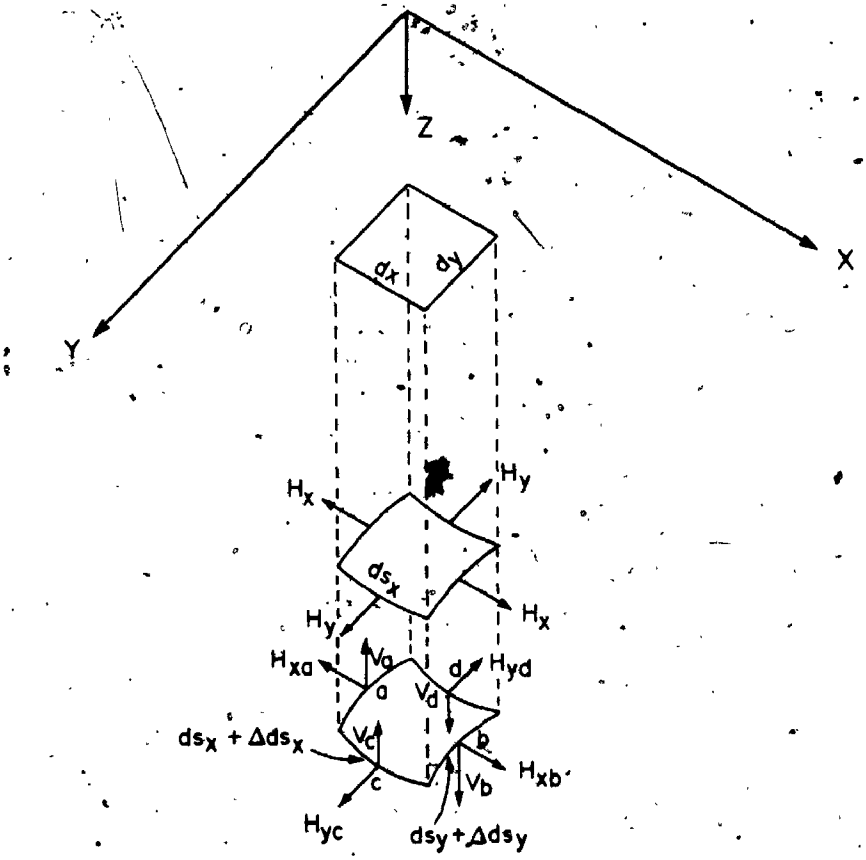

FIGURE 4.10 DEFORMED ELEMENT dx dy AND LOAD RESULTANT DEFINITION AND NOTATION.

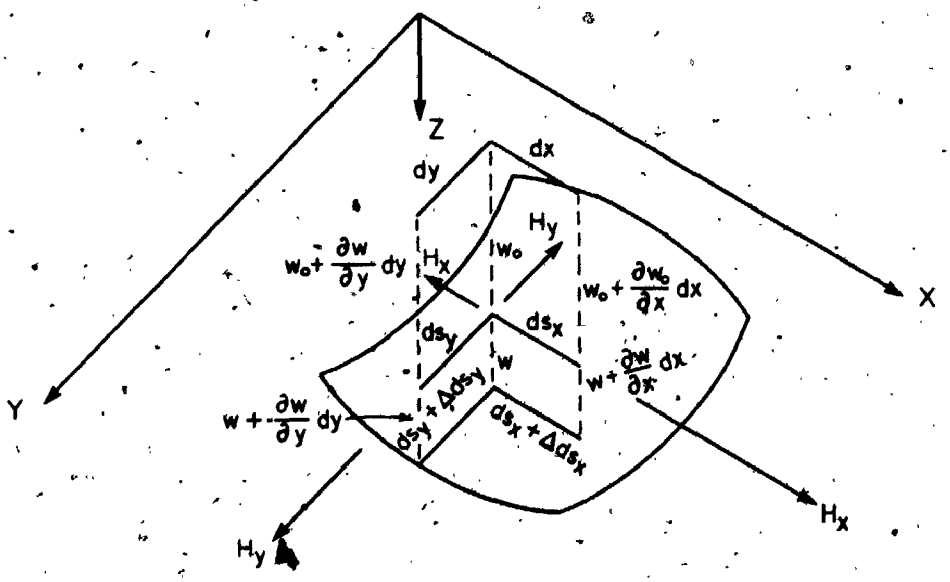

FIGURE 4.11 GEOMETRICAL DEFINITION FOR DEFORMED ELEMENT dx dy AND NOTATION.

$$w(x,y,o) = f(x,y) \qquad (4.94a)$$

and initial velocity at time t = θ, given by

$$\frac{\partial w(x,y,o)}{\partial t} = g(x,y) \qquad (4.94b)$$

The membrane will vibrate due to these initial conditions. Denote the displacement of the free oscillation at any point x,y on the membrane and time t by w(x,y,t).

Due to these oscillations, the tension in the membrane will increase by ΔH, while H is the tension in the membrane under the static equilibrium and known from static analysis.

Apply Newton's second law to the differential element dx dy in the vertical direction, giving [76,80]:

$$-V_{za} + V_{zb} - V_{zc} + V_{zd} + q\,dxdy = m\frac{\partial^2 w}{\partial t^2}dxdy \qquad (4.95)$$

where:

$$H_{xa} = (H_x + \Delta H_x)dy$$

$$H_{xb} = [(H_x+\Delta H_x)]dy + [\frac{\partial(H_x+\Delta H_x)}{\partial x}dx]dy$$

$$H_{yc} = (H_y + \Delta H_y)dx$$

$$H_{yd} = (H_y + \Delta H_y)dx + [\frac{\partial(H_y+\Delta H_y)}{\partial y}dy]dx$$

and

$$\frac{V_x}{H_x} = \frac{\partial (w_o+w)}{\partial x}$$

$$\frac{V_y}{H_y} = \frac{\partial (w_o+w)}{\partial y}$$

Hence,

$$V_{za} = -(H_x+\Delta H_x) \frac{\partial (w_o+w)}{\partial x} dy$$

$$V_{zb} = (H_x+\Delta H_x) \frac{\partial (w_o+w)}{\partial x} dy + \frac{\partial [(H_x+\Delta H_x) \frac{\partial (w_o+w)}{\partial x}]}{\partial x} dxdy$$

$$V_{zc} = -(H_y+\Delta H_y) \frac{\partial (w_o+w)}{\partial y} dx$$

$$V_{zd} = (H_y+\Delta H_y) \frac{\partial (w_o+w)}{\partial y} dx + \frac{\partial [(H_y+\Delta H_y) \frac{\partial (w_o+w)}{\partial y}]}{\partial y} dydx$$

$$\frac{\partial (w_o+w)}{\partial x} = \frac{\partial w_o}{\partial x} + \frac{\partial w}{\partial x}$$

$$\frac{\partial (w_o+w)}{\partial y} = \frac{\partial w_o}{\partial y} + \frac{\partial w}{\partial y}$$

From static equilibrium, $q = -H_x \frac{\partial^2 w}{\partial x^2} - H_y \frac{\partial^2 w}{\partial y^2}$ where q is the static load per unit area, $m = q/g$ is the mass per unit area of the membrane, and g is gravity acceleration.

Substitute the above definitions into Eq. 4.95, divide by dxdy, and assume ΔH is constant with respect to space, i.e.

$$\frac{\partial \Delta H}{\partial i}\, di = 0 \quad , \quad i = x,y$$

The equation of motion of the vibrating membrane gives:

$$H_x \frac{\partial^2 w}{\partial x^2} + \Delta H_x \left(\frac{\partial^2 w_o}{\partial x^2} + \frac{\partial^2 w}{\partial x^2}\right)$$

$$+ H_y \frac{\partial^2 w}{\partial y^2} + \Delta H_y \left(\frac{\partial^2 w_o}{\partial y^2} + \frac{\partial^2 w}{\partial x^2}\right) = m \frac{\partial^2 w}{\partial t^2} \qquad (4.96)$$

The increment in the horizontal tension components ΔH_x, ΔH_y may be determined using the elastic properties of the membrane material and the condition of compatibility of the deformations.

Apply Hooke's law to the differential increment, Figure 4.11:

$$\Delta ds_x = \frac{\sigma_{sx} ds_x}{E_x} = \frac{\Delta H_{sx} ds_x}{E_x h} = \frac{\Delta H_x (ds_x)^2}{E_x h\, dx} \qquad (4.97a)$$

Similarly for y

$$\Delta ds_y = \frac{\Delta H_y (ds_y)^2}{E_y h\, dy} \qquad (4.97b)$$

where E_x and E_y are Young's modulus of the membrane material in x and y directions respectively and h its thickness. Assume isotropic membrane with uniform thickness, then, $E_x = E_y = E$. From compatibility of deformations:

$$(ds_x)^2 = (dx)^2 \left[1 + \left(\frac{\partial w_o}{\partial x}\right)^2\right] \qquad (4.98a)$$

$$(ds_y)^2 = (dy)^2 \left[1 + \left(\frac{\partial w_o}{\partial y}\right)^2\right] \qquad (4.98b)$$

and

$$\Delta ds_x = \frac{\frac{\partial w_o}{\partial x}\frac{\partial w}{\partial x}(dx)^2}{ds_x} \qquad (4.99a)$$

$$\Delta ds_y = \frac{\frac{\partial w_o}{\partial y}\frac{\partial w}{\partial y}(dy)^2}{ds_y} \qquad (4.99b)$$

Substitute from Eqs. 4.98 and 4.99 into Eqs. 4.97 and carry out necessary integration; the horizontal increments in membrane tension become

$$\Delta H_x = \frac{Eh}{2a}\int_{-a}^{a} \frac{\partial w_o}{\partial x}\frac{\partial w}{\partial x}\,dx \qquad (4.100a)$$

and

$$\Delta H_y = \frac{Eh}{2b}\int_{-b}^{b} \frac{\partial w_o}{\partial y}\frac{\partial w}{\partial y}\,dy \qquad (4.100b)$$

Substitution of ΔH_x and ΔH_y into Eq. 4.96 gives,

$$H_x\frac{\partial^2 w}{\partial x^2} + \frac{Eh}{2a}\left[\int_{-a}^{a}\frac{\partial w_o}{\partial x}\frac{\partial w}{\partial x}\,dx\right]\left(\frac{\partial^2 w_o}{\partial x^2} + \frac{\partial^2 w}{\partial x^2}\right)$$

$$+ H_y\frac{\partial^2 w}{\partial y^2} + \frac{Eh}{2b}\left[\int_{-b}^{b}\frac{\partial w_o}{\partial y}\frac{\partial w}{\partial y}\,dy\right]\left(\frac{\partial^2 w_o}{\partial y^2} + \frac{\partial^2 w}{\partial y^2}\right) = m\frac{\partial^2 w}{\partial t^2} \qquad (4.101)$$

Equation 4.96 is the general equation of free vibration of a curved membrane surface, defined under static equilibrium by the function $w_o(x,y)$. However, we are far from

reaching a solution to this equation; a numerical solution or further simplifications appear necessary. The author derives such a simplified solution as follows.

Since we assume small oscillation, a separated solution for the oscillations may be written as

$$w(x,y,t) = X(x)Y(y)T(t) \qquad (4.102)$$

To avoid mathematical complications in deriving the solution of Eq. 4.101, approximate assumptions must be introduced.

Since $w << w_o$ then

$$\frac{\partial^2 w_o}{\partial x^2} >> \frac{\partial^2 w}{\partial x^2} \text{ and } \frac{\partial^2 w_o}{\partial y^2} >> \frac{\partial^2 w}{\partial y^2}$$

and $\frac{\partial^2 w}{\partial x^2}$ and $\frac{\partial^2 w}{\partial y^2}$ may be neglected in the parenthesis of Eq. 4.101. This results in

$$H_x \frac{\partial^2 w}{\partial x^2} + \frac{Eh}{2a}\left[\int_{-a}^{a} \frac{\partial w_o}{\partial x}\frac{\partial w}{\partial x}\,dx\right]\left(\frac{\partial^2 w_o}{\partial x^2}\right)$$

$$+ H_y \frac{\partial^2 w}{\partial y^2} + \frac{Eh}{2b}\left[\int_{-b}^{b} \frac{\partial w_o}{\partial y}\frac{\partial w}{\partial y}\,dy\right]\frac{\partial^2 w_o}{\partial y^2} = m\frac{\partial^2 w}{\partial t^2} \qquad (4.103)$$

Now we will solve this equation for the hyperbolic paraboloid membrane, whose surface under static equilibrium is given by Eq. 4.93 and whose boundaries are fixed and given by

$$w(-a,y,t) = w(a,y,t) = w(x,-b,t) = w(x,b,t) = 0 \tag{4.104}$$

Substituting Eqs. 4.93 and 4.102 into Eq. 4.103 and dividing both sides by XYT

$$\left(H_x \frac{X''}{X} + \frac{2Ehf_x^2}{a^5} \frac{\int_{-a}^{a} x\, X'dx}{X}\right) + \left(H_y \frac{Y''}{Y} + \frac{2Ehf_y^2}{b^5} \frac{\int_{-b}^{b} y\, Y'dy}{Y}\right) = m \frac{T''}{T} \tag{4.105}$$

The three parts of Eq. 4.105 include only one variable each and thus, each term must be constant, giving

$$H_x \frac{X''}{X} + \frac{2Ehf_x^2}{a^5} \frac{\int_{-a}^{a} x\, X'dx}{X} = -\lambda^2 \tag{4.106a}$$

$$H_y \frac{Y''}{Y} + \frac{2Ehf_y^2}{b^5} \frac{\int_{-b}^{b} y\, Y'dy}{Y} = -\beta^2 \tag{4.106b}$$

$$m \frac{T''}{T} = -(\lambda^2 + \beta^2) \tag{4.106c}$$

In the integral,

$$\int_{-a}^{a} x\, X'dx = x\, X \Big|_{-a}^{a} - \int_{-a}^{a} X\, dx$$

the first term on the right-hand side vanishes due to the boundary conditions (4.104), giving

$$\int_{-a}^{a} x\, X'dx = - \int_{-a}^{a} X\, dx$$

Similarly,

$$\int_{-b}^{b} y\, Y' dy = -\int_{-b}^{b} Y\, dy$$

Then, Eqs. 4.106a and 4.106b, after rearranging, give

$$\frac{\partial^2 X}{\partial x^2} + \nu_x^2 X - \frac{1}{C_x}\int_{-a}^{a} X\, dx = 0 \qquad (4.107a)$$

and

$$\frac{\partial^2 Y}{\partial y^2} + \nu_y^2 Y - \frac{1}{C_y}\int_{-b}^{b} Y\, dy = 0 \qquad (4.107b)$$

where

$$\nu_x^2 = \frac{\lambda^2}{H_x}\,,\quad \nu_y^2 = \frac{\beta^2}{H_y}\,,\quad C_x = \frac{H_x a^5}{2Ehf_x^2}\,,\quad C_y = \frac{H_y b^5}{2Ehf_y^2}$$

Equations 4.107 are integro-differential equations and their solution may be written in the form [77]

$$X(x) = A\cos \nu_x x + B \sin \nu_x x + K \qquad (4.108a)$$

$$Y(y) = C\cos \nu_y y + D \sin \nu_y y + Q \qquad (4.108b)$$

where A, B, C and D are arbitrary constants to be determined from the initial conditions.

Substituting Eq. 4.108a into Eq. 4.107a and Eq. 4.108b into Eq. 4.107b, we get the following relation for K and Q:

$$K = \frac{1}{\nu_x^2 C_x}\int_{-a}^{a} X(x)dx \qquad (4.109a)$$

and

$$Q = \frac{1}{\nu_y^2 C_y} \int_{-b}^{b} Y(y)dy \qquad (4.109b)$$

Substituting Eq. 4.108a into Eq. 4.109a and carrying out the integration results in an equation relating A and K as

$$A\left(\frac{2}{\nu_x} \sin \nu_x a\right) + K(2a - \nu_x^2 C_x) = 0 \qquad (4.110a)$$

Applying the boundary conditions (2.104) to Eq. 4.108a, two more equations are available, i.e.

$$A \cos \nu_x a + B \sin \nu_x a + K = 0 \qquad (4.110b)$$

$$A \cos \nu_x a - B \sin \nu_x a + K = 0 \qquad (4.110c)$$

Equations 4.110 are three homogeneous equations in A, B and K having a nontrivial solution only when their determinant is zero. Thus,

$$\begin{array}{c|ccc|} & A & B & K \\ A & \frac{2}{\nu_x} \sin \nu_x a & 0 & (2a-\nu_x^2 C_x) \\ B & \cos \nu_x a & \sin \nu_x a & 1 \\ K & \cos \nu_x a & -\sin \nu_x a & 1 \end{array} = 0$$

Expanding the determinant and arranging as necessary,

$$2 \sin \nu_x a \left[2 \frac{\sin \nu_x a}{\nu_x} - \cos \nu_x a (2a - \nu_x^2 C_x)\right] = 0 \qquad (4.111)$$

Equation 4.111 has two solutions:

(a) $$\sin(\nu_x a) = 0 \qquad (4.112)$$

This yields an infinite sequence of eigenvalues determined by

$$\nu_{n_1 x} a = n\pi \quad , \; n = 1,2,3,... \qquad (4.113)$$

Substituting for $\nu_{n_1 x}^2 = \frac{\lambda_{n_1}^2}{H_x}$

$$\lambda_{n_1}^2 = H_x \frac{n^2 \pi^2}{a^2} \qquad (4.114)$$

(b) Putting the second factor equal to zero and dividing by $\sin \nu_x a$, leads to the equation

$$\tan(\nu_x a) = \nu_x (a - \tfrac{1}{2} \nu_x^2 C_x) \qquad (4.115)$$

This transcendental equation yields the infinite set of positive roots denoted by

$$\nu_{n_2 x}(C_x) \quad , \quad n_2 = 1,2,3,... \qquad (4.116)$$

and determines a set of eigenvalues. Plotting the left-hand and right-hand sides of Eq. 4.115, the solutions are obtained as the points of intersection between the branches of the $\tan(\nu_x a)$ curve and the third degree curve, Figure

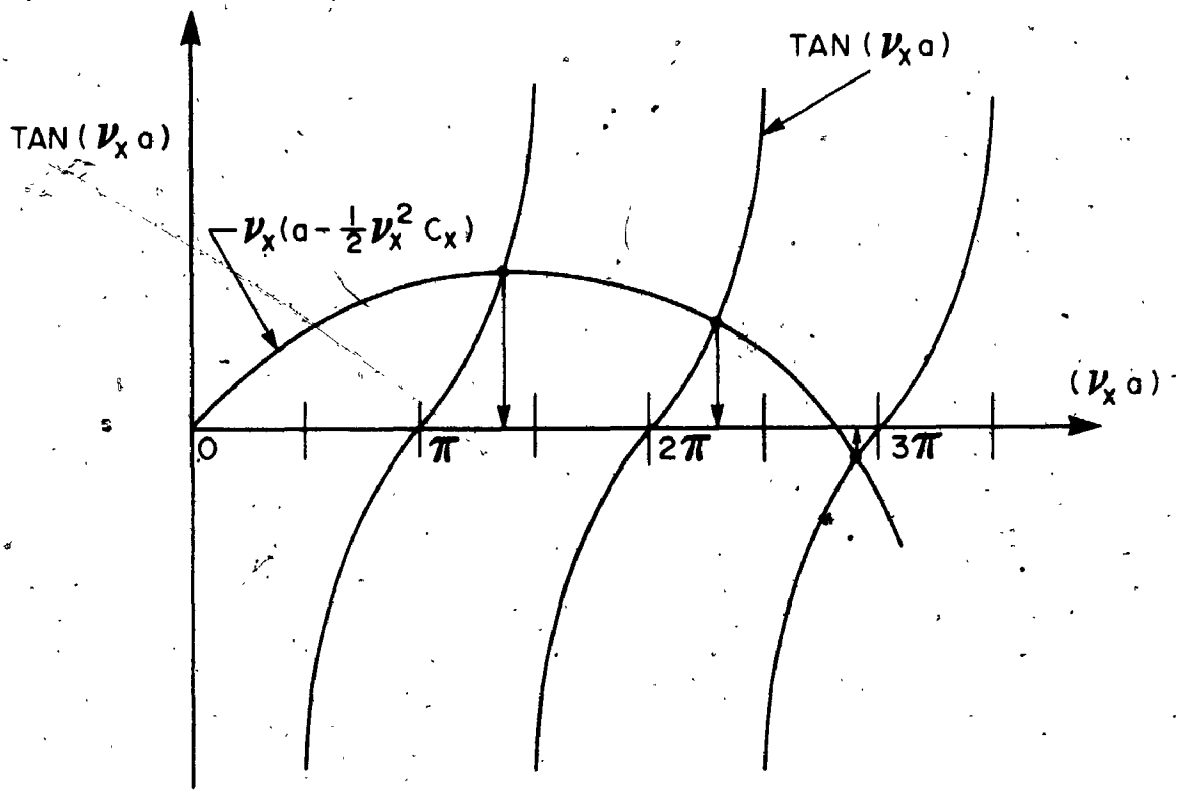

FIGURE 4.12 GRAPHICAL SOLUTION OF EQUATION (4.115)

4.12.

The first solution, resulting in K and B being equal to zero, gives the eigenfunction

$$X_{n_1}(x) = B \sin \frac{n_1 \pi}{a} x \quad , n_1 = 1,2,3,... \qquad (4.117)$$

These eigenfunctions are antisymmetric with respect to $x = 0$.

For the second solution, $B = 0$ and $K = -A \cos \nu_{n_2 x} a$, and the eigenfunction becomes

$$X_{n_2}(x) = A(\cos \nu_{n_2 x} x - \cos \nu_{n_2 x} a), \quad n=1,2,3... \qquad (4.118)$$

These functions are symmetric with respect to $x = 0$. Let us now arrange the eigenvalues $\nu_{n_1 x}, \nu_{n_2 x}$ in order of increasing magnitude. The corresponding sequence is denoted by

$$\nu_{nx}(C_x) \quad , n = 1,2,3... \text{ where } \nu_n \leq \nu_{n+1}$$

and determines the complete set of eigenvalues, obtained from Eqs. 4.113 and 4.116. The corresponding complete set of eigenfunctions, made up of all the functions (4.117) and (4.118), is denoted

$$X_n(C_x, x) \quad , \quad n = 1,2,3,...$$

Similarly, from Eq. 4.107b and the boundary conditions (4.104), the following results are obtained:

1. For the first solution,

$$\sin(\nu_y b) = 0 \tag{4.119}$$

and the corresponding eigenvalues are

$$\nu_{m_1 y} b = m \ , \quad m = 1,2,3,... \tag{4.120}$$

with the corresponding antisymmetric functions

$$Y_{m_1}(x) = D \sin \frac{m\pi}{b} y \ , \ m = 1,2,3,... \tag{4.121}$$

2. The second solution gives the eigenvalue equation

$$\tan(\nu_y b) = \nu_y (b - \frac{1}{2} \nu_y^2 C_y) \tag{4.122}$$

with the eigenvalues obtained from Eq. 4.121 as

$$\nu_{m_2 y}(C_y) \ , \ m = 1,2,3,...$$

and the corresponding symmetric eigenfunctions

$$Y_{2m}(y) = C(\cos\nu_{m_2 y} b - \cos\nu_{m_2 y} y), \ m = 1,2,3,... \tag{4.123}$$

The eigenvalues arranged in increasing order from Eqs. 4.120 and 4.121 are denoted by

$$\nu_{m_y}(C_y) \ , \ m = 1,2,3,...$$

The possible eigenfunctions, as the outcome of Eqs. 4.121 and 4.123 are denoted by

$$Y_m(C_y,y) \quad , \quad m = 1,2,3,...$$

At this stage of the analysis, the mode shapes of the system (4.102) are completely defined:

$$w(x,y) = X_n(C_x,x)Y_m(C_y,y) \quad n,m = 1,2,3,... \qquad (4.124)$$

The complete definition of the eigenvalues ν_{nx}, ν_{mx} (4.106c) results in

$$T'' + \frac{1}{m}[H_x \nu_{nx}^2(C_x) + H_y \nu_{my}^2(C_y)]T = 0 \qquad (4.125)$$

The solution of Eq. 4.125 gives

$$T(t) = F_{nm} \cos\omega_{nm}t + G_{nm} \sin\omega_{nm}t \qquad (4.126)$$

where

$$\omega_{nm}^2 = \frac{1}{m}[H_x \nu_{nx}^2(C_x) + H_y \nu_{my}^2(C_y)] \qquad (4.127)$$

The complete solution of the free vibration may be written now in the final form as

$$w(x,y,t) = X_n(C_x,x)Y_m(C_y,y)\{\bar{A}_{nm}\cos\omega_{nm}t + \bar{B}_{nm}\cos\omega_{nm}t\} \qquad (4.128)$$

where

$X_n(C_x,x) = \sin\nu_{nx}x$ when ν_{nx} is given by Eq. 4.113

$$\nu_{nx} = n\pi/a$$

$= (\cos\nu_{nx}a - \cos\nu_{nx}x)$ when ν_{nx} is given by Eq. 4.115.

Similarly,

$Y_m(C_y,x) = \sin\nu_{my}y$ when ν_{my} is given by Eq. 4.120

$$\nu_{my} = \frac{m\pi}{b}$$

$= (\cos\nu_{my}b - \cos\nu_{my}y)$ when ν_{my} is given by Eq. 4.122.

$\bar{A}_{nm}$ and $\bar{B}_{nm}$ are arbitrary constants to be determined from initial conditions (4.94) in the same way as in the case of membranes stretched over rectangular or circular fixed boundaries.

It appears that the solutions available for Eq. 4.111 of the determinant for the eigenvalues and the eigenfunctions may include the flat stretched rectangular membrane. This argument is based on the first solution which is independent of the function C_x and therefore of the rise and the sag of the hyperbolic paraboloid. This solution gives the eigenvalues for the membrane as

$$\omega_{nm}^2 = \frac{\pi}{m}\left[H_x\frac{n^2}{a^2} + H_y\frac{m^2}{b^2}\right] \quad n,m = 1,2,3,\ldots$$

and the eigenfunction,

$$w(x,y) = \sin n\pi\frac{x}{a}\sin m\pi\frac{y}{b}, \quad n,m = 1,2,3,\ldots,$$

which is the same solution as was obtained for the rectangular flat stretched membrane.

The above simplified solution formulated by the author leads to the following conclusions:

1. If the hyperbolic paraboloid is very shallow, the second solution of Eq. 4.111 may be ignored and the roof vibrates nearly as a flat membrane.
2. Furthermore, since the antisymmetric modes did not cause additional tension in the membrane, then we may conclude that the solution 1 which is independent of the tension increment ΔH, gives the same modes as the flat membrane with ΔH equal to zero.

4.2.2.6 Free Vibration of Circular Hyperbolic Paraboloid

Consider a hyperbolic paraboloid membrane of mass per unit area m, stretched uniformly all around a rigid boundary circular in plan, with tension per unit length of arc T, as shown in Figure 4.13. The general solution outlined above is extended by the author to include this case of the hyperbolic paraboloid in the following fashion:

The surface of the membrane under static equilibrium may be described in Cartesian coordinates by,

$$w_o(x,y) = f_1\left(\frac{x}{a}\right)^2 - f_2\left(\frac{y}{a}\right)^2 \qquad (4.129)$$

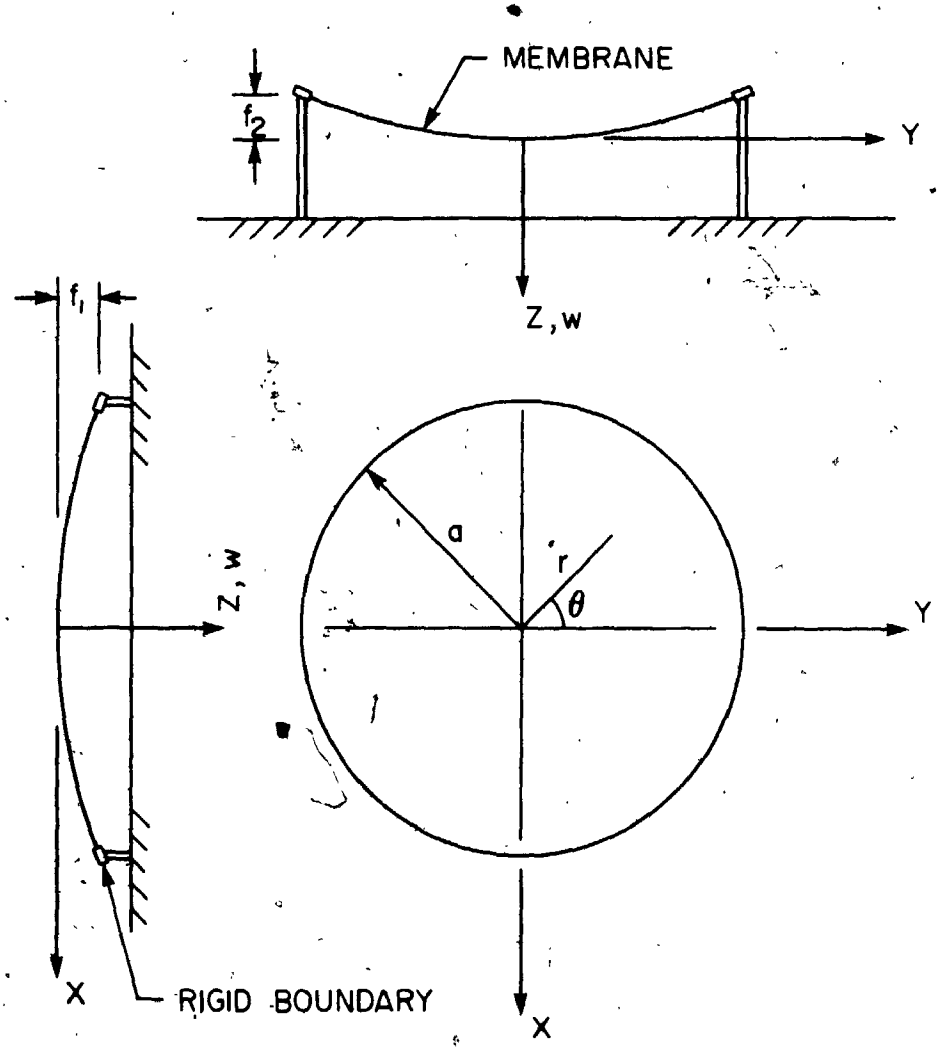

FIGURE 4.13 CIRCULAR HYPERABOLIC PARABOLOID COORDINATES AND DEFINITION.

where f_1 = the drop along the x axis ($\theta = 0, \pi$), f_2 = the sag along the y axis ($\theta = \frac{\pi}{2}, \frac{3}{2}\pi$) and a is the radius of the plane circle.

In polar coordinates, Eq. 4.129 takes the form,

$$w_o(r,\theta) = f_1\left(\frac{r}{a}\right)^2 \cos^2\theta - f_2\left(\frac{r}{a}\right)^2 \sin^2\theta \qquad (4.130)$$

with the transformation from Cartesian to polar coordinates $x = r\cos\theta$, $y = r\sin\theta$, and the equation of the plane circle at the boundary $r = a$.

The general equation of motion of a free vibrating curved membrane surface, developed in the previous section, may be redeveloped in polar coordinates applying the following relations between Cartesian and polar coordinates:

$$\frac{\partial w}{\partial r} = \cos\theta \frac{\partial w}{\partial r} - \frac{\sin\theta}{r} \frac{\partial w}{\partial \theta} \qquad (2.131a)$$

$$\frac{\partial w}{\partial r} = \sin\theta \frac{\partial w}{\partial r} - \frac{\cos\theta}{r} \frac{\partial w}{\partial \theta} \qquad (2.131b)$$

$$\frac{\partial^2 w}{\partial x^2} = \cos^2\theta \frac{\partial^2 w}{\partial r^2} + \frac{\sin^2\theta}{r^2} \frac{\partial^2 w}{\partial \theta^2} - \frac{2\sin\theta\cos\theta}{r} \frac{\partial^2 w}{\partial r \partial \theta}$$

$$+ 2\frac{\sin\theta\cos\theta}{r^2} \frac{\partial w}{\partial \theta} + \frac{\sin^2\theta}{r} \frac{\partial w}{\partial r} \qquad (2.131c)$$

and

$$\frac{\partial^2 w}{\partial y^2} = \sin^2\theta \frac{\partial^2 w}{\partial r^2} + \cos^2\theta \frac{\partial^2 w}{\partial \theta^2} + 2 \frac{\sin\theta\cos\theta}{r} \frac{\partial^2 w}{\partial r \partial \theta}$$

$$- 2 \frac{\sin\theta\cos\theta}{r^2} \frac{\partial w}{\partial \theta} + \frac{\cos^2\theta}{r} \frac{\partial w}{\partial r} \qquad (2.131d)$$

Assuming that the membrane vibrates linearly about the static equilibrium of Eq. 4.130, the increase in membrane tension due to vibration is independent of space and time (i.e., $\frac{\partial \Delta H}{\partial i} di = 0$; $i = r, \theta, t$). Assume that the initial horizontal tension H in the membrane is constant, hence, the additional (increase) horizontal component of membrane tension ΔH, due to linear vibrations will be uniform throughout the membrane.

Based on these assumptions, the general equation of vibrating curved membrane surface (4.96), developed earlier, may be recalled here, and after rearrangement may be written in the form:

$$(H+\Delta H)\nabla^2 w + \Delta H \nabla^2 w_o = m \frac{\partial^2 w}{\partial t^2} \qquad (4.132)$$

in which ∇^2 is the Laplacian operator and ΔH is the increase in membrane tension due to linear vibration.

The solution of Eq. 4.132 is very complex and further simplifications have to be considered. Since $\Delta H << H$ and $\nabla^2 w << \nabla^2 w_o$, the second order of ΔH, $\nabla^2 w_o$, or their product may be ignored. Based on this assumption, Eq. 4.132 may be reduced to

$$H\nabla^2 w + \Delta H \nabla^2 w_o = m \frac{\partial^2 w}{\partial t^2} \tag{4.133}$$

The additional tension may be determined from the elastic properties of the membrane material and compatibility of the deformations.

The equations of elastic and geometric compatibility (4.97) and (4.99) may be written in terms of the area element dxdy by assuming the transverse displacement w only is significant (i.e., the displacements of the membrane in its plan are negligible) which gives

$$\frac{\Delta H}{Eh}\, dxdy + \frac{\Delta H}{Eh}\, dydx = \frac{\partial w_o}{\partial x}\frac{\partial w}{\partial x}\, dxdy + \frac{\partial w_o}{\partial y}\frac{\partial w}{\partial y}\, dydx \tag{4.134}$$

Since ΔH is assumed constant everywhere, Eq. 4.134 may be expressed in integral form, which, rearranged, gives

$$\Delta H = \frac{Eh}{2S} \int_S \int \left[\frac{\partial w_o}{\partial x}\frac{\partial w}{\partial x} + \frac{\partial w_o}{\partial y}\frac{\partial w}{\partial y}\right] dxdy \tag{4.135}$$

Here, S = the plane area of the membrane (πa^2), h,E = the membrane thickness and its material modulus of elasticity respectively; the double integral is taken over the plane area of the membrane.

Assuming the boundaries are rigid, the right-hand side of Eq. 4.135 may be further simplified by integration by parts. Applying the boundary conditions which imply that w vanishes at the boundaries, Eq. 4.135 yields

$$\Delta H = - \frac{Eh}{2S} \nabla^2 w_o \int \int w \, dxdy \qquad (4.136)$$

in which $\nabla^2 w_o$ is constant and given by

$$\nabla^2 w_o = \frac{2}{a^2} (f_1 - f_2) \qquad (4.137)$$

The Laplacian operator in polar coordinates is

$$\nabla^2 = \frac{\partial^2}{\partial r^2} + \frac{1}{r} \frac{\partial}{\partial r} + \frac{1}{r^2} \frac{\partial}{\partial \theta^2} \qquad (4.138)$$

Substituting Eqs. 4.136, 4.137 and 4.138 into Eq. 4.133 and rearranging, the equation of free vibration of the circular hyperbolic paraboloid is obtained as,

$$\frac{\partial^2 w}{\partial r^2} + \frac{1}{r} \frac{\partial w}{\partial r} + \frac{1}{r^2} \frac{\partial^2 w}{\partial \theta^2} = \frac{1}{\nu^2} \frac{\partial^2 w}{\partial t^2} + \frac{1}{a^4 C^2} \int_o^{2\pi} \int_o^a w \, r dr d\theta \qquad (4.139)$$

in which $C^2 = \frac{\pi a^2 H}{2Eh} / (f_1 - f_2)^2$, r under the double integral is the Jacobian for transformation from Cartesian to polar coordinates and $\nu^2 = \frac{H}{m}$.

An equation similar to Eq. 4.139 was obtained by Irvine in 1981 [18], using a completely different approach, but he did not give a solution for it due to its complexity. In this work, an attempt has been made to reach a solution to Eq. 4.139.

Assume a separated solution of the form,

$$w(r,\theta,t) = R(r)\phi(\theta)T(t) \qquad (4.140)$$

Substituting Eq. 4.140 into Eq. 4.139 and dividing both sides by $R(r)\phi(\theta)T(t)$, gives

$$\frac{1}{R(r)}\frac{\partial^2 R(r)}{\partial r^2}+\frac{1}{rR(r)}\frac{\partial R(r)}{\partial r}+\frac{1}{r\phi(\theta)}\frac{\partial^2\phi(\theta)}{\partial\theta^2}=\frac{1}{\nu^2 T(t)}\frac{\partial^2 T(t)}{\partial t^2}$$

$$+\frac{1}{a^4C^2}\frac{\int_0^{2\pi}\int_0^a R(r)\phi(\theta)\,r\,dr\,d\theta}{R(r)\phi(\theta)} \qquad (4.141)$$

After integration by parts of the double integral on the right-hand side of Eq. 4.141, it may be seen that the double integral vanishes for $R(r)\phi(\theta)$ representing anti-symmetric modes but not symmetric modes. Therefore, Eq. 4.141 may be split into two parts: one, for anti-symmetrical modes, takes the form:

$$\frac{1}{R(r)}\frac{\partial^2 R(r)}{\partial r^2}+\frac{1}{rR(r)}\frac{\partial R(r)}{\partial r}+\frac{1}{r^2}\frac{1}{\phi(\theta)}\frac{\partial^2\phi(\theta)}{\partial\theta^2}=\frac{1}{\nu^2 T(t)}\frac{\partial^2 T(t)}{\partial t^2} \qquad (1.142)$$

The other, for symmetrical modes, which are independent on the coordinate θ, takes the form:

$$\frac{1}{R(r)}\frac{\partial^2 R(r)}{\partial r^2}+\frac{1}{rR(r)}\frac{\partial R(r)}{\partial r}-\frac{1}{a^4C^2R(r)}\int_0^a rR(r)\,dr$$

$$=\frac{1}{\nu^2}\frac{1}{T(t)}\frac{\partial^2 T(t)}{\partial t} \qquad (4.143)$$

The solution of Eq. 4.142 is similar to that for the circular flat membrane given previously by Eq. 4.58, in which ν is now $(\frac{H}{m})^{1/2}$.

Equation 4.143 is a simple form of integro-differential equation and its solution may be possible after separating the variables.

One side of Eq. 4.143 is independent of the other and separation of variables technique implies that each side must be equal to a negative constant. Let this constant be $-\omega^2$, then for T(t), we get

$$\frac{\partial^2 T(t)}{\partial t^2} + \nu^2\omega^2 T(t) = 0 \qquad (4.144)$$

and for the function R(r), we have the following, rearranged equation:

$$r^2 \frac{\partial^2 R(r)}{\partial r^2} + r \frac{\partial R(r)}{\partial r} + \left(\frac{\omega^2}{\nu^2} r^2\right) R(r) - \frac{r^2}{a^4 C^2} \int_o^a rR(r)dr = 0 \qquad (4.145)$$

The solutions for this equation are sought in the limits $0 \leq r \leq a$, with the boundary condition $R(a) = 0$. It can be shown that this in fact is a self-adjoint, positive definite eigenvalue problem.

The integral $\int_o^a rR(r)dr$ is independent of r, so the general solution may be written in the form

$$R(r) = AJ_o\left(\frac{\omega r}{\nu}\right) + BY_o\left(\frac{\omega r}{\nu}\right) + I \qquad (4.146)$$

where A, B and I are constants to be determined from the boundary conditions. As in the previous discussion of circular flat membrane free vibration, in order to avoid

infinite deflection of the function R(r) by Y_k, B must vanish; then Eq. 4.146 takes the form

$$R(r) = AJ_o(\frac{\omega r}{\nu}) + I \tag{4.147}$$

Substituting Eq. 4.147 into Eq. 4.145, carrying out the necessary mathematical formulations, which are based mainly on Bessel function properties, and rearranging we get

$$I = (\frac{\nu}{a^2\omega C})^2 \int_o^a R(r) r \, dr \tag{4.148}$$

This relation gives the value of the constant I; it is seen from Eq. 4.148 that I is independent of r and is determined by the integral limits.

Substituting Eq. 4.147 into Eq. 4.148, integrating and rearranging we get the following equation:

$$A[(\frac{a\nu}{\omega})J_1(\frac{\omega a}{\nu})] + I[\frac{a^2}{2} - (\frac{\omega C}{a^2\nu})^2] = 0 \tag{4.149}$$

Applying the boundary conditions to Eq. 4.147, which implies that R(r) vanishes at a,

$$AJ_o(\frac{\omega a}{\nu}) + I = 0 \tag{4.150}$$

To get a nontrivial solution for the constants A and I from Eqs. 4.149 and 4.150, their determinant must vanish, i.e.,

$$\begin{vmatrix} \frac{a\nu}{\omega} J_1(\frac{\omega a}{\nu}) & [\frac{a^2}{2} - (\frac{\omega C}{a^2\nu})^2 \\ \vdots & \\ J_o(\frac{\omega a}{\nu}) & 1 \end{vmatrix} = 0 \qquad (4.151)$$

This condition yields

$$\frac{J_1(\frac{\omega a}{\nu})}{J_o(\frac{\omega a}{\nu})} = \frac{\omega a}{\nu} [\frac{1}{2} - (\frac{a\omega C}{\nu})^2] \qquad (4.152)$$

Equation 4.152 is the frequency equation of the symmetric modes of the circular hyperbolic paraboloid, and its solution gives the different frequencies of the symmetric modes of vibration.

The ratio of the Bessel functions is (see, e.g. [83])

$$\frac{J_1(\frac{\omega_{om} a}{\nu})}{J_o(\frac{\omega_{om} a}{\nu})} = \sum_m^\infty [\frac{2(\frac{\omega_{om} a}{\nu})}{j_{o,m}^2 - (\frac{\omega_{om} a}{\nu})^2}] \qquad (4.153)$$

where, $j_{o,m}$ = are the zeroes of the Bessel function

$J_o(\frac{\omega_{om} a}{\nu})$, m = 1,2,3,...

Equating Eqs. 4.152 and 4.153,

$$(\frac{\omega_{om} a}{\nu})[\frac{1}{2} - (\frac{a\omega_{om}}{\nu})^2 C^2] = \sum_m^\infty [\frac{2(\frac{\omega_{om} a}{\nu})}{j_{o,m}^2 - (\frac{\omega_{om} a}{\nu})^2}] \qquad (4.154)$$

Equation 4.154 is the frequency equation of all symmetric modes ω_{om}, m = 1,2,3,..., of the circular hyperbolic paraboloid

cable tension roof. This equation leads to the following equation for the frequency of mode ω_{o1}:

$$\omega_{o1} = \frac{1}{a}\left(\frac{H}{m}\right)^{1/2}\left\{\frac{1}{4C^2} + \frac{1}{2}j_{0,1}^2 \pm \frac{1}{2}\left[j_{0,1}^4 - \frac{j_{0,1}^2}{C^2} + \frac{1}{4C^4} + \frac{8}{C^2}\right]^{1/2}\right\}^{1/2} \tag{4.155}$$

The non-dimensional parameter

$$C^2 = \frac{\pi a^2 H}{2Eh}/(f_1 - f_2)^2$$

plays a significant role in this equation. When $f_1, f_2 \to 0$, $C^2 \to \infty$, and Eq. 4.155 reduces to

$$\omega_{o1} = \frac{j_{0,1}}{a}\left(\frac{H}{m}\right)^{1/2}$$

which is the equation of the first mode of a circular flat tension roof. Hence, the theory of free vibration of circular flat membrane is obtained as a special case.

When $f_1, f_2 \neq 0$, the mode ω_{o1} of the hyperbolic paraboloid roof has much higher frequency than the flat roof.

The hyperbolic paraboloid roof under experimental investigation (Chapter 6) has a value for $C^2 = 0.009$. For this value substituted into Eq. 4.155 gives a frequency for mode ω_{o1} is about three times higher than that for a flat roof. These theoretical results are in agreement with experimental results obtained from experiments described in Chapter 6.

It may be concluded that the mode ω_{o1} of the hyperbolic paraboloid roof is about nine times stiffer than the corresponding mode of a flat roof. This suggests that the hyperbolic paraboloid roof is too stiff to move up and down as a whole in the first symmetric mode, and therefore it tends to move in its antisymmetric modes which need less energy than the symmetric modes. The mode shapes are defined by substituting Eq. 4.149 into Eq. 4.147 and by using the result obtained in Eq. 4.152. We get

$$R(r) = A[J_o(\frac{\omega r}{\nu}) - J_o(\frac{\omega a}{\nu})] \qquad (4.156)$$

Equation 4.156 is the equation for the symmetric vibration modes of the circular hyperbolic paraboloid.

The complete solution for the free vibration is obtained by combining the solution of Eq. 4.144, obtained in previous analysis in this work, with the solution of the mode shape equation. This gives the complete configuration as,

$$w_{om}(r,t) = \sum_m [J_o(\frac{\omega_{om} r}{\nu}) - J_o(\frac{\omega_{om} a}{\nu})](a_{om}\cos\omega_{om}t + b_{om}\sin\omega_{om}t)$$

$$+ \sum_n J_n(\frac{\omega_{n1} r}{\nu})\{[(C_{n1}\cos n\theta + d_{n1}\sin n\theta)\cos\omega_{n1}t]$$

$$+ [(e_{n1}\cos n\theta + g_{n1}\sin n\theta)\sin\omega_{n1}t]\}$$

for $m = 1,2,3,\ldots$ and $n = 1,2,3,\ldots$ (4.157)

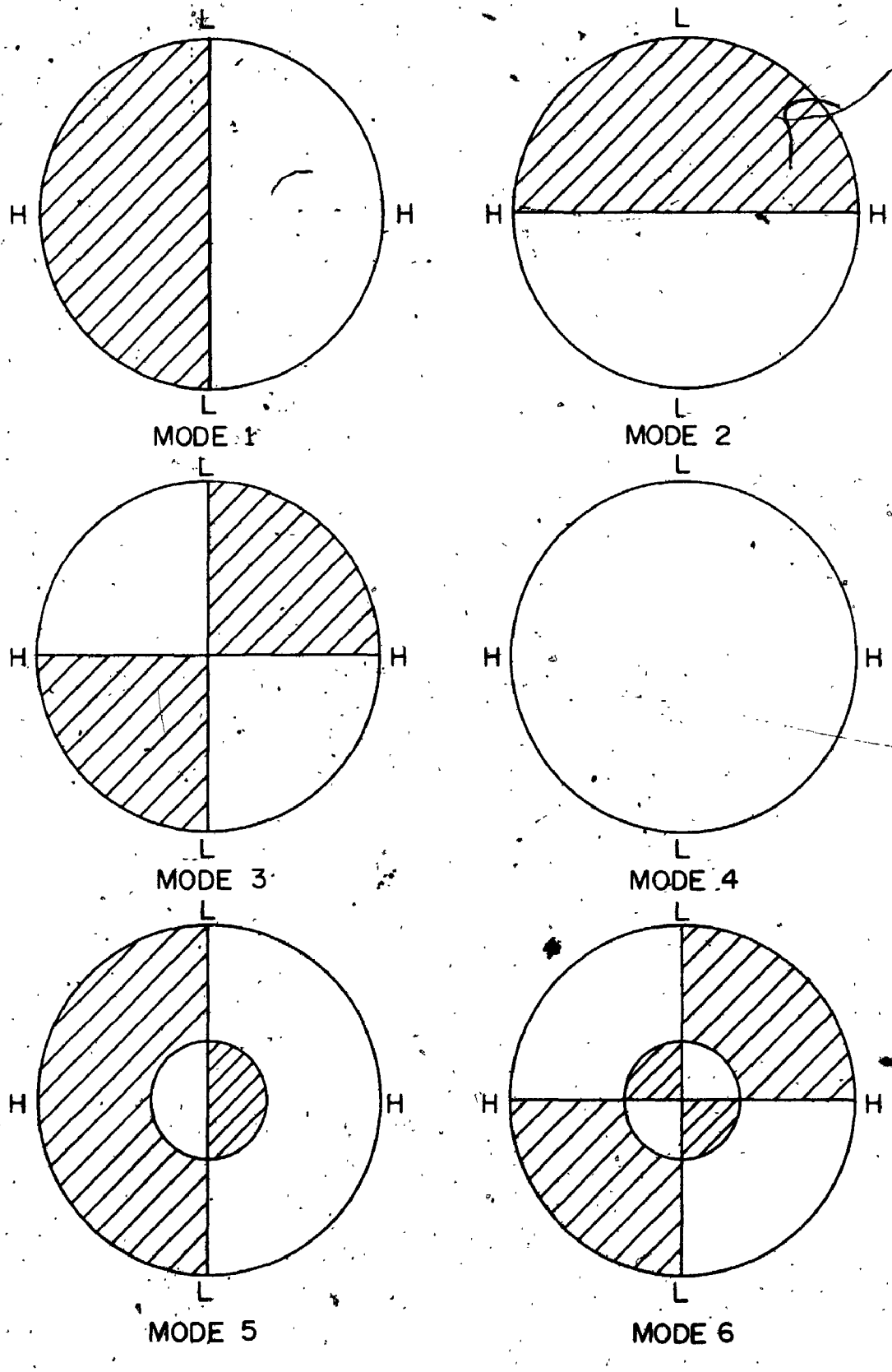

FIGURE 4.14. POSSIBLE VIBRATION MODES OF A CIRCULAR HYPERABOLIC PARABOLOID TENSION ROOF.

The possible vibration modes are shown in Figure 4.14. It is interesting and significant that Eq. 4.156, obtained in this work for the symmetric modes of vibration, was suggested without proof by Kinsler and Frey [78] in their study of propagation of sound within cylindrical enclosures.

4.3 FREE VIBRATION OF CABLE ROOF BACKED BY A CAVITY

4.3.1 Introduction

A study of the free vibration of an isolated cable roof is rarely applicable. More often, a structure is enclosed and has openings (doors and windows) and the air movement through them due to roof movement during vibration affects the dynamic characteristics of the roof, especially the natural frequency of those modes which cause a large change in the air volume of the cavity. This change in volume is accompanied by a change in pressure of the air inside the enclosure.

As the roof vibrates, the air inside the enclosure is alternatively compressed and expanded. During the compression action, a volume of air moves out through the openings and as the air expands, a volume of air moves in. This movement of air is due to the change of the air pressure within the enclosure caused by the change of the volume during roof vibration.

The problem of a completely closed cavity has been

studied by many authors (e.g. Kinsler and Frey [78]), but the problem of cavity with openings is more difficult. In this work, an attempt is made by the author to explore this problem and reach a solution.

4.3.2 Free Vibration of Circular Cable Roof Backed by Closed Cavity

For a circular cable roof having a fixed boundary of radius a, the mode shapes of the equivalent membrane may be given by Eq. 4.58 as

$$w_{nm}(r,\theta) = J_n(\frac{\omega_{nm} r}{\nu}) A_{nm} \cos n\theta \qquad (4.158)$$

in which ω_{nm} is the natural frequency of mode w_{nm}, $\nu = \sqrt{\frac{T}{m}}$ where T, m are the uniform tension per unit length and the mass per unit area of the membrane respectively, and A_{nm} is the displacement amplitude. The average amplitude of displacement of the membrane surface s, in mode nm, may be defined as

$$\bar{w}_{nm} = \frac{\int_s w_{nm} ds}{\pi a^2} \qquad (4.159)$$

in which $ds = 2\pi r dr$. An inspection of the $J_{nm}(\frac{\omega_{nm} r}{\nu})$ function shows that a membrane vibrating at frequencies other than its fundamental frequency (ω_{01}) produces little net displacement of the surrounding air.

For symmetrical modes (n = 0), all parts of a

ring-shaped surface element, $ds = 2\pi r\, dr$, contained between r and r+dr, have the same displacement amplitude and it is possible to carry out the indicated surface integration of Eq. 4.159 by merely integrating over r from o to a. Then

$$\bar{w}_{om} = \frac{\int_o^a A_{om} J_o\left(\frac{\omega_{om} r}{\nu}\right) 2\pi r\, dr}{\pi a^2} \qquad (4.160)$$

which upon integration becomes

$$\bar{w}_{om} = \frac{2\nu A_{om}}{a\omega_{om}} J_1\left(\frac{\omega_{om} a}{\nu}\right) \qquad (4.161)$$

in which A_{om} = the displacement amplitude at the centre. For the fundamental mode (m = 1),

$$\bar{w}_{o1} = 0.432\, A_{o1}$$

and for the second symmetrical mode (m = 2),

$$\bar{w}_{o2} = -0.123\, A_{o2}$$

where the negative sign indicates that the average displacement amplitude is oppositely directed to the displacement at the centre. When the displacement amplitudes at the centre are equal, i.e. $A_{o1} = A_{o2}$, the fundamental mode of vibration is more than three times as effective for displacing the air as is the second symmetrical model.

This shows that the fundamental mode of vibration

produces a large change in volume, Figure 4.15, but that a membrane vibrating at natural frequencies other than its fundamental frequency, produce little net volume change of the enclosed air.

In many problems encountered in the study of sources of sound waves, the characteristics of the sound wave are dependent on the amount of air displaced, i.e. the volume displacement amplitude and not on the exact shape of moving surface. Then the radiating source may be replaced by an equivalent simple piston, such that the product of its area and displacement amplitude is equal to the volume displacement amplitude of the true surface.

As the membrane vibrates, the air in the enclosure is alternately compressed and expanded. These changes in pressure occur within the enclosure behind the membrane as the volume of entrapped air is altered by vibration of the membrane. Since the radial velocity of transverse waves along the membrane is much less than the speed of sound in air, the pressure resulting from the compression and expansion of the air in the enclosure may be assumed uniform over the entire extent of the membrane, i.e. it is not a function of radial position and depends only on the average displacement $\bar{w}$.

When the surface of the membrane is displaced an

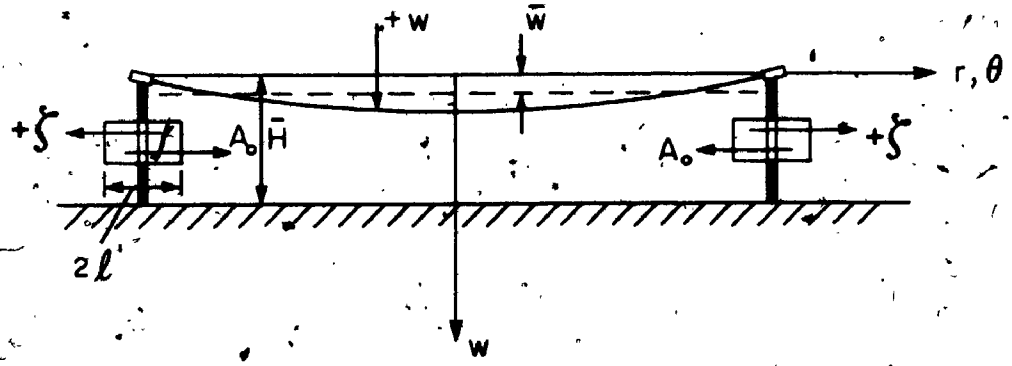

FIGURE 4.15 VIBRATION OF A CIRCULAR MEMBRANE BACKED BY A CAVITY, AND NOTATION.

average amount $\bar{w}$, the increment in the volume of the enclosed air is

$$\Delta V = \pi a^2 \bar{w} \tag{4.162}$$

where a is the radius of the membrane. If the equilibrium volume inside the enclosure is V_o and the equilibrium pressure is p_o, and the alternations of volume are adiabatic, the new pressure p and volume V are related by,

$$pV^\gamma = p_o V_o^\gamma = \text{constant} \tag{4.163}$$

where γ here represents the ratio of the specific heat of the entrapped air at constant pressure to its specific heat at constant volume. By differentiation of this equation, it is possible to show that the increase in pressure Δp inside the enclosure will be

$$\Delta p = -\frac{\gamma p_o}{V_o} \Delta V = -\frac{\gamma p_o}{V_o} \pi a^2 \bar{w} \tag{4.164}$$

The introduction of a force given by Eq. 4.164 as acting upon each unit area of the membrane modifies the equation of motion (4.32) which now becomes,

$$\nu^2 \nabla^2 w = \frac{\partial^2 w}{\partial t^2} + \frac{\gamma p_o}{m V_o} \pi a^2 \bar{w} \tag{4.165}$$

where $\bar{w}$ is an integral function of all the allowed modes of vibration, Eq. 4.59 and m = mass per unit area of the membrane. A general solution of Eq. 4.165 is complex.

However, if only one mode of vibration is present, the solution of Eq. 4.165 is greatly simplified. If only the frequency ω of the symmetrical mode is present, we may assume a solution in the form

$$w = R(r)e^{i\omega t} \tag{4.166}$$

Then, Eq. 4.165 becomes

$$\frac{d^2R(r)}{dr^2} + \frac{1}{r}\frac{dR(r)}{dr} + \frac{\omega^2}{\nu^2}R(r) = \frac{\gamma p_o}{TV_o}\int_o^a R(r)2\pi r\, dr \tag{4.167}$$

The solution for this type of integro-differential equation was obtained in the previous section and may be used here:

$$R(r) = A[J_o(\tfrac{\omega}{\nu}r) - J_o(\tfrac{\omega}{\nu}a)]. \tag{4.168}$$

With this solution, the right-hand term of Eq. 4.167 may be integrated and becomes

$$\frac{\gamma p_o}{TV_o}\int_o^a R(r)2\pi r\, dr = \frac{\pi a^2 \gamma p_o}{TV_o} A\, J_2(\tfrac{\omega}{\nu}a) \tag{4.169}$$

where $J_2(\frac{\omega}{\nu}a)$ is a second order Bessel function of the first kind.

Substituting Eq. 4.168 and the result of Eq. 4.169 into Eq. 4.167 leads to the frequency equation

$$(\tfrac{\omega a}{\nu})^2 \frac{J_o(\frac{\omega a}{\nu})}{J_2(\frac{\omega a}{\nu})} = -\alpha_o \tag{4.170}$$

where $\alpha_o = \frac{\pi a^4 \gamma p_o}{T V_o}$ is a non-dimensional constant measuring the relative importance of the restoring force, owing to the compression of the air in the enclosure and the tension, T, applied to the membrane. This constant α_o is small if either the volume of the enclosure or the tension in the membrane is large. In the limit where the constant α_o approaches zero, the allowed frequencies are those corresponding to $J_o(\frac{\omega}{v}a) = 0$. The condition corresponds to the one previously determined for free vibration of a circular membrane. Hence, the theory of free vibration of circular membrane in vacuo is obtained. This solution is due to Kinsler and Frey [78].

4.3.3 Free Vibration of Cable Roof Backed by Cavity With Openings

Most often a cable roof structure is enclosed and has openings. The air movement through them due to roof movement affects the frequency characteristics of the roof, especially the frequency of those modes which cause a change in the air volume of the cavity. This change in volume, as stated before, is accompanied by a change in pressure of the air inside the enclosure.

The problem of a completely closed cavity only has been studied by many authors in acoustic lectures and was reviewed in the previous paragraph. The problem of

a vibrating membrane backed by a cavity was studied briefly by the author, [108], and is completed in this work, accompanied by experimental verification of the theory (Chapter 6).

Since the dimensions of cable roof structure (radius and cavity depth) are small in comparison with the wave length of sound waves, as stated earlier, we may assume the enclosure under the roof will act like a Helmholtz Resonator; and the roof will act like a membrane piston on the enclosure.

The increase in pressure inside the resonator, which results when a volume of air ΔV moves in through an opening of area A_o, is given by [78],

$$\Delta p = -\gamma p \frac{\Delta V}{V_o} = -\rho c_o^2 \frac{\Delta V}{V_o} \tag{4.171}$$

in which ρ = mass density of air, c_o = speed of sound in air and V_o = original volume of the resonator.

The acoustic force acting on the opening, due to this change of internal pressure, is

$$\Delta p \, A_o = \rho c_o^2 \frac{\Delta V}{V_o} A_o \tag{4.172}$$

in which Δp = acoustic pressure acting at an opening of area A_o. The resulting differential equation for the inward displacement ξ of the air in the resonator openings

of number N, assuming the damping is very small, may be written as

$$\rho \ell' NA_o \frac{d^2\xi}{dt^2} - \rho c_o^2 \frac{\Delta V}{V_o} (NA_o) = 0 \qquad (4.173)$$

in which ℓ' = the effective length of the air mass in a single hole and is equal to 1.20 to 1.70 the radius of the opening a_o, depending on whether the openings have flanged ends or not.

For a cable roof with N wall openings, each of area A_o, the change in volume due to the average movement of the membrane $\bar{w}$ and the existence of the openings is

$$-\Delta V = NA_o\xi - \pi a^2\bar{w} = NA_o\xi(1-\alpha_c) = \pi a^2\bar{w}(1 - \frac{1}{\alpha_c}) \qquad (4.174)$$

in which

$\alpha_c = \frac{\pi a^2\bar{w}}{NA_o\xi}$ is the ratio between the volume of air displaced due to the membrane movement and the air which moves through the openings.

Substitute for $-\Delta V$ into Eq. 4.173 and the equation of motion for the inward displacement ξ of the air inside the enclosure beneath the roof is

$$[\rho \ell' NA_o] \frac{d^2\xi}{dt^2} + [\rho c_o^2 \frac{(NA_o)^2}{V_o}(1 - \alpha_c)]\xi = 0 \qquad (4.175)$$

The natural frequency of the whole system is given by

$$\omega^2 = \left(\frac{c_o^2 NA_o}{\ell' V_o}\right)(1 - \alpha_c) \qquad (4.176)$$

or

$$\frac{\omega^2}{\omega_R^2} = (1 - \alpha_c) \simeq -\left(1 - \frac{1}{\alpha_c}\right) \qquad (4.177)$$

This approximation is possible because $\omega^2 << \omega_R^2$ where ω = frequency of the whole system, and ω_R = frequency of the resonator. When the membrane is rigid, $\bar{w} = 0$, therefore $\alpha_c = 0$ and the frequency of the system is equal to the frequency of the resonator

$$\omega^2 = \omega_R^2 = \frac{c_o^2 NA_o}{\ell' V_o}$$

But when the surface of the membrane is displaced by an average amount $\bar{w}$, and the air moves through the openings, this change in volume of the enclosed air causes an increase in the pressure inside the cavity.

If the equilibrium volume inside the enclosure is V_o and the equilibrium pressure is p_o, and assuming that the alternations of air volume are adiabatic, the pressure increase, as stated earlier, may be given as

$$\Delta p = -k\frac{\Delta V}{V_o} = -\gamma p_o \frac{\Delta V}{V_o} = -\rho c_o^2 \frac{\Delta V}{V_o} \qquad (4.178)$$

in which k = air bulk modulus and γ = air specific heat ratio.

The introduction of a force given by Eq. 4.178 as acting upon each unit area of the membrane surface modifies Eq. 4.32, of the free vibration, which now becomes

$$\nu^2\nabla^2 w = \frac{\partial^2 w}{\partial t^2} + \left(\frac{\rho c_o^2}{m}\frac{\Delta V}{V_o}\right) \tag{4.179}$$

in which m = mass per unit area of the membrane. Substituting for $-\Delta V$ from Eq. 4.174, the equation of motion reduces to

$$\nabla^2 w = \frac{1}{\nu^2}\frac{\partial^2 w}{\partial t^2} - \frac{\rho c_o^2 \pi a^2}{m V_o}\left(1 - \frac{1}{\alpha_c}\right)\bar{w} \tag{4.180}$$

In this equation $\bar{w}$ is an integral function of all the allowed modes of vibration. A general solution is too involved to be considered for practical application. If only one frequency ω is present, a solution of the following form may be assumed:

$$w = R(r)e^{i\omega t} \tag{4.181}$$

Substituting Eq. 4.181 into Eq. 4.180 gives

$$\frac{d^2R(r)}{dr^2} + \frac{1}{r}\frac{dR(r)}{dr} + \nu^2 R(r) = -\frac{\rho\omega^2}{TV_o}\left(1 - \frac{1}{\alpha_c}\right)\int_o^a R(r)2\pi r\, dr \tag{4.182}$$

in which T = the tension per unit length in the membrane. It is found that this equation is satisfied by a function of the form (see Eq. 4.153),

$$R(r) = A[J_o(\tfrac{\omega}{\nu}r) - J_o(\tfrac{\omega}{\nu}a)] \qquad (4.183)$$

With this solution, the right-hand side of Eq. 4.182 may be integrated and becomes

$$\frac{2\pi\rho c_o^2}{TV_o}(1-\alpha_c)A\left[\frac{rJ_1(\frac{\omega}{\nu}r)}{(\frac{\omega}{\nu})} - \frac{r^2}{2}J_o(\tfrac{\omega}{\nu}a)\right]_o^a$$

$$= \frac{\pi a^2\rho c_o^2}{TV_o}(1 - \frac{1}{\alpha_c})A\,J_2(\tfrac{\omega}{\nu}a) \qquad (4.184)$$

Substituting Eqs. 4.183 and 4.184 into Eq. 4.182 shows that

$$(\tfrac{\omega}{\nu})^2 J_o(\tfrac{\omega}{\nu}a) = -\frac{\pi a^2\rho c_o^2}{TV_o}(1 - \frac{1}{\alpha_c})\,J_2(\tfrac{\omega}{\nu}a) \qquad (4.185)$$

or, with regard to Eq. 4.174,

$$(\tfrac{\omega a}{\nu})^2 \frac{J_o(\frac{\omega a}{\nu})}{J_2(\frac{\omega a}{\nu})} = -\alpha_o(1 - \frac{1}{\alpha_c}) \approx \alpha_o(1 - \alpha_c) \qquad (4.186)$$

Substituting for $(1 - \alpha_c)$ from Eq. 4.176 into Eq. 4.186 and rearranging gives

$$\frac{J_o(\frac{\omega a}{\nu})}{J_2(\frac{\omega a}{\nu})} = \alpha_o \frac{\omega^2 \ell' V_o}{c_o^2 NA_o(\omega a/\nu)^2} = \frac{\rho\pi a^2 \ell'}{mNA_o} \qquad (7.187)$$

This yields the parameter

$$\beta_c = 1.2 - 1.7\frac{\rho a^2}{mNA_o} = (\frac{m_a}{m})/(\frac{NA_o}{A}) = \frac{m_r}{A_r} \qquad (4.188)$$

where m_r = the ratio of mass per unit area of air "attached" to the membrane to the mass per

unit area of the membrane, $m_r = \frac{m_a}{m}$;

A_r = the ratio of opening to the total area of the membrane, $A_r = \frac{NA_o}{A}$;

$$\alpha_o = \frac{\pi a^4 \rho c_o^2}{TV_o}$$

and

$$\alpha_c = \frac{\pi a^2 \bar{w}}{NA_o \xi} \doteq \frac{(\bar{w}/\bar{H})}{(NA_o/2\pi a\bar{H})(2\xi/a)} \qquad (4.189)$$

The non-dimensional constant α_o is exactly the same as for a completely closed cavity, which, as stated earlier, measures the relative importance of the restoring force resulting from the compression of air in the enclosure and the initial tension T applied to the membrane. This value is small if either the volume of the enclosure behind the roof is large or the tension applied to the roof is high. In the limiting case when α_o approaches zero, the possible frequencies are those corresponding to $J_o(\frac{\omega}{\nu}a) = 0$, which is the frequency equation of a membrane freely vibrating in vacuo.

The non-dimensional term $(1 - \frac{1}{\alpha_c})$ measures the relative importance of the total area of the openings in the walls of the enclosure as well as the relative movement of the air within the openings with respect to the dimensions of the enclosure (radius a and depth $\bar{H}$).

If the opening area ratio $(\frac{NA_o}{2\pi a\bar{H}})$ or the movement of the air ratio $(\frac{2\xi}{a})$ is too small, the term $(1 - \frac{1}{\alpha_c})$ approaches 1, since $(\frac{1}{\alpha_c} \to 0)$, and the membrane vibrates as if it were backed by a complete closed cavity. Conversely, if the volume of air displaced by the membrane is equal to the volume of air moving through the openings, the term $(1 - \alpha_c)$ vanishes and the membrane vibrates as if it were in vacuo.

The frequencies of symmetric modes of an open membrane vibrating in vacuo are the roots of the equation $J_o(\frac{\omega a}{\nu}) \doteq 0$. Considering those frequencies as reference frequencies denoted by ω^*, a reduced frequency equation may be obtained.

Since [82]

$$\frac{2}{z} J_n(z) = J_{n+1}(z) + J_{n-1}(z) \qquad (4.190)$$

we get for

$$\beta_c = \frac{J_o(\frac{\omega a}{\nu})}{J_2(\frac{\omega a}{\nu})} = \frac{2\, J_1(\frac{\omega a}{\nu})}{(\frac{\omega}{\nu}a) J_2(\frac{\omega a}{\nu})} - 1 \qquad (4.191)$$

For the fundamental frequency ω_{oi}, $\frac{\omega a}{\nu} \simeq 2.404$ and

$$\frac{J_1(2.404)}{J_2(2.404)} = 1.202$$

Then Eq. 4.191 gives the additional mass ratio

$$\beta_c = \frac{J_o(\frac{\omega_{o1} a}{\nu})}{J_2(\frac{\omega_{o2} a}{\nu})} = [\frac{2.404}{(\frac{\omega_{o1}}{\nu})}]^2 - 1$$

or

$$\omega_{o1}^2 = \frac{\nu}{a} 2.404^2 \frac{1}{1+\beta_c}$$

Dividing by ω^*_{o1} (in vacuo) gives

$$[\frac{\omega_{o1}}{\omega^*_{o1}}]^2 = \frac{1}{1+\beta_c} \qquad (4.192)$$

When the area ratio $A_r \to \infty$, the additional mass ratio $\beta_c \to 0$ by Eq. 4.188, $[\frac{\omega_{o1}}{\omega^*_{o1}}] \to 1$ and the membrane vibrates as if the cavity behind it did not exist.

It may be concluded that when β_c increases due to the decrease in area of the openings, the frequency of the system decreases and vice versa. This seemingly surprising result holds only for very taut membranes for which the behaviour of the roof with the cavity resembles the behaviour of a Helmholtz resonator.

The reduction in frequency $\frac{f_{o1}}{f^*_{o1}}$ due to β_c is shown in Table 4.2 and Figure 4.16 and it is in general agreement with results obtained in experimental work (Figure 6.7). The fundamental frequency f^*_{o1} for the membrane vibrating in vacuo is not available and it is taken for the membrane model with its base completely open.

The trends observed in Figures 4.16 and 6.7 are in agreement with the theory formulated, and suggest that the behaviour of the cable roof backed by a cavity with openings can be similar to that of a Helmholtz resonator. For this resonator the natural frequency also increases with the area of opening A_o (actually with $\sqrt{a_o}$); this is so because the air moving through the opening generates pneumatic stiffness of the resonator proportional to A_o^2 while the associated mass is proportional to A_o (and $\ell' a_o$) [78]. The behaviour of a roof-cavity system with openings depends on its parameters and may fall between two limiting cases: a Helmholtz resonator if the roof is very rigid and a "Kettledrum" if the openings are absent. A more general theory which would include both limiting cases as well as the intermediate case should be developed.

TABLE 4.2 Reduction in Fundamental Frequency Due to Wall Openings (Comparison Between Theory and Experimental Results)

No.	N	β_c	$\frac{1}{1+\beta_c}$	$\frac{f_{ol}}{f^*_{ol}}$	$\frac{f_{ol}}{f^*_{ol}}$ experimental
1	50	0.1455	0.8730	0.9343	
2	40	0.1819	0.8461	0.9198	
3	30	0.2426	0.8049	0.8971	
4	25	0.2911	0.7745	0.8800	
5	20	0.3638	0.7332	0.8563	
6	15	0.4851	0.6733	0.8206	
7	12	0.6064	0.6225	0.7890	
8	9	0.8085	0.5529	0.7436	0.8059
9	6	1.2128	0.4519	0.6722	0.713
10	3	2.425	0.2919	0.5403	0.5468
11	1	7.277	0.1208	0.3476	

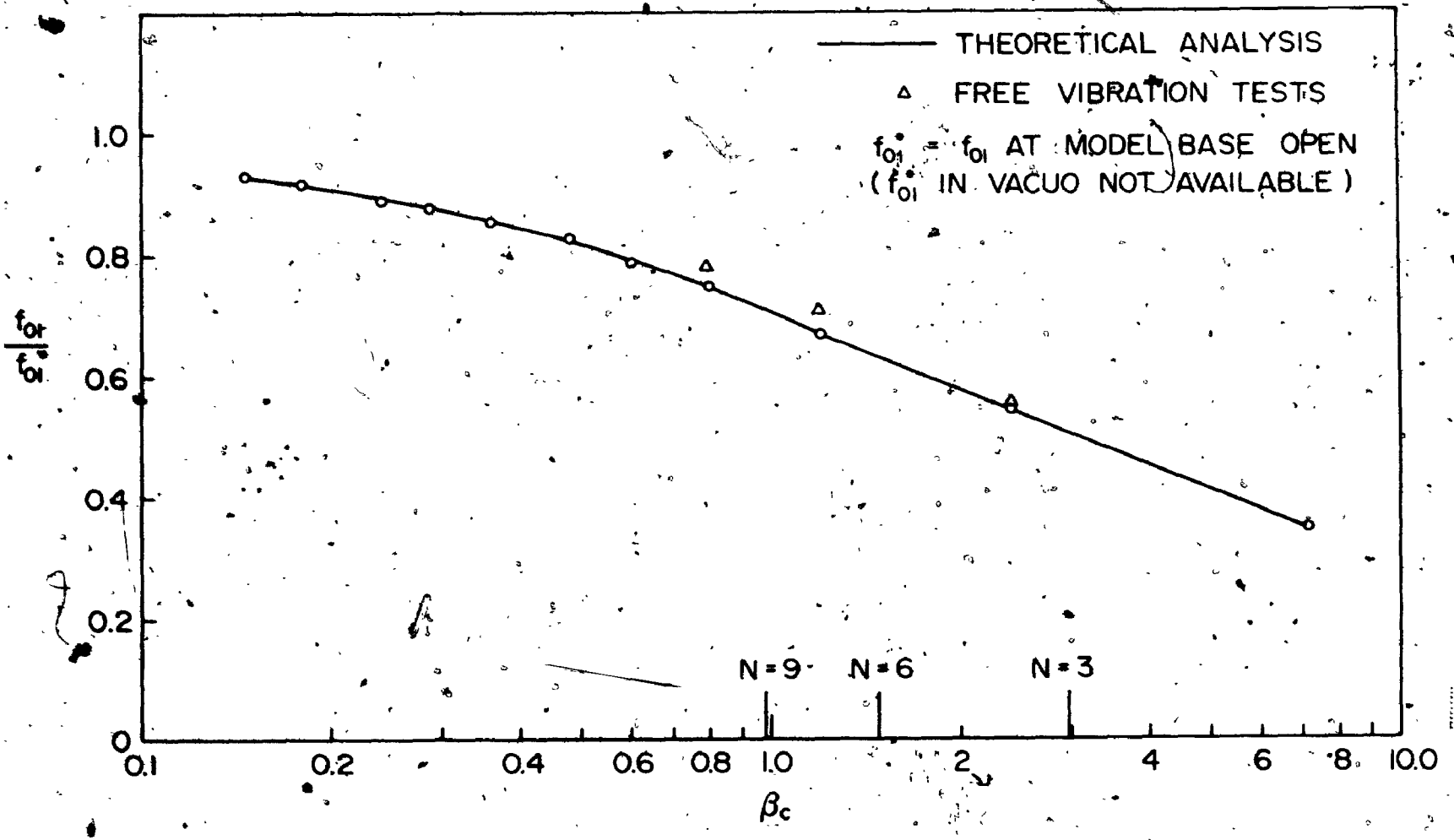

FIGURE 4.16 FREQUENCY REDUCTION WITH CAVITY OPENINGS PARAMETER

$$\beta_c = 1.2 - 1.70 \frac{\rho a^2}{m N a_o}$$

CHAPTER 5

DYNAMIC RESPONSE OF TENSION ROOFS TO TURBULENT WIND

5.1 INTRODUCTION

Tension roof structures belong to the class of light and flexible structural systems which are sensitive to vibrations. Therefore, the design and construction of these structures requires an examination of their dynamic behaviour. An examination of the dynamic behaviour of tension roofs is necessary to secure a safe and serviceable design. For small dynamic displacements the examination can be separated into two parts: the determination of the actual forces acting and the analysis of the response of the structure to these forces.

The dynamic forces on a tensile roof are mainly caused by wind. Due to the turbulent nature of the wind, the problem of wind loading has to be founded on experimental work and statistical methods.

The wind induced dynamic excitation experienced by the structure can be categorized under four separate headings:

1. The first physical phenomenon which causes dynamic excitation is the shedding of vortices from the structure.

If the frequency of vortex shedding ($f_s = \frac{\bar{V}S}{D}$) is nearly equal to one of the natural frequencies of the structure then large amplitude vibration may develop. Past experience has shown [84,85,86] that dynamic excitation by vortex shedding is apparently not a problem for the type of structures considered here.

2. dynamic excitations caused by shedding of vortices by other structures.

3. aeroelastic instability of flutter or galloping type; as well as the case listed as (2) are beyond the scope of this study.

4. The final type of dynamic excitation is that caused by the buffeting of wind gusts. For tension roof structures the fourth type mentioned is most important [15,87].

Tension roofs are exposed to large deflections and changes of geometry; therefore, an accurate dynamic analysis is fraught with problems. Strictly speaking, the oscillations of tension roofs are nonlinear. However, the usual approach is to assume that the motion is confined to small displacements about the static equilibrium position.

The dynamic analysis of tension roofs under wind

loading in this work will be based upon the assumption that linear oscillations take place about the quasi-static position defined by the mean wind loading, and that the dynamic response of the structure due to the randomly fluctuating component can be superimposed upon the quasi-steady response to give the total response of the system. Furthermore, an attempt is made to explore the influence of the surrounding air on the free side and below the roof within the enclosure on its behaviour.

5.2 WIND LOADING

The wind, by definition, is a movement of free air caused, on a large scale, by the thermal and pressure differentials above the earth's surface. By virtue of the mass and velocity of the moving air, the wind possesses kinetic energy. If an obstacle is placed in the path of the wind so that the moving air is stopped or deflected from its path, all or part of the kinetic energy of the moving air is transformed into the potential energy of pressure.

A general expression for wind pressure on the structure is given by Davenport [44] as,

$$q(x,y,z,t) = \frac{1}{2}\rho C_q(x,y,z,t)V(x,y,z,t)|V(x,y,z,t)| + C_m \rho \frac{A}{D}\frac{dV(x,y,z,t)}{dt} \qquad (5.1)$$

where, $q(x,y,z,t)$ = force per unit area at coordinates x,y,z of the structure at time t

$V(x,y,z,t)$ = velocity of the air at coordinates x,y,z at time t

ρ = mass density of air

$C_q(x,y,z,t)$ = pressure coefficient at coordinates x,y,z at time t

C_m = coefficient of virtual mass (including what is known as the additional or associated mass coefficient)

D = diameter of the object

A = reference area for the virtual mass (generally $\frac{\pi D^2}{4}$)

Two different physical mechanisms are responsible for the terms on the right-hand side of Eq. 5.1. The first term is the familiar expression which reflects the contribution of the drag forces to the pressure, while the second term is the inertial reaction associated with the acceleration of the wind. The second term may be important in cases with rapid wind speed and direction changes, such as tornadoes and squalls, but, for the usual storms of engineering consideration, it is not as important as the first term, which will be considered in this work.

It is useful, for several reasons, to consider the

wind as having a mean value $\bar{V}(x,y,z)$ upon which gusts (fluctuations) in wind speed $v(x,y,z,t)$ are superimposed. This may be written as stated earlier by

$$V(x,y,z,t) = \bar{V}(x,y,z) + v(x,y,z,t) \qquad (5.2)$$

Based on this assumption, the mean wind problem and the fluctuating wind problem may be considered separately. The mean and fluctuating components of wind speed represent the sources of static and dynamic wind loading respectively on a structure. The response of the structure will similarly have static and dynamic components.

The total wind pressure, neglecting the second part of Eq. 5.1, is given by

$$q(x,y,z,t) = \frac{1}{2} \rho C_q(x,y,z,t) [\bar{V}(x,y,z)+v(x,y,z,t)]^2 \qquad (5.3)$$

At present, theoretical methods are inadequate to determine pressure coefficients for all but the most elementary shapes. As a result, experimental methods such as wind tunnel tests must be used. Davenport [88] has emphasized the importance of using boundary layer wind tunnel tests to predict the response of structures, not only because they reflect the turbulent nature of the wind, but also because they reflect the influence which surrounding structures may have upon the pressure coefficients. Caution must be taken when trying to apply

uniform flow wind tunnel test results to actual structures. Davenport [88] has shown that both the pressure distribution and the magnitudes of pressure coefficients for boundary layer wind tunnel tests results differ significantly from uniform flow test results. Furthermore, instability of the structure may depend on turbulence as shown by Novak [120], Novak and Tanaka [121].

Although boundary layer wind tunnel tests are clearly more representative of atmospheric turbulence than uniform flow tests, few studies have been made of pressure on cable roofs in boundary layer wind tunnels [89,90,91]. It has been recognized that in a fluctuating flow the pressure coefficient may vary with time, therefore the pressure coefficient is written as $C_q(x,y,z,t)$. Implicit in the variation of the pressure coefficient with time is the Reynolds number effect and the fact that the angle of attack of the wind may vary with time. The pressure coefficients available for cable roofs which will be used in this work are obtained from boundary layer wind tunnel tests [89,91] and from a uniform flow wind tunnel test [94].

For uniform flow wind tunnel tests, it will be assumed that the pressure coefficient will not be time dependent and may be written as $C_q(x,y,z)$. This assumption is based

on the idea that the Reynolds number effect is negligible and that the gusts will always be in the direction of the mean wind, and therefore $C_q(x,y,z)$ will be defined by the mean wind direction.

A representation of the fluctuating wind velocity is difficult to obtain, and the best way to describe the fluctuating component is in a statistical sense. Wind records sometimes are available, however the information about the spatial distribution of the wind pressure as a function of time is still limited. For large structures, this point is of importance. The most elementary approach, assuming that the same velocity acts on all points on a structure simultaneously, is acceptable for small (point) structures but is quite far from reality for large structures like cable roofs.

A slightly more refined approach is a plane wave assumption; in the sense of Taylor's Hypothesis that the velocity fluctuations recorded at a point travel unchanged in the direction of the mean wind at the mean wind velocity. A computational investigation of the wind effect on a cable net structure based upon the plane wave assumption has been carried out [84]; field tests on another cable net structure also justified a plane wave assumption for wind gusts [92]. Therefore, in this work, the plane

wave assumption is used in the dynamic analysis of tension roofs.

5.2.1 Static Wind Pressure

5.2.1.1 Uniform Flow Approach

A pressure coefficient obtained from uniform flow wind tunnel tests may be assumed to be independent of time and is written as $C_q(x,y,z)$. In this sense, the mean wind velocity $\bar{V}(x,y,z)$ may be considered to cause a pressure on the suspension roof defined as

$$\bar{q}(x,y,z) = \frac{1}{2} \rho C_q(x,y,z) \bar{V}^2(x,y,z) \qquad (5.4)$$

This pressure may be added to the live and dead loads on the structure to form a quasi-static load. Using the nonlinear solution described in Chapter 2, the quasi-static equilibrium position may be obtained. The term $(\frac{1}{2} \rho \bar{V}^2(x,y,z))$ is the dynamic head associated with the mean velocity $\bar{V}(x,y,z)$ at the roof height Z which can be obtained from the gradient velocity $\bar{V}_G$ using the power law or the logarithmic laws, Equations 3.2, 3.3 and 3.5 respectively. Sometimes it is more convenient to measure the pressure coefficients in respect to the dynamic pressure at the gradient height Z_G. The conversion factors $[\bar{V}_G/\bar{V}(x,y,z)]^2$ are easily estimated from the velocity profiles for each exposure.

The mean-pressure coefficient C_q on tension roof surface actually varies with time over the structure not only because the direction of the wind is not constant, but also because the configuration of the tension roof surface changes under dynamic excitation. This can be simplified by two assumptions:

(1) First, it is assumed that the direction of the wind is constant and is always in the direction of the mean wind. Thus, the coefficients corresponding to the mean wind direction are those used in this approach.

(2) Second, if, in addition to the assumption of linear oscillations, it is also assumed that the deflection of the tension roof surface from its original configuration to the mean wind configuration is sufficiently small, then the magnitude and distribution of pressure coefficients from the original configuration may be used for the dynamic analysis. These pressure coefficients are measured on rigid models in wind tunnels.

The mean pressure coefficient C_q was measured by Ishizaki and Yoshikawa [93], on a model roof of different sag/span ratios and height/span ratios laid across the total width of a wind tunnel creating conditions of two-dimensional flow. In their experiments, a large pressure coefficient (-1.5) was measured on the leading edge of

the roof. Its magnitude decreased from the edge and tended to the value of -0.30 at the rear. For sagged roofs, the pressure coefficients are more uniformly distributed than for flat roofs and the average pressure coefficient is much larger, about -0.9, Figure 5.1.

Beutler [94] measured the mean pressure coefficient on a circular concave model and a rectangular hyperbolic paraboloid model, Figure 5.2a,b. In his experiment, a large pressure coefficient (-0.9) was measured on the leading edge of the circular concave model. Its magnitude decreased from the leading edge and tended to the value +0.1 at the rear. For the hyperbolic paraboloid model with angle of attack at the lower edge, the pressure coefficient was positive (+0.06) and decreased toward the rear having a maximum negative value (-1.0) at about the centre area, Figure 5.2b.

Both authors [93,94] concluded that the distribution of pressure coefficients on the top of the circular model were dependent on both absolute model height as well as the aspect ratio (height/diameter ratio). They concluded also that because of the separation in the flow always created by the leading edge, the Reynolds number effect on the pressure coefficients of flat roofs is negligible; this is not the case for the hyperbolic paraboloid model,

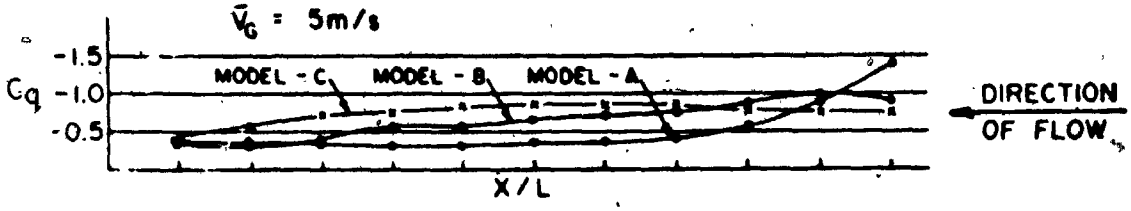

FIGURE 5.1 Variation of Pressure Distribution Among Three Models (sag/span ratio: A = 0, B = 0.1, C = 0.2) (from Ishizaki and Yoshikawa [93])

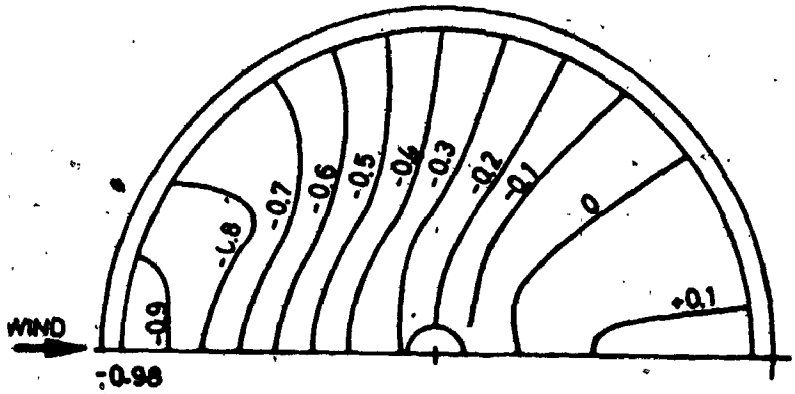

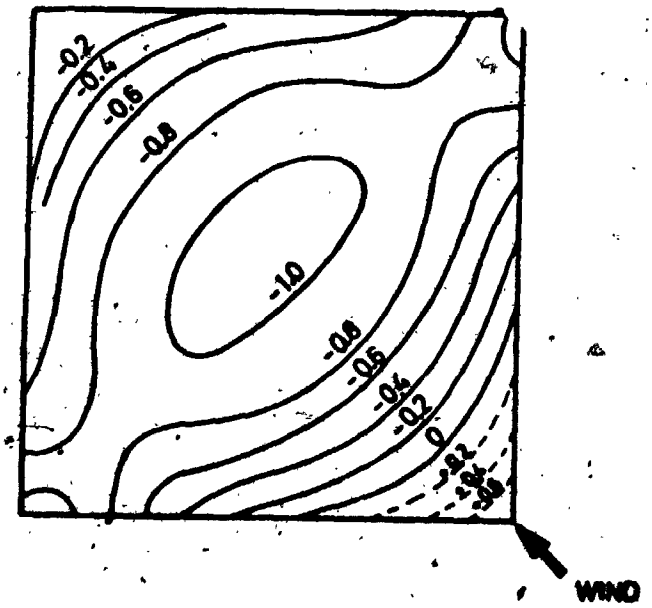

FIGURE 5.2 Pressure Coefficient Distribution; a) Circular Concave Roof, b) Hypar Roof (from Beutler [94])

where the separation is Reynolds number dependent.

5.2.1.2 Turbulent Flow Approach

It has been recognized that in a fluctuating flow, the pressure coefficients vary with time; therefore, the pressure coefficient is written as $C_q(x,y,z,t)$.

In tension roofs, large deflections are possible under wind loading and therefore change in geometry can also influence the wind pressure coefficient.

Therefore, boundary layer flow tests are more realistic than uniform flow tests, not only because they reflect the turbulent nature of the wind but also because they reflect the influence which surrounding structures may have upon the pressure coefficients.

The best way to describe the pressure coefficient on the tension roof surface is in a statistical sense; i.e., as maximum, minimum, mean and RMS coefficients for each individual roof point (x,y,z). The local pressure coefficients can be developed from a time history, and defined as:

$$C_{q_{max}}(x,y,z) = \frac{q_{max}(x,y,z)}{q_d(z)} \qquad (5.5a)$$

$$C_{q_{min}}(x,y,z) = \frac{q_{min}(x,y,z)}{q_d(z)} \qquad (5.5b)$$

$$C_{\bar{q}}(x,y,z) = \frac{\bar{q}(x,y,z)}{q_d(Z)} \qquad (5.5c)$$

$$C_{\sigma_q}(x,y,z) = \frac{\sigma_q(x,y,z)}{q_d(Z)} \qquad (5.5d)$$

where $q_{max}(x,y,z)$ = maximum instantaneous pressure at point (x,y,z)

$q_{min}(x,y,z)$ = minimum instantaneous pressure at point (x,y,z)

$\bar{q}(x,y,z)$ = mean pressure at point (x,y,z)

$$= \frac{1}{\tau}\int_0^\tau q(x,y,z,t)\,dt$$

$\sigma_q(x,y,z)$ = root mean square (RMS) pressure

$$= \left\{\frac{1}{\tau}\int_0^\tau [(q(x,y,z,t)-\bar{q}(x,y,z)]^2 dt\right\}^{1/2}$$

$q_d(Z)$ = $\frac{1}{2}\rho\,\bar{V}^2(x,y,z)$: dynamic head pressure associated with the mean velocity at the roof height Z

Here, τ is the sampling period, related to approximately one hour sampling period in full scale.

For strong winds, it appears possible to assume [96] that the mean velocity is independent of x and y and can be written as $\bar{V}(z)$. Therefore, the dynamic head is dependent on the coordinate z only.

A major difficulty in describing the effective loading

on the structure is the fact that the fluctuating forces vary spatially as well as temporally, especially for large span structures like the tension roofs. Davenport et al. [89], suggested that it is highly advantageous to represent these fluctuating forces on the roof surface in terms of mathematical mode shape functions having orthogonal properties. Denoting the ith orthogonal function by $\phi_i(x,y,z)$; the instantaneous pressure field on the roof, denoted by $q(x,y,z,t)$, is represented as:

$$q(x,y,z,t) = \sum_i q_i(t)\ \phi_i(x,y,z) \qquad (5.6)$$

The pressure field can now be defined in terms of the fluctuating components $q_i(t)$ and the modal function $\phi_i(x,y,z)$.

The mean load for any wind direction θ can be written as [89],

$$\bar{q}(x,y,z,\theta) = q_d(z) \sum_i \overline{C_{q_i}(\theta)}\ \phi(x,y,z) \qquad (5.7)$$

The overbars denote time average values and $\overline{C_{q_i}(\theta)}$ is the mean force coefficient for mode i, for wind direction θ. The mean square value (variance) does not contain cross terms on account of the orthogonality conditions

$$\int_A \phi_i(x,y,z)\phi_j(x,y,z)\,dA = 0$$

if $i \neq j$ and is constant for $i = j$. So the mean square pressure fluctuation is:

$$\sigma_q^2(x,y,z,\theta) = q_d^2(Z) \sum_i \sigma_{C_{q_i}}^2(\theta) \phi_i^2(x,y) \qquad (5.8)$$

where $\sigma_{C_{q_i}}(\theta)$ is the ith root-mean-square fluctuating generalized force coefficient for the ith mode for wind direction θ.

From Eqs. 5.7 and 5.8, the maximum and minimum pressure field can be written as:

$$\hat{q}(x,y,z) = q_d(Z)\left[\sum_i \overline{C_{q_i}(z)}\phi_i(x,y) \pm g_i \sqrt{\sum_i \sigma_{C_{q_i}}^2(z)\phi_i^2(x,y)}\right] \qquad (5.9)$$

In this equation, g_i is a statistical peak factor, usually in the range 3 to 4, associated with each mode i.

The loading representation by Eq. 5.9 can be presented in an alternative and generally simpler form, [89]

$$\hat{q}(x,y,z) = q_d(Z)\sum_i \{[\overline{C_{q_i}(z)} \pm g_i\, \sigma_{C_{q_i}}(z)]\phi_i(x,y)\} \qquad (5.10)$$

in which the g_i are statistical peak factors.

Davenport et al. [89] tested a hyperbolic paraboloid model for the Olympic Coliseum to be built in Calgary, Alberta, Canada. They found that peak minimum pressure coefficients are maximum (-0.91) at the leading edge and decrease toward the rear when the wind is blowing along

the line joining the high points of the roof, Figures 5.3 and 5.4. In their analysis of the results, they found that the most severe cases are likely to be felt when the wind is at 0° or 180°, that is, when blowing along the line joining the high points of the roof. They suggested that this was because it caused a strong asymmetric load in this direction mainly associated with first asymmetric mode in this direction, Figure 5.5.

Christiano et al. [91] tested a circular concave cable roof model in a boundary layer flow where water is used as a fluid rather than air. From their experiment, they made the following observations:

(1) the flow separates from the leading edge of the structure and may or may not reattach, depending primarily on the value of the height/diameter (aspect ratio) of the building and the velocity distribution of the approach flow;

(2) the resulting static time-smoothed average pressure distribution is asymmetric about an axis perpendicular to the flow axis, Figure 5.6;

(3) ground roughness, the result of buildings and vegetation cover surrounding the building, has a significant effect on the velocity profile of the approaching flow and on the resulting pressure distribution and

(4) the RMS values of the pressure coefficients increased

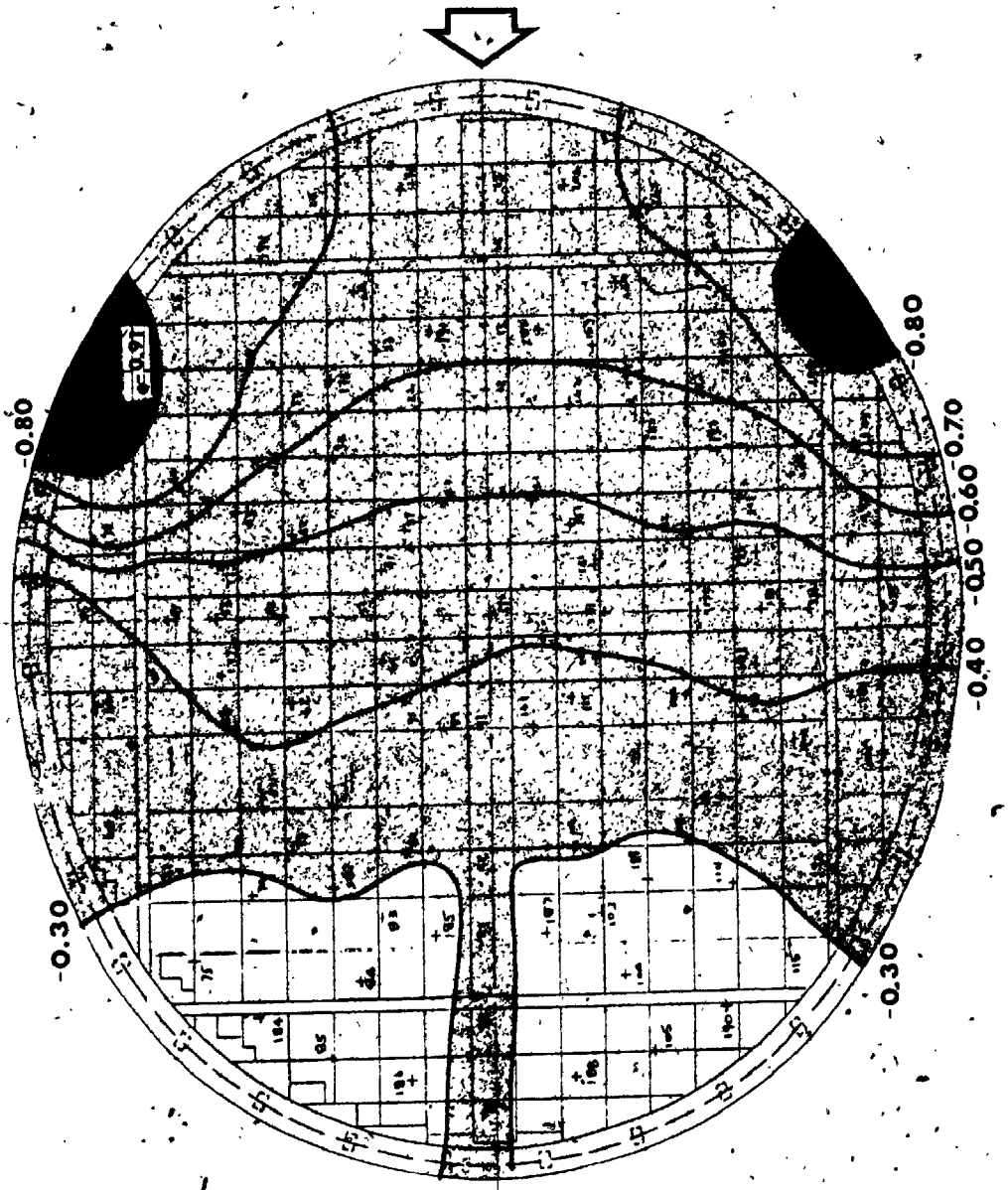

FIGURE 5.3 Contours of Peak Min. Pressure Coefficients on H.P. Roof (from Davenport et al. [89])

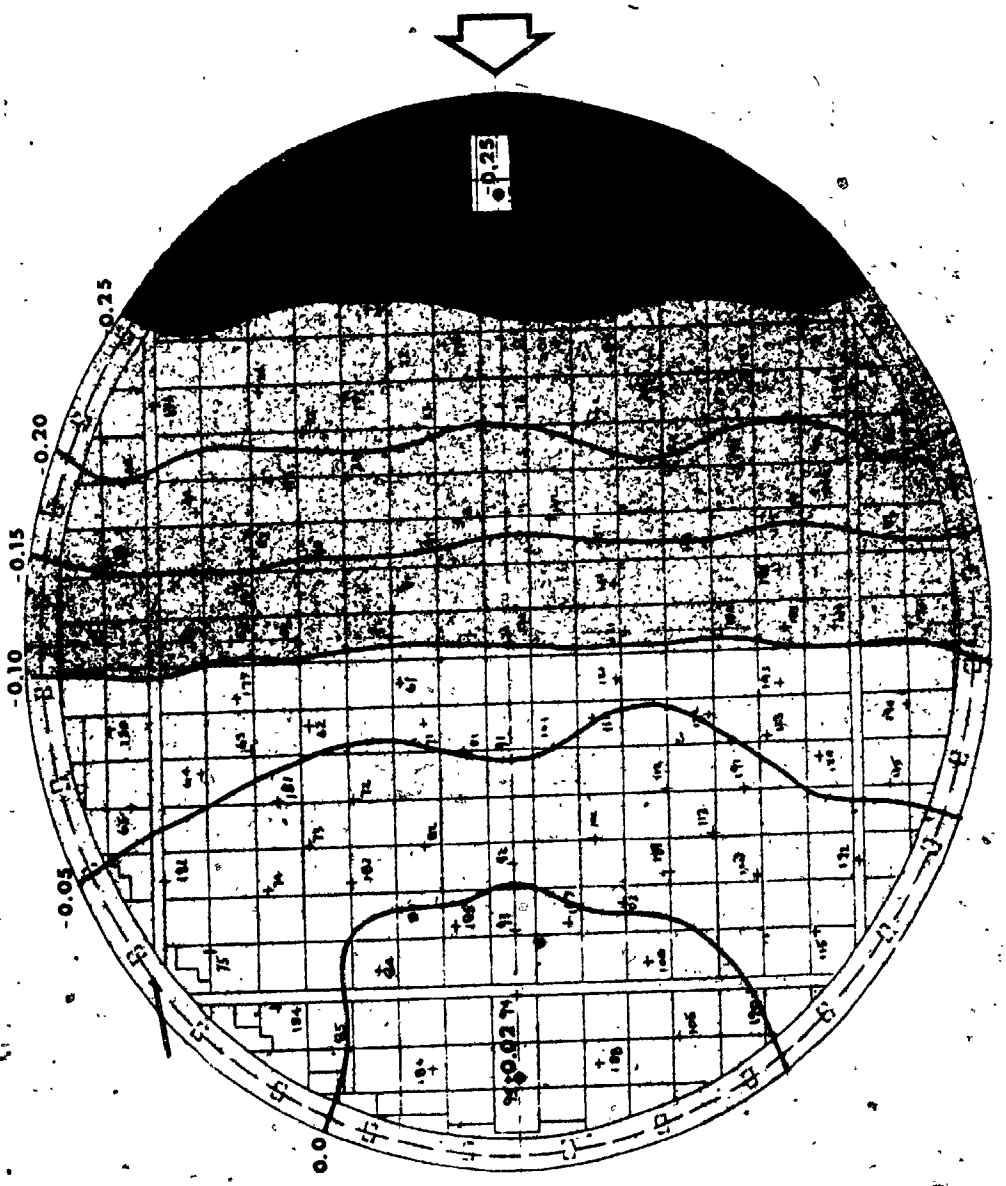

FIGURE 5.4 Contours of Mean Pressure Coefficients on H.P. Roof (from Davenport et al. [89])

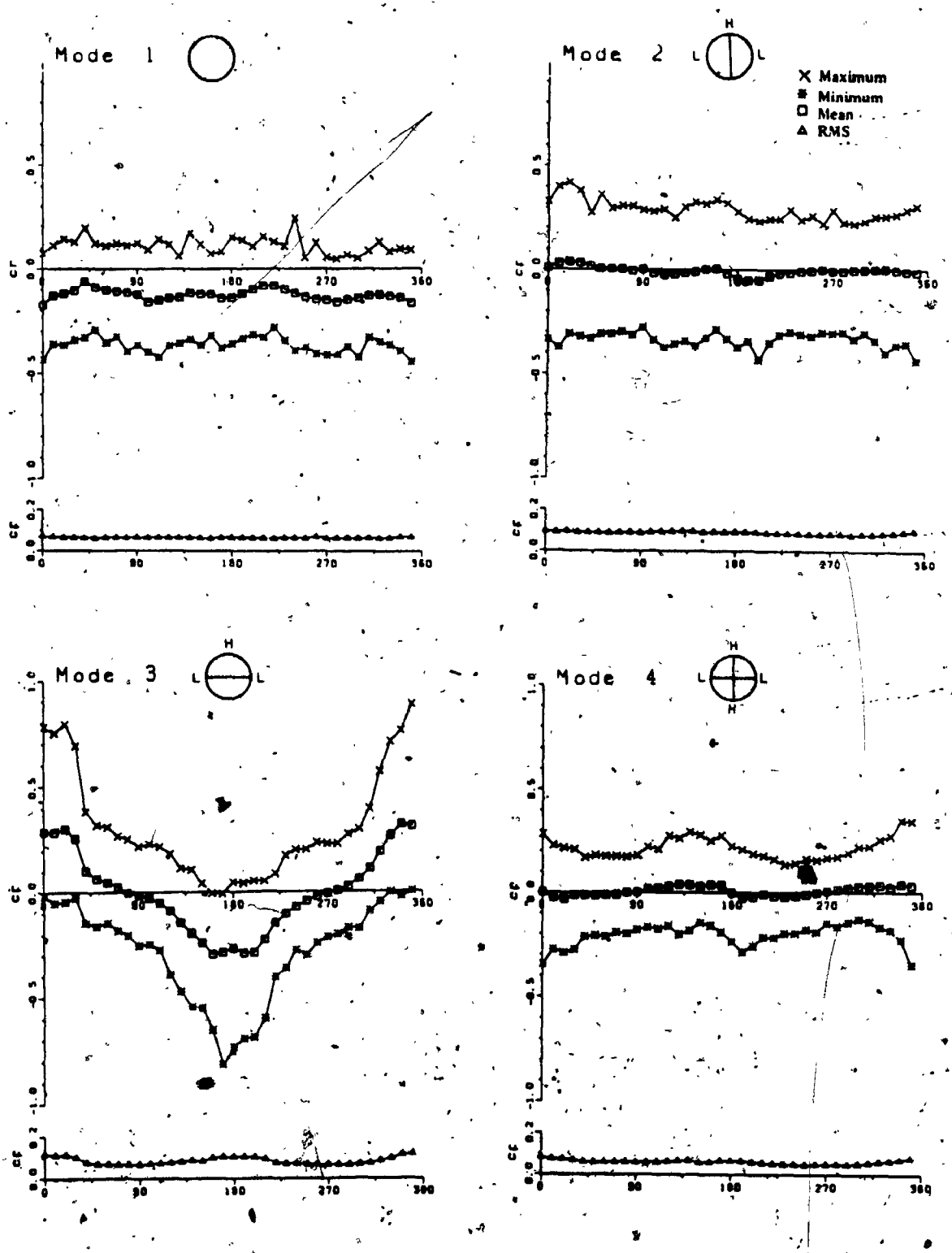

FIGURE 5.5 Generalized Force Coefficient for Modes of Vibration as Function of Wind Direction (from Davenport et al. [89])

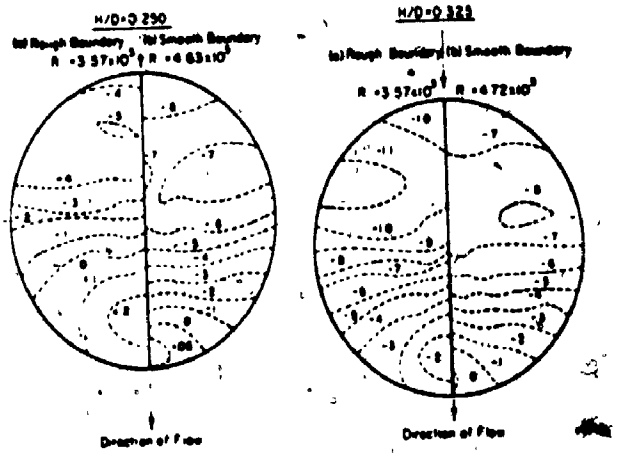

FIGURE 5.6 Distribution of Pressure Coefficients on Concave Roof, From Water Tunnel Experiment [91]

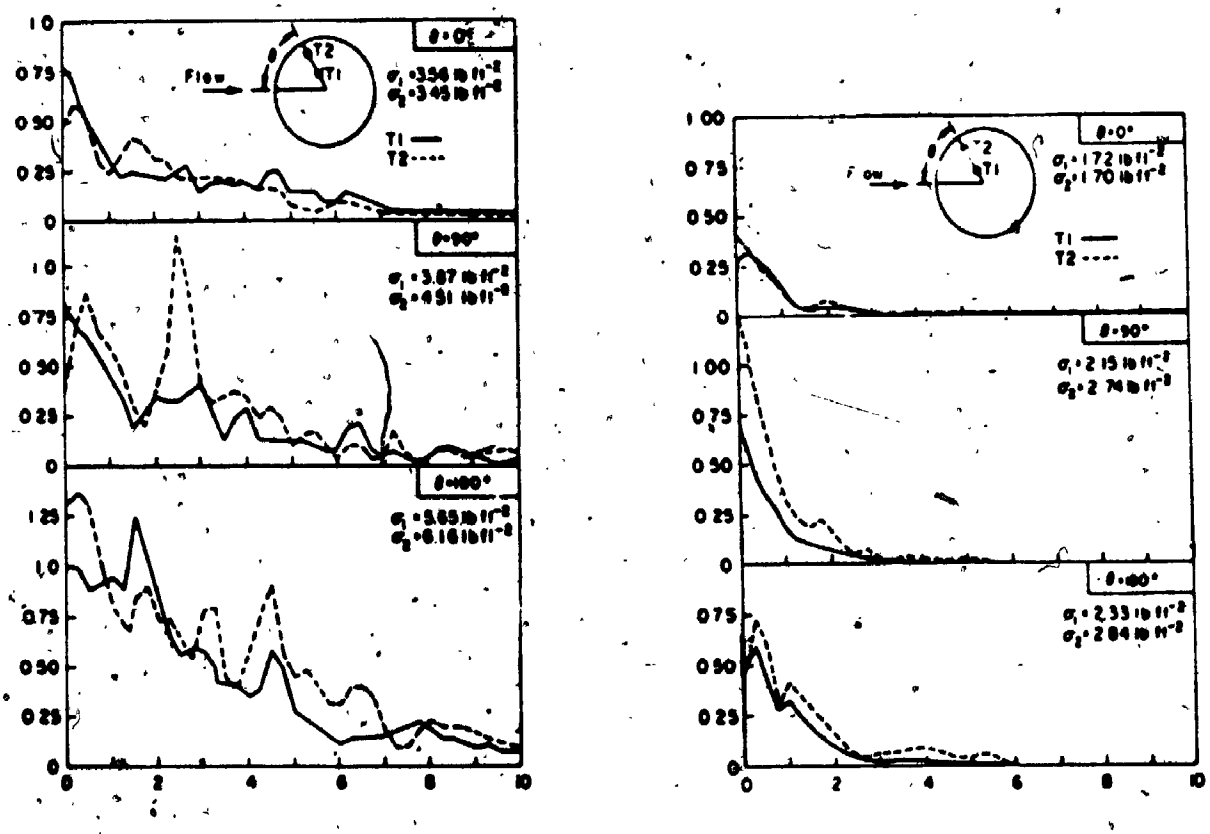

H/D=0.25 H/D=0.325

FIGURE 5.7 Power Spectral Density of Measured Pressure Fluctuations From Water Tunnel Experiment [91]

downstream, regardless of the reattachment, and an increase in aspect ratio resulted in an increase in the RMS values of the pressure coefficients, Figure 5.7.

We may conclude from the work that in both uniform and boundary layer flows, the pressure coefficient distributions on tension roof surfaces are dependent on the geometry of the structure, mainly the height/diameter ratio, the direction of flow, Reynolds number and the turbulence in the approaching flow.

In codes of practice, nothing is mentioned about pressure coefficients for tension roofs in particular [95]. The Swiss code of practice and the draft of the American ASA Standard [20,97,98] gave a minimum external suction pressure coefficient of (-0.7) to be used for roofs with a wall height to least width ratio of less than 2.5. For closed tanks of height equal to the diameter the external pressure coefficient suggested is -1.0 and in both cases the computed pressure is assumed uniform over the entire roof area.

Since suspension-cable roofs have a height to diameter ratio of about 1/4, it may be assumed that, for the design of these structures for the influence of mean wind, a uniform pressure coefficient distribution of magnitude -1.0 acting on the entire roof area may be assumed.

The internal pressure coefficient distribution, $C_{q,\ell}$, depends on the number, shape and area of wall openings, and on their orientation to the wind direction.

The Swiss code of practice [97] indicates that when the openings are uniformly distributed, the internal pressure coefficient is the same for all low structures and is equal to $\pm$ 0.20. If the openings are not uniformly distributed, a positive internal pressure (i.e. pushing the roof upwards) exists when the openings are facing the wind direction, and negative when they are in the rear.

In this work, the internal pressure fluctuations inside an aeroelastic model of a concave suspension roof with openings (windows) are measured in boundary layer wind tunnel tests (Chapter 6). Assuming that the internal pressure field was the same everywhere within the enclosure, it was found that the internal pressure coefficients were dependent on the velocity of the approaching flow, the number of openings and the locations of the openings with respect to the approaching flow. For a velocity of approaching flow $\bar{V}_G$ = 28 ft/sec (8.534 m/s) and with openings fairly uniformly distributed (N=9) with area parameter β_a = 5.3% ($\beta_a = \frac{NA_o}{A_c}$ %), it was found that the mean pressure coefficient $C_{\bar{q}_\ell}$ = -0.43

and the rms pressure coefficient $C_{q_{\sigma_\ell}} = 0.085$. For the same area parameter, but with wind velocity $\bar{V}_G$ = 38 ft/sec (11.58 m/s), both coefficients increased to $C_{\bar{q}_\ell} = -0.6$ and $C_{q_{\sigma_\ell}} = 0.13$.

For wind velocity of $\bar{V}_G$ = 28 ft/sec (8.534 m/s), but the area parameter $\beta_a = 3.54\%$, the coefficient dropped to $C_{\bar{q}_\ell} = -0.37$ and $C_{q_{\sigma_\ell}} = 0.07$ (see Table 6.6).

It follows that the net static pressure may be given by

$$q_s = q_u - q_\ell \qquad (5.11)$$

in which q_u is the upper static pressure and q_ℓ is the lower (internal) wind pressure = $C_{q_\ell}(\frac{1}{2}\rho\bar{V}^2)$, where $\bar{V}$ relates to the gradient height.

In practice, the net static wind pressure is commonly assumed uniform over the entire roof surface.

5.2.2 Dynamic Wind Pressure

It has been recognized for many years that the wind is turbulent in nature and thus behaves randomly in space and time. In the previous sections, a deterministic analysis was made for wind loadings; however, due to the random nature of the wind, a much more rational way to

describe the dynamic wind pressure is by using the theory of random processes.

Based on the assumptions made in Chapter 3, the randomly fluctuating component of the wind will be considered to be homogeneous and isotropic and will be described by a stationary Gaussian process.

Recalling the division of the wind into quasi-static and randomly fluctuating components and the assumption of neutral strong wind, for which the mean velocity $\bar{V}$ is dependent only on the level Z above the ground, the randomly fluctuating component of the wind pressure is given by

$$q(x,y,z,t) = \frac{1}{2} C_q(x,y,z)[2\bar{V}(Z)v(x,y,z,t)+v^2(x,y,z,t)] \quad (5.12)$$

where $V(x,y,z,t) = \bar{V}(Z)+v(x,y,z,t)$ and $C_q(x,y,z)$ is the mean pressure coefficient.

Consider a structure of area A, situated in the atmospheric boundary layer, which is sufficiently small with respect to the wave length of the turbulence of gusting that we may regard the flow past the structure as quasi-steady. Then the fluctuating force may be written as;

$$F(x,y,z,t) = \frac{1}{2} \rho C_q(x,y,z)A[2\bar{V}(Z)v(x,y,z,t)+v^2(x,y,z,t)] \quad (5.13)$$

If the fluctuating wind component is small with respect to the mean wind component, the term involving $v^2(x,y,z,t)$ may be ignored and Eq. 5.13 may be rewritten as

$$F(x,y,z,t) = \rho A C_q(x,y,z)\bar{V}(Z)v(x,y,z,t) \quad (5.14)$$

The dropping of the terms involving $v^2(x,y,z,t)$ is a crucial assumption, since it means that the forcing function is now linear in $v(x,y,z,t)$.

Harris [101] and others have investigated the error in neglecting $v^2(x,y,z,t)$ and the inertia terms of Eq. 5.1 by using the results of communication theory and expressed their results in terms of the intensity of turbulence $I_v = \sigma_v/\bar{V}(Z)$. Harris found that for the range of greatest practical significance characterized by $0.20 < I_v < 0.50$, the approximation underestimates the mean pressure by between 4% and 25%. Harris concluded that in light of uncertainty involved in obtaining the aerodynamic coefficients, the approximation is perfectly satisfactory for the majority of cases.

The power spectrum of $F(x,y,z,t)$ is then related to the velocity spectrum, Eq. 5.14, as follows:

$$S_F(f) = [\rho A C_q \bar{V}(Z)]^2 S_v(f) \qquad (5.15)$$

or

$$S_F(f) = 4\left[\frac{\bar{F}(x,y,z)}{\bar{V}(Z)}\right]^2 S_v(f) \qquad (5.16)$$

where $\bar{F}(x,y,z) = \frac{1}{2} \rho A C_q(x,y,z)\bar{V}^2(Z)$ is the static force of the wind acting on the surface of area A. If the size of the structure ceases to be small, some adjustment must be made for the reduced spatial correlation of the forces. The influence of the disturbance in relation to the size of the structure is introduced through an aerodynamic admittance function of the form [41], $|\chi(\frac{fD}{\bar{V}})|^2$, where $||$ denotes the absolute value and D is a characteristic dimension of the structure. It was suggested that $D = \sqrt{A}$ be taken, where A is the total area of the surface. Hence, Eq. 5.16 may be written, after introducing the aerodynamic admittance function, as [41],

$$S_F(f) = 4\left[\frac{\bar{F}(x,y,z)}{\bar{V}(Z)}\right]^2 \chi^2\left(\frac{f\sqrt{A}}{\bar{V}(Z)}\right) S_v(f) \qquad (5.17)$$

This equation gives the relationship between the spectrum of the load fluctuations on the structure and the spectrum of the longitudinal component of turbulence in the uniform turbulent flow in which the structure is placed. The parameter $(\frac{f\sqrt{A}}{\bar{V}(Z)})$ is dimensionless frequency which relates the wave length $\lambda = \bar{V}(Z)/f$ and size of the structure $\sqrt{A}$. Therefore, the dominant or characteristic frequency in

the flow region f_s can be associated with a characteristic wave length λ_s or length scale, $L_s = \frac{\bar{V}(Z)}{f_s}$, which may be considered to be the average size of the eddies rolling in the direction of the flow.

The effectiveness of a gust in producing a load on a large structure depends largely on the gust size in relation to the size of the structure, i.e. the ratio $(\lambda/\sqrt{D})$ or $(\bar{V}(Z)/f\sqrt{A})$. In the case of high frequency components, the ratio $\lambda/\sqrt{A} << 1$ and the pressures produced are only correlated or well organized over quite small areas of the surface; their total effect is small since in some areas they will tend to produce increased loads while simultaneously at other parts of the structure, there will be a decrease in load. Thus, the pressure due to high frequency components of the wind is poorly correlated over the surface as a whole. The very low frequency components of gustiness are associated with $\lambda/\sqrt{A} >> 1$, and in this case their influence is felt over the whole, or at least large areas, of the surface simultaneously.

As $f\sqrt{A}/\bar{V}(Z) \to 0$, we can anticipate that $\chi^2 \to 1$ and further as $f\sqrt{A}/\bar{V}(Z) \to \infty$, we might anticipate $\chi^2 \to 0$.

Theoretical estimates of the function $\chi^2(f\sqrt{A}/\bar{V}(Z))$, suggested by Vickery [100], have been made using somewhat oversimplified theoretical models of the flow of a turbulent

stream past a bluff object. The empirical model suggested by Vickery [100] has the form

$$\chi(f) = \frac{1}{1 + [\frac{2f\sqrt{A}}{\bar{V}(Z)}]^{4/3}} \qquad (5.18)$$

While the model employed is an oversimplification, it has been found that the theoretical estimates of $\chi^2(f\sqrt{A}/\bar{V}(Z))$ are in satisfactory agreement with observations, Figure 5.8.

Consequent to the assumptions that the longitudinal velocity distribution is Gaussian and that oscillation is linear about the quasi-static equilibrium configuration, both the forcing function and the displacement response for the system are Gaussian. Because the fluctuating part of the wind pressure may be assumed to be a stationary random process, it is fully described by the probability distribution, the spectral densities and the cross-correlation functions.

The cross-correlations are defined as the average of the product of the pressure at one point (r) in space and time (x_1, y_1, z_1, t_1) with that at another point, s, (x_2, y_2, z_2, t_2) and is defined by

4

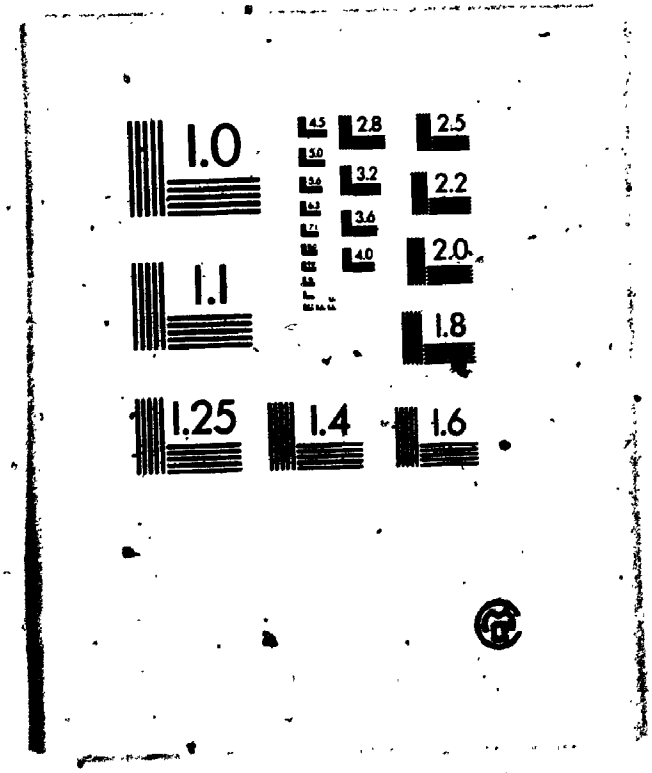

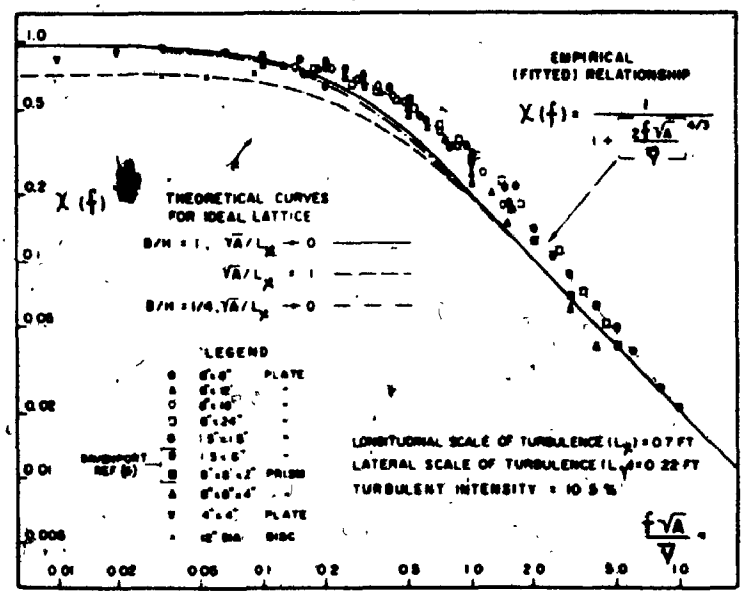

FIGURE 5.8 Aerodynamic Admittance Function for Flat Plates and Prisms Normal to the Flow (from Vickery [100])

$$R_{q_r q_s}(x_1,x_2;y_1,y_2;z_1,z_2;t_1,t_2)$$

$$= \langle q_r(x_1,y_1,z_1,t_1) q_s(x_2,y_2,z_2,t_2) \rangle \qquad (5.19)$$

Previous work of many authors (e.g. Corcos [102]), has shown that, if the turbulent boundary layer thickness is constant and the mean pressure gradient small, the turbulent wall-pressure fluctuations constitute a stationary homogeneous random phenomenon, that is, the pressure cross-correlation is a function of the separations, $|x_1-x_2|$, $|y_1-y_2|$, $|z_1-z_2|$, and not the location of the points in space nor the time. Thus, for horizontal surfaces, Eq. 5.19 may be written with some approximation as

$$\langle q_r(x_1,y_1,z,t_1) q_s(x_2,y_2,z,t_2) \rangle$$

$$= R_{q_r q_s}(|x_1-x_2|,|y_1-y_2|,0,\tau) \qquad (5.20)$$

The Fourier transform of the cross-correlation function $R_{q_r q_s}$ with respect to time yields the cross-spectral density function

$$S_{q_r q_s}(|x_1-x_2|,|y_1-y_2|,0,f)$$

$$= 2 \int_{-\infty}^{\infty} R_{q_r q_s}(|x_1-x_2|,|y_1-y_2|,0,\tau) e^{-i2\pi f\tau} d\tau \qquad (5.21)$$

in which $S_{q_r q_s}$ is the one-sided cross-spectral density function.

The correlation measurements by Willmarth and Wooldridge [103], and many other authors, show that the pressure fluctuations are convected downstream and decay after travelling a few boundary-layer thicknesses.

The convection velocity of pressure-producing eddies is defined as the velocity of a reference frame in which the rate of decay of the pressure correlation is the least. The convection velocity V_c is related to the length scale of longitudinal turbulence $L_x(v)$ in the direction of convection and the life expectancy of the turbulence eddies Γ [104], as follows:

$$L_x(v) = V_c \Gamma \tag{5.22}$$

Morri [105] found that the fluctuating pressure decays downstream from the edge rapidly for a small ratio of model height/ground roughness, ($\bar{H}/z_o = 50$), and slowly for a large ($\bar{H}/z_o = 130$), both for open terrain. He also found that the convection velocity varies from $V_c/\bar{V}_G = 0.30$ at $f\bar{H}/\bar{V}_G = 0.1$ to $V_c/\bar{V}_G = 0.50$ at $f\bar{H}/\bar{V}_G = 0.50$, where f is the frequency in cycles per second.

Maestrello [106] and Bull [107], among others, measured pressure spectra on a wall parallel to flow at high velocities. Morri [105], Ishizaki and Yoshikawa [93] and Christiano [91] measured pressure spectra on low flat or curved roofs in two- and three-dimensional flows at low

velocities. These measurements showed the following general results:

1. Except near the ends or near irregularities, a boundary-layer pressure field is nearly stationary in time.
2. The correlation of a boundary-layer pressure field is characterized by a time decay as well as by a convection velocity in the direction of the flow.
3. The mean-square pressure is nearly constant within the correlation area.

Based on these results, an expression was given by the author [108] and Abu-Sitta and the author [12] for the pressure cross-spectrum, assuming homogeneous turbulence, in the following form:

$$S_{q_r q_s}(|x_1-x_2|,|y_1-y_2|,0;\omega) = \frac{\sigma_q^2}{\omega_e} \exp\{-\pi(|\Delta x'|^2 + 2i|\Delta y'|\mu+\mu^2)\} \qquad (5.23)$$

In which $\mu = \frac{\omega}{\omega_e}$, ω = the frequency in radians per second, ω_e = equivalent convection frequency = $\frac{\pi V_c}{L_x(v)}$, $|\Delta x'| = \frac{|x_1-x_2|}{2L_x(v)}$ = separation in direction of flow, and $|\Delta y'| = \frac{|y_1-y_2|}{2L_x(v)}$ = separation in direction perpendicular to the flow. Finally, V_c = convection velocity taken as $0.45\ \bar{V}_G$ and σ_q^2 = the variance of the homogeneous pressure field,

$$\sigma_q^2 = \langle q(x,y,z,t) \rangle = R_{q_r q_s}(0;0;0;0;0) = C_{\sigma_q} q_d^2 \tag{5.24}$$

where C_{σ_q} = the R.M.S. pressure distribution coefficient of the pressure fluctuations and q_d is the dynamic pressure head of the free flow.

Morri [105] measured the R.M.S. pressure fluctuations on a low roof at low velocities and found that the coefficient C_{σ_q} varies from 0.10 to 0.015 and depends on the ratio model height/boundary layer thickness, $(\bar{H}/\delta)$, and little on the model height/roughness ratio $(\bar{H}/z_o)$, and velocity of the flow.

Ishizaki and Yoshikawa [93] measured the R.M.S. pressure fluctuations on low flat and curved roofs at low velocities. They found that the averaged coefficient $\bar{C}_{\sigma_q}$ is largest on a flat roof (0.60) and smallest on a curved roof (0.05), and showed also that C_{σ_q} takes the maximum value on the windward edge and decreases leeward on each roof.

A more recent study was conducted by Davenport et al. [89] on the Calgary Olympic Coliseum model with a hyperbolic paraboloid shape surface, at the Wind Tunnel Laboratory, in London, Ontario, Canada.

In their study, they found that C_{σ_q} takes a maximum value of 0.09 on the windward edge and decreases rapidly to 0.03 about the centre of the model on the line joining the two high points, and remains about constant toward the lee of the roof.

The pressure spectrum at a point can be described by an empirical expression,

$$S_q(0,0,0;\omega) = \frac{\sigma_q^2}{\omega_e} \exp(-\pi\mu^2) \qquad (5.25)$$

showing a decay of the pressure fluctuations proportional to ω^2. Figure 5.9 shows this spectrum in the logarithmic form compared with measurements by Ishizaki and Yoshikawa [93]. These results show general agreement with Eq. 5.25. Although this agreement is not rigorously substantiated, it should be adequate for an approximate analysis at least.

The definition of the coherence function, γ, similar to that introduced in Chapter 3 for the turbulent components of turbulence is,

$$\gamma^2_{q_r q_s} = \frac{|S_{q_r q_s}(x_1,y_1,z_1,x_2,y_2,z_2;\omega)|^2}{S_{q_r}(x_1,y_1,z_1;\omega) S_{q_s}(x_2,y_2,z_2;\omega)} \qquad (5.26)$$

The square of modulus of the cross spectra is,

$$|S_{q_r q_s}(x_1,y_1,z_1,x_2,y_2,z_2;\omega)|^2 = C^2(\omega) + Q^2(\omega) \qquad (5.27)$$

in which $C(\omega)$ is the real part (co-spectrum) and $Q(\omega)$ is

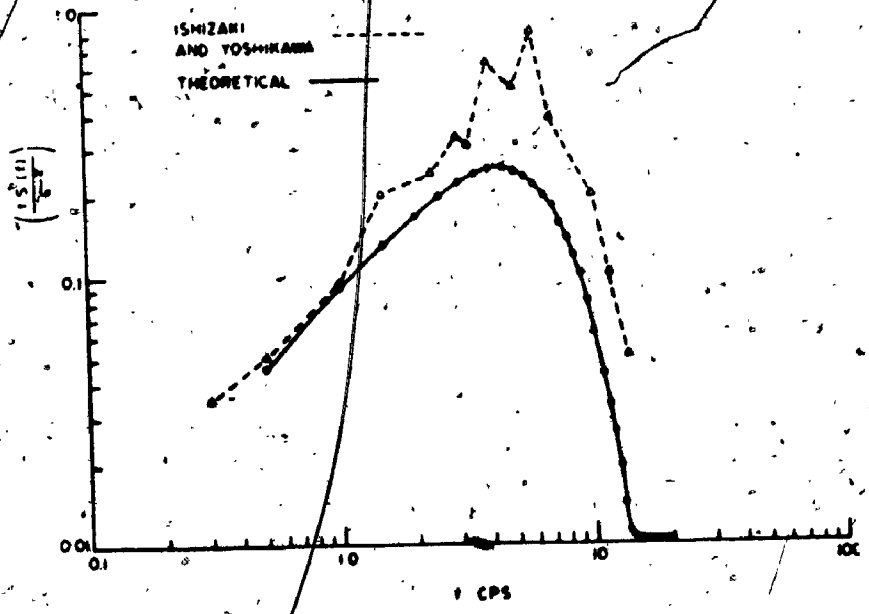

FIGURE 5.9 Power Spectrum of Pressure Fluctuations (Comparison With Ishizaki and Yoshikawa Measurements [93])

the imaginary part (quadrature) of the cross spectrum.

Assuming the pressure field is homogeneous, then

$$S_{q_r}(x_1,y_1,z_1;\omega) = S_{q_s}(x_2,y_2,z_2;\omega) = S_q(0,0,0;\omega) \tag{5.28}$$

and similarly, as discussed before,

$$S_{q_rq_s}(x_1,y_1,z_1,x_2,y_2,z_2;\omega) = S_{q_rq_s}(|\Delta x|,|\Delta y|,|\Delta z|;\omega) \tag{5.29}$$

For a horizontal surface $\Delta z = 0$, and Eq. 5.29 may be written as:

$$S_{q_rq_s}(x_1,y_1,z,x_2,y_2,z;\omega) = S_{q_rq_s}(|\Delta x|,|\Delta y|,0;\omega) \tag{5.30}$$

Accordingly, the square of the coherence function may be written as follows:

$$\gamma^2_{q_rq_s} = \frac{|S_{q_rq_s}(|\Delta x|,|\Delta y|,0;\omega)|^2}{S_q^2(0,0,0;\omega)} \tag{5.31}$$

Then the modulus of spectrum may be written as:

$$|S_{q_rq_s}(|\Delta x|,|\Delta y|,0;\omega)|^2 = \frac{\sigma_q^4}{\omega_e^2}\exp\{-2\pi(\Delta x'^2+\mu^2)-4\pi|\Delta x'|\mu^2\} \tag{5.32}$$

and

$$S_q^2(0,0,0;\omega) = \frac{\sigma_q^4}{\omega_e^2}\exp(-2\pi\mu^2) \tag{5.33}$$

and

$$\gamma^2_{q_r q_s} = \exp\{-2\pi\Delta y'^2 - 4\pi|\Delta x'|\mu\} \qquad (5.34)$$

and

$$\gamma_{q_r q_s} = \exp\{-\pi(\Delta y'^2 + 2|\Delta x'|\mu)\} \qquad (5.35)$$

Equation 5.35 is the coherence function of the pressure spectrum.

Substituting for $|\Delta x'|$ and $\mu = \frac{\omega}{\omega_e}$, where

$$\omega_e = \frac{\pi V_c}{L_x(v)} = \frac{\pi B \bar{V}_G}{L_x(v)} \quad (B = 0.45, \text{ Morri [105]}),$$

the coherence function for points on the x-axis only is

$$\gamma_{q_r q_s}(f) = e^{-\theta^* \frac{(2\pi f)|\Delta x'|}{\bar{V}_G}} \qquad (5.36)$$

where $\theta^* = 2.0$.

Morri [105], in his experimental work found experimentally that $\theta^* = 0.60$. This difference in θ^* may be due to the assumption of homogeneity of the pressure field and the independence of the cross spectrum mathematical model on $\bar{H}/\delta$ or $\bar{H}/z_o$. (For $\theta^* = 2.0$, the response of the structure to pressure fluctuations is underestimated.)

It may be concluded from the coherence function equation (5.35), that the coherence decay is proportional to $|\Delta x'|$, $(\Delta y')^2$ and the circular frequency ω. When $\gamma^2_{q_r q_s}(\omega) = 0$ at a particular frequency, the pressure

fluctuations at points r and s are incoherent (uncorrelated) at that frequency, but if $\gamma^2_{q_r q_s}(\omega) \equiv 0$ for all frequencies, then the pressure fluctuations are statistically independent: finally, when $\gamma^2_{q_r q_s}(\omega) = 1$ for all the frequencies (ω), the pressure fluctuations at points r, s are fully correlated.

As stated earlier, the coherence function γ describes the frequency dependence of two processes, as well as their spatial correlation.

The area under the cross-correlation coefficient with respect to time gives a measure of time over which the two processes are correlated, as

$$T = \int_0^\infty \rho_{q_r q_s}(\tau) d\tau \qquad (5.37)$$

and is called the time scale, T. This expression is similar to the length scale of turbulence, $L_x(v)$ obtained in Chapter 3, where the integrations were carried out with respect to spatial separation.

5.3 RESPONSE OF TENSION ROOFS TO DYNAMIC WIND PRESSURE

Cable roofs may be treated mathematically as discrete or continuous systems. In the continuous approach, simultaneous partial differential equations are utilized to represent the real structure, assuming the structural

properties may be adequately represented as uniform or slightly varying.

The physical and analytical understanding of the dynamic response of tension roofs is dependent on the knowledge of the natural frequencies, the vibration mode shapes and the damping capacity of the structure.

The analysis of free vibration of suspension roofs with many configurations in plane and surface shape is shown in Chapter 4 in which the natural frequencies, mode shapes and the effect of the air enclosure are studied and defined.

The damping capacity of tension roofs is important in the investigation of the dynamic response of these structures. In general, the damping results from many different and highly complicated energy loss mechanisms. Different types of damping can be explained as material damping, structural damping, acoustic damping and aerodynamic damping. Furthermore, the damping ratio can be different for the different vibrating modes.

General information about damping capacity can be obtained by full scale and model tests. In experimental work, the testing methods are of importance.

The material, structural and acoustic damping may be

obtained from free vibration tests in still air. These procedures have been carried out and the results are presented in Chapter 6, for different modes of vibration of a circular suspension roof model. The damping ratios are obtained from the logarithmic decrement of the auto-correlation curves of vibration. The total damping of the structure including the aerodynamic damping may be obtained from wind tunnel tests; results of these experimental analyses are presented in detail in Chapter 6.

Tension roofs belong to the class of nonlinear structural systems due to their large deflections and have to be analyzed according to the degree of nonlinearity which they exhibit [61 to 64].

It was assumed earlier that the dynamic response is small enough to be superimposed on the nonlinear quasi-static response. Results of model tests conducted by Jensen [92] have indicated that the nonlinearity of tension roof systems does not appear very distinct with respect to their dynamic response behaviour.

5.3.1 Modal Analysis of Tension Roofs

If the assumption of dynamic linearity is accepted, the dynamic response can be adequately represented in terms of mode shapes.

In the modal analysis technique, the response in each mode may be treated as that of an independent one degree of freedom system by introducing generalized coordinates which have uncoupled properties. The response is described in terms of the modes of free vibration whose orthogonality facilitates the solution and the complete motion of the system may be obtained by summing the modal contributions.

Let the dynamic vertical displacement of a circular tension roof be given in polar coordinates by

$$w(r,\theta,t) = \Sigma\, z_{nm}(t)\Phi_{nm}(r)\cos n\theta + \Sigma\, z'_{nm}(t)\Phi_{nm}(r)\sin n\theta \qquad (5.38)$$

in which r,θ = polar coordinates, Figure 5.10, $z_{nm}(t)$, $z'_{nm}(t)$ = symmetric and antisymmetric time dependent amplitudes (generalized coordinates), $\Phi_{nm}(r)$ = the nmth modal shape function depending on r only, n = number of nodal diameter and m = number of nodal circle in the mode shape (Chapter 4).

The equation of motion of the nmth symmetric mode may then be given by (Novak [58]),

$$M_{nm}\ddot{z}_{nm} + C_{nm}\dot{z}_{nm} + K_{nm}z_{nm} = F_{nm} \qquad (5.39)$$

in which M_{nm}, C_{nm}, K_{nm}, F_{nm} = generalized mass, damping, stiffness and loading of the nmth natural mode respectively. The uncoupling of this equation in terms of modal

time-dependent amplitudes $z_{nm}(t)$ is only possible if the mass, stiffness and damping are independent of frequency and if damping is proportional to either mass or stiffness [122]; this is only approximately the case for tension roofs due to the inertia effects of the air in the enclosure under the roof.

The generalized mass is defined by

$$M_{nm} = \int_o^{2\pi} \int_o^a m_t \, \phi_{nm}^2(r) \cos^2(n\theta) r dr d\theta \qquad (5.40)$$

in which m_t is the sum of mass per unit area of the roof material and the air "attached" to the roof surface during movement.

The generalized loading,

$$F_{nm} = \int_o^{2\pi} \int_o^a q_t(t) \phi_{nm}(r) \cos(n\theta) r dr d\theta \qquad (5.41)$$

in which

$$q_t(t) = q(t) + q_r(t) - q_\ell(t) \qquad (5.42)$$

where $q(t)$ = fluctuating pressure due to wind turbulence, $q_r(t)$ = radiated pressure due to roof movement, $q_\ell(t)$ = internal pressure in the enclosed volume under the roof, a function of wind velocity, roof movement and number and size of wall openings, as was found in the experimental work in Chapter 6.

The damping C_{nm} is the sum of material, structural, acoustic and aerodynamic damping. The stiffness K_{nm} is modified due to enclosed air effects.

Here, it is assumed that the normal displacement w is representative of the roof motion and as such, is sufficient to describe the response. If this were not the case, similar equations for the tangential displacement could be written.

The equation of the antisymmetric motion may similarly be given by

$$M_{nm}\ddot{z}'_{nm} + C_{nm}\dot{z}'_{nm} + K_{nm}z'_{nm} = F'_{nm} \tag{5.43}$$

in which the antisymmetric generalized load is given by

$$F'_{nm} = \int_0^{2\pi} \int_0^a q_t(t)\phi_{nm}(r)\sin(n\theta)\,r\,dr\,d\theta \tag{5.44}$$

Similar to one degree of freedom, the solution of the equation of motion (5.39), with random excitation, is defined by the spectrum of the generalized coordinate z_{nm} in the mode nm only as [109]

$$S_{z_{nm}}(\omega) = \frac{|H_{nm}(\omega)|^2}{K_{nm}^2} S_{F_{nm}}(\omega) \tag{5.45}$$

in which $|H_{nm}(\omega)|^2$ is the square of the frequency response function (mechanical admittance) modulus, defined as

$$|H_{nm}(\omega)|^2 = \{[1-(\frac{\omega}{\omega_{nm}})^2]^2 + 4(\frac{\omega}{\omega_{nm}})^2\beta_{nm}^2\}^{-1} \tag{5.46}$$

where β_{nm} = the critical damping ratio for the total damping and ω_{nm} = the natural circular frequency of the undamped nmth mode of the system, and ω = frequency of the random excitation.

5.3.2 Spectra of the Response

The response spectrum of the displacement in the nmth mode including both symmetrical and antisymmetrical components may be written as

$$S_{w_{nm}}(\omega) = \phi^2_{nm}(r)\cos^2 n\theta \frac{|H_{nm}(\omega)|^2}{K^2_{nm}} S_{F_{nm}}(\omega) + \phi^2_{nm}(r)\sin^2 n\theta \frac{|H_{nm}(\omega)|^2}{K^2_{nm}} S_{F'_{nm}}(\omega) \quad (5.47)$$

The spectrum of the total response is given by,

$$S_w(\omega) = \sum_{n=0}^{\infty} \sum_{m=1}^{\infty} [\phi^2_{nm}(r)\cos^2 n\theta \frac{|H_{nm}(\omega)|^2}{K^2_{nm}} S_{F_{nm}}(\omega) + \phi^2_{nm}(r)\sin^2 n\theta \frac{|H_{nm}(\omega)|^2}{K^2_{nm}} S_{F'_{nm}}(\omega)] \quad (5.48)$$

in which $S_{F_{nm}}(\omega)$ and $S_{F'_{nm}}(\omega)$ = the spectra of the symmetrical and antisymmetrical generalized forces $F_{nm}(t)$, $F'_{nm}(t)$ respectively.

The coupling between modes in Eq. 5.48 is put equal to zero. Anticipating the results of the experimental work, Chapter 6, it is found that in the model under study

only the modes nm = 01, 11, 21 and 02 are of importance. The coupling between the modal responses 01 and 02 is negligible because they are widely separated in frequency and the coupling between the modes 11, 21 and 01, 02 can be shown to vanish (see section 5.3.3). Also, the coupling between symmetric and antisymmetric modes is neglected.

Therefore, the spectrum of the total response (due to the first four modes) is approximated by

$$S_w(\omega) = \sum_{m=1,2} [\phi^2_{0m}(r) \frac{|H_{0m}(\omega)|^2}{K^2_{0m}} S_{F_{0m}}(\omega)]$$

$$+ [\phi^2_{11}(r) \frac{|H_{11}(\omega)|^2}{K^2_{11}} S_{F_{11}}(\omega) + \phi^2_{21}(r) \frac{|H_{21}(\omega)|^2}{K^2_{21}} S_{F_{21}}(\omega)] \cos^2\theta$$

$$+ [\phi^2_{11}(r) \frac{|H_{11}(\omega)|^2}{K^2_{11}} S_{F'_{11}}(\omega) + \phi^2_{21}(r) \frac{|H_{21}(\omega)|^2}{K^2_{21}} S_{F'_{21}}(\omega)] \sin^2\theta \quad (5.49)$$

in which the last term of Eq. 5.49 is the antisymmetric component of the response spectrum.

5.3.3 Spectra of the Generalized Wind Force

The generalized force spectra $S_{F_{nm}}(\omega)$, $S_{F'_{nm}}(\omega)$ typically are related to the actual pressure spectrum, in polar coordinates, acting on a horizontal surface ($\Delta z=0$), $S_q(r,\theta;r',\theta';\omega)$ by,

$$S_{F_{nm}}(\omega) = \int_A\int_A S_q(r,\theta,r',\theta',\omega)\phi_{nm}(r)\phi_{nm}(r')\cos(n\theta)\cos(n\theta')\,dAdA'$$

$$= \int_0^{2\pi}\int_0^{2\pi}\int_0^a\int_0^a S_q(r,\theta,r',\theta',\omega)\phi_{nm}(r)\phi_{nm}(r')rr'$$

$$\cos(n\theta)\cos(n\theta')drdr'd\theta d\theta'$$

$$= S_q(0,0;\omega)A^2 \int_0^{2\pi}\int_0^{2\pi}\int_0^a\int_0^a$$

$$\frac{S_q(r,\theta,r',\theta';\omega)\phi_{nm}(r)\phi_{nm}(r')rr'\cos n\theta\cos n\theta'}{S_q(0,0;\omega)A^2}$$

$$drdr'd\theta d\theta' = S_q(0,0;\omega)A^2|I_{nm}(\omega)| \qquad (5.50)$$

Similarly,

$$S_{F'_{nm}}(\omega) = S_q(0,0;\omega)A^2 \int_0^{2\pi}\int_0^{2\pi}\int_0^a\int_0^a$$

$$\frac{S_q(r,\theta,r',\theta',\omega)\phi_{nm}(r)\phi_{nm}(r')rr'\sin(n\theta)\sin(n\theta')}{S_q(0,0,\omega)A^2}$$

$$drdr'd\theta d\theta'$$

$$= S_q(0,0,\omega)A^2|I'_{nm}(\omega)| \qquad (5.51)$$

in which A=a representative area of the structure.

The nondimensional generalized spectra $|I_{nm}(\omega)|$, $|I'_{nm}(\omega)|$ are called the <u>joint acceptance functions</u>. They define the sensitivity of the interaction between the

fluctuating pressure and the structural modes of vibration and hence determine the response of the structure. The general characteristics of these functions indicate the important link between the gust fluctuations (described by the velocity spectrum) and the modal force fluctuations and displacements. Also, these functions depend on the mode shape and the velocity field, hence the pressure field, which varies from structure to structure; they show that the effectiveness of the pressure in exciting a mode involves also the geometry of the structure and the mode shape.

To evaluate the integrals in the joint acceptance, we substitute for the mode shape $\phi_{nm}(r)$ from Eq. 4.58 and for the spectra $S_q(r,\theta,r',\theta',\omega)$ and $S_q(0,0,\omega)$ in polar coordinates from Eqs. 5.23 and 5.25 respectively.

The symmetric component of the joint acceptance function, after introducing the coherence function γ from Eq. 5.31 and assuming the pressure field to be fully correlated, may be written as follows:

$$I_{nm}(\omega) = \int_0^a \int_0^a \gamma \frac{J_n(\frac{\omega_{nm} r}{\nu}) J_n(\frac{\omega_{nm} r'}{\nu}) rr' dr dr'}{A^2} \int_0^{2\pi} \int_0^{2\pi} \cos(n\theta)\cos(n\theta') d\theta d\theta' \qquad (5.52)$$

where γ = $\sqrt{\text{the coherence function}}$,

J_n = Bessel function of the first kind of order n, ω_{nm} the natural frequency of mode nm and $\nu = \sqrt{T/m}$; T is the tension in the roof per unit length and m its mass density per unit area.

The integral

$$\int_0^{2\pi}\int_0^{2\pi} \cos n\theta \cos n\theta' = 2\pi^2 \quad , \text{ for } n\theta = n\theta' \qquad (5.53a)$$

$$= 0 \quad , \text{ for } n\theta \neq n\theta' \qquad (5.53b)$$

This result shows that the joint acceptance function is equal to zero when $n\theta \neq n\theta'$ and exists only when $n\theta = n\theta'$. It may be concluded that the coupling between modes of different nodal diameters n is equal to zero.

Similarly, since the integral

$$\int_0^{2\pi}\int_0^{2\pi} \sin(n\theta)\sin(n\theta') = 2\pi^2 \quad , \text{ for } n\theta = n\theta' \qquad (5.54a)$$

$$= 0 \quad , \text{ for } n\theta \neq n\theta' \qquad (5.54b)$$

then,

$$I_{nm}(\omega) = I'_{nm}(\omega) \quad , \text{ for } n = m \qquad (5.55)$$

The joint acceptance function of modes 01, 11, 21 and 02 may therefore be evaluated as follows:

$$I_{om}(\omega) = \frac{2\pi^2\gamma}{A^2} \int_0^a J_o\left(\frac{\omega_{om} r}{\nu}\right) r\,dr \int_0^a J_o\left(\frac{\omega_{om} r'}{\nu}\right) r'\,dr'$$

$$= \frac{2\pi^2\gamma}{A^2} \left[\frac{\nu a J_1\left(\frac{\omega_{om} a}{\nu}\right)}{\omega_{om}}\right]^2 \quad , m = 1,2 \qquad (5.56)$$

Similarly,

$$I_{n1}(\omega) = \frac{2\pi^2\gamma}{A^2}\int_o^a J_1(\frac{\omega_{n1}r}{\nu})rdr \int_o^a J_1(\frac{\omega_{n1}r'}{\nu})r'dr'$$

$$= \frac{\pi^4\gamma}{2A^2}\{\frac{a}{K_{n1}}[J_1(\frac{\omega_{n1}a}{\nu})H_o(\frac{\omega_{n1}a}{\nu})$$

$$- J_o(\frac{\omega_{n1}a}{\nu})H_1(\frac{\omega_{n1}a}{\nu})]\}, \quad n = 1,2 \qquad (5.57)$$

in which J_o, J_1 are Bessel functions of the first kind and order zero and one respectively, and H_o, H_1 are the Struve functions of zero order and first order respectively (see Appendix B).

5.3.4 Evaluation of Peak Response

With the knowledge of all the pressure spectra $S_q(r,\theta,r',\theta',\omega)$, the spectra of the displacements (or strains, stresses, etc.) may be calculated as indicated in Eq. 5.49, by replacing modal displacements by other modal quantities.

From the spectra of response we can calculate the standard deviation as follows:

$$\sigma^2_{(w)} = \int_o^\infty S_w(\omega)d\omega \qquad (5.58)$$

The total peak response is

$$\hat{w}_t = w_{q,st} + g\,\sigma_{(w)} \qquad (5.59)$$

in which $w_{q,st}$ = the quasi-static deflection, g = a peak factor, defined in Chapter 3.

For the total quasi-static and dynamic response given by Eq. 5.59, we assume that the quasi-static response is determined by appropriate linear or nonlinear analysis.

5.3.5 Coincidence Phenomenon

The symmetric and antisymmetric components of the joint acceptance function of mode nm, Eq. 5.55, are

$$I_{nm}(\omega) = I'_{nm}(\omega) = 2\pi^2 \int_0^a \int_0^a \gamma \, J_n(\frac{\omega_{nm} r}{v}) J_n(\frac{\omega_{nm} r'}{v}) rr' dr dr', \quad n = m \tag{5.60}$$

Substituting for the coherence function γ from Eq. 5.35, Eq. 5.60 may be written as

$$I_{nm}(\omega) = I'_{nm}(\omega) = 2\pi^2 \int_0^a \int_0^a J_n(\frac{\omega_{nm} r}{v}) J_n(\frac{\omega_{nm} r'}{v}) rr' \, e^{-\pi[\frac{y_1-y_2}{2L_x(v)}]^2} \cos(2\pi f_{nm} \frac{|x_1-x_2|}{V_c}) dr dr', n=m \tag{5.61}$$

where $|x_1-x_2| = \Delta r \cos\theta^*$, $|y_1-y_2| = \Delta r \sin\theta^*$, $\Delta r = \sqrt{\Delta x^2+\Delta y^2}$ and θ^* = the angle between the separation Δr and the direction of flow. From the above equation, it may be seen that the joint acceptance functions $I_{nm} = I'_{nm}$ (n=m).

have a maximum value around frequencies,

$$f_{c,j} = \frac{jV_c}{2a} \quad , \quad j = 1,2,3,... \qquad (5.62)$$

These frequencies are called coincidence frequencies.

This coincidence phenomenon occurs when the convection frequency of the pressure field $\frac{jV_c}{2a}$ is equal to the natural frequency of the tension roof, f_{nm} (n=m). A large response will result in the mode corresponding to f_{nm}.

This phenomenon is known as the coincidence phenomenon and it is in general agreement with experimental work carried out and submitted in Chapter 6. It was found that the major response in the aeroelastic model tested in the boundary layer wind tunnel under turbulent wind is due to the first antisymmetric mode 11 (n=m=1), where the coincidence phenomenon may occur.

Also, this theoretical result for the coincidence effect is in general agreement with Morri [105] and Lin [110] analysis for a rectangular rigid panel.

5.4 AIR STRUCTURE INTERACTION

Tension roofs are subject to large deflections and two special problems arise under wind loading. First, large deflections and change of geometry can influence

the wind pressure; second, the change of geometry, and, consequently, the changes in velocity and acceleration of the vibrating structure under the fluctuating wind loading indicate that the surrounding air of the structure has to be taken into account. If the change of the geometry is to influence the wind pressure, the deflections have to be really large. An examination of this problem is possible by wind tunnel tests.

A more exact expression for the wind pressure can be considered as (Davenport [44],

$$q(x,y,z,t) = \frac{1}{2}\rho\, C_q(x,y,z,t)V_t^2(x,y,z,t) + C_m\,\rho\,\frac{A}{D}\,\frac{dV_r(x,y,z,t)}{dt} \qquad (5.63)$$

where the last term expresses the inertial reaction associated with the acceleration of the turbulent wind. A and D express a reference area for a virtual mass, and the diameter of the object, while C_m is a coefficient of an additional air mass, and

$$V_r(x,y,z,t) = V(x,y,z,t) - \dot{w}(x,y,z,t) \qquad (5.64)$$

where V_r = the relative velocity, V = velocity of turbulent flow above the roof and $\dot{w}$ is the velocity of the vibrating membrane under the action of the turbulent wind.

The existence of this latter term of Eq. 5.63 has seldom been alluded to in relation to wind loading, although in the case of flexible vibrating structures like tension roofs, which cover a large area and undergo large changes in geometry, it has to be considered.

Tension roof structures have an enclosure with openings (doors and windows) and a realistic analysis should include the effect of the air within the enclosure.

As the roof vibrates, the air pressure inside fluctuates and should be considered in the analysis.

This problem of air-structure interaction is very complicated and, to the knowledge of the writer, has not been recognized or studied by researchers. An attempt is made in this study to analyze this problem and explore the behaviour of tension roofs under the effect of turbulent wind above its surface and the air enclosed below its surface.

The "Plane Wave" assumption (analogous to Taylor's hypothesis) implies that the wind velocity fluctuations recorded at a point travel along the surface of the roof unchanged in the direction of the mean wind velocity. If this assumption is accepted, a simplification can be made by assuming that the plane wave for wind gusts is similar

to sound waves acting on a flexible wall. The following analysis is outlined according to this simplification.

If a loudspeaker excitation acts on a flexible wall forming one panel of an enclosure bounded by rigid walls (or a membrane sheet attached to a cylindrical drum head) [111], there are three or four different sound waves:

1. The incident sound wave.
2. The reflected wave, which derives from the pressure on a rigid panel and which results in the doubling of the effective excitation pressure on the panel.
3. The radiated waves,
   a. In opposite direction to the sound wave. This is radiated back by virtue of the motion of the wall.
   b. In the direction of the sound wave. This is radiated to the inside of the enclosure by virtue of the motion of the wall and is called the transmitted wave.

Since the membrane is very flexible, we may assume that the reflected wave has negligible effect in this analysis.

The radiated wave due to the membrane movement in the opposite direction to the sound wave exists due to

the negative velocity of the panel $\dot{w} = \frac{dw}{dt}$ which exerts a negative acoustic pressure proportional to this velocity, (i.e. $q_r = -\rho c_o \frac{dw}{dt}$, where ρ is the density of air and c_o is the speed of sound in air) and will appear in the equation of motion of the panel as a damping term. This term is the acoustic damping and it plays an important part in the vibration of some structures.

If we assume the plane wave of turbulence acting on the roof with its associated air mass ρ, is similar to the plane wave of sound acting on a flexible panel, the relative movement of the membrane to this plane wave produces a damping term. Let us examine the first term of Eq. 5.63. After substituting the value of V_R from Eq. 5.64 then

$$q(x,y,z,t) = \frac{1}{2} \rho C_q(x,y,z)[V(x,y,z,t)-\dot{w}(x,y,z,t)]^2 \tag{5.65}$$

By expanding Eq. 5.65, we get

$$q(x,y,z,t) = \frac{1}{2} \rho C_q(x,y,z,t)[V^2(x,y,z,t)-2V(x,y,z,t)\dot{w}(x,y,z,t) + \dot{w}^2(x,y,z,t)] \tag{5.66}$$

By assuming small amplitudes of vibration, the term $\dot{w}^2$ may be ignored and Eq. 5.66 reduces to.

$$q(x,y,z,t) = \frac{1}{2} \rho C_q V^2(x,y,z,t)$$

$$- \rho C_q(x,y,z,t)V(x,y,z,t)\dot{w}(x,y,z,t) \quad (5.67)$$

The first term is the total effect of the turbulent pressure field including the quasi-static effect of the mean wind velocity $\bar{V}$ and the gusty component effect v as studied in detail in previous sections.

The second term represents a force proportional to the velocity of the structure; it has an effect similar to the structural damping forces and is termed the aerodynamic damping force. While those forces are small compared with the inertia and stiffness forces of a structure they are appreciable in comparison with the forces due to structural damping. They can markedly influence the behaviour of a structure in wind and may be added to the equation of motion of the system.

The wave transmitted to the enclosure is caused mainly by movement of the roof which, in the fundamental mode of vibration only, causes a change in the air volume under the membrane, as discussed in Chapter 4. Due to this change in air volume, the pressure inside the enclosure will increase or decrease.

As stated earlier in Chapter 4, because the sound

wave length in the air is much larger than the enclosure dimensions, the increase or decrease in pressure due to air volume change may be assumed uniform everywhere within the enclosure. This change in pressure is obtained in a manner similar to Kinsler [78] and is assumed to be a function of the averaged panel displacement $\bar{w}$, with respect to membrane area and the air movement effect through the wall openings, if any. This pressure acts on the lower surface of the roof and has to be included in its equation of motion.

From the theoretical analysis presented in Chapter 4, and the experimental work in Chapter 6, it was found that the only mode of vibration largely affected due to the air movement is the fundamental mode 01.

We turn now to the determination of the frequency response function (mechanical admittance) in mode 01, in which are included the effects of the enclosure under the roof, the aerodynamic damping term, and the openings in the wall, on the response.

This function can be obtained in a manner similar to Lin [110] by considering the steady state motion of the system under a suitable harmonic excitation. For this, we can choose the following plane standing wave of wind acting on the circular membrane surface from the free

side. Let the plane wind wave be given by:

$$V(z,t) = \bar{V}(z)e^{i\omega t} \tag{5.68}$$

in which $\bar{V}(z)$ = the amplitude (mean velocity at the height of the roof z) and ω = frequency of the wind wave respectively. Due to this plane wind wave, the membrane vibrates, a radiated pressure q_r develops and an increase or decrease in internal pressure q_ℓ occurs.

The equation of motion of the membrane in its fundamental mode which includes the effects of inertia, structural resistance and stiffness may be written as follows:

$$M_{01}\ddot{Z}_{01}(t)+C_{01}\dot{Z}_{01}(t)+K_{01}Z_{01}(t) = F_{i_{01}}(t)+F_{r_{01}}(t)-F_{\ell_{01}}(t) \tag{5.69}$$

in which M_{01}, C_{01}, K_{01} = the generalized mass, structural damping and stiffness of mode 01 respectively; $F_{i_{01}}(t)$, $F_{r_{01}}(t)$, $F_{\ell_{01}}(t)$ = the generalized incident wind force, the generalized force due to radiated pressure and the generalized force due to change in internal pressure, of mode 01 respectively; $Z_{01}(t)$ is the generalized coordinate of mode 01 related to the displacement as,

$$w_{01}(r,t) = \Phi_{01}(r)Z_{01}(t) \tag{5.70a}$$

where $\Phi_{01}(r)$ = the fundamental mode shape 01, and is a function of r only.

The internal pressure increase or decrease $q_\ell(t)$. is derived in Chapter 4 (Eqs. 4.148, 4.182) and is dependent on the average displacement of the fundamental mode $\bar{w}_{01}(r,t)$, ($q_\ell = 0$ for $nm \neq 01$). Therefore, the displacement of mode 01, in this analysis, may be written in the form

$$w_{01}(r,t) = \bar{w}_{01} e^{i\omega t} \tag{5.70b}$$

where $\bar{w}_o$ is the average amplitude of mode 01, Figure 5.10, given by

$$\bar{w}_{01} = \frac{\int_o^{2\pi}\int_o^a \phi_{01}(r)\,r\,dr\,d\theta}{\pi a^2} \tag{5.71}$$

and the average internal pressure may be written as

$$q_{\ell_{01}}(t) = -\left[\frac{\rho c_o^2}{V_o}\left(1 - \frac{1}{\alpha_c}\right)\int_o^{2\pi}\int_o^a \phi_{01}(r)\,r\,dr\,d\theta\right] e^{i\omega t} \tag{5.72}$$

in which V_o = the original volume of air within the enclosure, ρ = air density and c_o = speed of sound in air.

Substitute for the fundamental mode shape, from Chapter 4, as $\phi_{01}(r) = A_{01} J_o\left(\frac{\omega_{01} r}{\nu}\right)$, evaluate the integral of Eq. 5.71 to get:

$$\bar{w}_{01}(t) = A_{01}\left[\frac{2\nu J_1\left(\frac{\omega_{01} a}{\nu}\right)}{\omega_{01} a}\right] \tag{5.73}$$

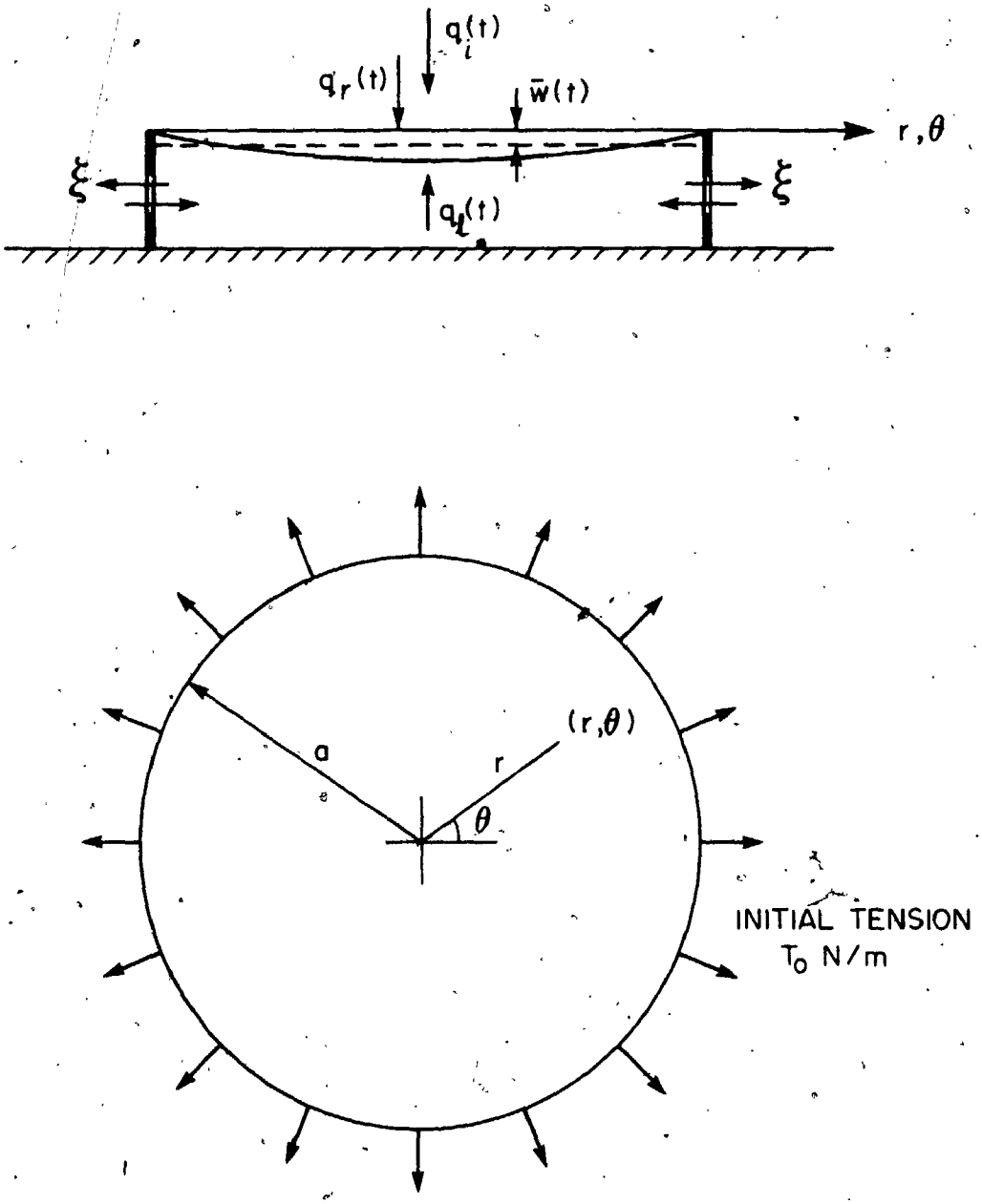

FIGURE 5.10 TIME DEPENDENT LOADING ON CIRCULAR SHALLOW ROOF (FLUCTUATING PRESSURE, RADIATED PRESSURE AND INTERNAL PRESSURE)

in which A_{01} = amplitude of vibration of mode 01. Substitute the value of $(1 - \frac{1}{\alpha_c}) = \frac{\omega^2 \ell' V_o}{c_o^2 N A_o}$ (Eq. 4.176), evaluate the integral in Eq. 5.72 and the internal pressure may be written as,

$$q_\ell(t) = \omega^2 A_{01} \left[\frac{2\rho \ell' \pi a^2}{N A_o} \times \frac{\nu J_1 (\frac{\omega_{01} a}{\nu})}{\omega_{01} a}\right] e^{i\omega t} \qquad (5.74)$$

in which N = number of wall openings of area A_o each, ℓ' = effective length of attached air through the openings and is equal to 1.20 to 1.70 times the equivalent radius of opening a_o depending on the shape of the opening and if it has flanged ends or not.

The generalized force due to change in internal pressure, from Eq. 5.74 after carrying out the necessary integration (Eq. 5.41) may be written as,

$$F_{\ell_{01}}(t) = (\omega^2 \pi \frac{\rho \ell' a^2}{N A_o}) \left[\frac{2\nu J_1 (\frac{\omega_{01} a}{\nu})}{\omega_{01}}\right] A_{01}^2 e^{i\omega t} \qquad (5.75)$$

The radiated pressure due to the roof (membrane) movement is given by Mead [111] as

$$q_r(t) = \rho c_o \bar{\dot{w}} \qquad (5.76)$$

in which $\bar{\dot{w}}$ = the average magnitude of displacement speed.

Carrying out the necessary integration (Eq. 5.41), the generalized force due to radiated pressure, from

Eqs. 5.71, 5.76 may be written as:

$$F_{r_{01}}(t) = -(i\omega\pi\rho c_o)\left[\frac{2\nu J_1(\frac{\omega_{01}a}{\nu})}{\omega_{01}}\right]A_{o1}^2 e^{i\omega t} \qquad (5.77)$$

We turn now to study the incident pressure $q_i(t)$ due to the plane wave given by Eq. 5.68 as

$$V(z,t) = \bar{V}(z)e^{i\omega t}$$

Due to this plane wind wave, a pressure is induced on the surface of the roof defined by

$$q(z,t) = \frac{1}{2}\rho C_q V_R^2(z,t) \qquad (5.78)$$

where

$$V_R(z,t) = V(z,t) - \bar{w}(t) \qquad (5.79)$$

where $V_R(z,t)$ = the velocity of the wind above the roof relative to the surface. Following the procedure outlined by Davenport [41] the following equation may be obtained:

$$\frac{dq(z,t)}{dV_R(z,t)} = \frac{\rho}{2}\left[V_R^2(z,t)\frac{\partial C_q}{\partial V_R(z,t)} + C_q\frac{\partial V_R^2(z,t)}{\partial V_R(z,t)}\right] \qquad (5.80)$$

If we assume C_q = the pressure coefficient is constant with respect to $V_R(z,t)$ then Eq. 5.80 reduces to:

$$\frac{dq(z,t)}{dV_R(z,t)} = \rho C_q V_R(z,t) = \rho C_q(V(z,t)-\bar{w}(t)) \qquad (5.81)$$

And, $q(z,t)$ may be written as

$$q(z,t) = \frac{1}{2}\rho C_q V^2(z,t) - \rho C_q V(z,t)\dot{w}(t) \qquad (5.82)$$

Substituting the plane wind wave definition from Eq. 5.68, Eq. 5.82 may be written as,

$$q(z,t) = \frac{1}{2}\rho C_q(\bar{V}e^{i\omega t})^2 - \rho C_q \bar{V}\dot{w}e^{i\omega t} \qquad (5.83)$$

Then the generalized wind force, after carrying out the necessary integration (Eq. 5.41), is

$$F_{\bar{V}_{01}}(z,t) = (\frac{1}{2}\pi\rho C_q a\bar{V}^2(z))[\frac{2\nu J_1(\frac{\omega_{01}a}{\nu})}{\omega_{01}}]A_{01}e^{i2\omega t} \qquad (5.84)$$

The generalized force due to relative movement of the roof, after carrying out the necessary integration (Eq. 5.41) may be written as,

$$F_{\dot{w}_{01}}(z,t) = -i\omega\pi\rho C_q\bar{V}(z)[\frac{2\nu J_1(\frac{\omega_{01}a}{\nu})}{\omega_{01}}]^2 A_{01}^2 e^{i\omega t} \qquad (5.85)$$

The generalized incident wind force $F_{i_{01}}$ in Eq. 5.69 is now to be replaced by summation of the generalized wind force $F_{\bar{V}_{01}}$ and the generalized force due to relative movement of the roof $F_{\dot{w}_{01}}$.

Substitute Eqs. 5.75, 5.77, 5.84 and 5.85 into the equation of motion (5.69). After calculating the generalized mass M_{01} (Eq. 5.40) and its relatives the generalized structural damping ($C_{01} = 2\alpha M_{01}$) and generalized

stiffness ($K_{01} = \omega_{01}^2 M_{01}$) and rearranging as necessary, we obtain the following equation:

$$\left[1 - \frac{\omega^2}{\omega_{01}^2}\left(1 + \frac{\rho \ell' a^2}{mNa_o^2}\right) + \frac{i\omega}{\omega_{01}}\left(\frac{2\alpha}{\omega_{01}} + \frac{\rho c_o}{m\omega_{01}} + \frac{\rho C_q \bar{V}(z)}{m\omega_{01}}\right)\right]$$

$$= \frac{\frac{1}{2}\rho C_q \bar{V}^2(z) e^{i2\omega t}}{\omega_{01}^2 m A_{01}\left[\frac{2\nu J_1\left(\frac{\omega_{01} a}{\nu}\right)}{\omega_{01}}\right]} \qquad (5.86)$$

From Eq. 5.86, after introducing the relation between the damping constant α and the damping ratio D_{01} for mode 01 as $\alpha = D_{01}\omega_{01}^*$, the frequency response function may be written as [58],

$$H_{01}(\omega) = \frac{1}{\left[1-\left(\frac{\omega}{\omega_{01}^*}\right)^2(1+\beta_c)\right] + i2D_{01}\left(\frac{\omega}{\omega_{01}^*}\right)(1+\beta_r+\beta_v)} \qquad (5.87)$$

in which β_c = the cavity ratio (the same as found in Chapter 4 in free vibration analysis, which represents an additional mass effect on the system)

$$= \frac{\rho \ell' a^2}{mNa_o^2} = 1.2 - 1.7\,\frac{\rho a^2}{mNa_o}$$

β_r = the acoustic damping ratio which derives from the radiated wave due to the vibration of the roof

$$= \frac{\rho c_o}{2D_{01} m\omega_{01}^*} = \frac{\rho c_o}{C} \qquad (5.88)$$

β_v = the aerodynamic damping ratio due to the velocity of wind stream relative to the roof movement

$$= \frac{\rho C_q \bar{V}(z)}{2D_{01} m\omega^*_{01}} = \frac{\rho\, C_q \bar{V}(z)}{C} \qquad (5.89)$$

where C = the damping coefficient of the roof and D_{01} its structural damping ratio for mode 01 and ω^*_{01} = natural frequency of mode 01 vibrating in vacuo.

Thus, it is assumed that the aerodynamic damping ratio is related to the flow velocity V(z,t) via the pressure coefficient C_q. This coefficient depends on the shape of the building and on the aspect ratio, $\bar{H}/D$. For high $\bar{H}/D$, the whole roof may vibrate in the wake while for a low $\bar{H}/D$, the flow may reattach over a large proportion of the roofs. Little information on the coefficient C_q is available and further research is needed.

The square of the response frequency function modulus (the mechanical admittance), for the fundamental mode of vibration, may be written as:

$$|H_{01}(\omega)|^2 = \frac{1}{[1-(\frac{\omega}{\omega^*_{01}})^2(1+\beta_c)]^2+4D^2_{01}[(\frac{\omega}{\omega^*_{01}})(1+\beta_r+\beta_v)]^2} \qquad (5.90)$$

The effect of the air within the enclosure with openings is accounted for by the cavity ratio β_c, and the effect of the acoustic damping of the system in the additional damping ratio β_r. The effect of the air stream on the unenclosed side is included in the aerodynamic damping ratio β_v.

If the area of the openings (NA_o) tends to infinity, the cavity ratio $\beta_c \to 0$, and the membrane (or roof) vibrates as if in vacuo (i.e., $\omega_{01} = \omega_{01}^*$, the natural frequency of vibration in vacuo). If the mass of membrane per unit area is large enough, the additional acoustic damping ratio β_r is small and the effect of the roof movement in producing an acoustic damping pressure may be ignored.

Finally, if either the pressure coefficient and/or the velocity of air is small with respect to a large mass per unit area of the roof, the aerodynamic damping is negligible; however, if the mass of the roof is light with respect to high pressure coefficients and/or high wind speeds, the aerodynamic damping ratio is significant.

According to the studies by Wardlaw, Irvine et al. [123] and Campbell [124], the effective mass of the vibrating roof should include the "added mass" of the air. Closed form formulae for this added mass are available [123,124].

CHAPTER 6

EXPERIMENTAL STUDY

6.1 INTRODUCTION

In many structural engineering problems an experimental study becomes necessary because either the problem is too complex for theoretical treatment or the analysis is too expensive. Further, no theories can be called exact because they are based on simplifying assumptions and approximations, and an experimental study may be essential to provide verification of a theory.

The design of a cable roof is quite often dictated by functional and architectural requirements and one is faced with a structure which may be both large and complex.

For a majority of cable roofs it would be difficult to determine wind-pressure coefficients using theoretical considerations. Therefore, a wind tunnel study of a roof model seems to be the best solution to determination of the roof pressure as well as for assessment of aerodynamic behaviour. It is for this purpose that roof models are used most. Another useful application is the evaluation of damping; here, a roof model permits a more realistic analysis for the dynamic response of the structure.

6.2 WIND TUNNEL MODELLING

The basis of all wind tunnel work is the hypothesis that all wind forces and structural reactions can be scaled in some proportion to wind conditions with structural scale factors. In every case, a dimensional analysis of all variables yields a proportionality constant which is a function of dimensionless groups of the variables.

Once a unique relationship has been established between the proportionality constant and its dimensionless groups, values of the constant are found, by experiment, for different values of the dimensionless number. If more than one number is involved, each relationship is found separately.

In many cases, the scaling requirements for one dimensionless correlation make it difficult or impossible to scale another one correctly. In addition, the wind tunnel itself limits the range of variables and certain assumptions are then made.

6.2.1 Laws of Similarity

The similarity requirements in model design which need to be satisfied in order that the results of tests carried out in a wind tunnel represent the behaviour of

a full-scale prototype in the natural wind will vary according to the problem under investigation. To achieve similarity, it is necessary to represent in the wind tunnel the relevant physical properties of both the structure and the natural wind.

The Laws of Similarity may be determined by the method of dimensional analysis or by a theoretical solution if it is available. Provided that all physical quantities are incorporated into the analysis, the method provides the functional relationship between the dimensionless values of the quantities and yields the Similarity Laws which permit full-scale predictions to be made from model test results. It can be assumed that the behaviour of structures under steady uniform wind conditions will depend on the aerodynamic shape and on the following eight physical properties:

$$E,\ \rho,\ V,\ D,\ \mu_o,\ g,\ \sigma,\ \delta_s$$

in which ρ, V, μ_o = density, velocity and dynamic viscosity of air; E, D, σ = modulus of elasticity, typical dimension and density of structure; δ_s = logarithmic decrement (structural damping parameter) and g = gravitational acceleration. (The compressibility of the air characterized by Mach number is, in general, also a factor but is not considered to be significant for the present study.)

From these eight quantities, five dimensionless parameters were derived [112]:

1. Logarithmic Decrement $\delta_s = \frac{\text{Energy dissipated per cycle}}{\text{Total energy of oscillation}}$

2. Elasticity Number $\frac{E}{\rho V^2} = \frac{\text{Elastic forces of the structure}}{\text{Inertia forces of the air}}$

3. Density Ratio Number $\frac{\sigma}{\rho} = \frac{\text{Inertia forces of the structure}}{\text{Inertia forces of the air}}$

4. Gravitational Number $\frac{gD}{V^2} = \frac{\text{Gravitational forces of the structure}}{\text{Inertia forces of the air}}$

5. Reynolds Number $\frac{\rho VD}{\mu_o} = \frac{\text{Inertia forces of the air}}{\text{Viscous forces of the air}}$

The dimensionless parameters 2 and 3 lead to the Strouhal Number (dimensionless frequency) $\frac{fD}{V}$ or its inverse, the dimensionless (reduced) velocity, V/fD. The Similarity Laws between model and prototype require, ideally, that all lengths, masses and times characterizing the prototype and natural wind satisfy the following ratios:

$$\frac{L_{1m}}{L_{1P}} = \frac{L_{2m}}{L_{2P}} = \ldots = \frac{\text{Dimensions of Model}}{\text{Dimensions of Prototype}} = \lambda_L \qquad (6.1)$$

$$\frac{M_{1m}}{M_{1P}} = \frac{M_{2m}}{M_{2P}} = \ldots = \frac{\text{Mass of Model}}{\text{Mass of Prototype}} = \lambda_M \qquad (6.2)$$

$$\frac{T_{1m}}{T_{1P}} = \frac{T_{2m}}{T_{2P}} = \ldots = \frac{\text{Time for Model}}{\text{Time for Prototype}} = \lambda_T \qquad (6.3)$$

in which λ_L, λ_M, λ_T = the length, mass and time scale respectively and subscript (m) referred to the model and

(P) to the prototype.

6.2.2 Types of Models

The five dimensionless parameters stated previously may be used in various combinations for different types of wind tunnel tests. The family of models obtained from various combinations may be categorized into two main types: rigid and aeroelastic models.

The rigid model is mainly used to measure the wind pressures and forces, while the aeroelastic model is used to measure the deflections and stresses induced by the wind forces.

6.3 MODELLING STUDY

It was stated that cable structures are prone to aerodynamic excitation or flutter since they are inherently flexible. The unusual feature of the experimental investigation is that it focuses on the dynamic behaviour under wind action of a membrane-like and wind-sensitive structure: a flexible roof of very large size. Two types of experimental work have to be considered important.

First, a rigid model is used to yield the aerodynamic pressure distribution on the exterior and interior surfaces of the roof for a variety of wind directions. From this information, the steady-state wind loads on the roof can

be calculated for any wind speed and direction.

Second, an aeroelastic model is employed to examine the possible aeroelastic response which could be induced by either turbulent (gusty) wind or periodic flow fields (vortex shedding) set up by the tension roof itself. The aeroelastic model studies can be extended to study the interaction between the roof movement and the external wind pressure and internal air pressure within the enclosure.

6.3.1 Aeroelastic Model Scaling

In practice, it is rarely possible to satisfy all the five dimensionless parameters mentioned earlier and to model the boundary layer of the earth accurately.

The Reynolds number is very important and it is difficult to achieve in the wind tunnel. It had been shown by tests carried out over a wide range of Reynolds numbers that the air flow pattern around a sharp-edged body is substantially independent of this parameter because the positions of flow separation are fixed by the sharp edges [112]. For some angles of attack, suspension roofs fall within this category but at other angles of attack, for certain types of suspension roofs, the effect of the Reynolds number may be significant.

For the observation of static deflection and stresses due to wind, only the elastic and gravitational parameters need to be considered, but for dynamic studies, both the inertial and the damping parameters have to be taken into account as well.

Therefore, similarity of inertial, elastic and damping forces for cable tension roofs requires equality of the following dimensionless quantities:

1. Similarity of inertial effects - $\frac{\sigma}{\rho}$,

2. Similarity of elastic effects - $\frac{E}{\rho V^2}$,

3. Similarity of structural damping - δ_s.

The model must have an external shape exactly corresponding to the full-scale although true reproduction of internal structural details is not necessary, provided that inertial and elastic stiffness requirements can be maintained.

Model and full-scale air densities are the same for tests in atmospheric wind tunnels and therefore, the structural densities at all corresponding positions must be the same on the model and the prototype.

6.3.1.1 The Mass Density Scaling

The density ratio parameter, which includes the effect

of the inertial requirement, can be rewritten in the form

$$\frac{\sigma}{\rho} \equiv \frac{M}{\rho D^3} \tag{6.4a}$$

Hence,

$$[\frac{M}{\rho D^3}]_m = [\frac{M}{\rho D^3}]_P = [\frac{M}{\rho D \times D^2}] \tag{6.4b}$$

in which M = the total mass. Therefore, the mass per unit area (m) scaling $\lambda_m = \lambda_L$ (where $\lambda_m = \frac{m_m}{m_P}$).

6.3.1.2 The Elasticity Scaling

In order that the elasticity parameter be compatible with the prescribed mass density scaling, the following relationship should be satisfied:

$$[\frac{E}{\rho V^2}]_m = [\frac{E}{\rho V^2}]_P \tag{6.5}$$

Suitable materials are not usually available and compromise has to be made to yield an equivalent stiffness effect for pure membrane action; therefore, elastic similarity implies similarity of the tension force per unit length. An alternative form of the elasticity parameter, when the elastic energy is basically extensional, may be derived as follows:

Multiply the elasticity parameter by h/D.

$$\left[\frac{E}{\rho V^2}\frac{h}{D}\right]_m = \left[\frac{E}{\rho V^2}\frac{h}{D}\right]_P \tag{6.6}$$

Therefore, when $[h/D]_m = [h/D]_P$:

$$\frac{[Eh]_m}{[Eh]_P} = \lambda_V^2 \lambda_L \tag{6.7}$$

where h is the membrane thickness, D is a characteristic building length and λ_V is velocity scaling. Therefore, the tension per unit length scaling is:

$$\lambda_{T_o} = \frac{[Eh]_m}{[Eh]_P} = \lambda_{Eh} = \lambda_V^2 \lambda_L \tag{6.8}$$

6.3.1.3 The Dynamic Stiffness Scaling

A cable roof structure is usually closed and has openings (windows and doors); the air movement through them due to roof movement affects the frequency characteristics of the roof, especially the frequency of those modes which cause a change in the air volume of the cavity. This change in volume is accompanied by a change in pressure of the air inside the enclosure. As the roof vibrates, the air inside the enclosure is alternatively compressed and expanded. During the compression action, a volume of air moves out through the opening and, during the expansion, a volume of air moves in. The problem of a vibrating tension roof enclosed by a cavity has been briefly studied by the author [108], and expanded in this work. It was found that a dimensionless constant

($\alpha_o = \frac{\pi a^4 \rho c_o^2}{T_o V_o}$), measures the relative importance of the restoring force owing to the compression of the air in the enclosure and to the initial tension applied to the membrane. In the formula, ρ = air density, c_o = speed of sound in air, a = horizontal dimension of the membrane, T_o = initial tension in the membrane per unit length and V_o = the original volume of the enclosure.

Although a few papers have been published in aeronautical journals on the effect of enclosed cavities on the vibrations of panels, little information is available on this effect in the structural engineering and wind tunnel modelling literature. In fact, there are indications that the modelling requirements for the correct simulation of internal volume effects have been overlooked in some tests of pneumatic structures; however, the importance of scaling the acoustic stiffness of volumes enclosed by such structures [113] has to be emphasized.

From the above-stated theoretical analysis by the author (in this work and in [108]), the volume scaling may be derived as follows:

$$\left[\frac{a^4 \rho c_o^2}{T_o V_o}\right]_m = \left[\frac{a^4 \rho c_o^2}{T_o V_o}\right]_p \qquad (6.9)$$

Since ρ, c_o are the same for model and prototype, the above relation may be rewritten as

$$[\frac{a^4}{T_o V_o}]_m = [\frac{a^4}{T_o V_o}]_P \tag{6.10}$$

Therefore, the volume scaling may be written as,

$$\lambda_{V_o} = \frac{V_m}{V_P} = \lambda_L^4/\lambda_{T_o} \tag{6.11}$$

Substitute for the tension per unit length scaling:

$$\lambda_{T_o} = \lambda_V^2 \lambda_L$$

the volume scaling is

$$\lambda_{V_o} = \lambda_L^3/\lambda_V^2 \tag{6.12}$$

This volume scaling, required to ensure similarity of the dynamic stiffness of the membrane, implies that the model volume has to be exaggerated by $1/\lambda_V^2$ beyond that required by the overall length scale, where λ_V is the velocity scaling.

It is interesting and significant that the same scaling relationship has been arrived at by Tryggvason and Isyumov [113] in considering the modelling of inflatable structures, and by Holmes [114] in his study for scaling the fluctuating internal pressures inside buildings, using a completely different analysis.

6.3.1.4 Summary of Aeroelastic Scaling Requirements

With the above considerations, the aeroelastic modelling requirements for tension cable roofs can be summarized as follows:

(i) Similarity of turbulent boundary layer flow defines the length scale λ_L

(ii) Scaling of all exterior dimensions of the structure according to λ_L

(iii) Scaling of internal volume according to $\lambda_{V_o} = \lambda_L^3/\lambda_V^2$

(iv) Scaling of mass per unit area of the cable roof as $\lambda_m = \lambda_L$ to achieve similarity of inertia forces

(v) Elastic similarity based on tension per unit length scaling

$$\lambda_{T_o} = \lambda_{EH} = \lambda_V^2 \lambda_L$$

(vi) Similarity of structural damping $\delta_s = 1$.

6.3.2 Rigid Model Scaling

The rigid model simulation is straightforward. It is achieved by maintaining the length scale λ_L and duplicating the exact external shape of the prototype.

Regarding the internal shape, it is difficult and not worthwhile to simulate the internal details, but the exaggerated volume scale, $\lambda_{V_o} = \lambda_L^3/\lambda_V^2$, should be maintained,

as in the aeroelastic volume modelling, if the internal pressure coefficients are to be measured.

6.4 THE PROTOTYPE

An example of the structure, which aroused considerable attention, is the suspension roof of the Calgary Olympic Coliseum, to be built in Calgary, Canada [32].

The proposed envelope of the Coliseum is generated from a sphere of 67.195 m radius. The base is bounded by a circle of 60 m radius, and the roof by a hyperbolic paraboloid membrane, a saddle shape (Figures 6.1 and 6.2).

The high points of the roof lie at the extreme longitudes of the equator; the low points on a zero meridian, at right angles to the meridian passing through high points, at angles of 17° southern altitude.

The membrane of the roof, a 10 cm thick equivalent lightweight concrete ribbed shell, is supported by a perimeter ring and an orthogonal cable net of double curvature. Vertical sections of the roof along the principal, perpendicular, directions are identical parabolas - concave in one direction and convex in the other.

In plan, the roof is an ellipse, with a major axis

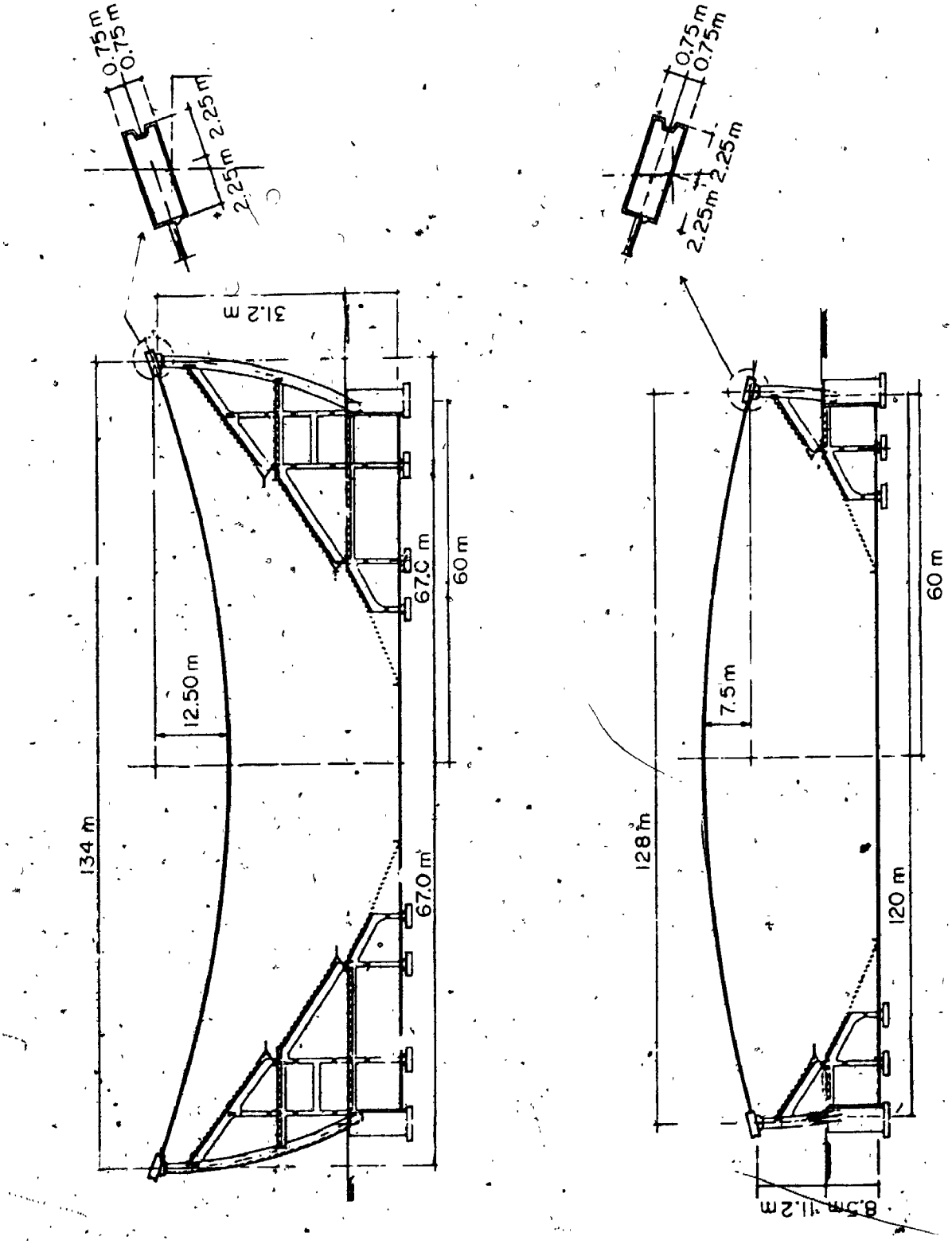

FIGURE 6.1 Elevation Views of The Calgary Olympic Coliseum [32]

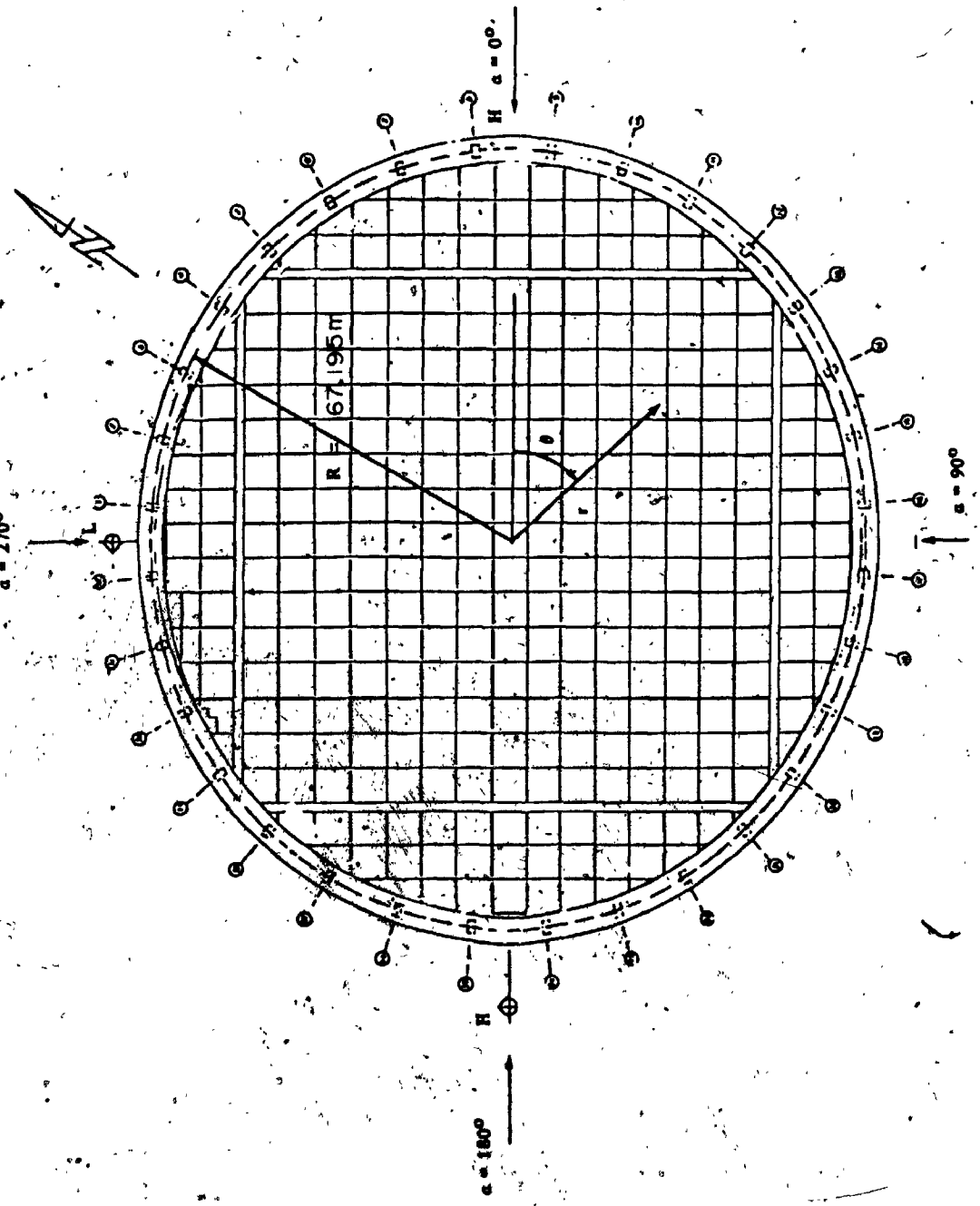

FIGURE 6.2 Plan View of the Calgary Olympic Coliseum [32]

of approximately 134 meters and a minor axis of 128 meters. The sag along the major axis is 12.5 m, followed by further drop along the hogg, on the minor axis, of 7.50 m, giving a total difference between high and low point of 20 m.

The roof is generated by a net of orthogonal cables spaced at 6 m in both directions. They are anchored in the perimeter beam, which is hollow inside and has an overall cross-section 1.50 x 4.5 m. Cable net supports lightweight concrete precast ribbed panels. These are interconnected by grouting the joints to form a monolithic membrane.

The cables are made of high strength steel and are prestressed in stages, as required, to control forces and stresses in the ring beam. The ring beam is supported on precast concrete columns which have slight but constant curvature. There are 32 perimeter columns. At the base, the columns are equally spaced along the perimeter. At the top, they support the ring beam, the horizontal projection of which is an ellipse.

The roof is insulated and is covered with plastic waterproofing membrane. The mass per unit area of the roof is 1.428 slug/ft^2 (= 6.97 Kg/m^2) of which

- the cable net = 0.093 slug/ft^2 (= 0.454 Kg/m^2)
- the roof shell = 1.335 slug/ft^2 (= 6.516 Kg/m^2)

A rigid model of the structure described was investigated in great detail in the Boundary Layer Wind Tunnel Laboratory [89]. To complement this program, the author undertook a study in which two aeroelastic models were used to predict the response to wind loading, and to study the interaction between roof movement, external wind pressure and the air pressure in the enclosure. The first, a simplified model, reproduced the basic dimensions, mass and stiffness but replaced the hyperbolic paraboloid by a shallow (flat) roof and the elliptical plan by a circle. The advantage of this simplification was that the approximate model was more amenable to the theoretical analysis in Chapter 4. The second model reproduced the prototype correctly.

6.5 CONSTRUCTION OF MODELS

The selection of the modelling scales is governed by roof membrane material available and the scale of the boundary layer wind tunnel.

The wind tunnel facility at the Boundary Layer Wind Tunnel Laboratory at The University of Western Ontario in London, Canada is capable of modelling the atmospheric

boundary layer at length scales ranging from about 1:300 to about 1:500 [113]. Within these bounds, the choice of the length scale is determined by available model membrane materials to correctly scale the mass per unit area and result in a velocity scale determined by elastic properties. This would permit wind tunnel testing over a representative range of wind speeds.

6.5.1 The Aeroelastic Models

An extensive study of material properties of various available membranes was carried out before the final length scale was determined. The overall length scale λ_L had to remain compatible with the length scales of the modelled wind.

A 0.01 inch (= 0.254 mm) thick TFE (Tetrafluoro-ethylene) membrane was chosen. This material [115] satisfied the mass scaling at a geometry scaling of λ_L = 1:384 and permitted a suitable velocity scale based on similarity of elastic properties.

A summary of the various other scaling parameters is presented in Table 6.1 and numerical values for the hyperbolic paraboloid model and the prototype scaling are given in Table 6.2.

TABLE 6.1 SUMMARY OF AEROELASTIC SCALE PARAMETERS

No.	Parameter	Aeroelastic Scaling	Numerical Value
1	Length	$\lambda_L = L_m/L_P$	0.002604 (1:384)
2	Mass/Unit Area	$\lambda_m = \lambda_L$	0.002604
2	Weight/ Unit Area	$\lambda_w = \lambda_L$	0.002604
4	Tension/ Unit Length	$\lambda_T = \lambda_L \lambda_V^2$	1.042×10^{-4}
3	Velocity	$\lambda_v = V_m/V_P$	0.20 (1:5)
5	Internal Volume	$\lambda_V = \lambda_L^3/\lambda_V^2$	4.414×10^{-7}
6	Density	$\lambda_\rho = \rho_m/\rho_P$	1.0
7	Time	$\lambda_t = \lambda_L/\lambda_V$	0.013 (1:76.8)
8	Force	$\lambda_F = F_m/F_P = \lambda_L^2 \lambda_V^2$	2.788×10^{-7}
9	Pressure	$\lambda_p = \lambda_F/\lambda_L^2 = \lambda_V^2$	0.04 (1:25)

TABLE 6.2 AEROELASTIC MODEL SCALING

No.	Parameter	Full Scale		Aeroelastic Model	
		Quantity	Dimension	Quantity	Dimension
1	Roof diameter (Average)	416	ft	13	inch
2a	Height (Sag)	110	ft	3.50	inch
b	Height (Hogg)	50	ft	1.50	inch
3	Equivalent Roof Thickness	4	inch	0.01	inch
4	Modulus of Elasticity (Light weight concrete)	1.50×10^6	psi	0.60×10^5	psi
5	Weight per unit area	46	lb/sq.ft	0.12	lb/sq.ft
6	Mass per unit area	1.428	slug/sq.ft	0.0037	slug/sq.ft
7	Gradient Velocity	100	MPH	29.33	ft/sec
8	Fundamental Frequency	0.3458	Hz(cps)	26.556	Hz(cps)
9	Enclosure Volume	9.0×10^7	cu.ft	6.86×10^3	cu.in.

(1 ft = 0.3048 m ; psi = 6895 N/m^2 ; lbf = 4.448 N ; slug = 0.4536 kg)

The aeroelastic models were designed and constructed to satisfy exactly the various similarity requirements presented in section 6.3.1.4. The plan view of this model is shown in Figure 6.3. The walls of the model are rigid, made from aluminum material, and reproduce only the exterior geometry. The model roof, made from TFE (Tetrafluoroethylene) membrane, is attached to the walls by a clamping ring made of rigid plexiglass, giving the correct overall geometry of surface of the ring beam in the prototype, Plate 6.1. Another ring is designed by which the tension in the membrane can be adjusted (Figure 6.3).

A scaled pressure chamber was mounted below the model to exaggerate the enclosed volume as required by the internal volume scaling. The pressure chamber was sealed to prevent any air leakage by inserting a rubber strip between the model base and the chamber flange. Baffles were placed into this volume in order to avoid any acoustic resonance.

In order to study the surrounding air-roof interaction, which in some aspects is more general, a simplified model of the Calgary roof was designed. This simplified model reproduces the basic dimensions, mass and stiffness but replaces the hyperbolic paraboloid by a shallow, flat roof and the elliptical plan by a circle. The advantage

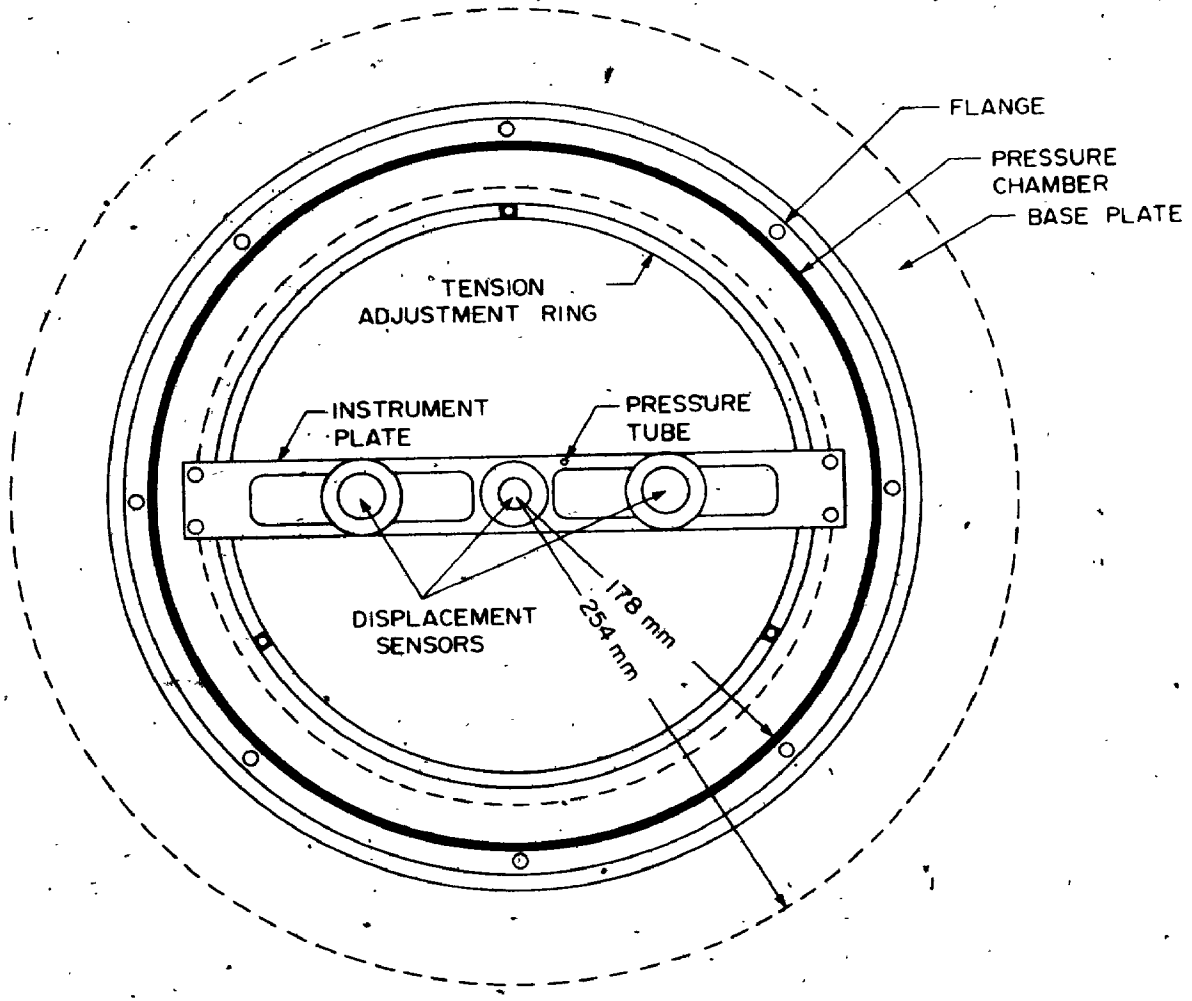

FIGURE 6.3 PLAN OF CABLE ROOF MODELS, DIMENSIONS AND INTERNAL INSTRUMENT ARRANGEMENTS

PLATE (6.1) Aeroelastic Model of the Calgary Olympic Coliseum (λ: 1:384)

of this simplification is that the approximate model is more amenable to the theoretical analysis, conducted in Chapters 4 and 5.

The numerical values of parameters for this simplified model and the averaged prototype geometrical scaling are given in Table 6.3. The same pressure chamber was used in both models. Plan and elevation views of this simplified model are shown in Figures 6.3 and 6.4. Furthermore, in order to simulate the existence of openings in the prototype (doors and windows), nine circular holes of 3/4 inch (≃ 19 mm) diameter each are drilled in the walls of the simplified model, Plate 6.2.* This allowed study of the effect of air movement through the openings on the frequency characteristics of the roof and the total damping ratio of the system.

6.5.2 Sensing Devices Used in Experiment

The sensing devices used to measure the vertical displacements were Kaman non-contact reactance sensors of the displacement type. These devices measure change in reactance of the air gap between the vibrating surface and the probe plate. To improve the conductivity of the TFE membrane, a small piece of metal aluminum foil is attached to the internal surface of the membrane at the

* For the Calgary coliseum the estimated leakage rate corresponds to the wall area parameter of about 5 to 8%.

TABLE 6.3 SIMPLIFIED AEROELASTIC MODEL SCALING

No.	Parameter	Full Scale		Simplified Aeroelastic Model	
		Quantity	Dimension	Quantity	Dimension
1	Roof diameter (average)	416	ft	13	inch
2	Height (average)	80	ft	2.50	inch
3	Equivalent Roof Thickness	4	inch	0.01	inch
4	Modulus of Elasticity	1.5×10^6	psi	0.6×10^5	psi
5	Weight per Square Foot	46	lb/sq.ft	0.12	lb/sq.ft
6	Mass Per Square Foot	1.428	slug/sq.ft	0.0037	slug/sq.ft
7	Gradient Velocity	100	MPH	29.22	ft/sec
8	Fundamental Frequency	0.3458	Hz (cps)	26.556	Hz (cps)
9	Enclosure Volume	9.0×10^7	cu.ft	6.86×10^3	cu.inch

(1 ft = 0.3048 m ; psi = 6895 N/m^2 ; lbf = 4.448 N ; slug = 0.4536 kg)

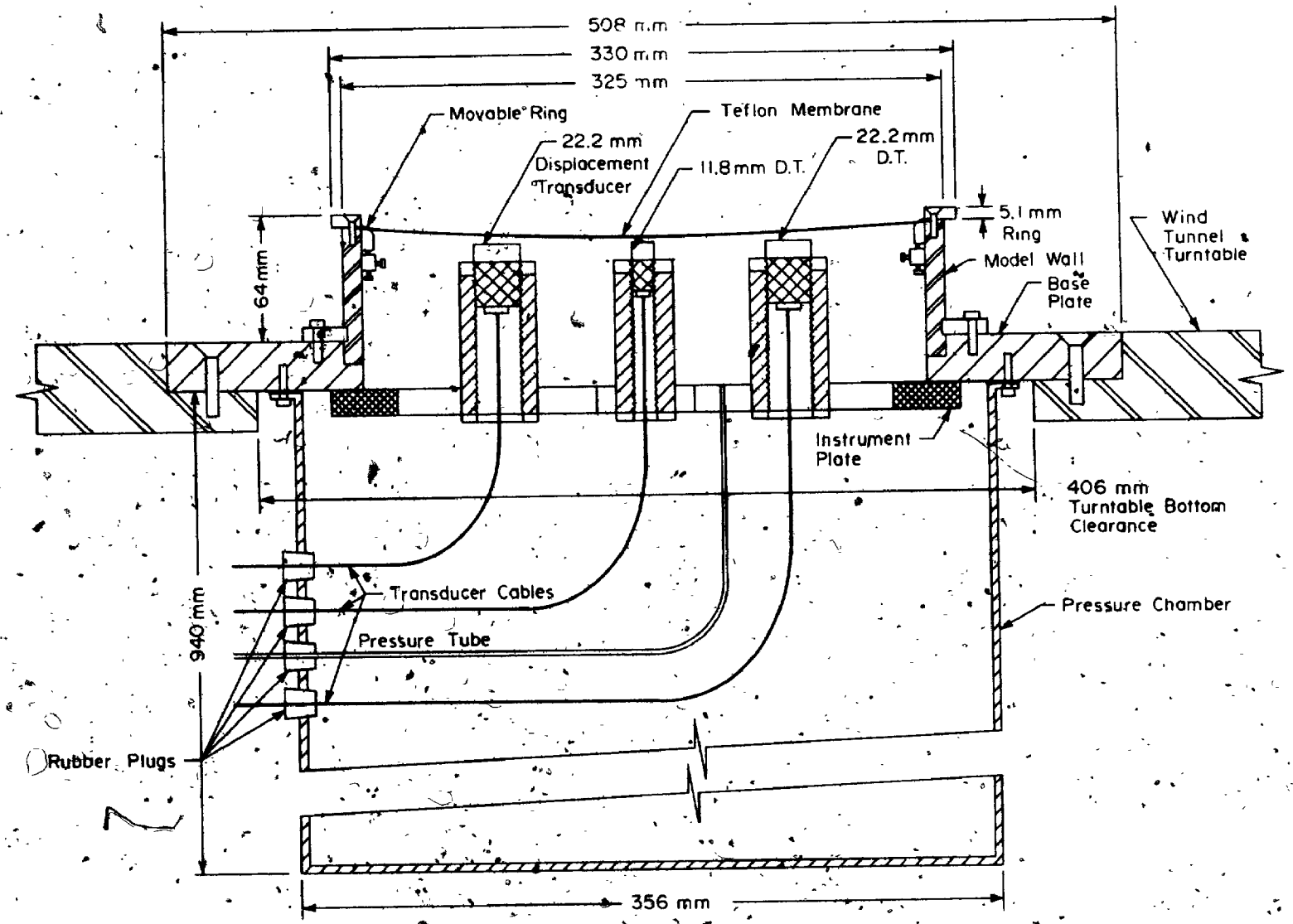

FIGURE 6.4 CROSS SECTION OF SHALLOW CIRCULAR GABLE ROOF MODEL

Plate (6.2) Simplified Aeroelastic Model

location of each Kaman probe. The Kaman sensors are calibrated each time they are used. The probes were located at the centre of the model and at an intermediate specific point of the base radius at distance r = 0.436a, Figure 6.5. The probe at the centre eliminated the asymmetrical modes f_{11} and f_{21} and the one at r/a = 0.436, eliminated mode f_{02}. Using the turntable in the wind tunnel floor, the latter position was related to θ = 0°, 45°, 90° with wind direction. This arrangement was done to separate the symmetric modes of vibration from the antisymmetric ones and to measure simultaneously the response at two points for cross-correlation analysis.

Due to instrumentation difficulties, the attempt to measure two records simultaneously failed and the response was measured separately.

6.6 EXPERIMENTAL TESTS

6.6.1 Simplified Aeroelastic Model

6.6.1.1 Experiments in Still Air

The model was first excited in still air by means of a loudspeaker, Figure 6.6 and Plates 6.3 and 6.4. It was observed that the first symmetric mode f_{01}, being the volume-displacing mode, is strongly dependent on the number of wall openings. It was found that the frequency of mode f_{01} is increased by increasing the number of

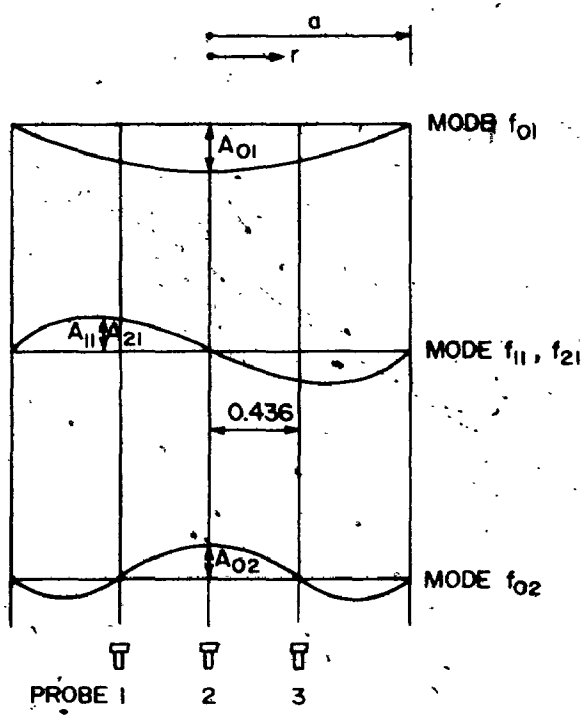

FIGURE 6.5. KAMAN DISPLACEMENT SENSORS ARRANGEMENT.

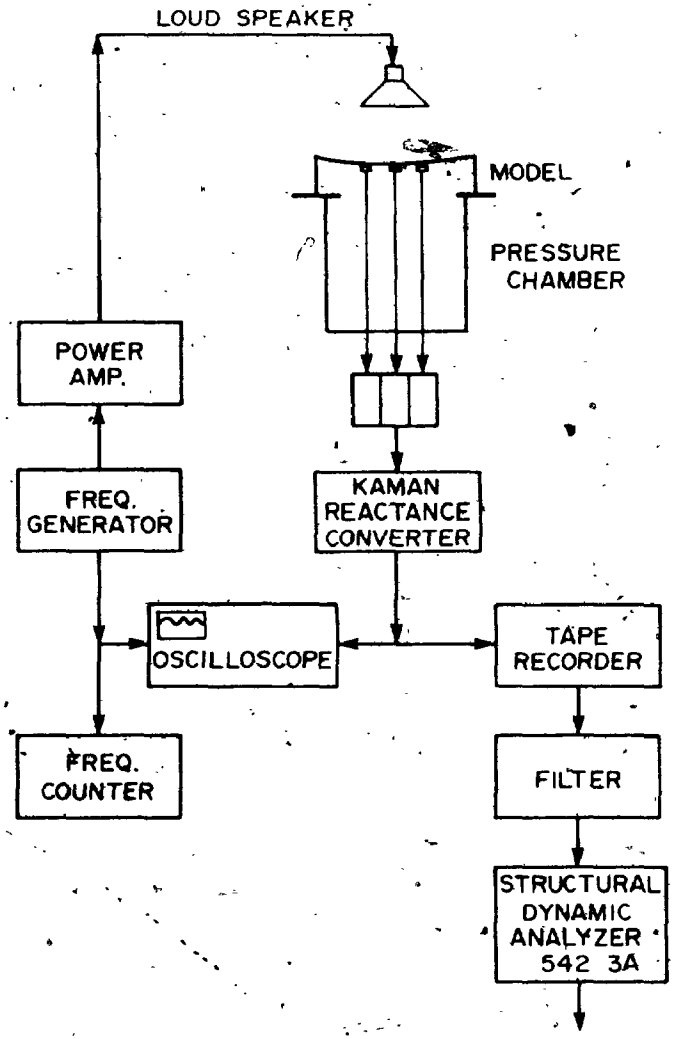

FIGURE 6.6. FREE VIBRATION EXPERIMENTAL SET-UP.

PLATE (6.3) Aeroelastic Model in Free Vibration Tests

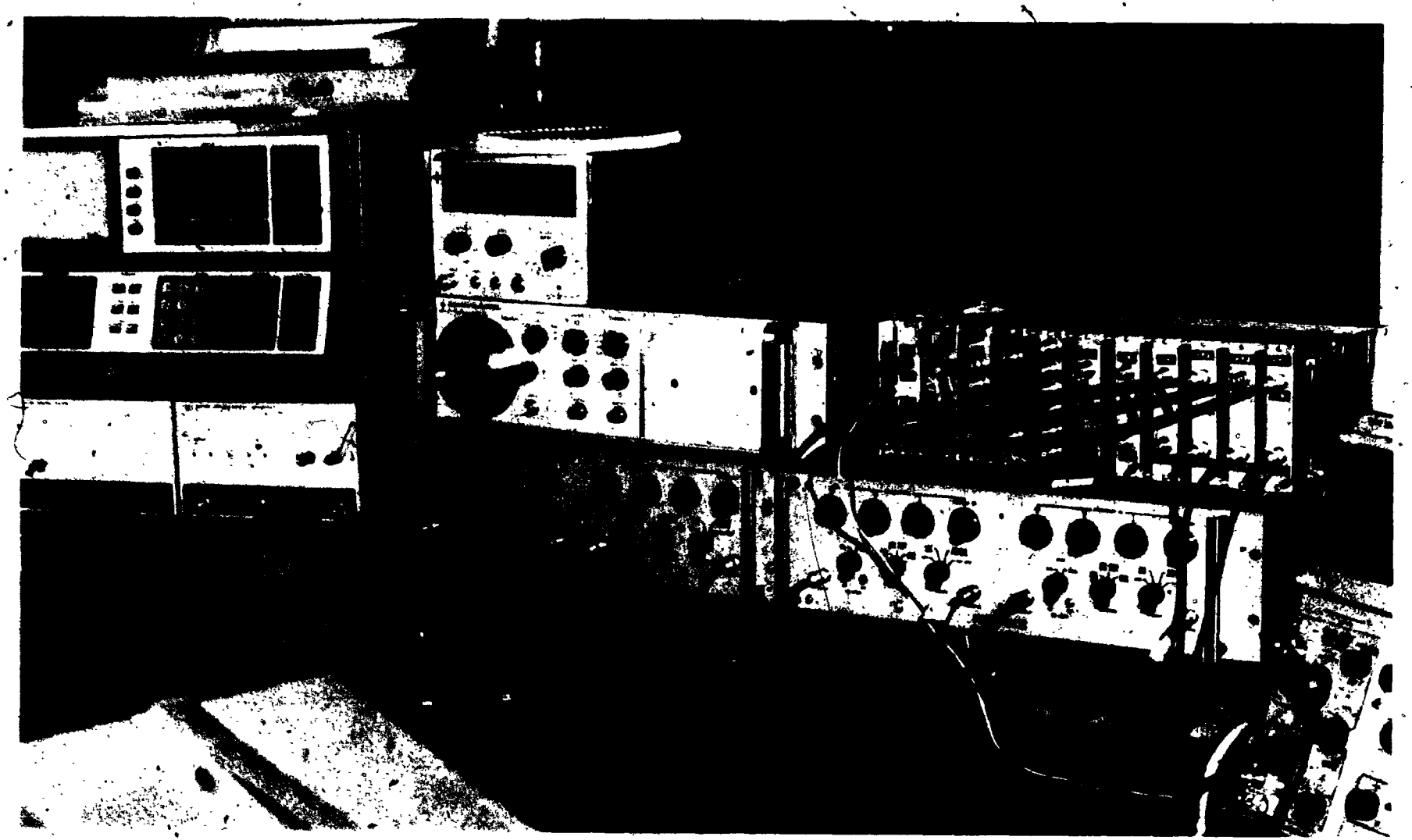

PLATE (6.4) Instrument Arrangement in Free Vibration Tests

openings while the other modes f_{11}, f_{21} and f_{02} were only slightly affected. The variation of the natural frequencies with the total area of openings is shown in Figure 6.7. The frequencies are plotted against the area parameter $\beta_a = (NA_o/A_c)x100$ in which N = number of openings, A_o = the area of one opening and A_c = the wall area. The natural frequencies were established from the spectra of the response to harmonic excitation for different openings and modes, Figure 6.7a. The spectra were obtained using the Structural Dynamics Analyzer 5423A of the Hewlett-Packard Co.

This analyzer also gives the total damping D_{nm}. The damping ratios found at different openings are presented in Table 6.4. This damping comprises all the material, structural and acoustical damping.

The acoustical damping is due to the movement of the membrane and is proportional to its velocity. As the frequency of mode f_{01} is decreased with the decrease of the area parameter β_a, the acoustic damping is decreased accordingly. The damping ratios of modes f_{11}, f_{21} and f_{02} are only slightly affected.

6.6.1.2 Wind Tunnel Tests

Flow Properties and Experimental Set-Up

The experiments were conducted in the Boundary Layer

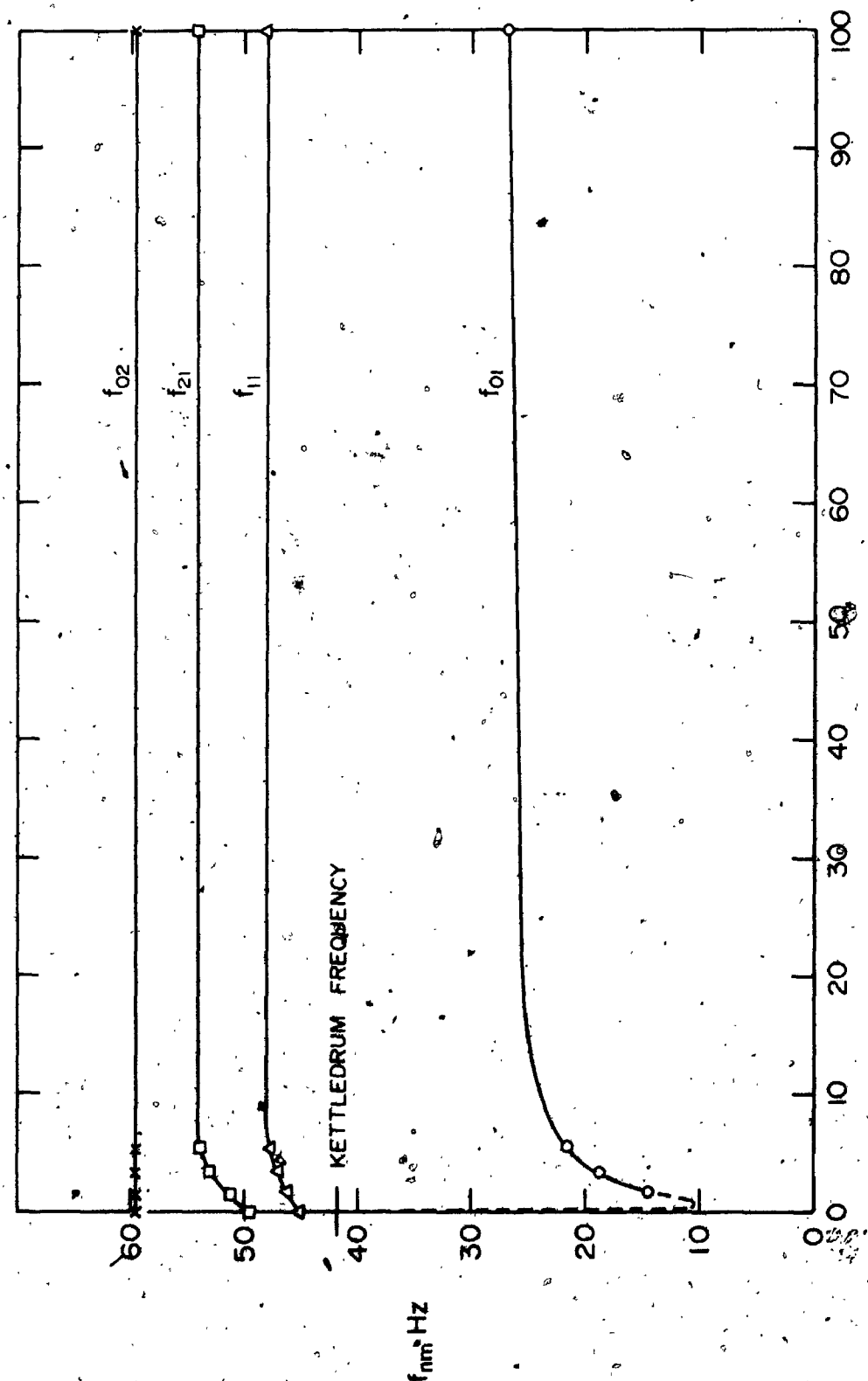

FIGURE 6.7 FREQUENCY OF MODES VERSUS AREA PARAMETER, IN FREE VIBRATION

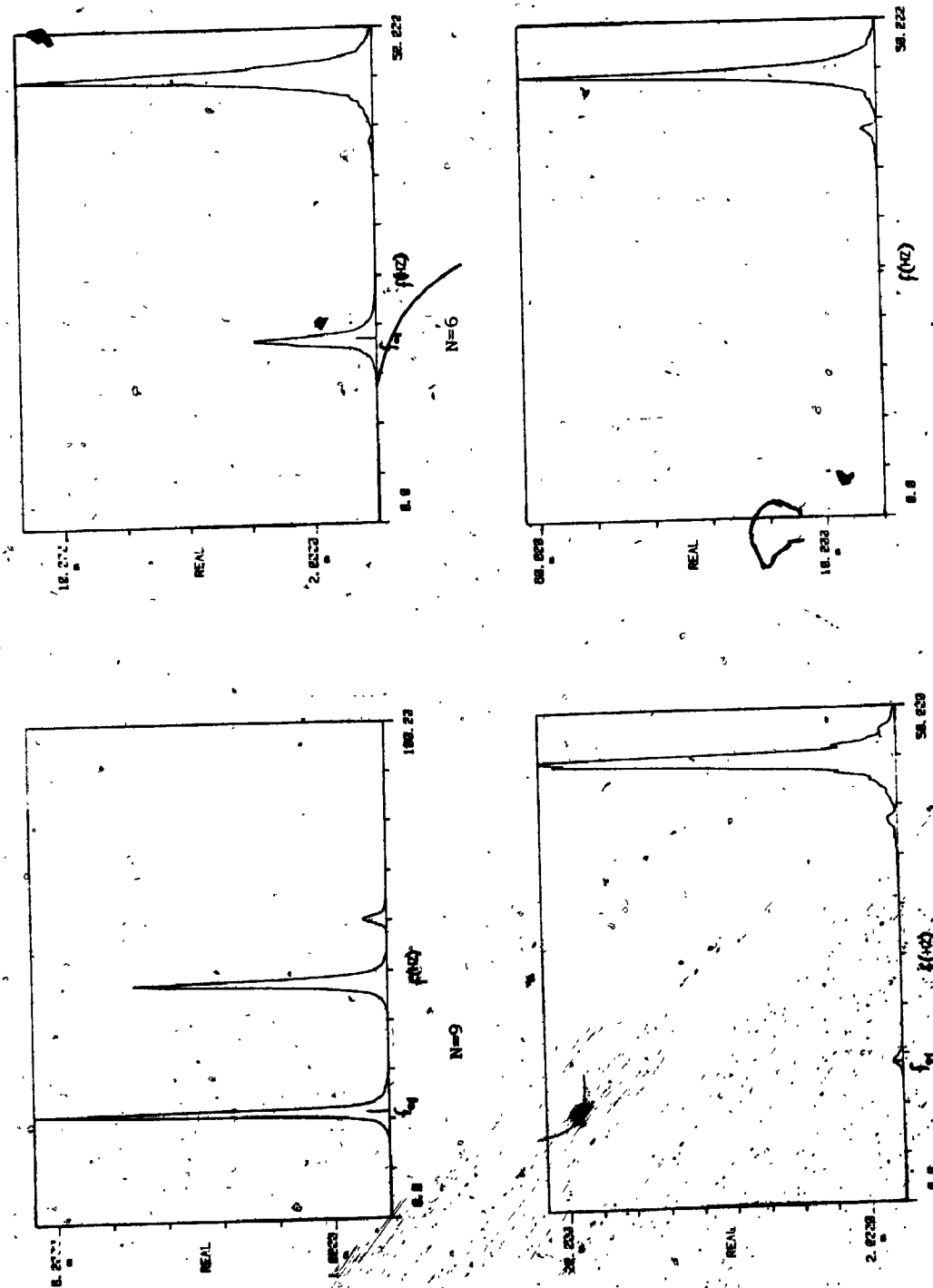

FIGURE 6.7a Spectra of Response to Harmonic Excitation for Different Openings (N)

TABLE 6.4 MODAL DAMPING RATIO AT DIFFERENT AREA PARAMETER β_a IN FREE VIBRATION TESTS

Number	Mode f_{nm}	Resonant Frequency Hz	Area Parameter $\beta_a = \frac{NA_o}{A_c} \times 100\%$	Damping Ratio D_{nm} %
1	f_{01}	26.556	Base open	3.110
2	f_{01}	21.402	5.30	2.565
3	f_{01}	18.931	3.54	2.616
4	f_{01}	14.523	1.78	2.22
5	f_{11}	48	Base open	-
6	f_{11}	47.586	5.30	1.389
7	f_{11}	46.922	3.54	1.343
8	f_{11}	46.075	1.78	1.466
9	f_{11}	44.914	0	1.053
10	f_{12}	52	Base open	0.668
11	f_{02}	54.766	5.3	1.306

Wind Tunnel Laboratory at The University of Western Ontario.

Two exposures were simulated at the wind tunnel floor. First, the tunnel floor was covered with randomly placed blocks of heights varying from 1/2 inch (= 12.7 mm) to 3 inches (= 76.2 mm) approximately, Plate 6.2.

The properties of the flow at the test section are shown in Figure 6.8, which shows the variation of mean wind speed velocity, $\bar{V}(z)$, and the standard deviation of the wind velocity fluctuation with height, $\sigma_v(z)$, at the test section. This velocity profile corresponds to the boundary layer of a built-up area [44], and its turbulence intensity is about 12% for V_G = 28.50 ft/sec (= 8.687 m/s) at the model height.

In the second phase of the experiments, the tunnel floor was covered with rough carpet. The properties of the flow at the test section for this exposure are shown in Figure 6.9, which also shows the variation of the mean wind velocity, $\bar{V}(z)$, and standard deviation of the wind velocity fluctuations with height, $\sigma_v(z)$, at the test section. This velocity profile corresponds to the boundary layer of open country area [44], and its turbulence intensity at the model height is about 8% for V_G = 31.30 ft/sec (= 9.54 m/s).

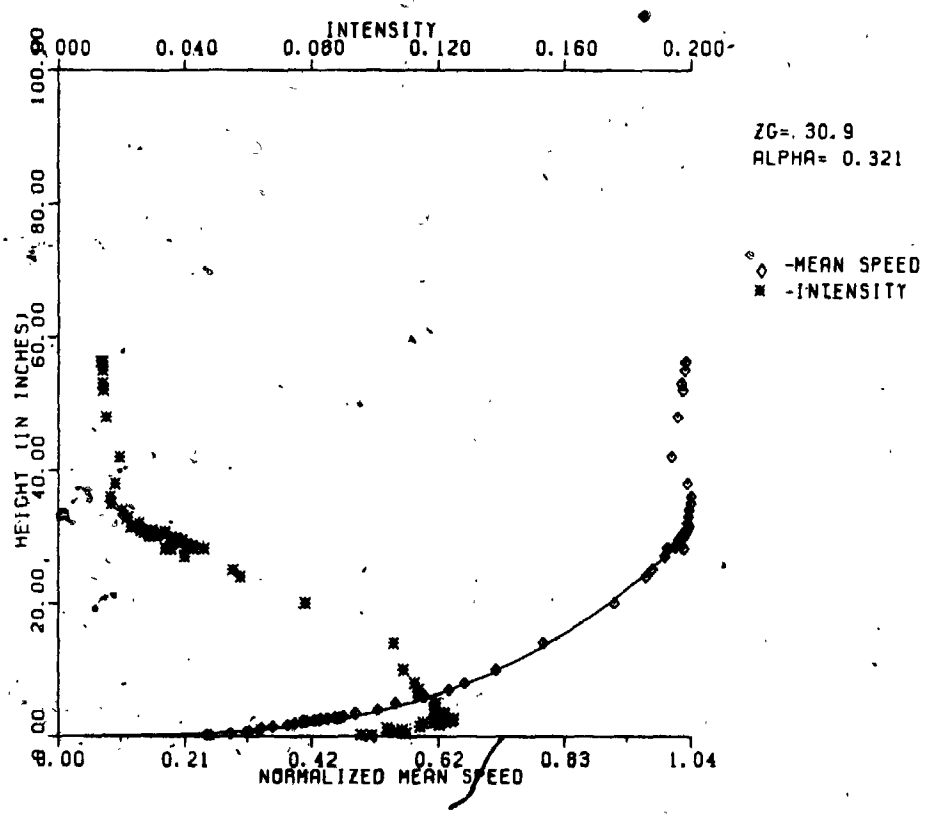

FIGURE 6.8 Wind Velocity Profile and Turbulence Intensity at Test Section (Built-Up Area, $\bar{V}_G$ = 28.5 ft/sec)

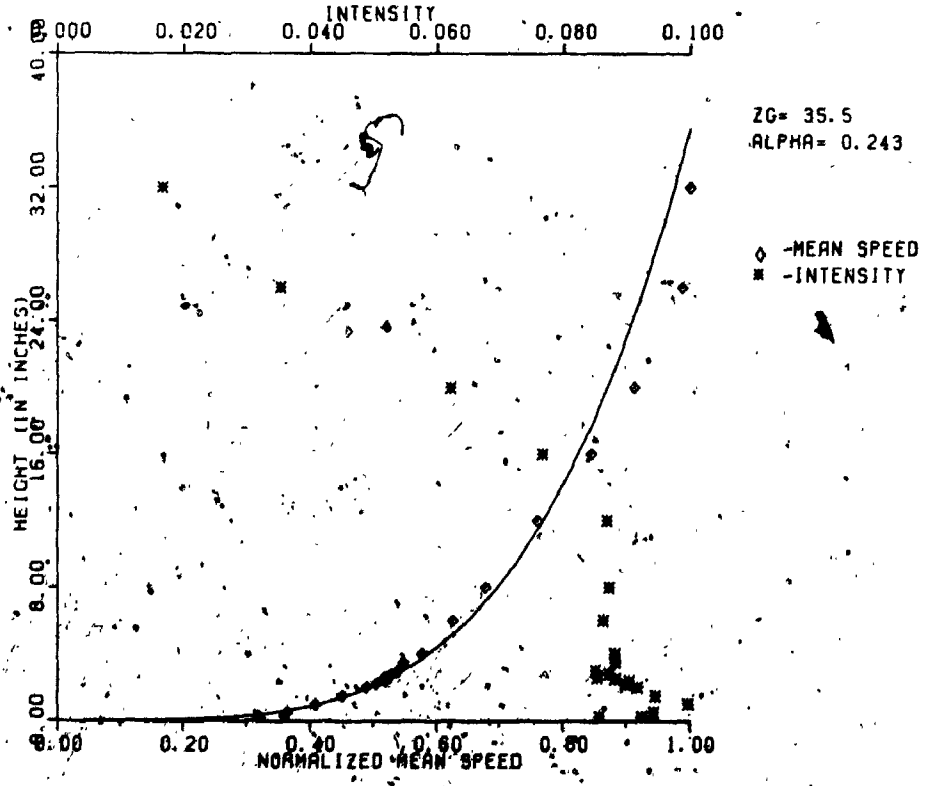

FIGURE 6.9 Wind Velocity Profile and Turbulence Intensity at Test Section (Open Country Exposure, $\bar{V}_G$ = 31.30 ft/sec)

The wind velocity was measured using a hot wire device. The spectrum of wind velocity at model height is presented in Figures 6.10 and 6.11 corresponding to built-up area and open country exposures respectively. The length scales calculated from the power spectrums were about 1 foot for built-up area and about 3.0 feet for open country exposure.

Measurements of membrane vertical displacement were made at the three different locations shown in Figure 6.5 using the Kaman probes. The output from the Kaman probes system was analyzed to determine the mean and the standard deviation of the response using a digital data acquisition system. The arrangement of the testing instruments is shown in Figure 6.12.

The HP 5423 A analyzer was employed for the computation of the autocorrelation functions. The number of correlation points sampled was 512 with a lag time interval of 0.60 milliseconds. The power spectrum of the membrane model response was obtained from the autocorrelation function by direct Fourier transformation. The mean response and the standard deviation were obtained after passing the total response signal into a digital acquisition system (PDP 11/60 computer).

To study the fluctuating internal pressure within

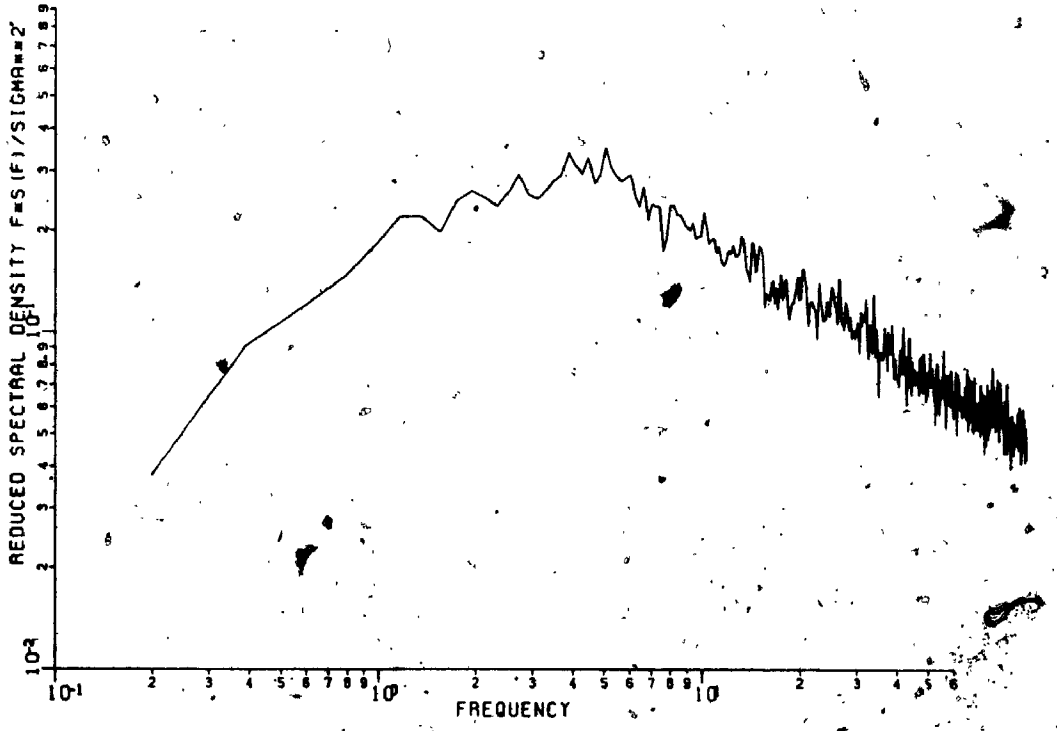

FIGURE 6.10 Power Spectrum of Velocity at Roof Height Level (Built-Up Area, $\bar{V}_G$ = 28.5 ft/sec)

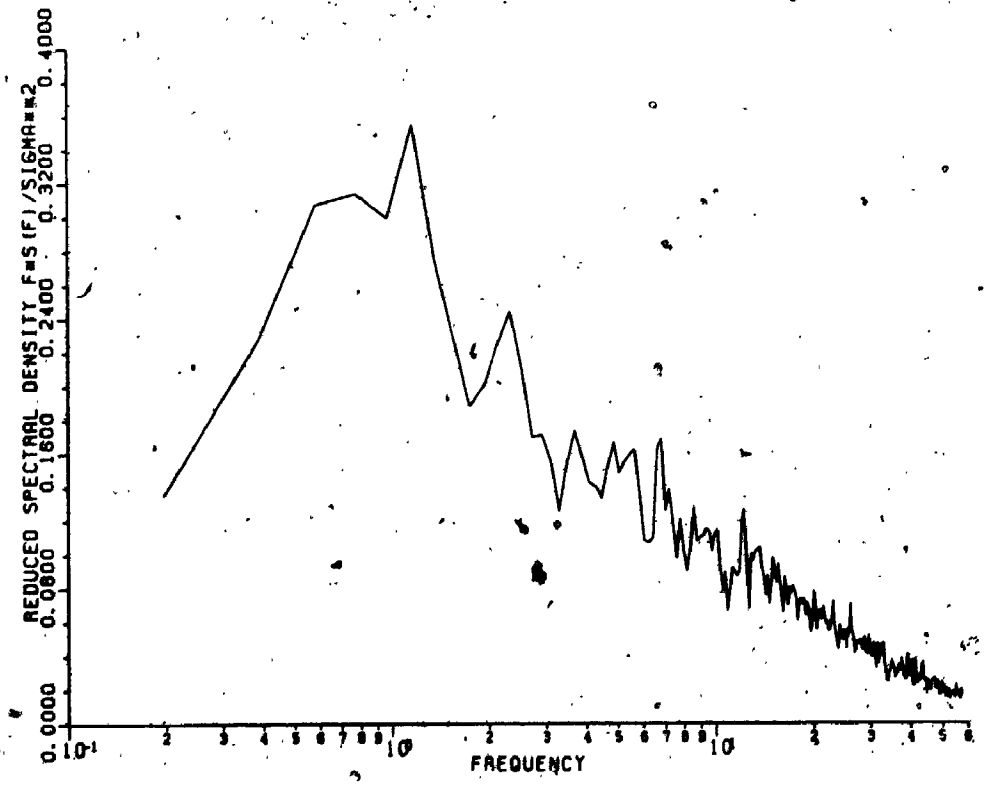

FIGURE 6.11 Power Spectrum of Velocity at Roof Height Level (Open Country Exposure, $\bar{V}_G$ = 31.3 ft/sec)

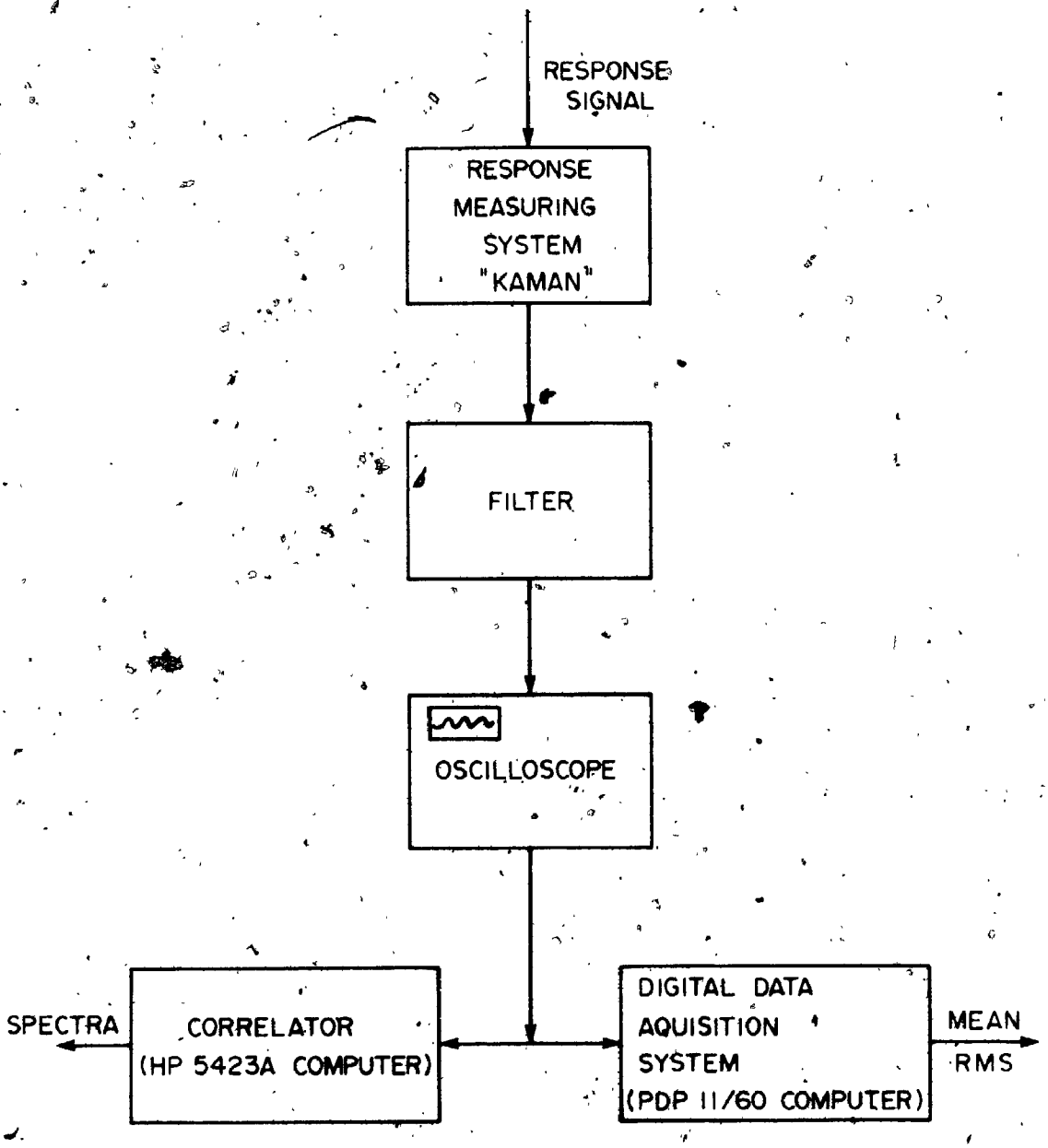

FIGURE 6.12. WIND TUNNEL EXPERIMENTAL SETUP

the enclosure due to the movement of the membrane under the turbulent wind, assuming that the internal pressure is homogeneous, a pitot tube was inserted at the instrument plate (see Figures 6.3 and 6.4).

Model Response

Several tests were conducted to assess the modal contributions and the effects of openings, terrain and wind velocity.

The mean and rms vertical deflection at r/a = 0 and $\pm$ 0.436 at angles θ = 0°, 45°, 90° with the wind direction were measured and are presented in Table 6.5. The spectra of response at centre and at r/a = 0.436 locations, for different area parameters (β_a = 5.3, 1.53, 0%) are presented in Figures 6.13 to 6.20.

When the Kaman probe is at the centre, modes f_{01} and f_{02} appear dominant. Mode f_{01} corresponds to internal volume changes while f_{02} is independent of these. Although the frequency of mode f_{01} decreases with smaller openings, and therefore response is likely to increase, the internal pressure builds up and the square of frequency response modulus decreases resulting in the virtual disappearance of resonance in mode f_{01}, Figure 6.15.

At r/a = 0.436, at which mode f_{02} is eliminated,

both the symmetric and antisymmetric components of mode f_{11} response are important in addition to the contribution of mode f_{01}, Figures 6.16 and 6.17.

When the model openings are completely closed, the only modes observed are modes f_{11}, f_{21} and f_{02} because the contribution of mode f_{01} has vanished.

The largest total mean response occurred at the angle of incidence $\theta = 0°$ at wind velocity 31.2 ft/sec (= 9.51 m/s) when the normal openings were completely closed. The largest total rms response was observed at r/a = 0.436 with $\theta = 0°$ to 90° and wind velocity 11.63 ft/sec (= 3.55 m/s) when the area parameter β_a was equal to 3.54% and 0%. This response is the largest of all points on the roof and was up to 250% larger than the response at the centre, Table 6.5.

With smaller openings (N = 0) and virtual disappearance of mode f_{01}, modes f_{11}, f_{21} and f_{02}, which are not affected by openings, remained the only main source of response.

Internal Pressure

The mean and the standard deviation for the internal pressure fluctuations were established and presented in Table 6.6 for different wind velocity and wall openings.

TABLE 6.5 VERTICAL TOTAL RESPONSE OF SIMPLIFIED MODEL

Probe Position r/a (no.)	Wind Velocity ft/sec	Wind Direction θ°	Mean Response $\bar{w}$ (inchx10^{-3}) Area Parameter B_a				RMS σ_w (inchx10^{-3}) Area Parameter B_a			
			5.3%	3.54%	1.78%	0%	5.3%	3.54%	1.78%	0%
0 (2)	11.63	0	0.30	0.70	0.20	3.50	5.20	5.70	4.40	5.50
0 (2)	11.60	45	0.30	0.50	0.30	3.10	3.70	5.60	4.60	4.50
0 (2)	11.63	90	0.20	0.70	0.30	2.30	4.60	6.40	5.00	4.00
0 (2)	19.91	0	0.0	0.0	-1.10	6.00	1.20	1.90	2.10	3.40
0 (2)	19.97	45	-0.20	-0.40	-0.80	6.20	1.20	1.80	2.10	2.00
0 (2)	19.95	90	-0.30	0.10	-0.20	4.10	1.20	1.80	1.90	1.7
0 (2)	31.21	0	-0.60	-0.50	-2.80	16.0	2.50	2.70	3.70	3.40
0 (2)	29.93	45	-1.10	-1.30	-2.20	6.30	2.20	5.50	3.30	3.10
0 (2)	29.96	90	-1.20	-0.30	-0.40	6.40	2.20	3.50	2.90	3.20
0 (2)	40.91	0	-1.90	-2.10	-6.90	11.50	4.00	4.50	5.40	5.50
0 (2)	40.79	45	-2.50	-3.30	-4.10	13.00	3.80	3.90	5.00	4.90
0 (2)	40.78	90	-3.00	-0.70	-0.80	9.40	4.20	4.10	4.90	5.40
0.436(1)	11.63	0	0.0	0.20	-0.20	2.20	6.20	8.60	8.20	12.80
0.436(1)	11.60	45	0.0	0.0	0.0	2.00	5.60	9.00	8.20	10.60
0.436(1)	11.63	90	0.0	0.20	0.20	1.20	7.20	10.80	11.60	9.40
0.436(1)	19.91	0	0.0	-0.20	-0.80	4.00	1.40	2.00	2.80	7.60
0.436(1)	19.97	45	-0.40	-0.40	-0.60	4.00	1.40	1.80	2.80	2.20
0.436(1)	19.95	90	-0.40	0.0	-0.10	2.60	1.40	2.0	2.40	2.40
0.436(1)	31.21	0	-0.20	-0.40	-1.80	11.20	2.00	4.60	5.60	4.60
0.436(1)	29.93	45	-0.60	-0.80	-1.40	4.40	1.80	10.00	4.00	3.60
0.436(1)	29.96	90	-1.00	-0.40	-0.40	4.20	2.00	4.0	3.20	3.80
0.436(1)	40.91	0	-0.60	-1.00	-3.80	8.60	3.00	3.20	5.20	10.80
0.436(1)	40.79	45	-1.40	-1.80	-2.20	9.60	2.80	2.80	5.00	7.00
0.436(1)	40.78	90	-2.20	-0.60	-0.40	6.40	3.20	3.40	5.20	11.80

TABLE 6.5 (cont'd)

0.436(3)	11.63	0	1.80	2.40	1.80	4.80	10:20	13.20	12.20	14.60
0.436(3)	11.60	45	1.20	2.00	2.00	4.40	8.00	11.80	12.60	13.20
0.436(3)	11.63	90	1.40	2.40	1.60	4.00	9.20	14.80	13.40	14.20
0.436(3)	19.91	0	0.60	0.40	0.00	6.20	3.00	4.40	6.40	6.00
0.436(3)	19.97	45	0.20	0.20	-0.40	6.20	3.20	4.40	4.80	5.20
0.436(3)	19.95	90	0.40	0.80	0.10	4.40	3.20	4.20	3.60	4.40
0.436(3)	31.21	0	0.00	0.40	-1.40	15.60	3.80	5.60	6.60	6.00
0.436(3)	29.93	45	-0.60	-0.20	-1.20	6.60	3.60	6.40	6.80	4.20
0.436(3)	29.96	90	-0.20	+0.60	0.0	6.80	3.60	4.20	4.20	4.80
0.436(3)	40.91	0	-1.40	-1.60	-5.80	10.60	5.20	6.20	8.20	9.00
0.436(3)	40.79	45	-2.00	-2.60	-3.40	12.00	4.80	6.00	7.00	6.20
0.436(3)	40.78	90	-2.00	0.0	+0.60	9.40	5.20	6.20	9.00	9.60

(1 inch = 0.0254 m ; ft/sec = 0.3048 m/s)

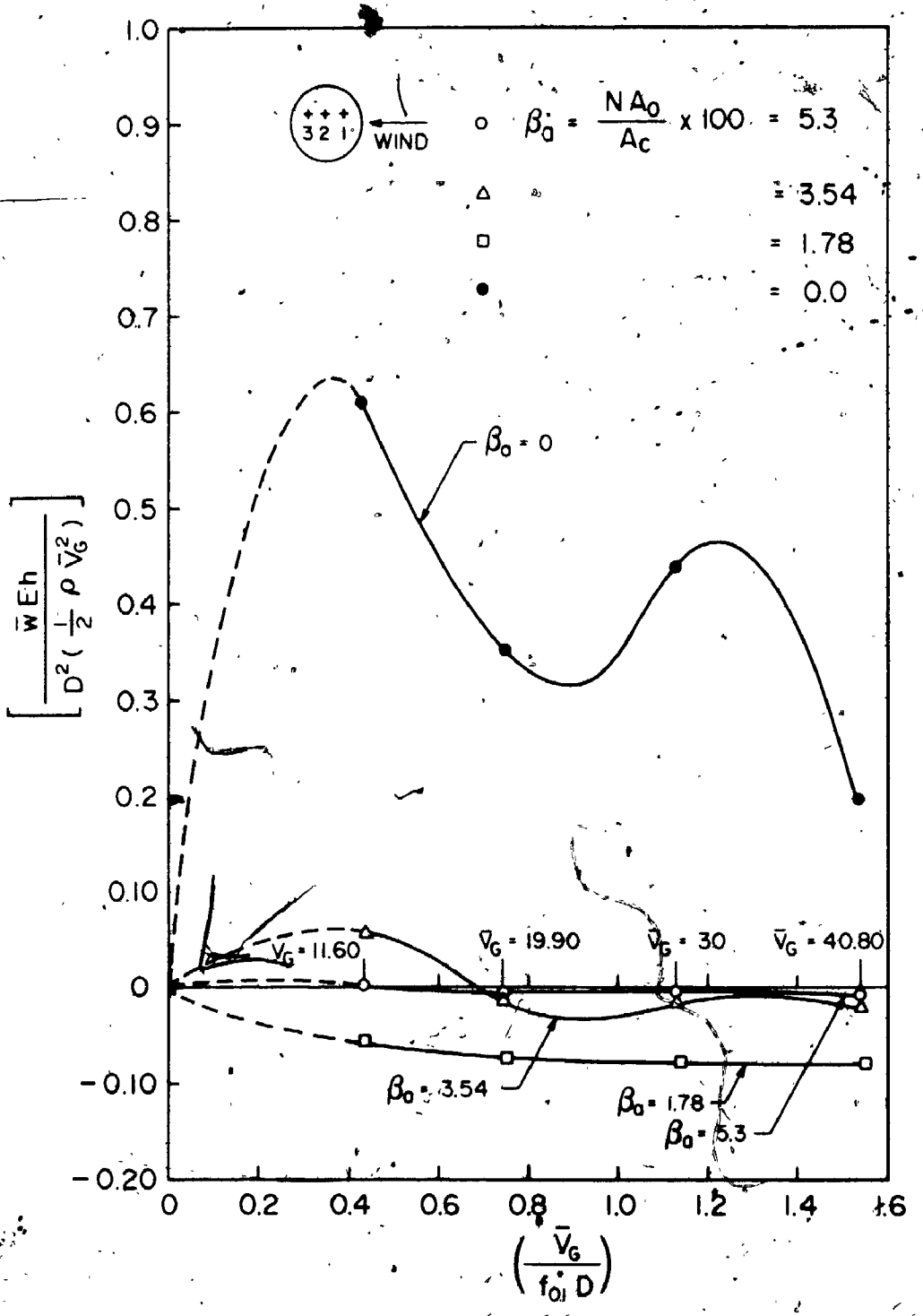

FIGURE 6.28 NON DIMENSIONAL MEAN RESPONSE AT $r/a = 0.436$ WITH WIND VELOCITIES AT DIFFERENT AREA PARAMETERS (PROBE NO. 1)

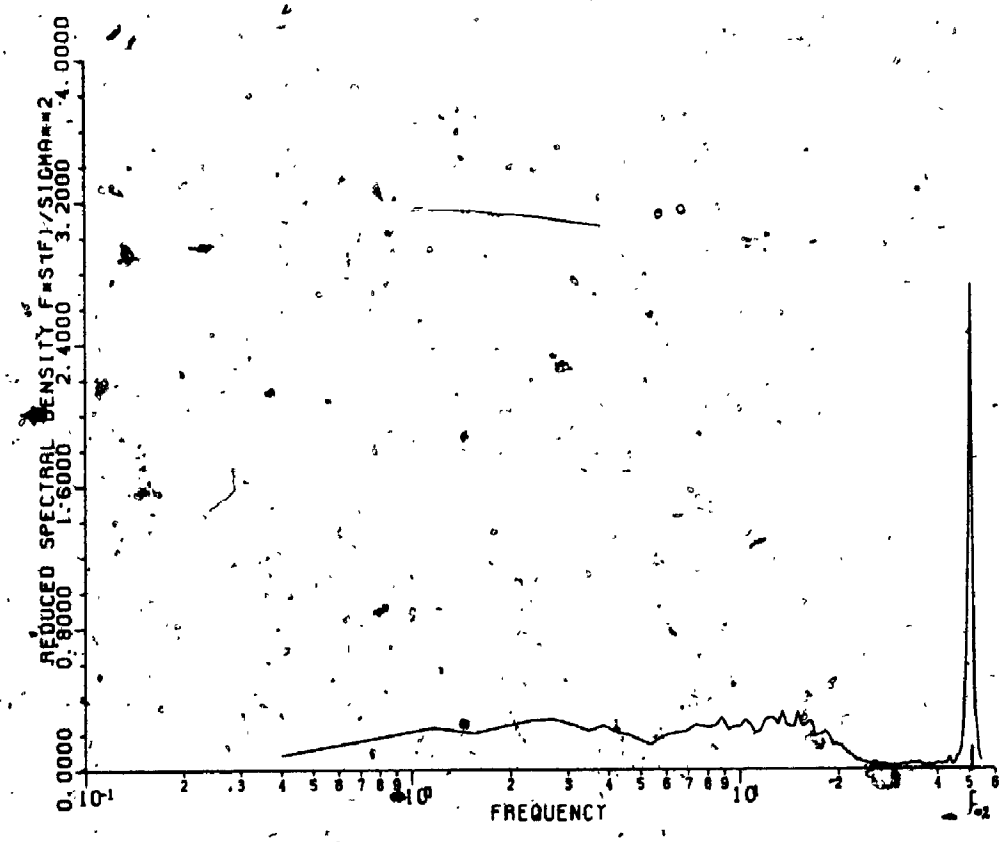

FIGURE 6.15 Power Spectrum of Response at $r/a = 0$, $\beta_c = 1.78\%$, $\theta = 0°$, $\bar{V}_G = 28$ ft/sec (Built-Up Area)

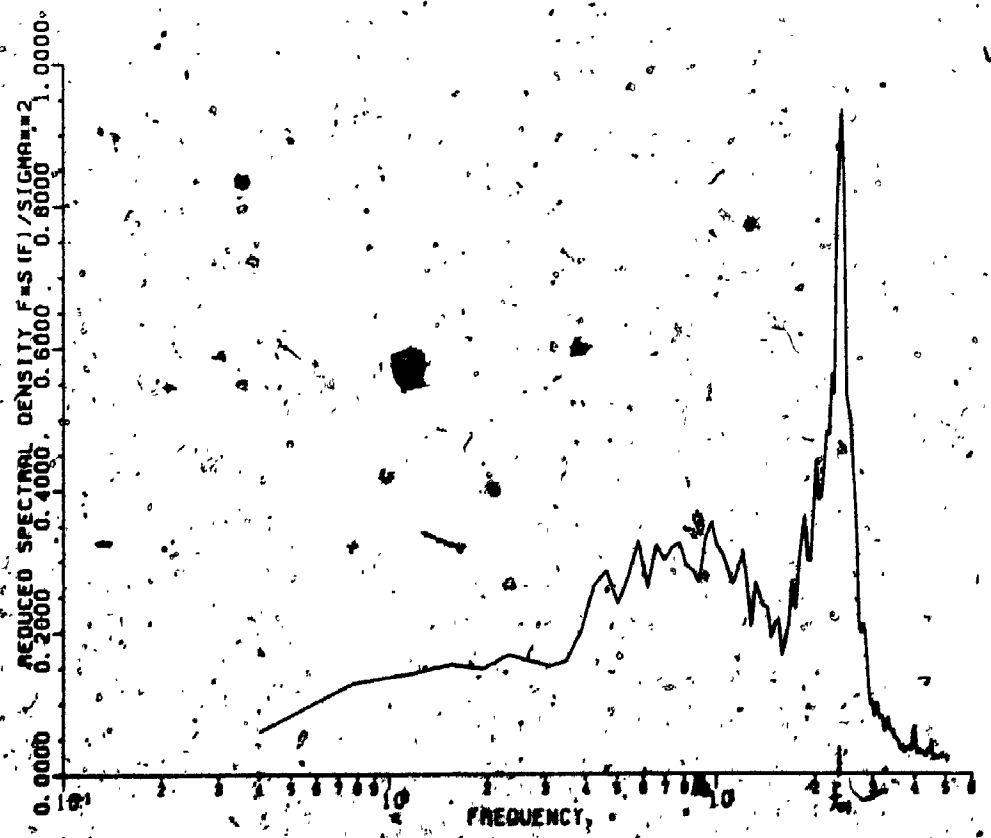

FIGURE 6.16 Power Spectrum of Response at $r/a = 0.426$, $\beta_c = 5.3\%$, $\theta = 0°$, $\bar{V}_G = 28$ ft/sec (Built-Up Area)

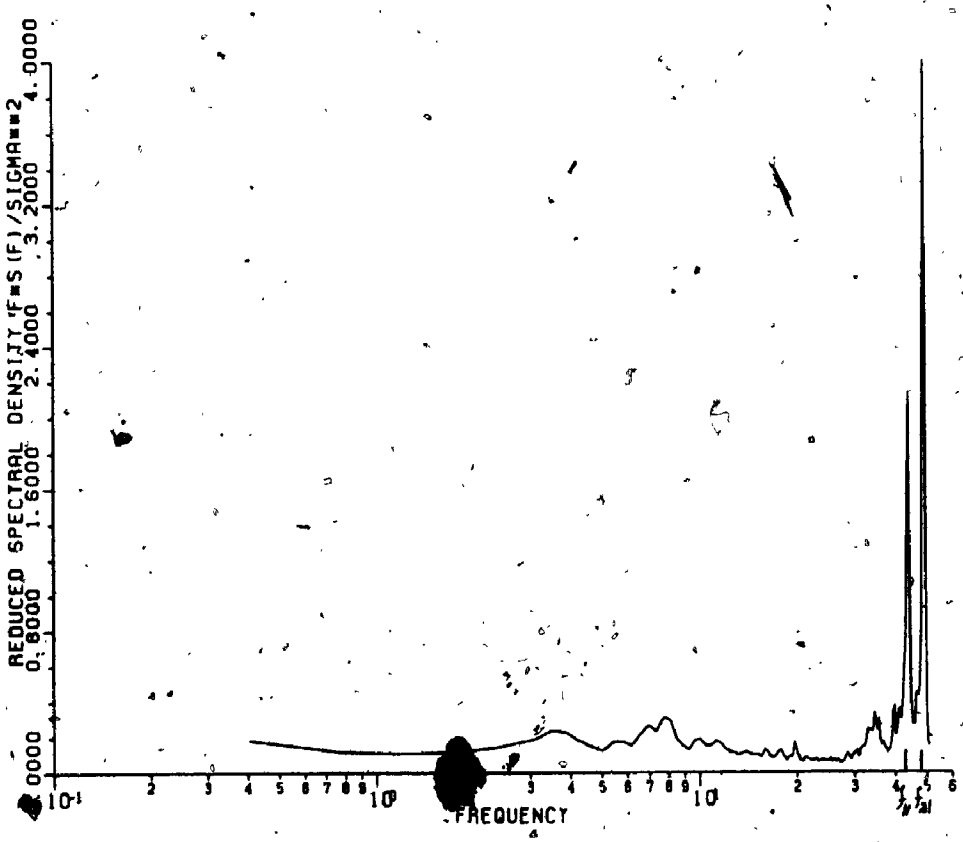

FIGURE 6.17 Power Spectrum of Response at r/a = 0.436, β_a = 0%, θ = 90°, $\bar{V}_G$ = 28 ft/sec.(Built-Up Area)

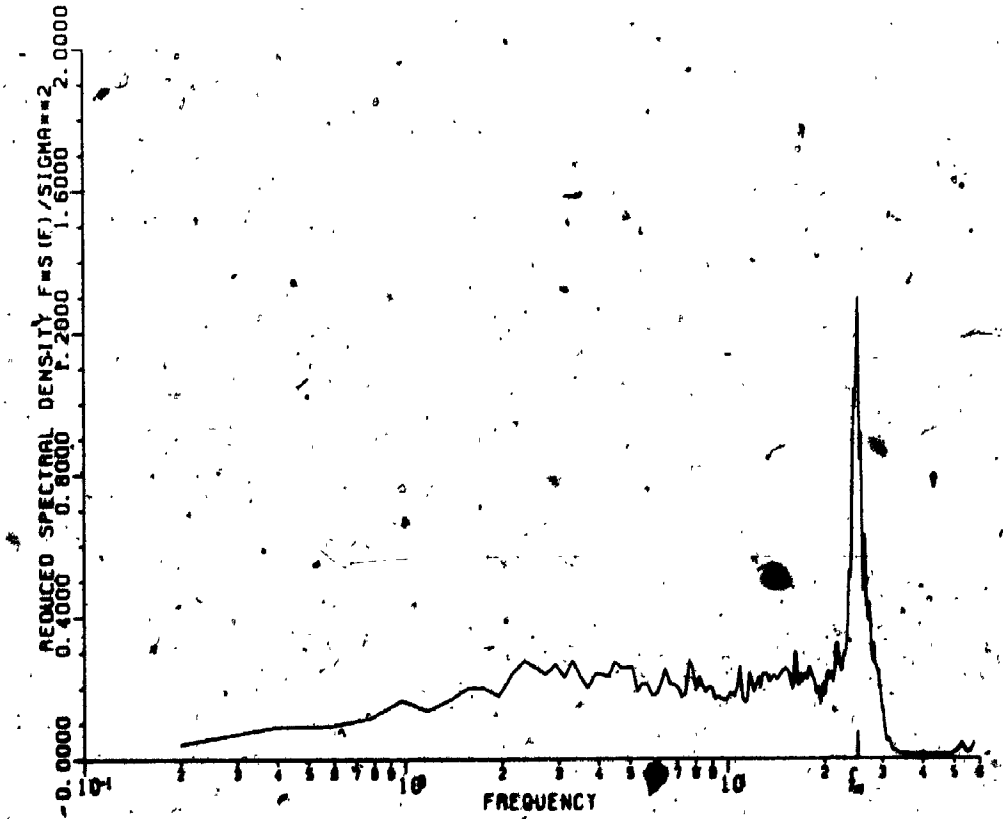

FIGURE 6.18 Power Spectrum of Response at r/a = 0, β_a = 5.30%, θ = 90° $\bar{V}_G$ = 28 ft/sec (Open Country Exposure)

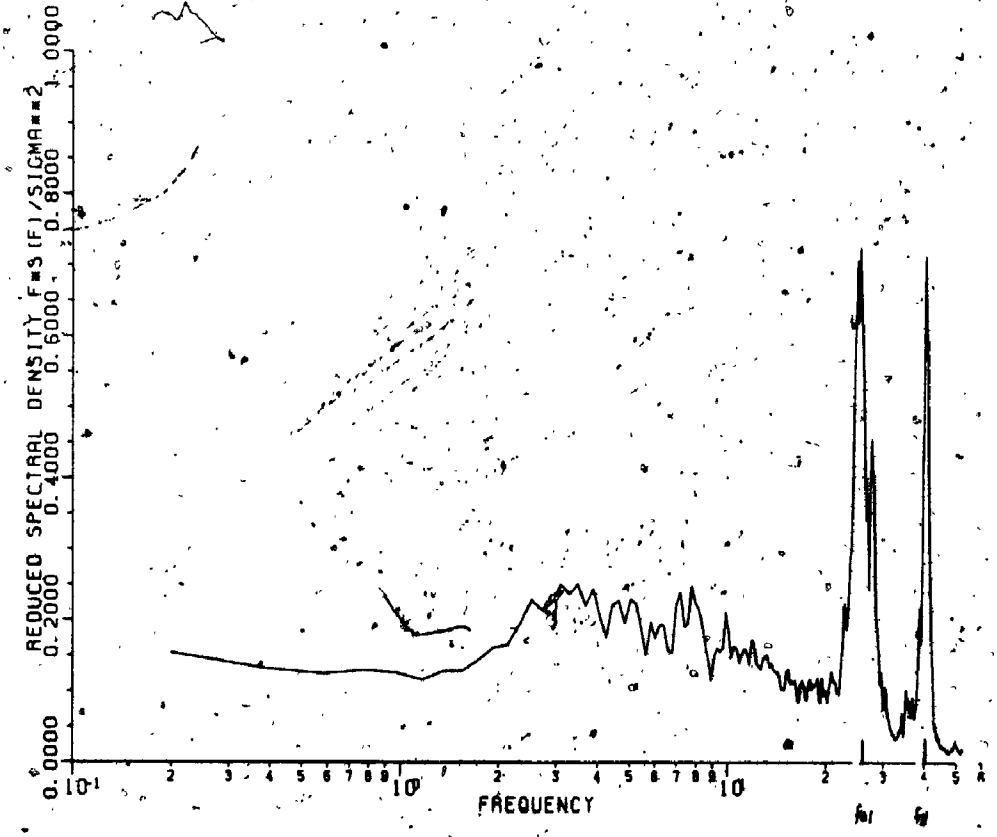

FIGURE 6.19 Power Spectrum of Response at r/a = 0.436, β_a = 5.31%, θ = 45°, $\bar{V}_G$ = 20 ft/sec (Open Country Exposure)

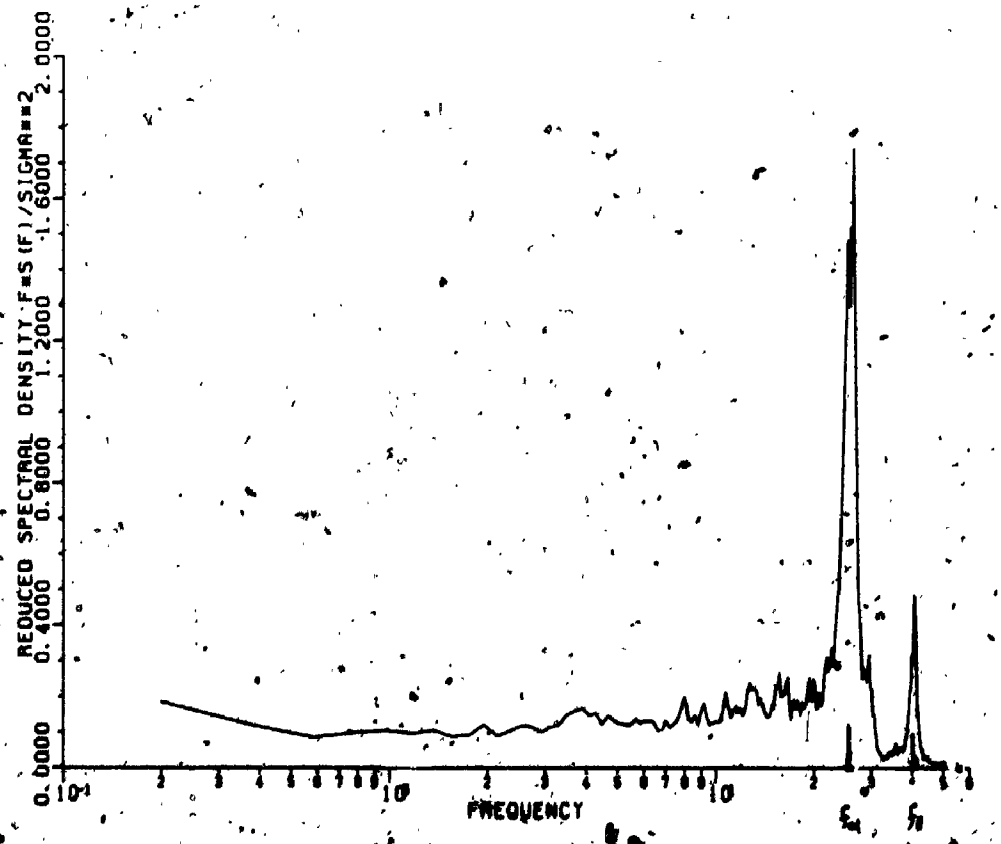

FIGURE 6.20 Power Spectrum of Response at r/a = 0.436, β_a = 5.31%, θ = 0°, $\bar{V}_G$ = 20 ft/sec (Open Country Exposure)

TABLE 6.6 INTERNAL PRESSURE COEFFICIENT FOR DIFFERENT WIND VELOCITIES AND AREA PARAMETER ($\beta_a = NA_o/A_c \times 100$)

Wind Direction θ°	Area Parameter β_a	Gradient Wind Speed $\bar{V}_G$ (ft/sec)	Pressure Coefficient C_q (mean)	C_{q_σ} (RMS)
0°	5.30	38.0	-0.60	0.13
45°	5.30	38.0	-0.61	0.13
90°	5.30	38.0	-0.63	0.13
0°	5.30	28.0	-0.40	0.080
45°	5.30	28.0	-0.43	0.085
90°	5.30	28.0	-0.43	0.090
0°	3.54	28.0	-0.37	0.07
45°	3.54	28.0	-0.40	0.10
90°	3.54	28.0	-0.45	0.06
0°	0	28.0	-0.20	0.04
45°	0	28.0	-0.18	0.05
90°	0	28.0	-0.19	0.06

(1 ft/sec = 0.3048 m/s)

For a velocity of approaching flow $\bar{V}_G$ = 28 ft/sec (= 8.534 m/s) and with openings fairly uniformly distributed (N = 9) with area parameter β_a = 5.30% ($\beta = \frac{NA_o}{A_c}$ %), it was found that the mean pressure coefficient $C_{\bar{q}_\ell}$ = -0.43 and the rms pressure coefficient $C_{q_{\sigma_\ell}}$ = 0.085. For the same area parameter but with wind velocity $\bar{V}_G$ = 38 ft/sec (= 11.58 m/s) both coefficients increased to $C_{\bar{q}_\ell}$ = -0.63 and $C_{q_{\sigma_\ell}}$ = 0.13.

For a wind velocity of $\bar{V}_G$ = 28 ft/sec (= 8.534 m/s), but the area parameter β_a = 3.54%; the coefficients dropped to $C_{\bar{q}_\ell}$ = -0.37 and $C_{q_{\sigma_\ell}}$ = 0.07.

Cross-Spectra of Wind Fluctuations Over Model Roof Surface

To understand the correlation between the fluctuating flow velocities over the roof model, the cross-spectra of the longitudinal fluctuating component of turbulent wind were measured at different locations just above the surface of the roof. These measurements showed almost no correlation of wind fluctuations along and across the roof model when the velocity of the approaching flow $\bar{V}_G$ = 8 ft/sec (= 2.438 m/s), Figures 6.21 to 6.24, and a small correlation over the roof surface along wind, when $\bar{V}_G$ = 31 ft/sec (= 9.45 m/s), Figures 6.25, 6.26.

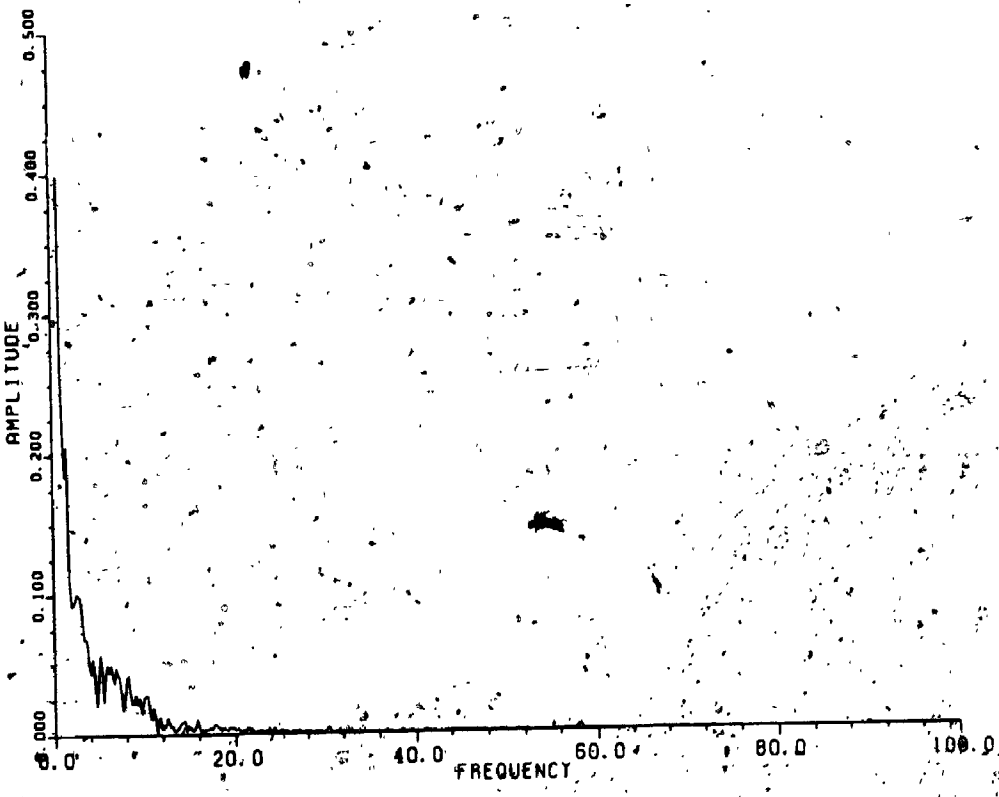

FIGURE 6.21 Cross-Correlation Coefficient (Coherence Function) of Wind Velocity, 8.0 ft/sec, at r/a = 0.436, 0.0 Along Wind

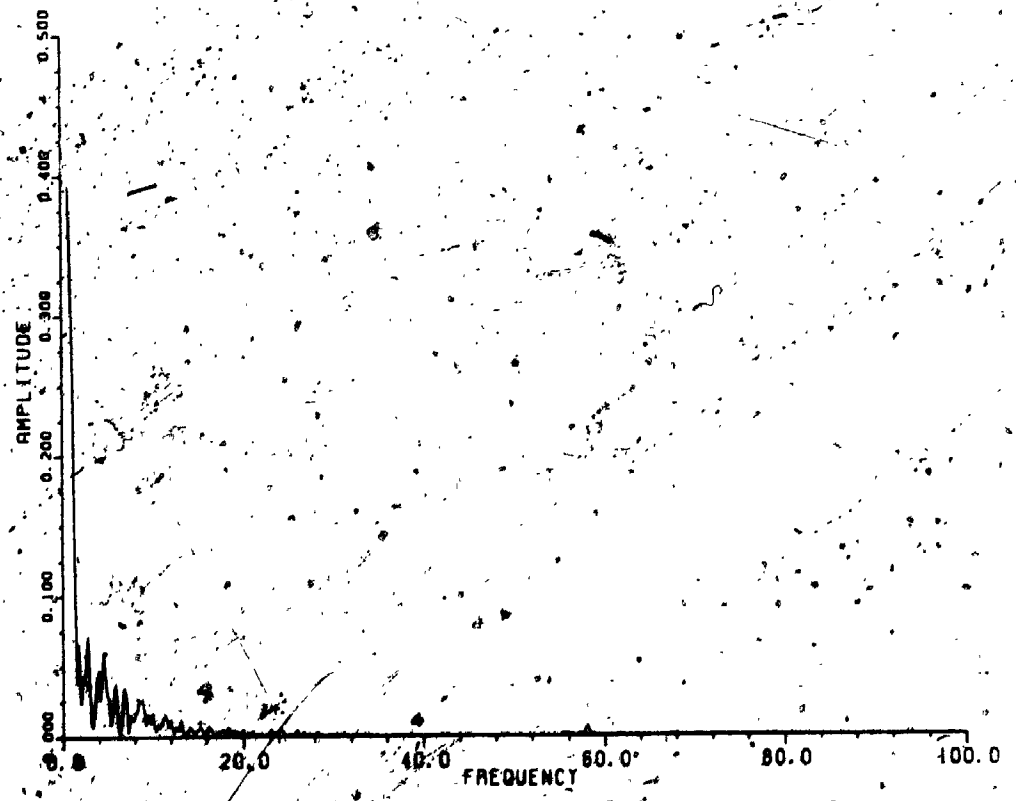

FIGURE 6.22 Cross-Correlation Coefficient (Coherence Function) of Wind Velocity, 8 ft/sec, at r/a = +0.436, −0.436 Along Wind

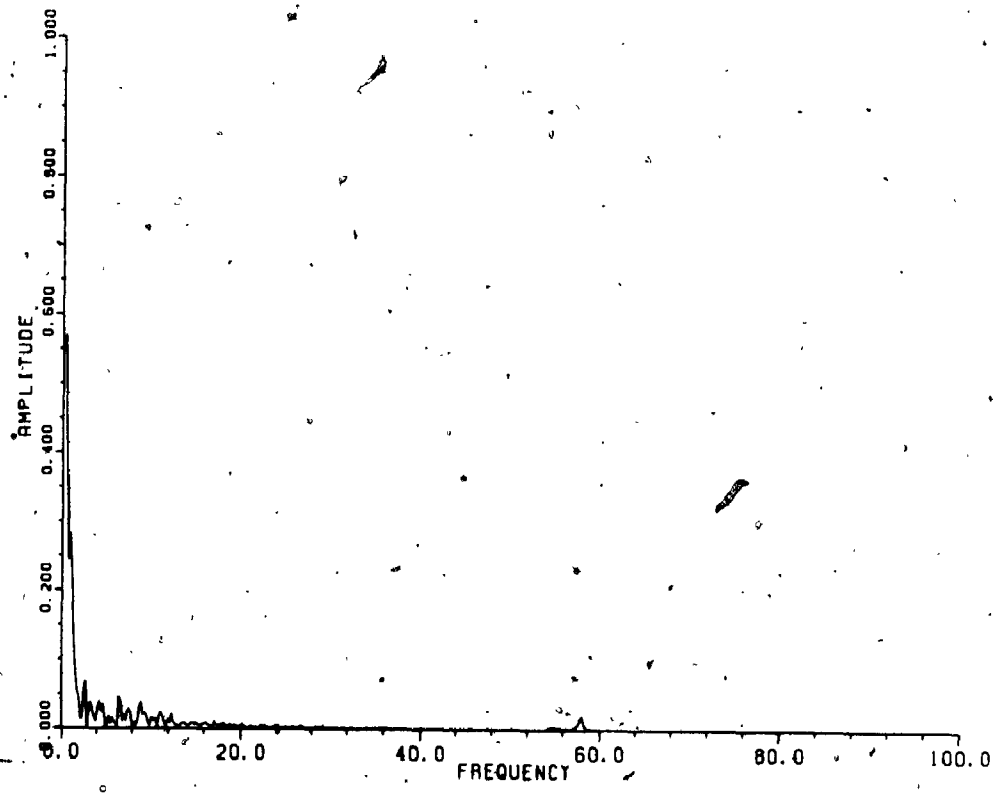

FIGURE 6.23 Cross-Correlation Coefficient (Coherence Function) of Wind Velocity, 8 ft/sec, at r/a = 0.0, +0.436 Across Wind

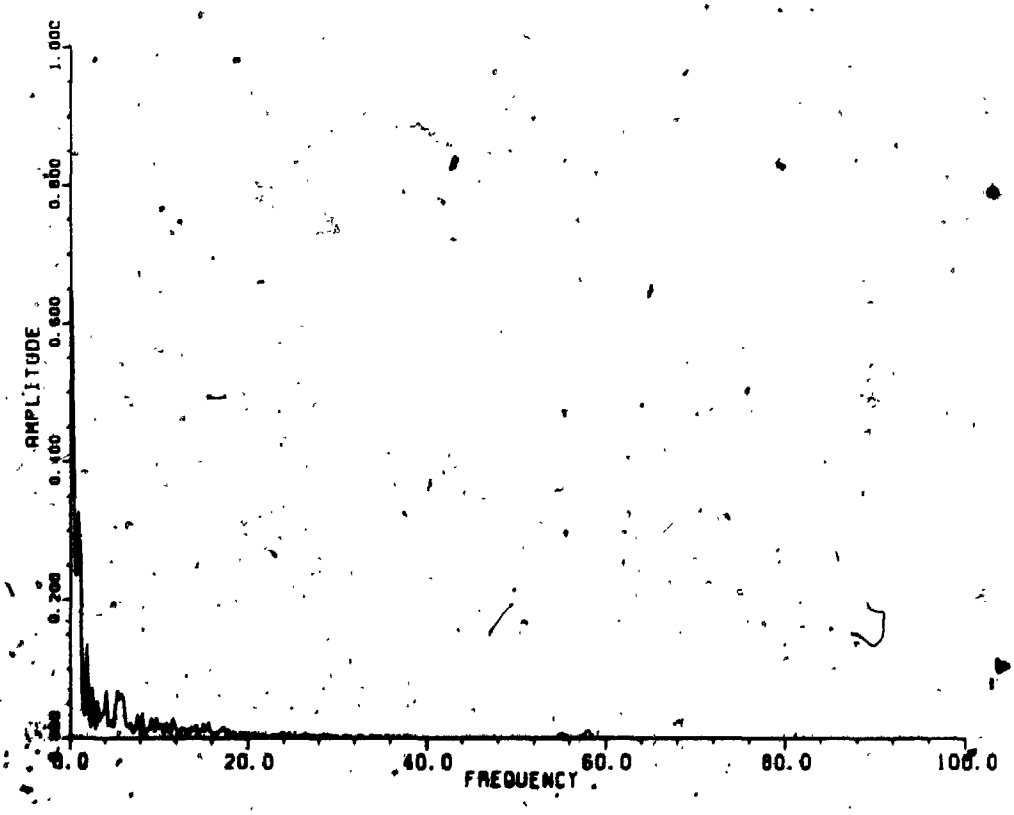

FIGURE 6.24 Cross-Correlation Coefficient (Coherence Function) of Wind Velocity, 8 ft/sec, at r = +0.436, -0.436, Across Wind

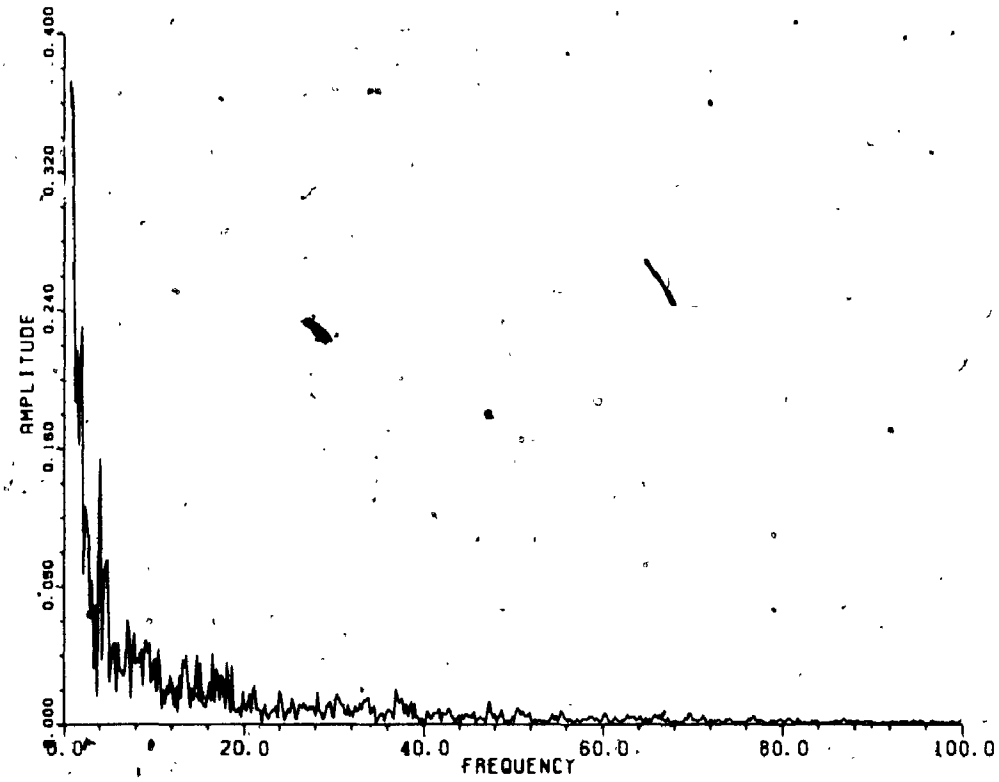

FIGURE 6.25 Cross-Correlation Coefficient (Coherence Function) of Wind Velocity, 31 ft/sec, at r/a = +0.436, -0.436 Across Wind

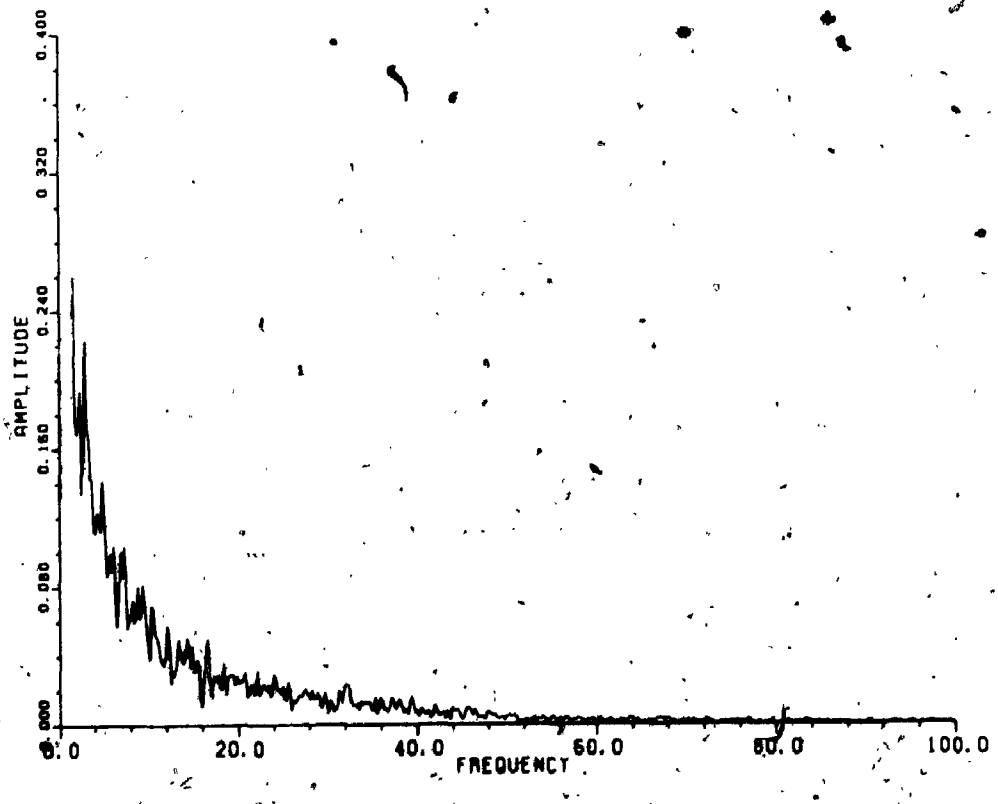

FIGURE 6.26 Cross-Correlation Coefficient (Coherence Function) of Wind Velocity, 31 ft/sec, at r/a = 0.436, 0.0 Along Wind

6.6.1.3 Effect of Cavity Openings on the Frequency Character

The variation of the model natural frequencies with total area parameter $\beta_a = \frac{NA_o}{A_c} \times 100$ is shown in Figure 6.7. Figure 6.7 indicates that the natural frequency of the first symmetrical mode is strongly dependent on the area parameter β_a, decreasing with the decrease of the total area of openings within the cavity wall, while the natural frequencies of the other modes are slightly affected.

For the first symmetrical mode, the variation of natural frequency with the cavity parameter $\beta_c = \ell' \frac{\rho a^2}{m\ Na_o}$ is shown in Figure 4.16 (Chapter 4). Figure 4.16 indicates that the natural frequency of this mode decreases due to the increase in the additional mass effect represented by the cavity parameter β_c.

For the light, highly taut roof tested, the natural frequencies increase with increasing area of openings indicating a behaviour similar to that of a Helmholtz resonator. The trends observed in Figures 4.16 and 6.7 are in agreement with the theory formulated in Chapter 4.

6.6.1.4 Effect of Wind Velocity and Cavity on Response

Figures 6.27 to 6.29 and Figures 6.30 to 6.32 show the variation of the dimensionless total mean and standard

deviation response respectively at different locations on the roof, for different wind velocities and area parameter β_a. In these figures it appears that the greatest response (a positive maximum, i.e. downwards) is attained when the model is completely closed; it occurs at the leeward position of r/a = 0.436 of the roof.

Figures 6.33 to 6.35 and Figures 6.36 to 6.38 show the dimensionless total mean and standard deviation response respectively at different locations on the roof, for different area parameter β_a at different wind velocities.

In these figures a significant phenomenon is observed. When the gust size, $(\frac{\overline{V}_G}{f})$ is about 0.33 of the structure size D, (i.e. $\frac{\overline{V}_G}{fD} \approx 0.33$), a peak response exists at all area parameters and everywhere on the roof.

6.6.1.5 Effect of Cavity and Wind Velocity on Damping

For free vibration tests, the total structural and acoustical damping ratio D_{nm} for each mode of vibration f_{nm} at different area parameter β_a is presented in Table 6.4.

The acoustical damping is due to the movement of the roof and is proportional to its vibration velocity. As

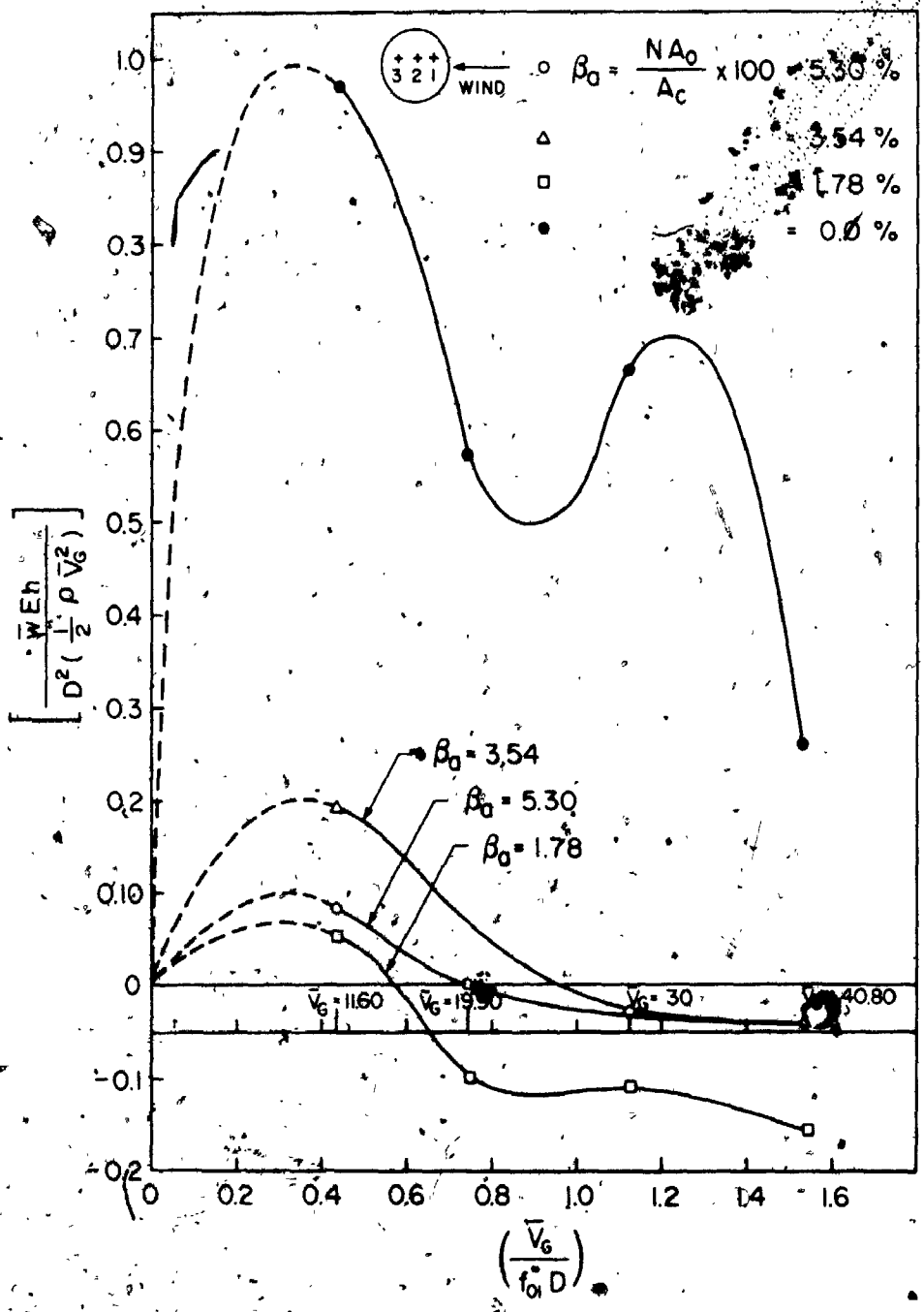

FIGURE 6.27 NON DIMENSIONAL MEAN RESPONSE AT CENTRE, r/a = 0.0 WITH WIND VELOCITIES AT DIFFERENT AREA PARAMETERS (PROBE NO. 2)

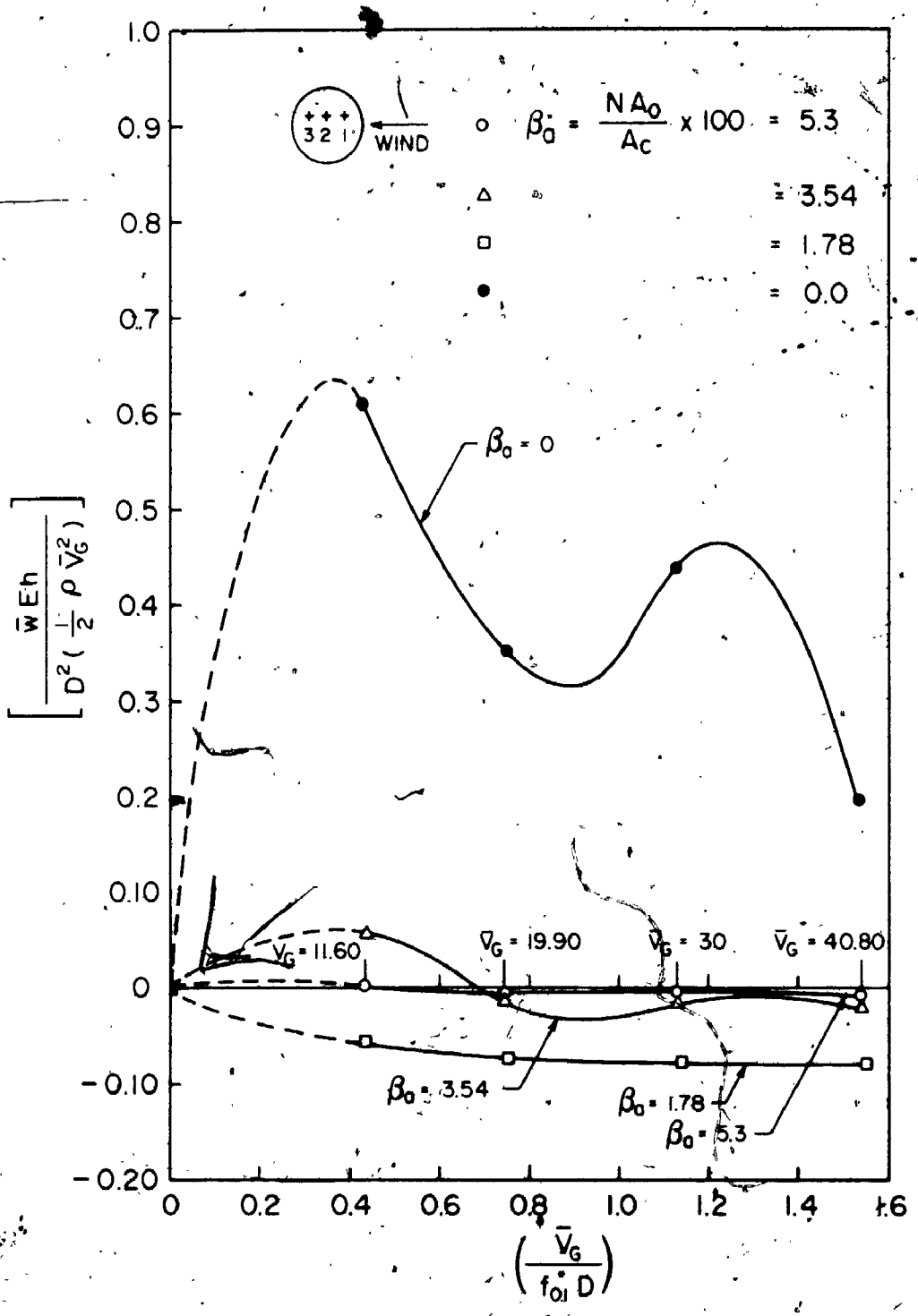

FIGURE 6.28 NON DIMENSIONAL MEAN RESPONSE AT $r/a = 0.436$ WITH WIND VELOCITIES AT DIFFERENT AREA PARAMETERS (PROBE NO. 1)

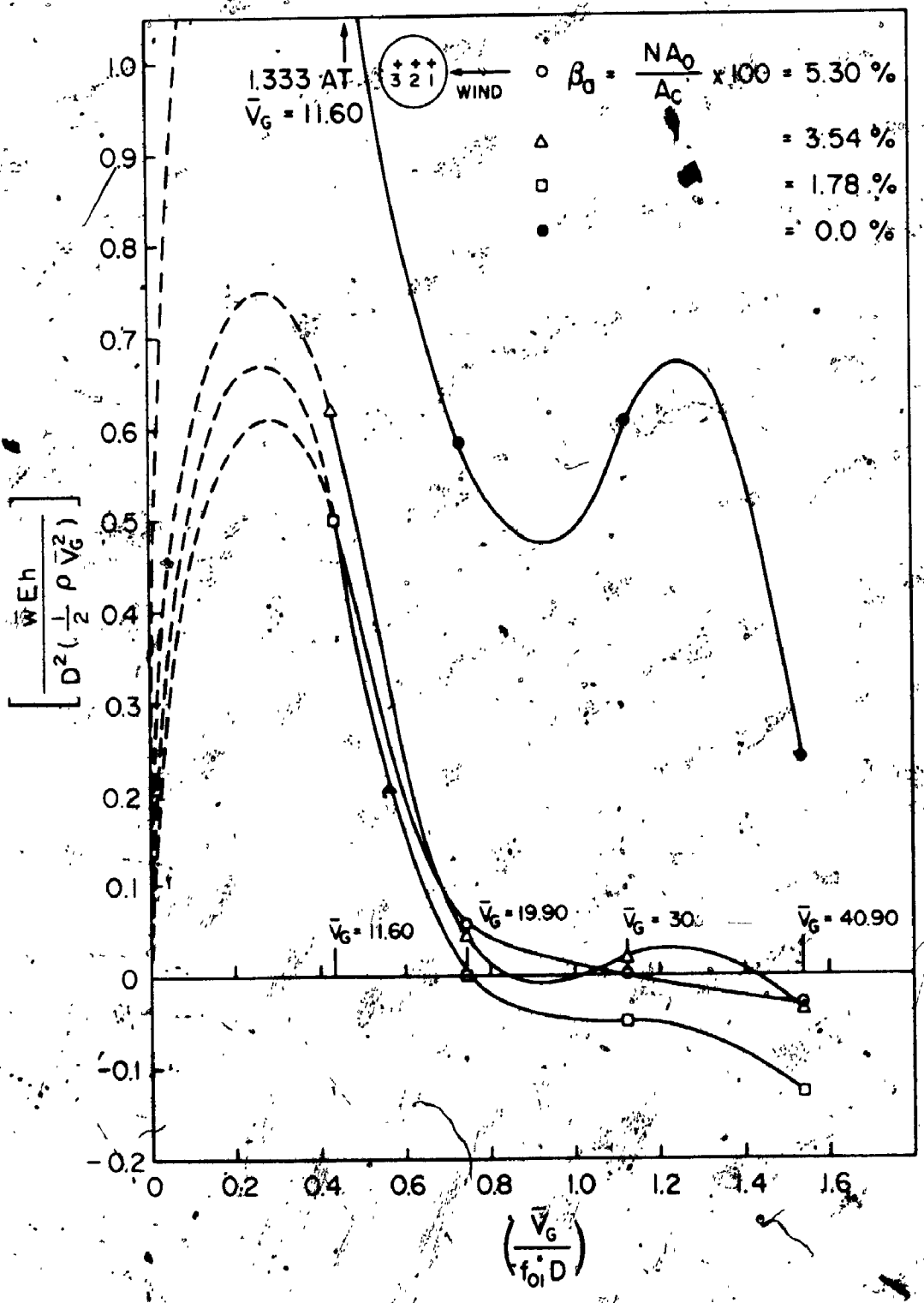

FIGURE 6.29 NON DIMENSIONAL MEAN RESPONSE AT r/a = 0.436 WITH WIND VELOCITIES AT DIFFERENT AREA PARAMETERS (PROBE NO. 3)

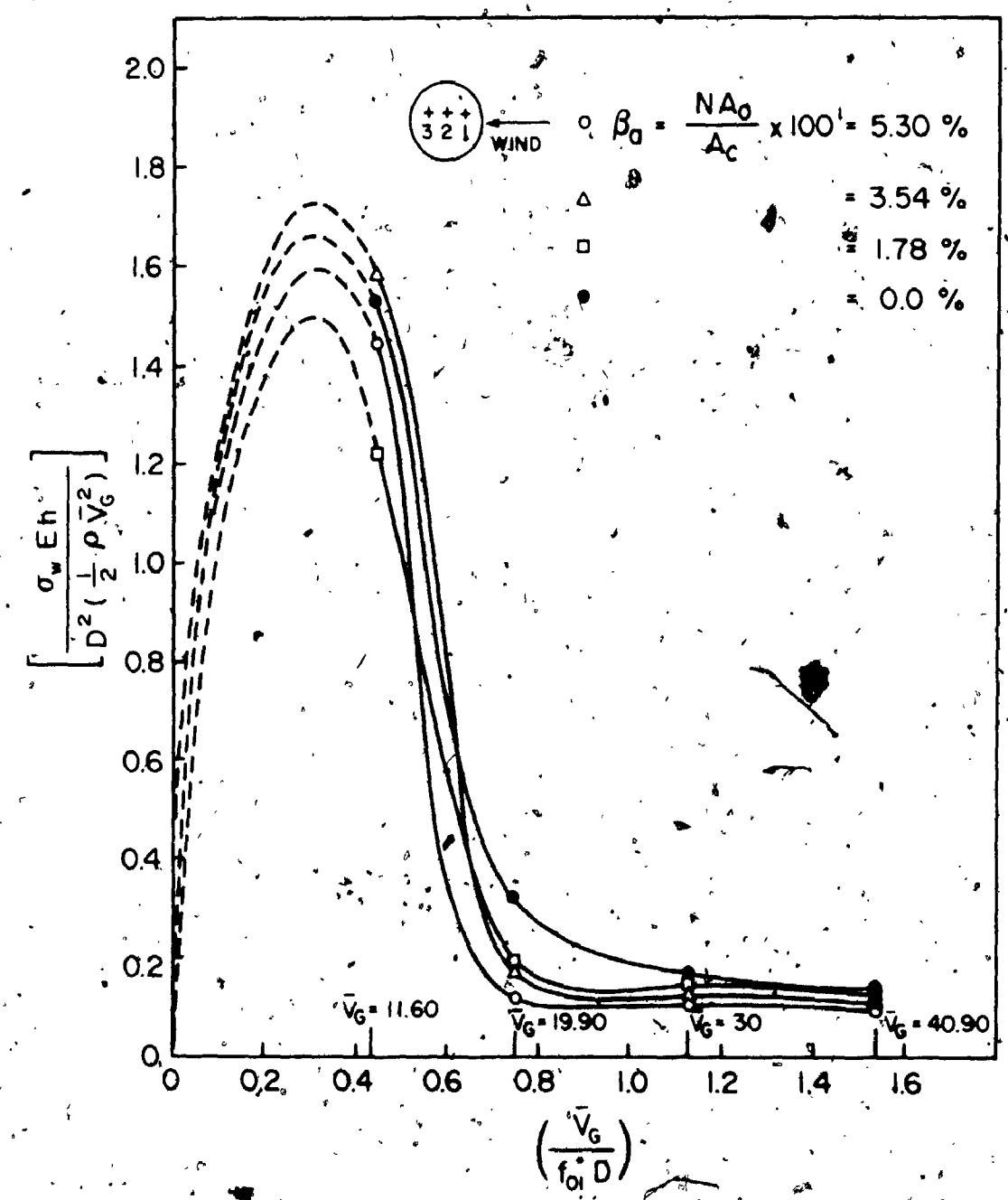

FIGURE 6.30 NON DIMENSIONAL RMS RESPONSE AT CENTRE WITH WIND VELOCITIES AT DIFFERENT AREA PARAMETERS (PROBE NO. 2).

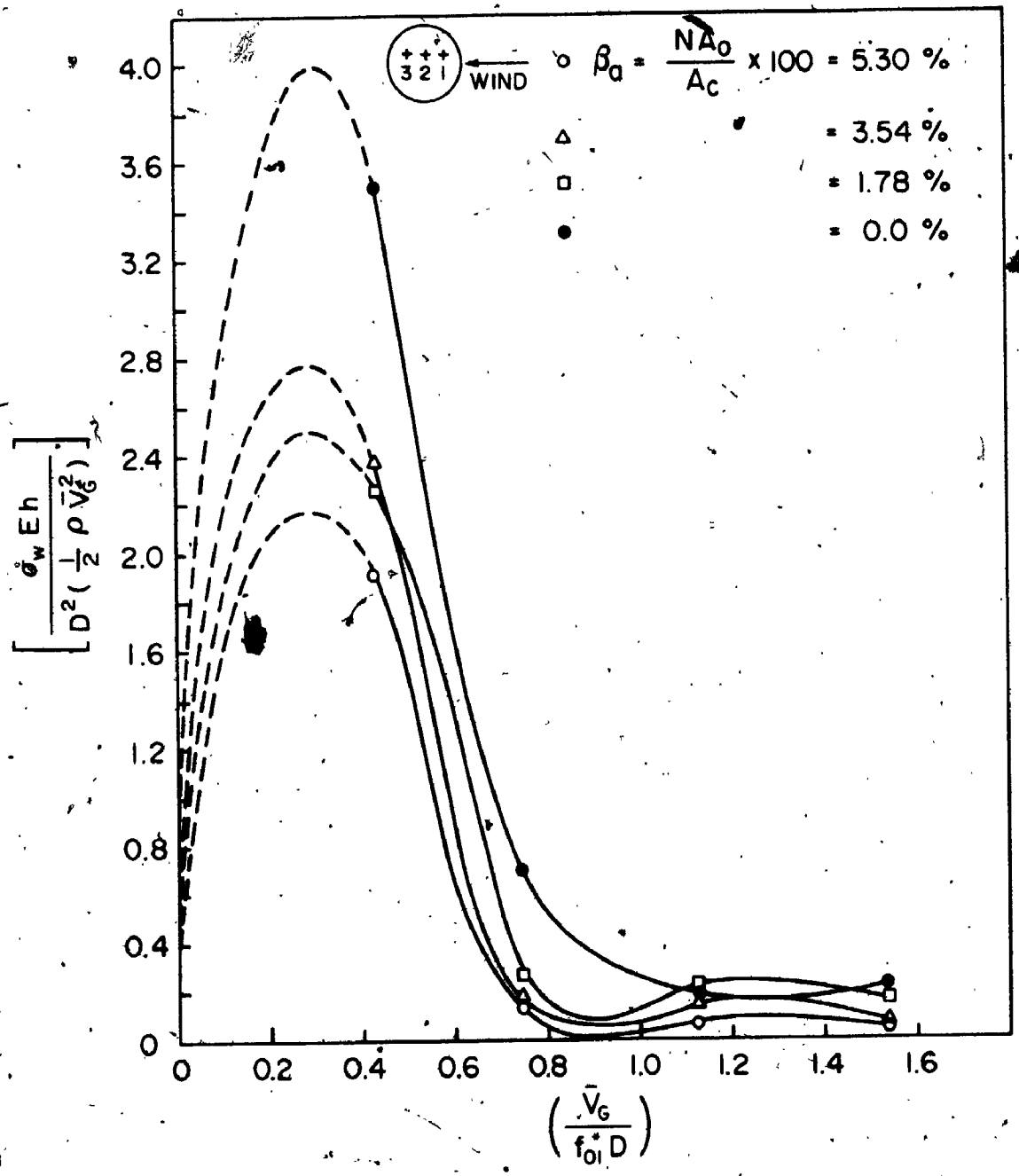

FIGURE 6.31 NON-DIMENSIONAL RMS RESPONSE AT $r/a = 0.436$ WITH WIND VELOCITIES AT DIFFERENT AREA PARAMETERS (PROBE NO. 1)

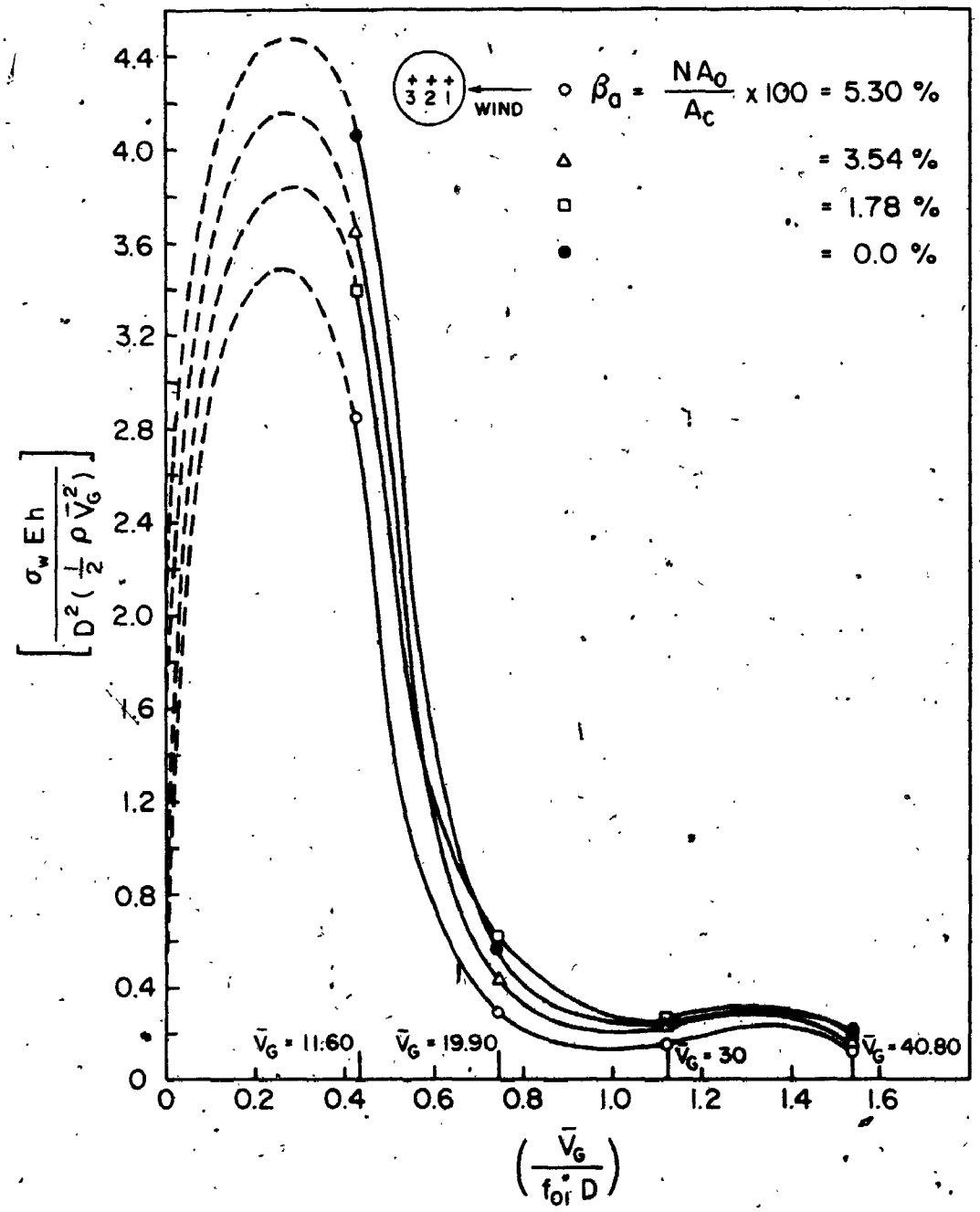

FIGURE 6.32 NON DIMENSIONAL RMS RESPONSE AT $r/a = 0.436$ WITH WIND VELOCITIES AT DIFFERENT AREA PARAMETERS (PROBE NO. 3)

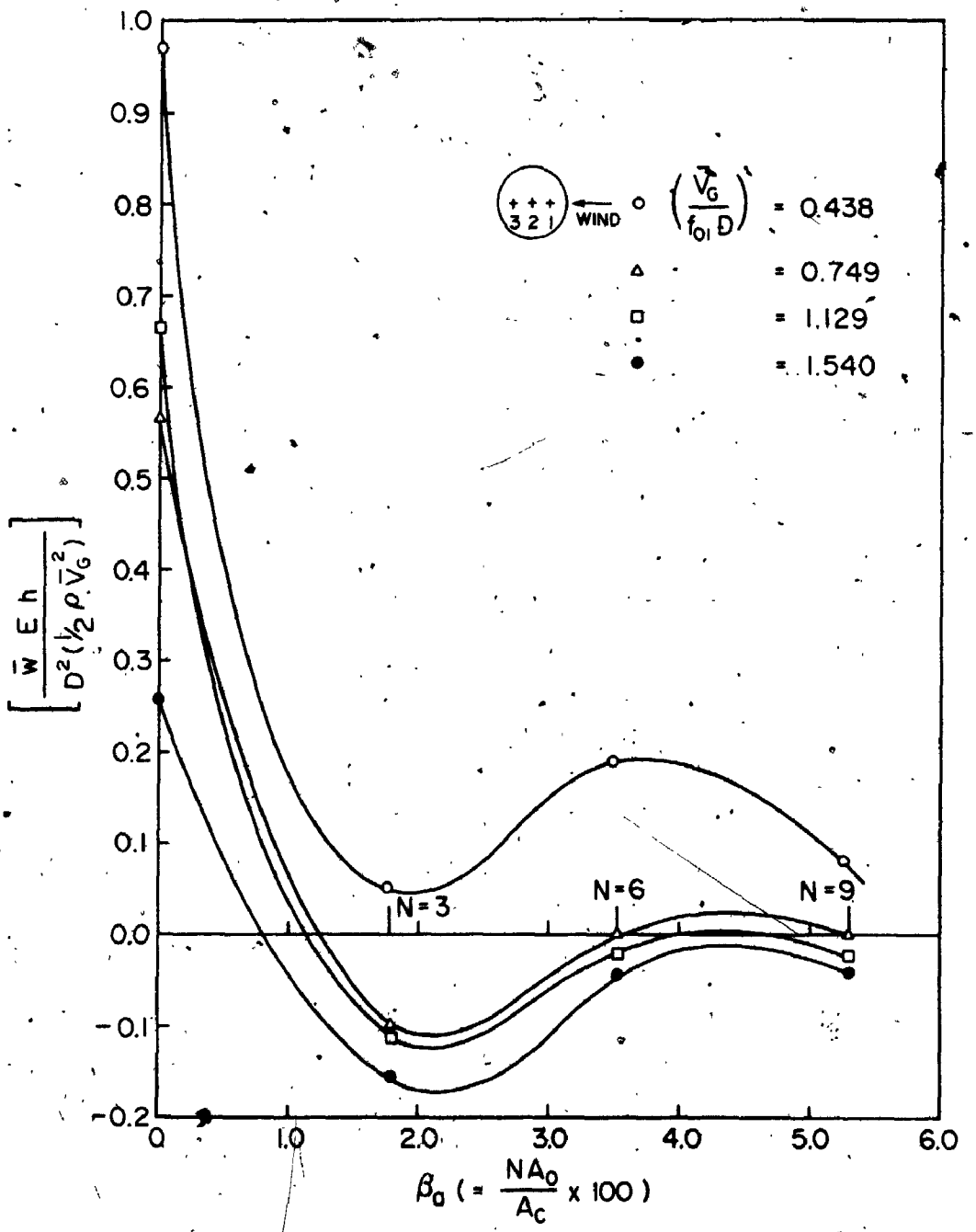

FIGURE 6.33 NON-DIMENSIONAL MEAN RESPONSE AT CENTRE r/a = 0.0 WITH AREA PARAMETER AT DIFFERENT VELOCITIES (PROBE NO. 2)

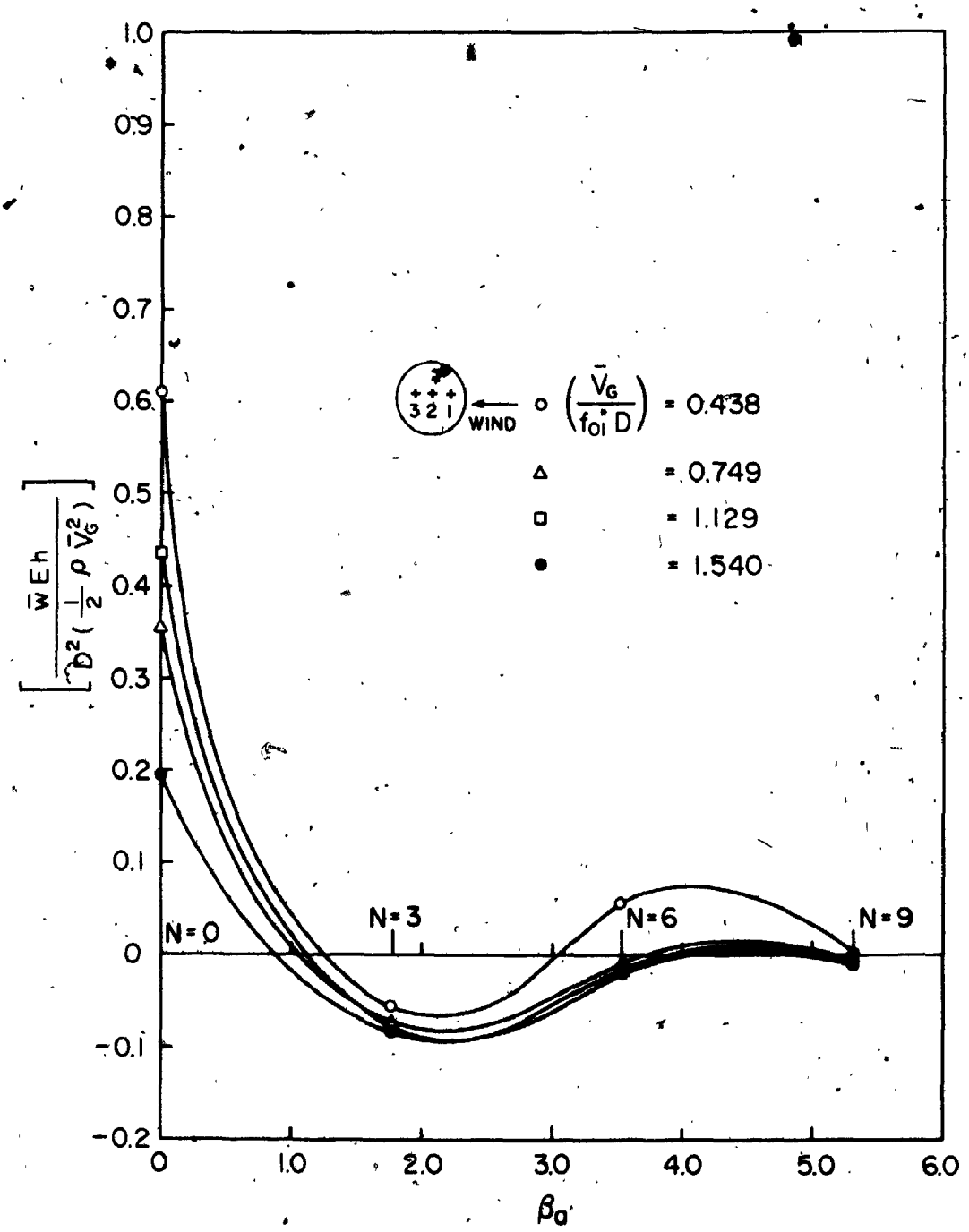

FIGURE 6.38 NON DIMENSIONAL MEAN RESPONSE AT $r/a = 0.436$ WITH AREA PARAMETERS AT DIFFERENT VELOCITIES (PROBE NO. 1)

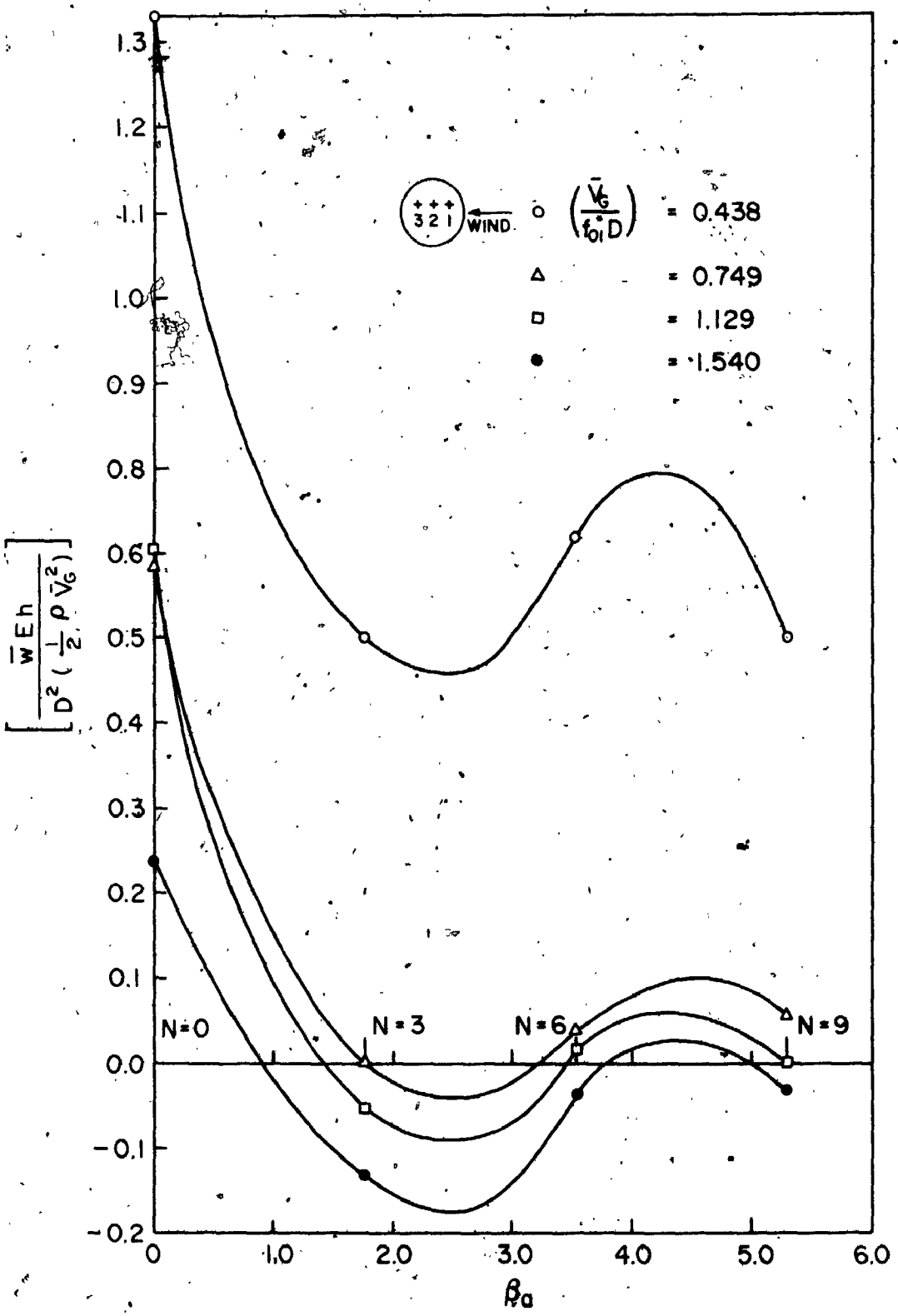

FIGURE 6.35 NON DIMENSIONAL MEAN RESPONSE AT r/a = 0.436 WITH AREA PARAMETER AT DIFFERENT VELOCITIES (PROBE NO. 3)

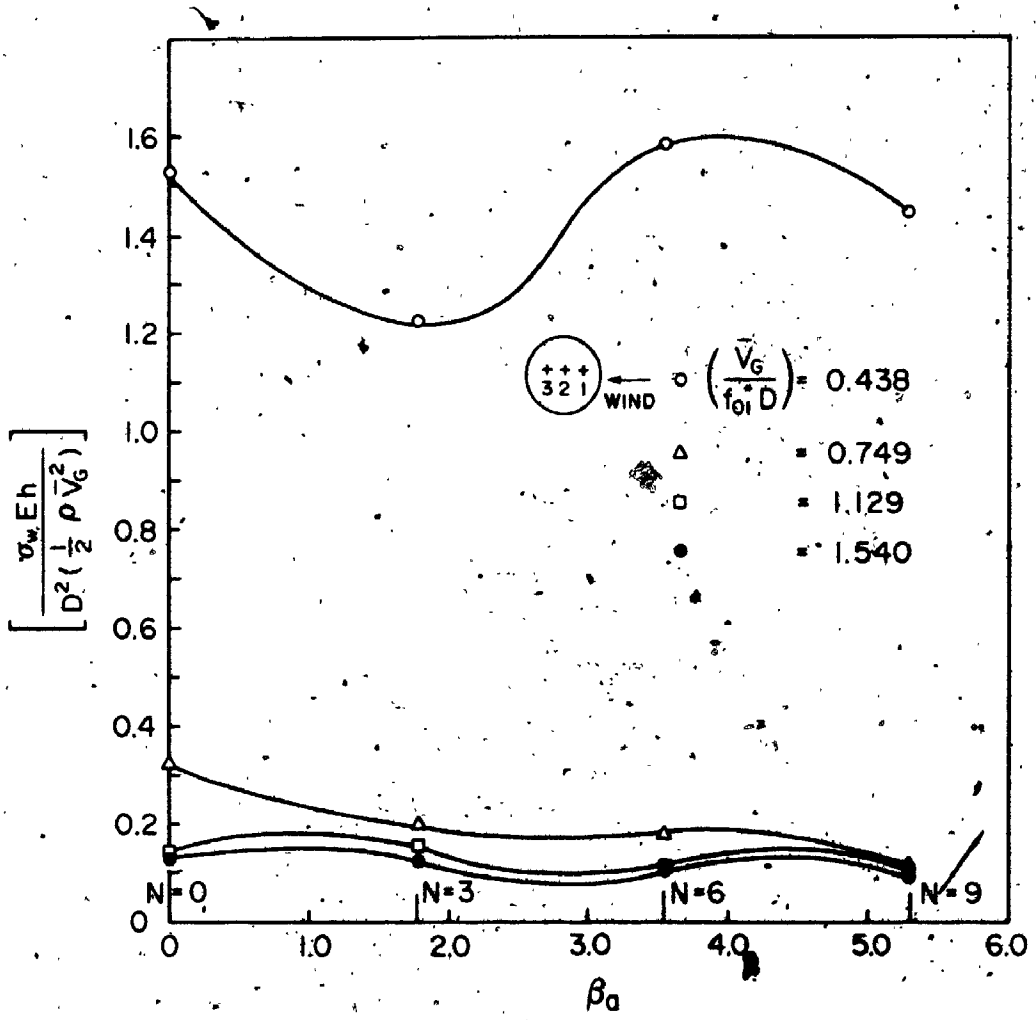

FIGURE 6.36 NON - DIMENSIONAL RMS RESPONSE AT CENTRE r/a = 0.0 WITH AREA PARAMETER AT DIFFERENT VELOCITIES (PROBE NO. 2)

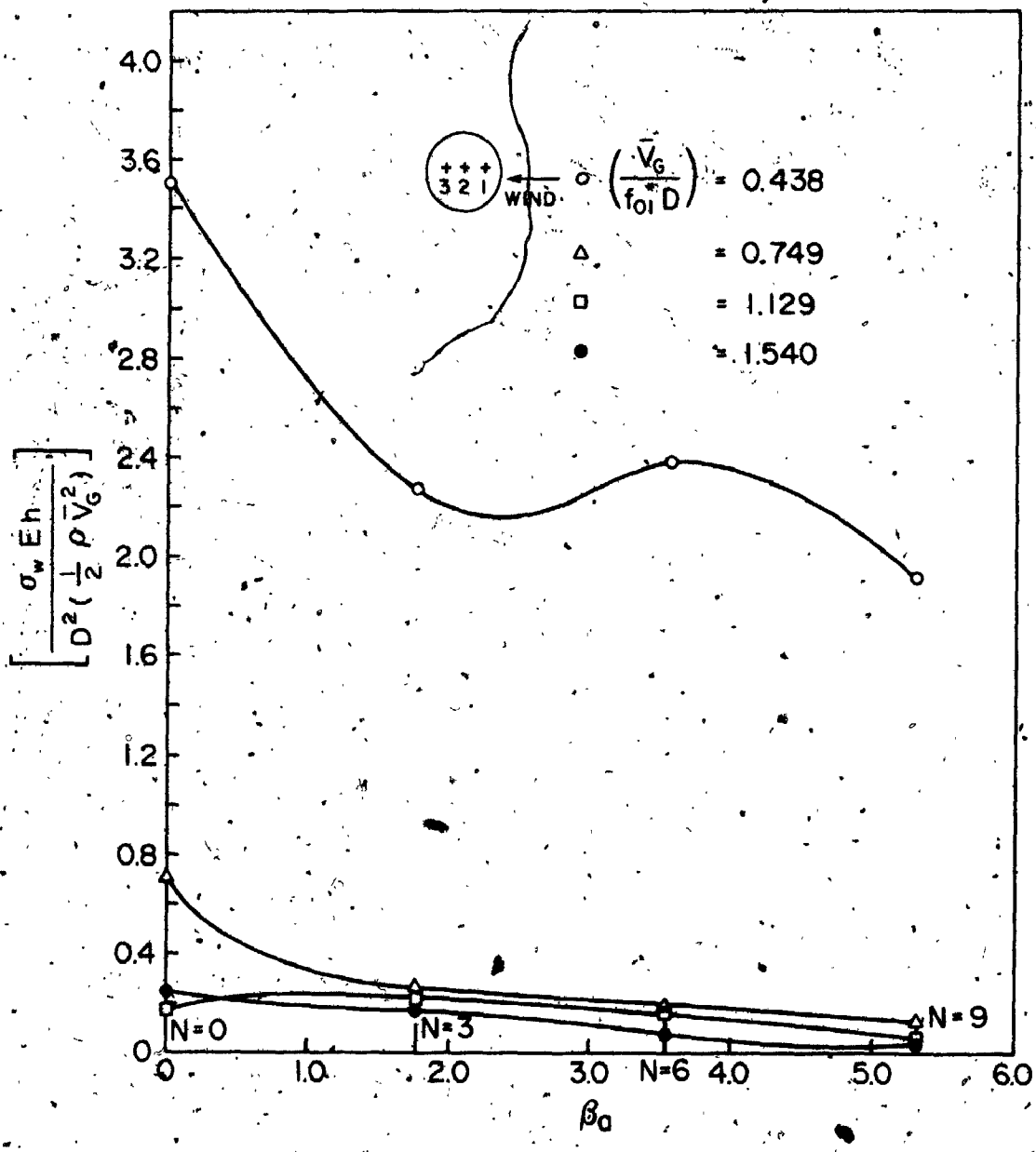

FIGURE 6.37 NON DIMENSIONAL RMS RESPONSE AT $r/a = 0.436$ WITH AREA PARAMETERS AT DIFFERENT WIND VELOCITIES (PROBE NO. 1)

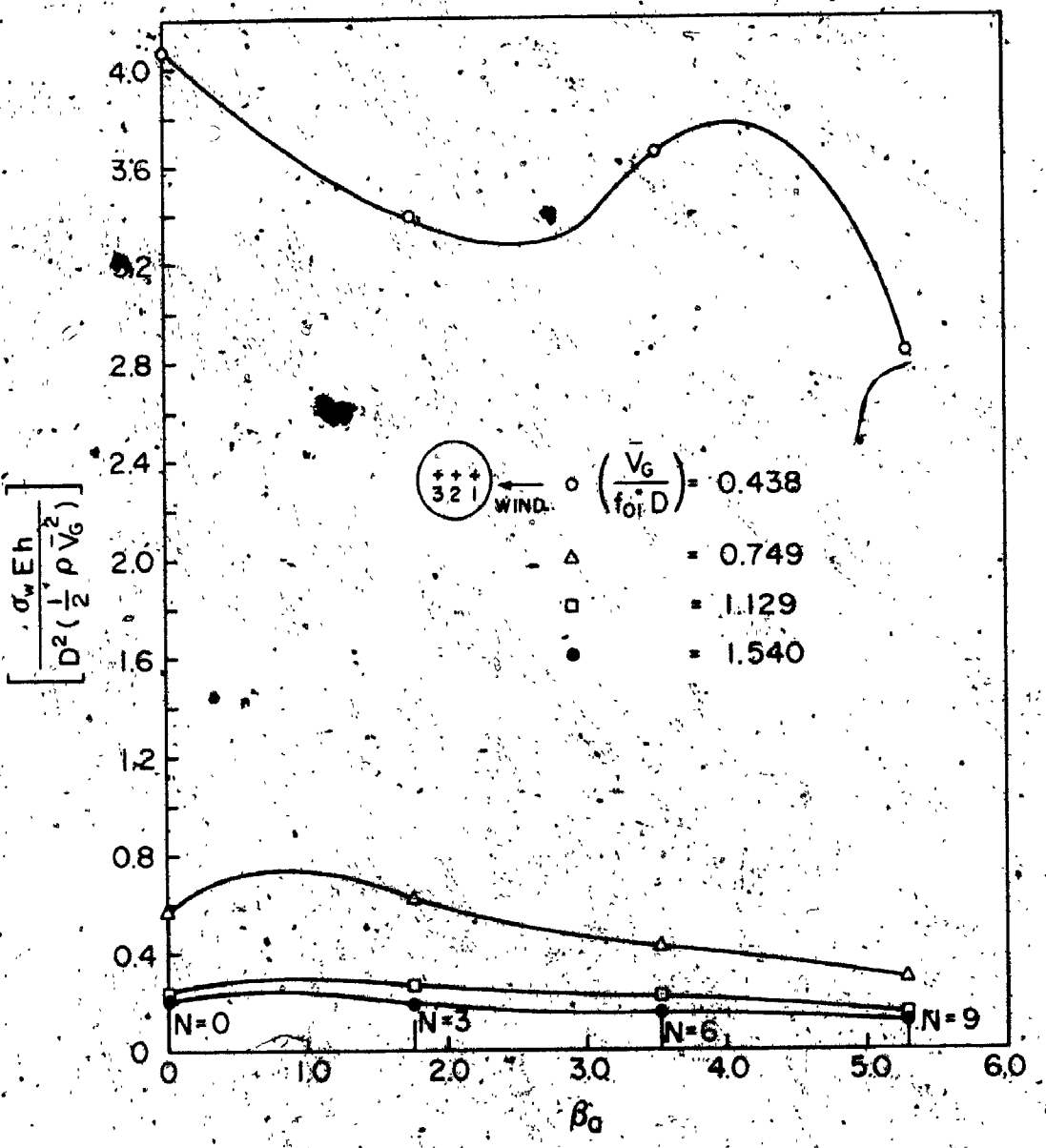

FIGURE 6.38 NON DIMENSIONAL RMS RESPONSE AT r/a = 0.436 WITH AREA PARAMETER AT DIFFERENT VELOCITIES. (PROBE NO. 3)

the frequency of the fundamental symmetric mode f_{01} decreases with the decrease of the area parameter β_a, the acoustic damping decreases, resulting accordingly in the decrease of the total damping of mode f_{01} while the damping of modes f_{11}, f_{21} and f_{02} are slightly affected.

In wind tunnel tests, the structural, acoustical and aerodynamic damping ratios for different modes of vibration at different wind velocities and area parameters are presented in Table 6.7.

For the open case (N = 9), the total damping ratio for mode f_{01} varies between 8% and 12% depending on wind velocity, and for modes f_{11}, f_{21} and f_{02} it is about 1.5% regardless of wind velocity.

Referring to Table 6.4, which gives the structural and acoustical damping ratio, the positive aerodynamic damping ratio for mode f_{01} varies between 5% and 10% (very high) depending on wind velocity and for the other modes it is about 0.10%, regardless of wind velocity. This experimental result is in general agreement with theoretical analysis conducted in Chapter 5.

6.6.1.6 Effect of Wind Velocity and Cavity on the Internal Pressure Coefficients

The variation of the internal pressure coefficients

TABLE 6.7 Total Damping Ratios for Different Modes and Area of Openings at Different Wind Speeds and Angle of Attack

Number	Mode f_{nm}	Resonant Frequency Hz at r/a= 0.0	Resonant Frequency Hz at r/a= 0.436	Area Parameter $\beta_a = \frac{NA_o}{A_c} \times 100$	Wind Velocity ft/sec	Angle of Attack θ	Total Damping Ratio $D_{t_{nm}}$ % at r/a=0.0	Total Damping Ratio $D_{t_{nm}}$ % at r/a=0.436
1	f_{01}	22.30	22.70	5.30	28.0	90°	8.77	6.90
2	f_{01}	21.70	21.70	5.30	28.0	45°	9.91	13.51
3	f_{01}	22.50	21.90	5.30	28.0	0°	9.57	12.50
4	f_{01}	18.70	-	3.54	28.0	0°	4.17	-
5	f_{11}	-	49.20	5.30	28.0	45°	-	1.59
6	f_{11}	-	48.60	0.0	28.0	0°	-	1.20
7	f_{11}	-	45.70	5.30	38.0	45°	-	1.71
8	f_{21}	-	53.5	5.30	28.0	45°	-	1.46
9	f_{21}	-	53.90	3.54	28.0	0°	-	2.90
10	f_{21}	-	54.70	5.30	38.0	90°	-	1.43
11	f_{02}	58.0	-	5.30	28	45°	-	1.01
12	f_{02}	57.6	-	0.0	28	45°	-	1.02

(1 ft = 0.4038 m)

(mean and standard deviation) are presented in Table 6.6.

In this table, the internal mean pressure coefficient varies between -0.2 and -0.63 and depends strongly on wind velocity and the area parameter β_a, and little on the angle of wind attack. The rms of the internal pressure coefficient was found to vary between 0.05 and 0.13, also depending strongly on the wind velocity and the area parameter and little on the wind angle of attack.

For the closed case (N = 0), the internal mean pressure coefficient is about -0.20. This value is used by the Swiss Code [97] in specifying the mean internal pressure coefficient for low buildings.

6.6.2 Hyperbolic Paraboloid Aeroelastic Model

The mean and rms total response for the Calgary Olympic Coliseum model are presented in Table 6.8 and the spectra of response at r/a = 0 and at r/a = 0.436 are presented in Figures 6.39 to 6.42.

For this model, it was observed that the largest total mean response occurred at r/a = -0.436, at wind velocity 30.18 ft/sec (= 9.20 m/s) and angle of incidence $\theta = 0°$. The largest total rms response was observed at model centre (r/a = 0) with $\theta = 0°$ to 90° and wind velocity 10.25 ft/sec (= 3.124 m/s). This response was

the largest over all the roof and was of the order of the mean response:

6.6.2.1 Effect of Wind Velocity and Angle of Attack on Response

Figures 6.43 to 6.45 and Figures 6.46 to 6.48 show the variation of the dimensionless total mean and standard deviation response respectively, at different locations on the roof and with wind velocity at different angles of attack.

These figures show that the maximum total mean response exists at the leeward position of r/a = 0.436 of the roof, but, unlike the shallow (flat) roof, the mean response was always negative, i.e. upwards, except when the wind velocity was very high (30 ft/sec, 9.144 m/s) and the angle of attack was $\theta = 90°$, when a positive (downward) response was observed. The maximum total rms response of the hyperbolic paraboloid model was observed at the centre, while that of the shallow (flat) roof was at location r/a = 0.436.

6.6.3 Comparison Between the Response of the Simplified Flat Model and the Hyperbolic Paraboloid Model Under Wind Loading

The response results obtained from the experimental tests conducted for the simplified shallow (flat) model

and the hyperbolic paraboloid model are presented in Tables 6.5 and 6.8.

In these tables it appears that the response of the flat roof is about 6 to 10 times the response of the hyperbolic paraboloid model under the same conditions (wind velocity and angle of attack). This significant and anticipated experimental result is in general agreement with the theoretical analysis conducted in Chapter 4.

TABLE 6.8 RESPONSE OF CALGARY ROOF MODEL UNDER DIFFERENT WIND VELOCITIES AND ANGLE OF ATTACK (OPEN TERRAIN)

No.	Wind Velocity ft/sec	Direction $\theta°$	Response (inch x 10^{-3})					
			At r/a = 0		At r/a = +0.436		At r/a = -0.436	
			Mean $\bar{w}$	RMS σ_w	Mean $\bar{w}$	RMS σ_w	Mean $\bar{w}$	RMS σ_w
1	10.25	0°	-1.90	2.80	-0.6	0.8	-2.0	0.2
2		45°	-1.20	3.10	-0.6	0.8	-1.6	0.4
3		90°	+0.10	2.50	-0.2	0.4	-0.8	1.0
4	20.40	0°	-1.20	1.60	0.0	0.20	-2.2	0.2
5		45°	-1.80	1.00	-0.60	1.00	-1.6	0.4
6		90°	+2.30	1.50	+0.4	0.0	-0.6	1.2
7	30.18	0°	-0.2	2.30	+1.0	0.20	-2.4	0.4
8		45°	-2.30	1.70	-0.80	1.0	-1.8	0.2
9		90°	+5.90	1.60	+1.60	1.0	0.0	1.4

(1 inch = 0.0254 m/s ; 1 ft/sec = 0.3048 m/s)

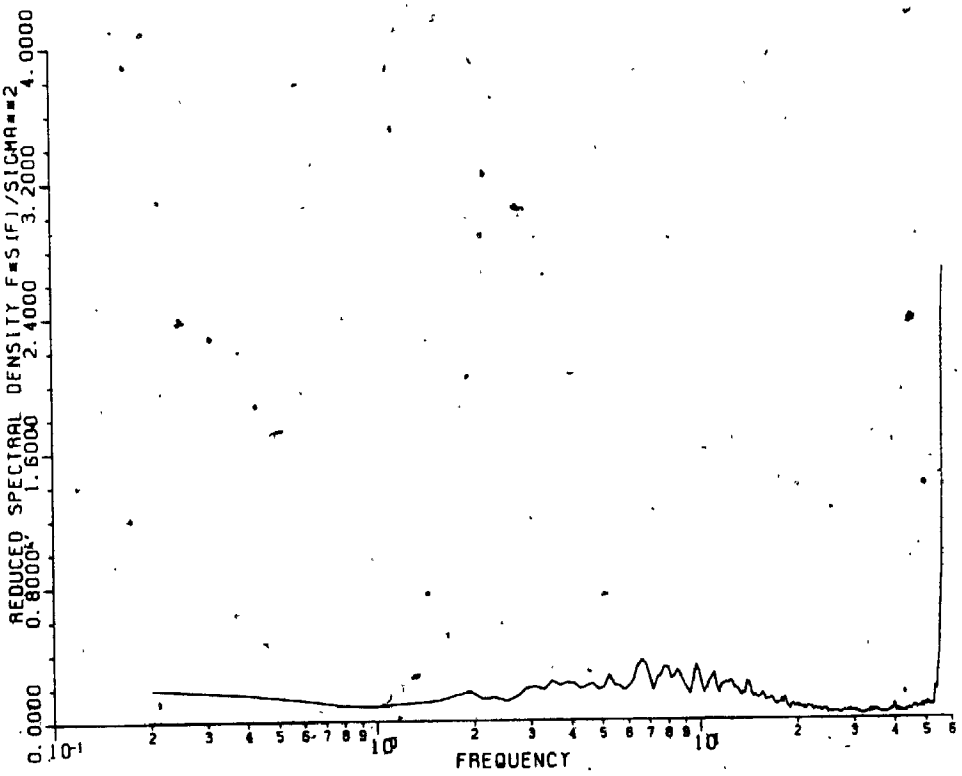

FIGURE 6.39 Power Spectrum of Response of the Hyper Model at r/a = 0, $\theta = 0°$, $\bar{V}_G$ = 30 ft/sec

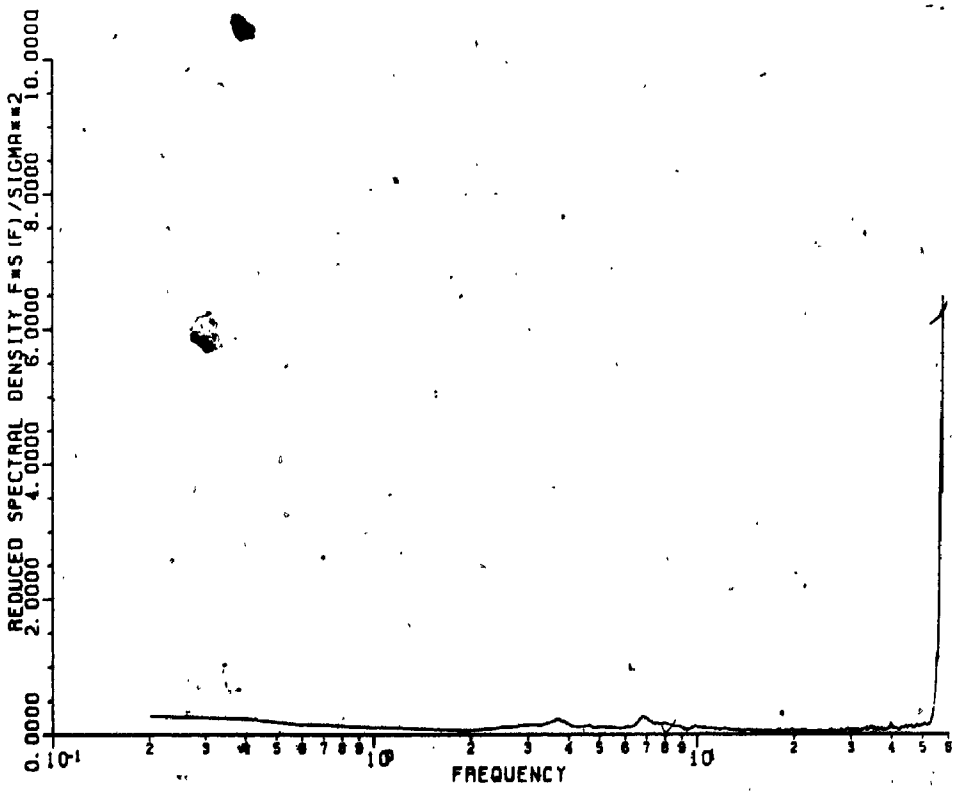

FIGURE 6.40 Power Spectrum of Response of the Hyper Model at r/a = 0, $\theta = 45°$, $\bar{V}_G$ = 30 ft/sec

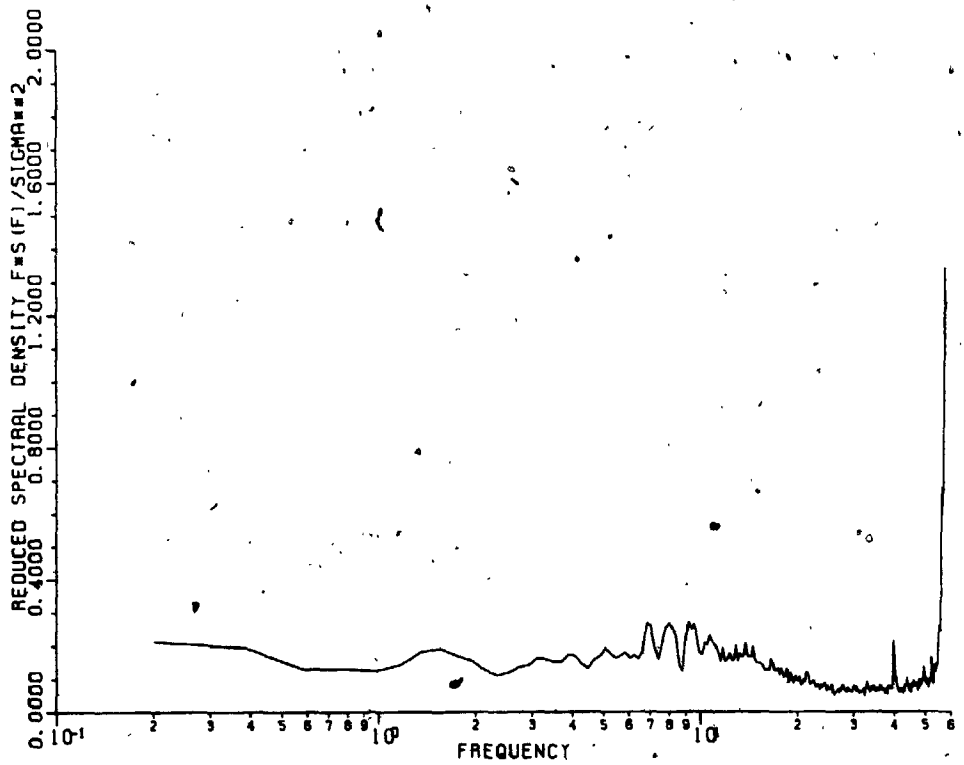

FIGURE 6.41 Power Spectrum of Response of Hyper Model at r/a = 0.436, $\theta = 0°$, $\bar{V}_G$ = 30 ft/sec

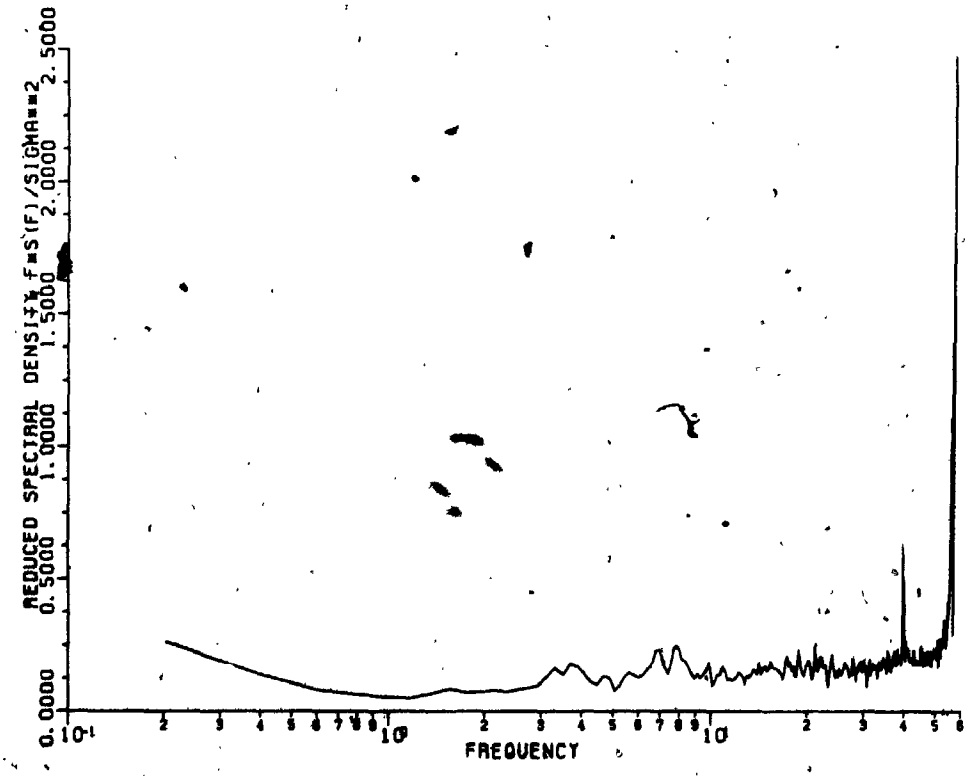

FIGURE 6.42 Power Spectrum of Response of Hyper Model at r/a = 0.436. $\theta = 45°$, $\bar{V}_G$ = 30 ft/sec

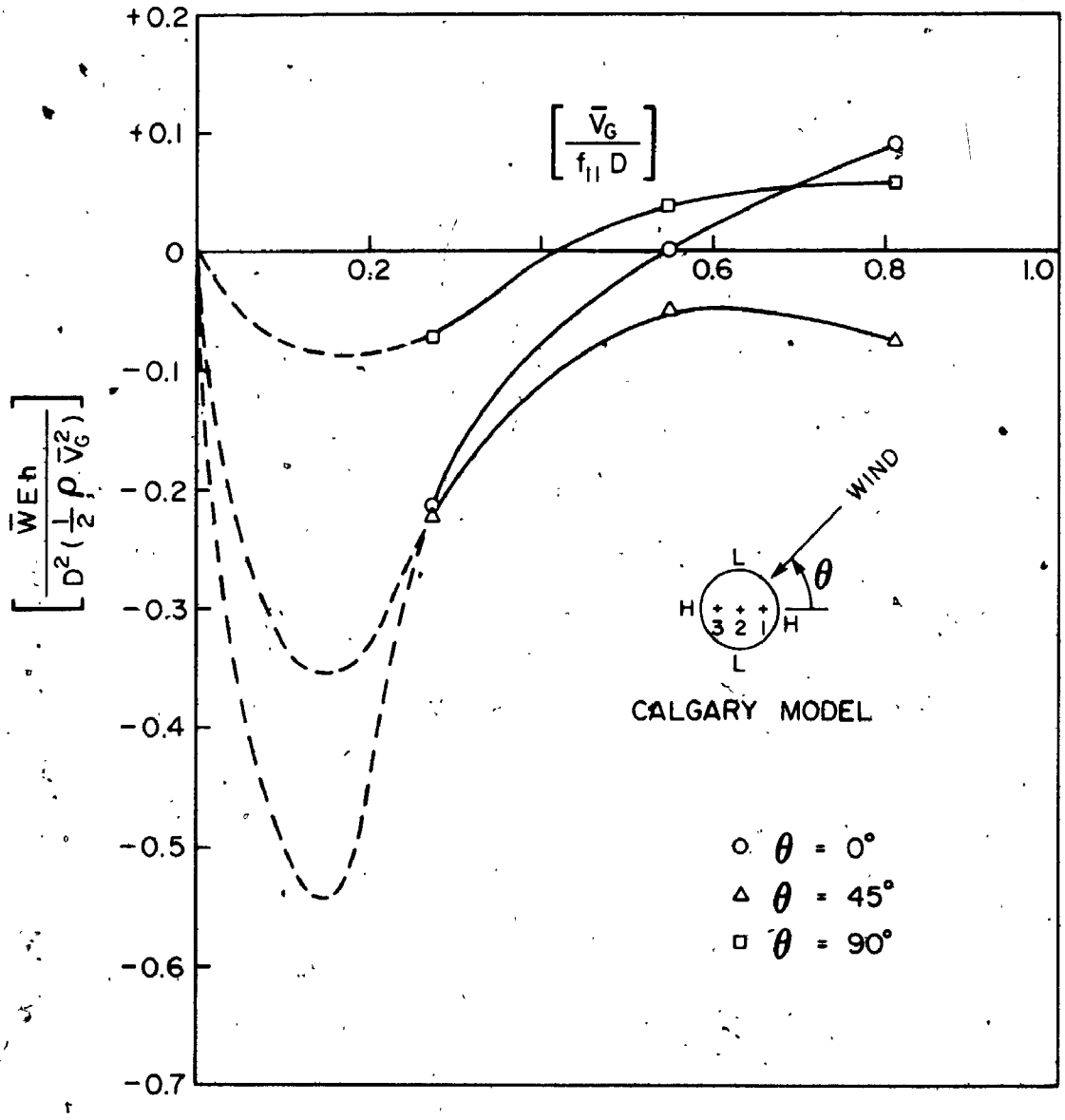

FIGURE 6.43 NON DIMENSIONAL MEAN RESPONSE AT r/a = 0.436 (PROBE 1) WITH WIND VELOCITY AT DIFFERENT ANGLES OF ATTACK, (OPEN TERRAIN)

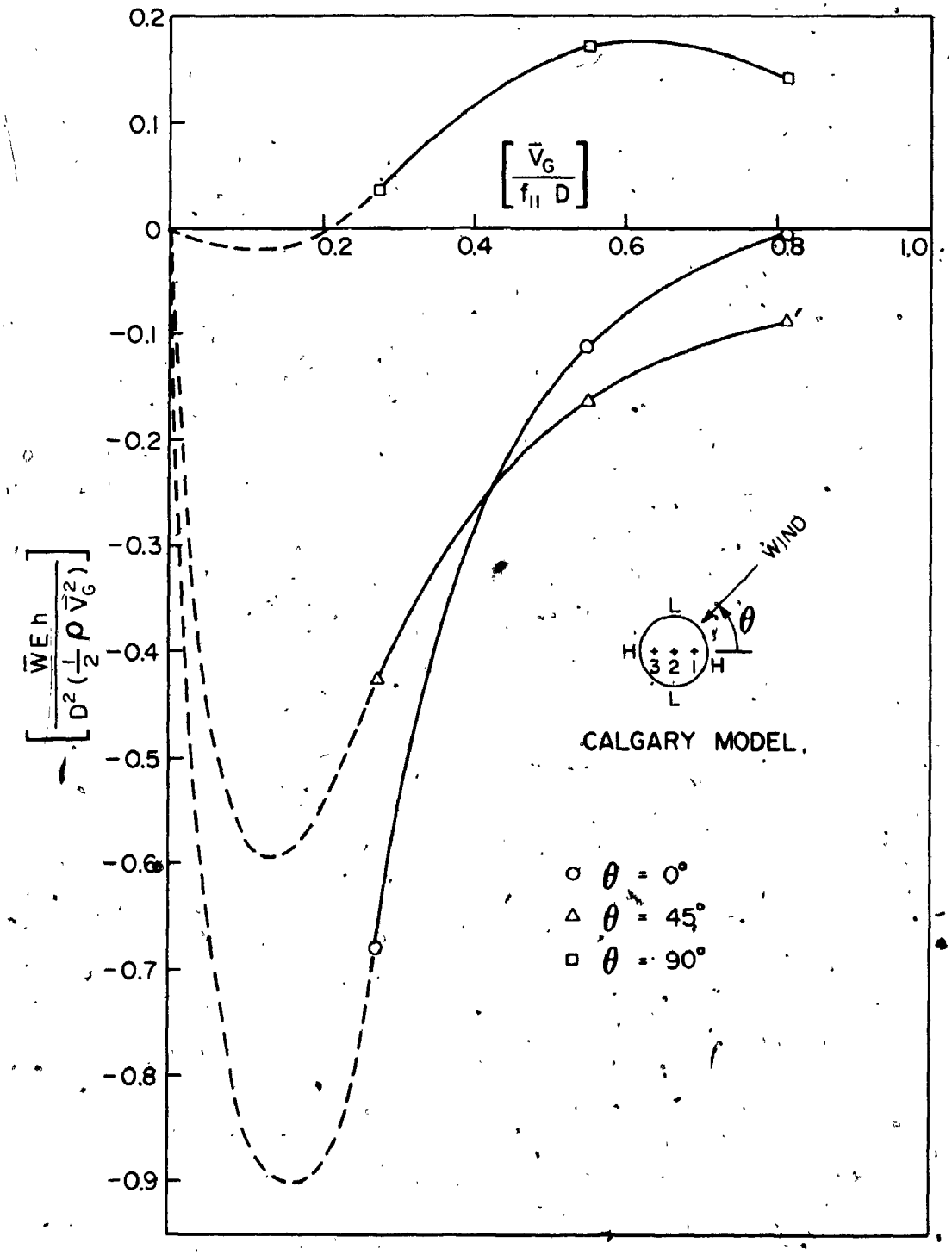

FIGURE 6.44 NON DIMENSIONAL MEAN RESPONSE AT r/a = 0 (PROBE 2) WITH WIND VELOCITY AT DIFFERENT ANGLES OF ATTACK, (OPEN TERRAIN)

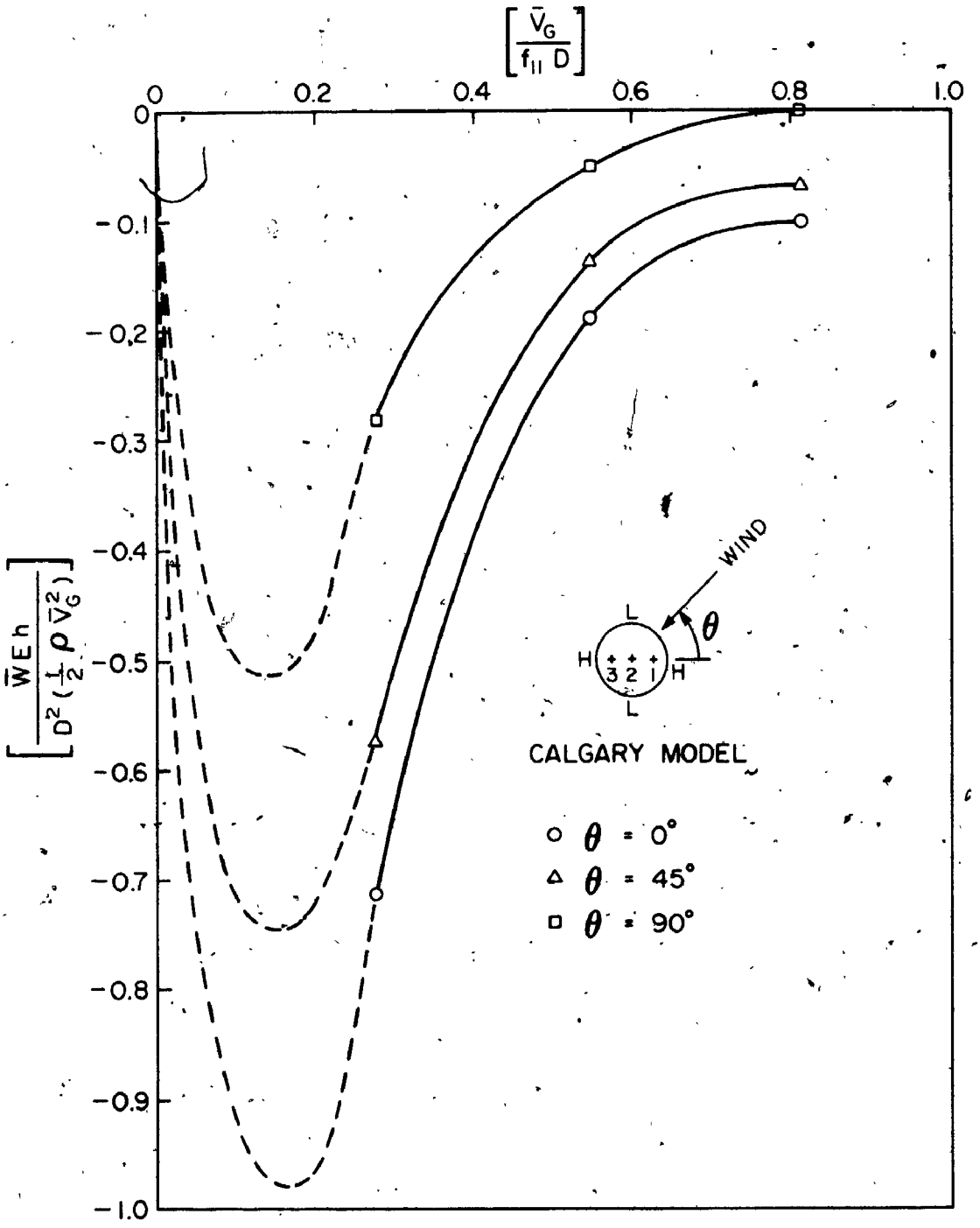

FIGURE 6.45 NON DIMENSIONAL MEAN RESPONSE AT r/a = 0.436, (PROBE 3) WITH WIND VELOCITY AT DIFFERENT ANGLES OF ATTACK, (OPEN TERRAIN)

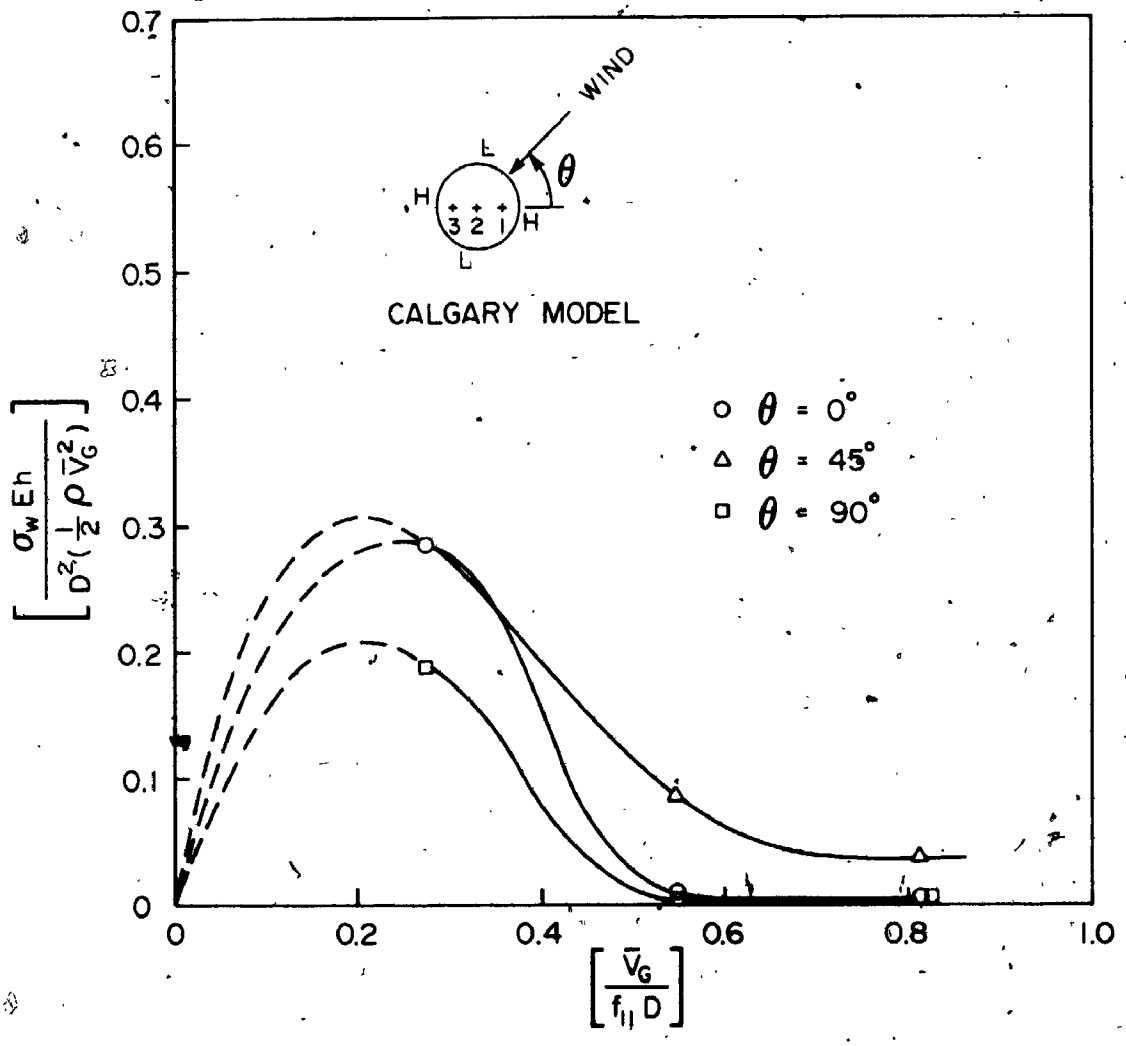

FIGURE 6.46 NON DIMENSIONAL RMS RESPONSE AT r/a = 0.436 (PROBE 1) WITH WIND VELOCITY AT DIFFERENT ANGLES OF ATTACK, (OPEN TERRAIN)

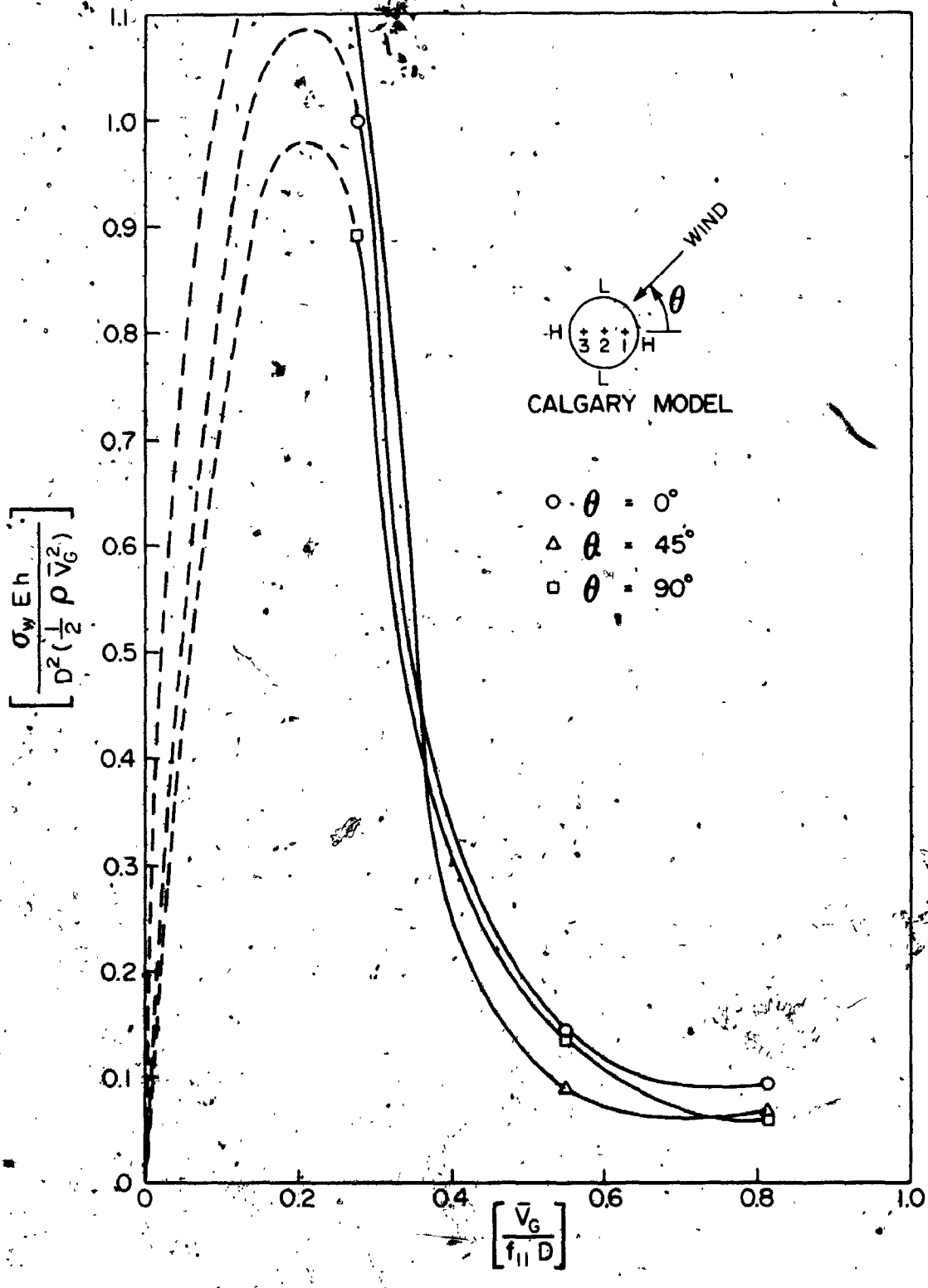

FIGURE 6.47 NON DIMENSIONAL RMS RESPONSE AT r/a = 0 (PROBE 2) WITH WIND VELOCITY AT DIFFERENT ANGLES OF ATTACK, (OPEN TERRAIN)

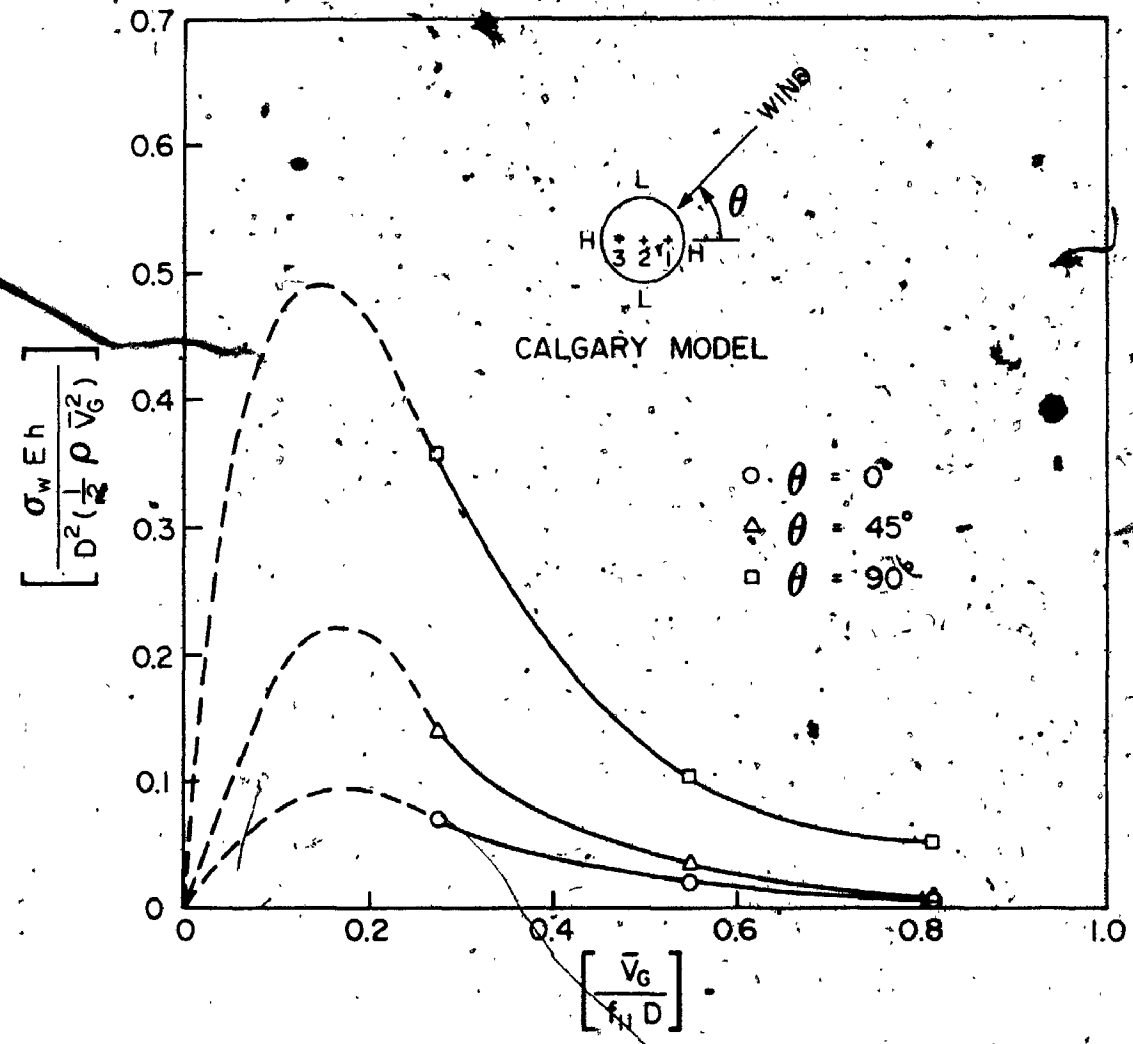

FIGURE 6.48 NON DIMENSIONAL RMS RESPONSE AT r/a = 0.436 (PROBE 3) WITH WIND VELOCITY AT DIFFERENT ANGLES OF ATTACK, (OPEN TERRAIN)

CHAPTER 7

SUMMARY AND CONCLUSIONS

7.1 SUMMARY

1. A nonlinear theory is developed to calculate the response of a single hanging cable to the effect of static load. The solution obtained may be linearized or adapted to apply to cables that are initially taut and flat. It is found that the nonlinear response is governed by the dimensionless parameter $\lambda^2 = (\frac{mg}{H_o})^2 \ell / (\frac{H_o L_e}{EA})$, in which mg = weight of cable per unit length, ℓ = horizontal span of cable, H_o = initial tension in cable, E = modulus of elasticity of cable material, A = cable cross-sectional area, L_e = cable extended length ($= \eta L_o$), L_o = cable original length and η = the extension factor.

Basically, this dimensionless parameter accounts for geometric and elastic effects and is of fundamental importance in the static response of suspended cables. When $mg \ll H_o$, $\lambda^2 \ll 1$, the increase in cable tension $\Delta H_o \to 0$, and the classical linear theory of the taut cable is recovered.

From the above stated theory, the static response of certain types of suspension roofs may be calculated (one way, single layer hanging roof).

2. A nonlinear theory is developed to calculate the response of two types of suspension roofs (rectangular and circular flat cable roofs) to static loads. The solution obtained for the rectangular type is governed by a dimensionless parameter $\bar{\lambda}^2 = (\frac{2Eh}{H_o})(\frac{2q_o a}{H_o})$, where h is the thickness of the roof and a its longer dimension. When the ratio of roof load per unit area/initial tension, q_o/H_o, is small, the increase in roof tension due to additional loading is negligible and the response may be obtained from classical linear theory; on the other hand, when this ratio is large, the response is strongly nonlinear.

This solution obtained for the rectangular flat roof is based on work by Timoshenko and Goodier using a membrane analogy.

The nonlinear static response for the circular flat roof is obtained from the Von Karman equations for clamped thin plates. The solution of the nonlinear equations was obtained by making some approximations. The results obtained are in agreement with results of other analyses.

3. Based on the assumption that the additional displacement due to additional loading on a curved surface is small, a linear theory is developed to estimate the static

response of rectangular and circular curved roofs to additional static and/or quasi-static loading. The equations formulated are based on work by Printer. The solutions obtained are in agreement with results derived using different approaches.

4. A theory is developed for the free vibration of an elliptical flat tension roof, utilizing elliptical coordinates. From the solution obtained it is found that the free undamped vibration of the elliptical flat roof is governed by the ratio of roof mass per unit area/initial tension, (m/T_o), and the semifocus of the ellipse. When these parameters are small, the elliptical flat roof may be approximated by an equivalent circular flat roof; on the other hand, when these parameters are large, the elliptical roof vibrates in a completely different way; the nodal circles in the mode shapes of the circular roof are replaced by nodal confocals and the nodal diameters are replaced by nodal hyperbolas.

5. A theory is developed for the free undamped vibration of a rectangular hyperbolic paraboloid tension roof, based on work by Printer.

From the analysis conducted, there are two forms of solution possible for this type of suspension roof.

The first type of solution is that of the rectangular flat roof (i.e., independent of the rise of the sag and the fall of the hogg). In the second solution, the symmetric modes of vibration are dependent on the increase in roof tension due to vibration while the asymmetric modes are independent of it.

6. The dynamic behaviour of circular hyperbolic paraboloid tension roofs was not known. In this work a theory is developed for determining its eigenfunctions and eigenvalues; the solution can be obtained after some approximation.

It is found by this theory that the asymmetrical vibration modes of the circular hyperbolic paraboloid are independent of the increase in tension due to vibration and are the same as for the circular flat roof, but the symmetric modes are completely different and are, additionally, tension dependent. In the solution obtained for the eigenvalues, it is found that the natural frequency of the first symmetric mode of the hyperbolic paraboloid roof is about three times that of the flat roof (i.e., the stiffness is about nine times greater). Also, in the solution obtained for the eigenfunctions, it is found that the nodal circles in the symmetric mode shapes of the hyperbolic paraboloid are shifted toward or away from the centre of the roof

depending on the argument of the Bessel function $J_n(\frac{\omega a}{v})$.

The results obtained for both the rectangular and circular hyperbolic paraboloid tension roofs emphasizes that, if the roofs are shallow, they may behave similar to rectangular and circular flat roofs respectively in free vibration.

7. The enclosure below a cable tension roof has a great effect on its frequency response, especially for those modes which cause a change in the air volume within the enclosure. It is found that the enclosure has a strong effect on the frequency of the fundamental mode, f_{01}, and causes the mode to be suppressed as the number of wall openings in the enclosure decreases, while the other modes are slightly affected.

It is found from free vibration and wind tunnel tests for the shallow (flat) circular roof model that the dynamic response in the fundamental mode with natural frequency f_{01} decreases with the decrease of area openings which provide contributions to the mass and the stiffness of a roof. This contribution depends on the number, shape and area of the wall openings and on the area and mass of the roof.

This problem may be treated mathematically by

representing the enclosure by an equivalent Helmholtz resonator. The theoretical analysis conducted and based on the above mathematical treatment is in general agreement with experimental test results.

8. The air above a cable tension roof and within the enclosure below it has a great effect on the total damping ratios of the roof. The relative movement of the roof with respect to the turbulent wind gives rise to a positive aerodynamic damping term which has a great effect on the total damping ratio of the fundamental mode of vibration f_{01}, and little effect on damping of other important modes f_{11}, f_{21} and f_{02}.

It is found that the aerodynamic damping for the mode with frequency f_{01} varies between 5% and 10% (very high) and depends on wind velocity and area parameter β_a; for other modes it is about 0.10% (small), and slightly affected by wind velocity and area parameter. Also, it is found in free vibration tests that the total structural and acoustical damping (due to roof movement) for the mode with natural frequency f_{01} is dependent on the area parameter β_a and decreases with the decrease in area parameter, while other modes are slightly affected.

These experimental results are in reasonable agreement with the air-roof interaction analysis.

9. The total dynamic response of tension roofs cannot be estimated by purely static analysis considerations. It is found that the resonant part of the response is about 250% that of the quasi-static response and does not necessarily increase with wind velocity. It is found from wind tunnel tests that when the characteristic wave length of the wind turbulence (gust size $\bar{V}/f$) is about 0.33 that of the diameter of the roof D (i.e. $\frac{\bar{V}}{fD} \simeq 0.33$), a peak response occurs for all values of area parameter and over all the roof surface.

This significant finding implies that the large vibration response of cable tension roofs to turbulent wind loading does not necessarily occur at high wind velocity but may depend on how the pressure induced by turbulent wind is distributed over the surface of the roof.

10. The dynamic response of cable tension roofs to turbulent wind loading is governed by the shape of the roof. For the circular flat roof model, the largest mean response is positive, i.e. downward, and is observed at the leeward position of $r/a = 0.436$ on the roof: this response can be up to 250% that of the response at the roof centre. This response occurs between $\theta = 0°$ and $45°$ with the wind direction at which it occurs depending strongly on the wind velocity.

For the hyperbolic paraboloid tension roof model, the maximum mean response was observed at the leeward position of r/a = 0.436 on the roof. Unlike the flat roof model, the response of the hyperbolic paraboloid roof model was always negative, i.e. upward, except when the velocity was very high with wind direction $\theta = 90°$. Under this particular condition, a positive response was observed.

The maximum rms response for the hyperbolic paraboloid roof model was observed at the centre, while the flat roof model had a maximum rms response at r/a = 0.436.

11. From the described theoretical and experimental investigation, the response of cable tension roofs to turbulent wind loading can be predicted by using the dynamic response obtained by linear modal analysis superimposed on the static response. This depends on the pressure spectrum used. The suggested model for the pressure spectrum, which is adapted from previous work by the author, gives reasonable agreement with experiments. Its further development should be promising.

12. A real structure can be simulated successfully with an aeroelastic model in the wind tunnel provided that it is scaled correctly. It is found from the theoretical analysis conducted that the relative importance of the

restoring force owing to the compression and expansion of the air in the enclosure below the roof and to the initial tension applied to the roof can be expressed in terms of the dimensionless parameter $\alpha_o = \frac{\pi a^4 \rho c_o^2}{T_o V_o}$. Using this parameter, the volume scaling of the enclosure derived is $\lambda_{V_o} = \lambda_L^3/\lambda_V^2$ in which λ_L = the geometric scaling λ_V = the wind velocity scaling. This significant finding for simulating the dynamic stiffness of the cable roof structure is in full agreement with results obtained recently by others, using completely different analyses and approaches.

From wind tunnel test results, the response of the real structure may be evaluated.

13. When the enclosure below the tension roof model is simulated correctly, the internal pressure coefficients may be evaluated from wind tunnel tests.

It is found that the mean and standard deviation of the internal pressure coefficients are strongly dependent on the area parameter β_a and wind velocity and are little affected by model orientation with respect to wind direction. For a wind velocity of $\bar{V}_G$ = 28 ft/sec (= 8.534 m/s), it is found that the internal pressure coefficient is -0.43 when the area parameter β_a = 5.30% (N=9) and

decreases to -0.20 when β_a = 0% (N=0); the rms internal pressure coefficient is 0.09 for β_a = 5.30% and decreases to 0.04 for β_a = 0%. These values also change with a change in wind velocity.

The mean internal pressure coefficient measured for the closed case (β_a = 0) is in agreement with what is specified in some standards.

14. The dynamic response is assumed to be linear, and modal analysis is utilized to calculate the response. The response in each mode is evaluated and the total response is the summation of all modal contributions.

In free vibration tests, it is found that the important modes with frequencies f_{01}, f_{11}, f_{21} and f_{02} have well-separated frequencies.

This result facilitates the use of the modal analysis approach.

15. For the two models tested in the Boundary Layer Wind Tunnel under different wind velocities and terrain conditions, no flutter or other dynamic instability was observed.

16. The behaviour of a roof-cavity system with openings depends on its parameters and may fall between two limiting cases: a Helmholtz resonator if the roof is very rigid and a "Kettledrum" if the openings are absent.

7.2 CONCLUSIONS

The dynamic behaviour of cable tension roofs under turbulent wind loading is governed by wind turbulence, air enclosed underneath, wall openings and the shape, mass, initial tension and dimensions of the roof.

As the size of the openings decreases, the natural frequency of a circular shallow (flat) roof decreases, internal pressure drops and the total dynamic response increases. This increase in response is mainly due to the pressure(which is negative (suction))on the upper surface. It decreases with wind direction and becomes positive at leeward. The internal pressure is negative (suction) and decreases in magnitude with decrease of area openings, resulting in a larger net pressure downwards, especially at the leeward position, where the maximum positive response was observed in experiments at r/a = 0.436.

The increase in the rms response is mainly due to the disappearance of the volume displacement mode with frequency f_{01}. Regardless of the openings, the modes with frequencies f_{11} and f_{21} are always present and in fact, because of their existence, the maximum dynamic deflection is not at the centre but at about 0.436 of the radius. The directions of the nodal diameters of the modes with frequencies f_{11} and f_{21} vary (between $\theta = 0^{\circ}$ and 45°) giving rise to

anti-symmetric components relative to flow direction, this may be due to weak correlation between the wind fluctuations over the roof surface.

With large openings, the response is reduced due to the presence of mode with frequency f_{01} and the large increase in the internal pressure.

A remarkable conclusion for cable tension roofs is that the maximum dynamic response does not necessarily occur at high wind velocities; when the characteristic wave length of the turbulent wind, corresponding to the peak of the wind velocity spectrum, is about 0.33 the roof diameter, a significant (peak) response occurs.

In tension roofs, the dynamic deflection can exceed two to three times the static deflection due to wind. A generalized gust factor is not easy to obtain because the mode with frequency f_{01} corresponds to symmetrical loads while the modes with frequencies f_{11} and f_{21} correspond to antisymmetric loads. The former depends critically on wall openings while the latter does not. 'Cable tension roofs are flexible and their movement under turbulent wind creates additional positive acoustical and aerodynamic damping effects which have a great influence on response due to air changing volume mode with frequency f_{01}.

Therefore, a proper assessment of cable roof behaviour in turbulent wind should include the effects of wind turbulence, wall openings, air enclosure, shape, mass, initial tension and dimensions of the roof as well as the internal pressure changes due to roof movement.

Such assessment may be successfully achieved by testing a properly designed aeroelastic model, taking into account the dynamic stiffness due to the enclosed air below the roof. This becomes important in view of the variety of cable roof systems and the difficulty of proposing a general theory for their free vibration and dynamic response analysis.

7.3 RECOMMENDATION FOR FUTURE RESEARCH

Much remains to be done in the field of cable tension roofs. In the field of statics, nonlinear response under additional loading and material nonlinearity should be considered.

However, the majority of unanswered questions lies in the field of dynamics. The large changes in geometry of tension roofs under wind loading influence the pressure coefficients and therefore in wind tunnel experiments the pressures should be measured on vibrating models rather than rigid models.

For cable tension roofs, the change in curvature during vibration should be accounted for in the solution and the theory should consider dynamic nonlinearity.

A more rigorous theory should be formulated to account for the air-structure interaction.

Finally, full scale observations are needed, in order to clarify Reynolds number effects and other features of roof response in natural wind.

APPENDIX A

A.1 ELLIPTICAL COORDINATES (from References [75,80])

Polar coordinates, r, θ, Figure A.1, may be regarded as specifying the position of a point as the intersection of a circle radius r, and a radial line at angle θ from an initial line. A change from Cartesian to polar coordinates is affected by means of the equations

$$r = \sqrt{x^2+y^2} \tag{A.1}$$

and

$$\theta = \arctan\frac{y}{x} \tag{A.2}$$

The first Eq. (A.1), when r is given various constant values, represents the family of circles. The second, when θ is given various constant values, represents the family of radial lines.

Equations A.1 and A.2 are a special case of equations of the form

$$F_1(x,y) = \xi \tag{A.3}$$

and

$$F_2(x,y) = \eta \tag{A.4}$$

When definite constant values are given to ξ and η, these equations represent two curves which intersect, if $F_1(x,y)$, $F_2(x,y)$ are suitable functions. Different values

of ξ and η will yield different curves and a different point of intersection. Thus, each point in the xy plane will be characterized by definite values of ξ and η - the values which make the two curves given by Eqs. A.3 and A.4 pass through it - and ξ, η may be regarded as "co-ordinates" of a point. Since given values of ξ, η define the point by means of two intersecting curves, they are called "curvilinear coordinates".*

If Eqs. A.3 and A.4 are solved for x and y, we shall have two equations of the form

$$x = f_1(\xi,\eta) \tag{A.5}$$

and

$$y = f_2(\xi,\eta) \tag{A.6}$$

Consider the two equations

$$x = d\ \cosh\xi\ \cos\eta \tag{A.7}$$

$$y = d\ \sinh\xi\ \sin\eta \tag{A.8}$$

where d is a constant. Elimination of η yields

$$\frac{x^2}{d^2\cosh^2\xi} + \frac{y^2}{d^2\sinh^2\xi} = 1 \tag{A.9}$$

---

*The general theory of curvilinear coordinates was developed by G. Lame in the book "Lecons sur les coordonees curvilingnes", Gauthier-Villars, Paris, 1859.

If ξ is constant, this is the equation of an ellipse with semiaxes $d\cosh\xi$, $d\sinh\xi$, and with foci $x = \pm d$. For different values of ξ we obtain different ellipses with the same foci - that is, a family of confocal ellipses, Figure A.2. On any of these ellipses ξ is constant and η varies through a range 2π, as on a circle in polar coordinates r is constant and θ varies. In fact, in the present case, η is the eccentric angle of a point on the ellipse.* If, on the other hand, we eliminate ξ from Eqs. A.7 and A.8 by means of equation $\cosh^2\xi - \sinh^2\xi = 1$, we have

$$\frac{x^2}{d^2\cos^2\eta} - \frac{y^2}{d^2\sin^2\eta} = 1 \qquad (A.10)$$

For a constant value of η this represents a hyperbola having the same foci $\pm d$ as the ellipses. Thus, Eq. A.10 represents a family of confocal hyperbolas, on any one of which η is constant and ξ varies.

These coordinates ξ, η are called Elliptic Coordinates and are very useful in physical problems involving elliptic boundaries.

The two equations (A.7) and (A.8) are equivalent to

* If a,θ are the polar coordinates of a point on the circle circumscribing an ellipse of semiaxes a, b, the perpendicular from this point to the x axis intersects the ellipse at the point $x = a\cos\theta$, $y = b\sin\theta$. θ is called the eccentric angle of the point on the ellipse.

$$x + iy = d \cosh(\xi+i\eta) \qquad (A.11)$$

in which the real part gives $x = d \cosh\xi \cos\eta$ and the imaginary part gives $y = d \sinh\xi \sin\eta$.

Referring to Figure A.2, at the extremities of the major axis of any confocal ellipse, $\eta = 0$, , $y = 0$ and $x = \pm d \cosh\xi = \pm a$. At the ends of the minor axis, $\eta = \frac{1}{2}\pi, \frac{3}{2}\pi$, $y = \pm d \sinh\xi = \pm b$. If e is the eccentricity of the ellipse, where $d = ae$, so $\cosh\xi = e^{-1}$, and when $e \to 1$, $\xi \to 0$, while $a \to d$. Thus, a long elliptical cylinder degenerates to a ribbon of equal length, whose width is 2d, i.e. the interfocal distance, Figure A.3. With a constant, if $e \to 0$, $\xi \to \infty$, and the ellipse tends to a circle of radius a.

Since $d = ae$, $d \to 0$, the foci tend to coalesce at the origin, and $h\cosh\xi \to h\sinh\xi \to a$. If d is constant, as $a \to \infty$, $\xi \to \infty$, and $e \to 0$, so that the confocal ellipses tend to become concentric circles. Now Eq. A.10 may be written as

$$\frac{x^2}{\cos^2\eta} - \frac{y^2}{\sin^2\eta} = d^2$$

As $h \to 0$, $y/x \to \pm \tan\eta$, so $\eta \to \theta$, $\cos\eta \to \cos\theta$, the confocal hyperbolas ultimately become radii of the circle and make angles θ with x axis, Figure A.4.

A.2 ARC LENGTH OF THE ELLIPTICAL COORDINATES

Referring to Figure A.5, the hyperbolic and elliptic arc lengths are, respectively:

$$dS_1 = [(\frac{\partial x}{\partial \xi})^2 + (\frac{\partial y}{\partial \xi})^2]^{1/2} d\xi \qquad (A.12)$$

and

$$dS_2 = [(\frac{\partial x}{\partial \eta})^2 + (\frac{\partial y}{\partial \eta})^2]^{1/2} d\eta. \qquad (A.13)$$

Now,

$$\frac{\partial x}{\partial \xi} = d \sinh\xi \cos\eta \qquad \frac{\partial y}{\partial \xi} = d \cosh\xi \sin\eta$$

and $$\frac{\partial x}{\partial \eta} = -d \cosh\xi \sin\eta \qquad \frac{\partial y}{\partial \xi} = d \sinh\xi \cos\eta$$

Substituting into Eqs. A.12 and A.13 gives the hyperbolic arc length as,

$$dS_1 = d[\cosh^2\xi \sin^2\eta + \sinh^2\xi \cos^2\eta]^{1/2} d\xi$$

$$= d(\cosh^2\xi - \cos^2\eta)^{1/2} d\xi$$

$$= \frac{d}{\sqrt{2}} (\cosh 2\xi - \cos 2\eta)^{1/2} d\xi \qquad (A.14)$$

And the elliptical arc length is:

$$dS_2 = \frac{d}{\sqrt{2}} (\cosh 2\xi - \cos 2\eta)^{1/2} d\eta \qquad (A.15)$$

Similarly, the distance of any point (x,y) from the origin, expressed in elliptical coordinates, is

$$r = (x^2+y^2)^{1/2} = d[\cosh^2\xi\cos^2\eta + \sinh^2\xi\sin^2\eta]^{1/2}$$

$$= d(\cosh^2\xi - \sin^2\eta)^{1/2}$$

$$= \frac{d}{\sqrt{2}} (\cosh 2\xi + \cos 2\eta)^{1/2} \qquad (A.16)$$

When ξ is large enough, $\cosh\xi \to \sinh\xi \to \frac{1}{2}e^{\xi}$, so with d constant $dS_1 \sim rd\xi \sim dr$, $dS_2 \sim rd\eta$ and $dS_1 dS \sim rdrd\eta$, as in polar coordinates.

A.3 TRANSFORMATION OF LAPLACIAN OPERATOR ∇^2, TO ELLIPTICAL COORDINATES

Write $Z = x + iy = d\cosh(\xi+i\eta)$, and $\bar{Z} = x-iy = d\cosh(\xi-i\eta)$, then $Z\bar{Z} = x^2 + y^2$, and

$$\frac{4\partial Z\bar{Z}}{\partial Z\partial\bar{Z}} = \left(\frac{\partial^2}{\partial x^2} + \frac{\partial^2}{\partial y^2}\right) Z\bar{Z} \qquad (A.17)$$

Putting $\xi = \xi+i\eta$, $\bar{\xi} = \xi-i\eta$, we get

$$Z = d\cosh\xi,\ \bar{Z} = d\cosh\bar{\xi} \text{ and } \xi\bar{\xi} = \xi^2+\eta^2.$$

Thus,

$$\frac{\partial\xi}{\partial Z} = \frac{1}{d\sinh\xi},\ \frac{\partial\bar{\xi}}{\partial\bar{Z}} = \frac{1}{d\sinh\bar{\xi}}$$

and

$$\frac{4\partial^2\xi\bar{\xi}}{\partial\xi\partial\bar{\xi}} = \left(\frac{\partial^2}{\partial\xi^2} + \frac{\partial^2}{\partial^2\eta^2}\right)\xi\bar{\xi}.$$

So

$$\frac{\partial \xi}{\partial z} = \frac{1}{d \sinh \xi} \frac{\partial}{\partial \xi}, \quad \frac{\partial}{\partial \bar{z}} = \frac{1}{d \sinh \bar{\xi}} \frac{\partial}{\partial \bar{\xi}}$$

and $$\frac{4\partial^2}{\partial \xi \partial \bar{\xi}} = \frac{\partial^2}{\partial \xi^2} + \frac{\partial^2}{\partial \eta^2}$$

Hence,

$$\frac{4\partial^2}{\partial z \partial \bar{z}} = \frac{\partial^2}{\partial x^2} + \frac{\partial^2}{\partial y^2} = \frac{4}{d^2(\cosh 2\xi - \cos 2\eta)} \left(\frac{\partial^2}{\partial \xi^2} + \frac{\partial^2}{\partial \eta^2}\right)$$

or

$$\nabla^2 = \left(\frac{\partial^2}{\partial x^2} + \frac{\partial^2}{\partial y^2}\right)$$

$$= \frac{2}{d^2(\cosh 2\xi - \cos 2\eta)} \left(\frac{\partial^2}{\partial \xi^2} + \frac{\partial^2}{\partial \eta^2}\right) \qquad \text{(A.18)}$$

Equation A.18 is the Laplacian operator expressed in elliptical coordinates ξ, η.

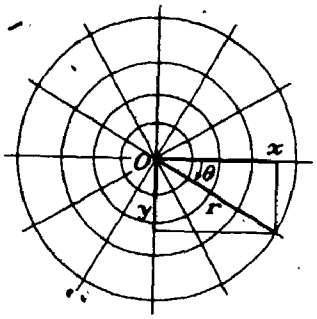

A-1

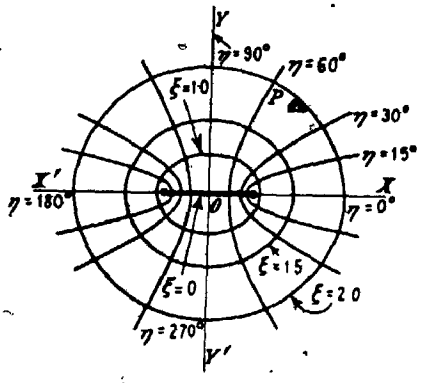

A-2

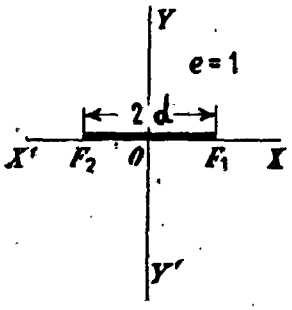

A-3

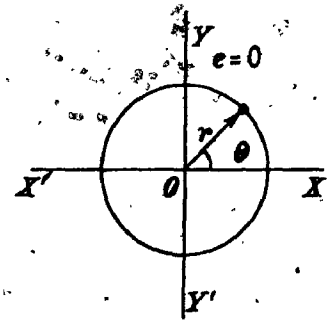

A-4

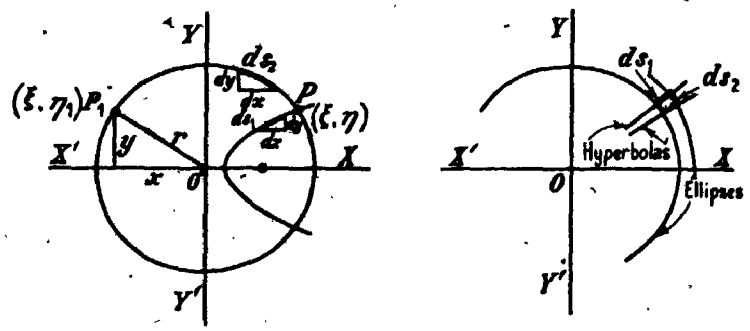

A-5

FIGURE (A) Elliptical and Polar Coordinates, Definition and Notation

APPENDIX B

BESSEL AND STRUVE FUNCTIONS DIAGRAMS

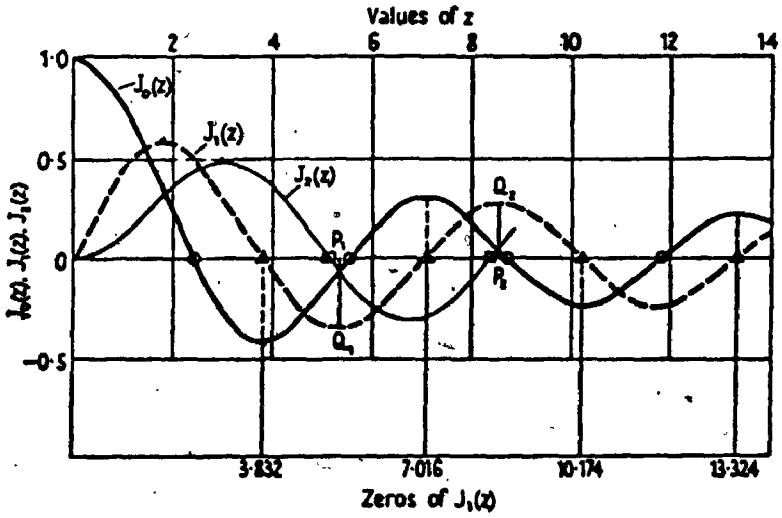

FIGURE B.1 Bessel Functions of the First Kind and Order 0, 1 and 2 ($J_o(z)$, $J_1(z)$, $J_2(z)$)

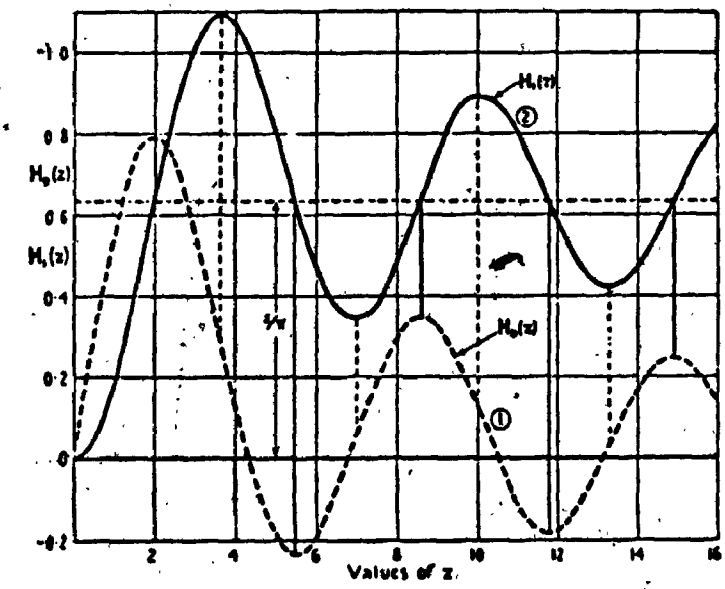

FIGURE B.2 Struve Functions of Order 0 and 1 ($H_o(z)$; $H_1(z)$)

REFERENCES

1. F.R. Khan, J.J. Zils, M. Salem. "Five Million Square Foot Tent Roof", Civil Engineering - ASCE, December 1980, pp. 68-71.

2. "Cable-Suspended Roof Construction State-of-the-Art", by the Subcommittee on Cable-Suspended Structures of the Task Committee on Special Structures, of the Committee of Metals, of the Structure Division, Journal of the Structural Division, ASCE, June 1971.

3. A.A. Butler. "Long Span Cable Roof Structures", Proc. Inst. Civ. Eng., Part 1, Paper 7559, November 1972, pp. 331-353.

4. C. Roland. "Frei Otto Tension Structures", Praeger Publications, Inc., New York, 1970.

5. L. Zetlin. "Suspension Roofs", Chapter 22, Structural Engineering Handbook, edited by E. Gaylord and C. Gaylord, McGraw-Hill Book Co., Inc., New York, 1968.

6. T.Y. Lin, B.W. Young. "Two Large Shells of Post-Tensioned Precast Concrete", Civil Engineering - ASCE, July 1965.

7. K. Gabriel (ed.). "Plane Cable-Structures", University of Stuttgart, Merkblatt - 496, August, 1980.

8. H.D. Buchholdt. "Discussion on Tension Structures", The Structural Engineer, Vol. 48, No. 10, October 1970, pp. 389-397.

9. H.A. Buchholdt, N.K. Das, A.T. Al-Hilli. "A Gradient Method for the Analysis of Cable Structures With Flexible Boundaries", The International Conference on Tension Roof Structures, Polytechnic of Central London, April 8-10, 1974.

10. H. Mollmann. "Analysis of Prestressed Cable Systems Supported by Elastic Boundary Structures", The International Conference on Tension Roof Structures, Polytechnic of Central London, April 8-10, 1974.

11. H. Sandi, S. Hagiescu. "Influence of the Boundary Structure on Behaviour of Cable Girders", The International Conference on Tension Roof Structures, Polytechnic of Central London, April 8-10, 1974.

12. S. Abu-Sitta, I. El-Ashkar. "The Dynamic Response of Tension Roofs to Turbulent Wind", The International Conference on Tension Roof Structures, Polytechnic of Central London, April 8-10, 1974.

13. W.C. Knudson. "Response of Cable-Net Structures Under Dynamic Loads", Proc. 1971 IASS Pacific Symposium Part II on Tension Structures and Space Frames, Tokyo and Kyoto, pp. 365-376, Paper No. 4-3, 1972, Architectural Institute of Japan.

14. H. Kunieda. "Parametric Resonance of Suspension Roofs in Wind", Journal of the Mechanical Division, ASCE, Feb. 1976.

15. J.J. Jensen. "Dynamics of Tension Roof Structures", The International Conference on Tension Roof Structures, Polytechnic of Central London, April 8-10, 1974.

16. L. Zetlin. "Basic Design Principles of Cable Roofs Including Statics, Dynamics and System", Cable Roof Structures, Booklet 2318, Bethlehem Steel Corp., Bethlehem, Pa., U.S.A.

17. L. Zetlin. "Elimination of Flutter in Suspension Roofs", Hanging Roofs, Booklet 2319, Bethlehem Steel Corp., Bethlehem, Pa., U.S.A.

18. H.M. Irvine. "Cable Structures", The MIT Press, Cambridge, Mass., 1981.

19. R. Weinstock, "Calculus of Variations", Dover Publications, Inc., New York, 1974.

20. P. Krishna. "Cable-Suspended Roofs", McGraw-Hill Book Company, New York, 1978.

21. S.P. Timoshenko, D.H. Young. "Theory of Structures", 2nd Ed., McGraw-Hill, New York, 1965.

22. A.G. Pugsley. "The Theory of Suspension Bridges", 2nd Ed., Edward Arnold, London, 1968.

23. D. Clarke. "Design of Counterstressed Cable Structures", Journal of the Structural Division, ASCE, November 1980, pp. 2259-2278.

24. H. Mollmann. "Analysis of Hanging Roofs by Means of the Displacement Method", Polyteknisk Forlag Lyngby, Denmark, 1974.

25. H.H. West, A.K. Kar. "Discretized Initial-Value Analysis of Cable Nets", International Journal of Solids Structures, Vol. 9, 1973.

26. S. Shore, G.N. Bathish. "Membrane Analysis of Cable Roofs", Space Structures, R.M. Davies, Ed., Blackwell Scientific Publications, England, 1967.

27. R. Trostel. "Calculation of Membranes", Tensile Structures, F. Otto, Ed., Part 2, Vol. 1, M.I.T. Press, Cambridge, Mass., 1967.

28. F.K. Schleyer. "Analysis of Cables, Cable Nets, and Cable Structures", Tensile Structures, F. Otto, Ed., Part 2, Vol. 2, M.I.T. Press, Cambridge, Mass., 1967.

29. D.L. Dean, C.P. Ugarte. "Analysis of Structural Nets", Publs. Int. Ass. Bridge Struct. Engrg., 23, 1963, pp. 71-90.

30. H.M. Irvine. "Analytical Solutions for Pretensioned Cable Nets", Journal of the Engineering Mechanics Division, ASCE, February 1976, pp. 43-59.

31. A. Siev, J. Eidelman. "Stress Analysis of Prestressed Suspension Roofs", Journal of the Structural Division, ASCE, August 1964.

32. T. Bobrowski and Partners Ltd. "Structural Assessment of Alternative Roof Designs for Calgary Olympic Coliseum", Feb. 17, 1981.

33. M. Pirner. "Vlastni Kmity Predpjakych Siti Tvaru Translačnich Ploch", Stavenbnicky Casopis SAV. XI, 10 - Bratislava, 1963 (in Czech.).

34. A.E.H. Love, "The Mathematical Theory of Elasticity", 4th Ed., Dover Publications, New York, Chapter 14.

35. S.P. Timoshenko, J.N. Goodier. "Theory of Elasticity", McGraw-Hill Book Company, New York, 1951.

36. L. Meirovitch. "Analytical Methods in Vibrations", The Macmillan Company, London, U.K., 1967.

37. S.P. Timoshenko, S.W. Krieger. "The Theory of Plates and Shells", McGraw-Hill Book Company, New York, 1968.

38. TH. Von Karman. "Encyklopadie Der Mathematishen Wissenschaften", Vol. IV, 1910, pp. 349.

39. P.C. Wang. "Numerical and Matrix Methods in Structural Mechanics", John Wiley and Sons Inc., 1966.

40. H.F. Bauer. "Nonlinear Response of Elastic Plates to Random Excitation", Transaction of the ASME, Journal of Applied Mechanics, March 1968, pp. 47-52.

41. A.G. Davenport. "Industrial Aerodynamics and Meteorology", Graduate Course Notes, Faculty of Engineering Science, University of Western Ontario, London, Ontario, Canada, 1981.

42. E. Simiu, R.H. Scanlan. "Wind Effects on Structures", A Wiley-Interscience Publication, John Wiley & Sons, New York, 1978.

43. P. Sachs. "Wind Forces in Engineering", Pergamon Press Ltd., Oxford, 1972.

44. A.G. Davenport. "The Application of Statistical Concepts to the Wind Loading of Structures", Proceedings Institute of Civil Engrg., London, Vol. 19, 6480, 1961, pp. 449-472.

45. A.G. Davenport. "The Relationship of Wind Structure to Wind Loading", Wind Effects on Buildings and Structures, Op. cit., 1965, pp. 53-102.

46. A.G. Davenport. "Gust Loading Factors", Journal of Structural Division, ASCE, Vol. 93, No. ST3, June 1967, pp. 11-34.

47. E. Simiu, D.W. Lozier. "The Buffeting of Tall Structures by Strong Winds", NBS Building Science Series 74, U.S. Dept. of Commerce, Oct. 1975, pp. 3-7.

48. R.I. Harris. "The Nature of the Wind", A CIRIA Seminar on the Modern Design of Wind-Sensitive Structures, London, June 18, 1970.

49. E. Simiu. "Wind Spectra and Dynamic Along Wind Response", Journal of Structural Division, ASCE, Vol. 100, No. ST9, Sept. 1974, pp. 1897-1910.

50. J.L. Lumley, H.A. Panofsky. "The Structure of Atmospheric Turbulence", Interscience Publishers, John Wiley and Sons, New York, 1964.

51. J.C. Kaimal et al. "Spectral Characteristics of Surface Layer Turbulence", J. Royal Meteorological Society, 98, 1972, pp. 563-589.

52. R.I. Harris. "Measurements of Wind Structures", Symp. Wind Loading on Structures, Bristol, June, 1972.

53. D.E.J. Walshe. "Wind Excited Oscillations of Structures", H.M.S.O., London, 1972.

54. J.S. Bendat, A.G. Piersol. "Random Data", Wiley Interscience, John Wiley and Sons Inc., 1971.

55. A.G. Davenport. "The Distribution of Largest Values of Random Function With Application to Gust Loading", Proceedings, Institution of Civil Engineering, London, Vol. 28, 1964, pp. 187-196.

56. A.G. Davenport. "The Buffeting of Large Superficial Structures by Atmospheric Turbulence", Conference on Large Steerable Radio-Antennas, Annals of N.Y. Academy of Science, Vol. 116, Art. 1, 1964, pp. 135-160.

57. J.D. Robson. "An Introduction to Random Vibrations", Edinburgh University Press, Edinburgh, U.K., 1970.

58. M. Novak. "Advanced Structural Dynamics", Graduate Course Notes, Faculty of Engineering Science, University of Western Ontario, London, Ontario, Canada, 1981.

59. A.G. Davenport. "The Response of Slender, Line-Like Structures to a Gusty Wind", Proceedings of the Institute of Civil Engineering, London, Vol. 27, November 1962, pp. 389-408.

60. American National Standard Building Code Requirements for Minimum Design Loads in Buildings and Other Structures, American National Standards Institute, ANSI A58.1, New York, 1972, pp. 12-45.

61. J.W. Leonard. "Curved Finite Element Approximations to Nonlinear Cables", Proceedings, Fourth Offshore Technology Conference, Paper No. OTC 1535, Houston, Texas, May 1972.

62. J.W. Leonard. "Incremental Response of 3-D Cable Networks", Journal of the Engineering Mechanics Div., ASCE, Vol. 99, No. EM3, Proc. Paper 9805, June, 1973, pp. 515-535.

63. J.H. Argyris, P.C. Dunne, T. Angelopoulos. "Dynamic Analysis of Tension Roofs", The International Conference on Tension Roof Structures, Polytechnic of Central London, April 8-10, 1974.

64. H. Tottenham, M.A. Khan. "Elastic Nonlinear Analysis of Prestressed Cable Networks Using Equivalent Continuum Theory", Proceedings 1971 IASS Pacific Symposium Part II, Architectural Institute of Japan, 1972, pp. 317-323.

65. A.J. Spencer et al. "Engineering Mathematics", Vol. 1, Von Nostrand Reinhold Company Ltd., London, 1980.

66. L. Meirovitch. "Elements of Vibration Analysis", McGraw-Hill, Inc., New York, 1975.

67. S. Shore, G.N. Bathish. "Membrane Analysis of Cable Roofs", Space Structures, R.M. Daves, Ed., Blackwell Scientific Publications, Oxford, England, 1967.

68. S. Shore, B. Chandhari. "Free Vibrations of Cable Networks Utilizing Analogous Membrane", Proceedings of the International Association for Bridge and Structural Engineering, 9th Congress, Amsterdam, The Netherlands, 1972.

69. A.I. Solar, H. Afshari. "On the Analysis of Cable Network Vibrations Using Galerkin Method", Journal of the Applied Mechanics Div., ASME, Series E, Vol. 37, No. 3, September 1970.

70. H. Tottenham, P.G. Williams. "Cable-Net Continuous System Analysis", Journal of the Engineering Mechanics Division, ASCE, Vol. 96, No. EM3, Proc. Paper 7347, June 1970.

71. P.S. Bhupinder. "Membrane Analogy for Linear and Nonlinear Vibrations of Cable Networks", Doctoral Thesis, Indian Institute of Technology, Kanpur, India, 1972.

72. B.P. Singh, B.L. Dhoopar. "Membrane Analogy for Anisotropic Cable Networks", Journal of the Structural Division, ASCE, Vol. 100, No. ST5, Proc. Paper 10544, May 1974.

73. Lord Rayleigh (1877). "Theory of Sound", Vol. II, Second Edition, Dover Publications, 1945.

74. R. Courant, D. Hilbert. "Methods of Mathematical Physics", Vol. 1, Interscience Publishers, Inc., New York, 1966.

75. N.W. McLachlan. "Theory and Application of Mathieu Functions", Oxford University Press, Amen House, E.C. 4, London, 1947.

76. M. Pirner. "Teorie Vlivu Statickych A Dynamickych Zatizeni Na Zavesene Strechy Sbornik Vysokej Skoly Dopravenj v Ziline, No. 4, 1965 (in Czech.).

77. H. Mollmann. "Analytical Solution for a Cable Net Over a Rectangular Plan", Structural Research Laboratory, Technical University of Denmark, Report NR. R25, 1971.

78. L.E. Kinsler, A.R. Frey. "Fundamentals of Acoustics", Second Edition, John Wiley and Sons, Inc., New York, 1962.

79. F.B. Hildebrand. "Advanced Calculus for Applications", Prentice-Hall, Inc., Englewood Cliffs, New Jersey, 1962.

80. I.S. Sokolnikoff, R.M. Redheffer. "Mathematics of Physics and Modern Engineering", McGraw-Hill Book Co., Inc., New York, 1958.

81. S.P. Timoshenko, J.N. Goodier. "Theory of Elasticity", McGraw-Hill Book Co., New York, Third Edition, 1970.

82. N.W. McLachlan. "Bessel Functions for Engineering", Second Edition, Oxford University Press, Amen Offices, London, 1955.

83. C.J. Tranter. "Bessel Functions With Some Physical Applications", The English Universities Press Ltd., St. Paul's House, Warwick Lane, London EC4, 1968.

84. W.C. Knudson. "Static and Dynamic Analysis of Cable-Net Structures", Ph.D. Thesis, Division of Structural Engineering and Structural Mechanics, University of California, Berkeley, April 1971.

85. A. Siev. "Experimental Study of Flutter in Suspended Roofs", IASS Bulletin No. 23, September 1965, pp. 3-10.

86. F.B. Farquarson. "Wind Forces on Structures Subject to Oscillations", Journal of Structural Division, ASCE, Vol. 84, July 1958.

87. P.L. Gould, S.H. Abu-Sitta. "Dynamic Response of Structures to Wind and Earthquake Loading", Pentech Press Ltd., Estover Road, Plymouth U.K., 1980.

88. A.G. Davenport. "Wind Forces on Cable Systems", Symposium on Architectural and Structural Design of Cable Systems, University of Pennsylvania, November 19-20, 1969.

89. A.G. Davenport, E. Holm, D. Surry. "A Report of the Wind Tunnel Measurements on the Olympic Coliseum, Calgary, Alberta", Boundary Layer Wind Tunnel Laboratory Report BLWT-5511-1981, The University of Western Ontario, Faculty of Engineering Science, London, Ontario, Canada, August 1981.

90. G.R. Seeley, H. Stefan, P. Christiano. "Static Wind Loads on Circular Concave Cable Roofs", Journal of the Structural Division, ASCE, April 1974, pp. 1593-1609.

91. P. Christiano, G.R. Seeley, H. Stefan. "Transient Wind Loads on Circular Concave Cable Roofs", Journal of the Structural Division, ASCE, November 1974, pp. 2323-2341.

92. J.J. Jensen. "Das Dynamische Verhalten eines Vorgespannten Kabelnetzes", Division of Structural Mechanics, The Norwegian Institute of Technology, University of Trondheim, Norway, Report 72.3, 1972.

93. H. Ishizaki, Y. Yoshikawa. "A Wind Tunnel Model Experiment of Wind Loading on Curved Roof", The Bulletin of the Disaster Prevention Research Institute, Koyo University, Vol. 21, March 1972.

94. J. Beutler. "Beitrag Zur Statistischen Windlasten Von Seilnetzwerken, Ergebnisse Von Windkanal-Untersuchungen", Proceedings of the IASS Colloquium of the Hanging Roofs, Paris, 1962.

95. D.C. Perry, M.D. Anderson, H.M. Thurston. "Current and Proposed Revisions of Wind Load Standards and Codes in the United States", Proceedings of the Fourth National Conference on Wind Engineering Research, University of Washington, Seattle, Washington, July 26-29, 1981.

96. R.I. Harris, D.M. Deaves. "The Structure of Strong Winds", Wind Engineering in The Eighties, Proceedings of the CIRIA Conference, London, U.K., November 12-13, 1980.

97. Swiss Code of Practice, No. 160, Article 20, 1956.

98. E. Cohen. "Draft of Proposed Revision of the Portions of the ASA Standard AS8 1-1955 which pertain to Wind Loads", 1968.

99. B.E. Lee and M. Hussain. "A Wind Tunnel Study of the Mean Pressure Forces Acting on Large Groups of Low-Rise Buildings", J.W.E. and I.A., October 1980, pp. 207-226.

100. B.J. Vickery. "Load Fluctuations in Turbulent Flow", Journal Engineering Mechanics Division, ASCE, Vol. 94, No. EM1, February 1968, pp. 31-46.

101. R.I. Harris. "The Response of Structures to Gusts", Wind Effects on Buildings and Structures, Op. Cit., 1965, pp. 394-421.

102. G.M. Corcos. "The Structure of the Turbulent Pressure Field in Boundary-Layer Flows", J. Fluid Mechanics, 1964, pp. 353-378.

103. W.W. Willmarth and C.E. Wooldridge. "Measurements of the Fluctuating Pressure at the Wall Beneath Thick Boundary Layer", J. Fluid Mechanics, Vol. 14, 1962.

104. L. Maestrello. "Use of Turbulent Model to Calculate the Vibration and Radiation Response of a Panel With Practical Suggestions for Reducing Sound Level", J. Sound Vibrations 5, July 1967, pp. 407-448.

105. T. Morri: "Pressure Fluctuations on Steps in Turbulent Boundary Layer", M.E.Sc. Thesis, Faculty of Engineering Science, University of Western Ontario, London, Ontario, Canada, 1971.

106. L. Maestrello. "Measurement and Analysis of the Response Field of Turbulent Boundary Layer Excited Panels", J. Sound Vibrations, Vol. 2, No. 3, 1965, pp. 270-292.

107. M.K. Bull. "Wall Pressure Fluctuations Associated With Subsonic Turbulent Boundary Layer Flow", J. Fluid Mechanics, Vol. 28, 1967, pp. 719-754.

108. I. El-Ashkar. "Dynamic Response of Tension Roofs to Turbulent Wind", M.E.Sc. Thesis, Faculty of Engineering Science, The University of Western Ontario, London, Ontario, Canada, 1974.

109. R.W. Clough, J. Penzien. "Dynamics of Structures", McGraw-Hill, Inc., New York, 1975.

110. Y.K. Lin. "Probabilistic Theory of Structural Dynamics", McGraw-Hill Book Co., Inc., New York, 1967.

111. D.J. Mead. "The Elements of Sound Transmission", Noise and Acoustic Fatigue in Aeronautics , E.J. Richards, D.J. Mead, Eds., John Wiley and Sons Ltd., London, 1968.

112. R.E. Whitebread. "Model Simulation of Wind Effects on Structures", Vol. 1, Symposium, Wind Effects on Buildings and Structures, National Physical Laboratory, U.K., June 1963, HMSO 1965.

113. B.V. Tryggvason, N. Isyumov. "A Study of the Wind Induced Response of the Air Supported Roof For the Dalhousie University Sports Complex", Boundary Layer Wind Tunnel Laboratory, University of Western Ontario, London, Ontario, Canada, BLWT-557-1977.

114. J.D. Holmes. "Mean and Fluctuating Internal Pressure Induced by Wind", 5th International Conference on Wind Engineering, Fort Collins, Colorado, July 1979.

115. E.R. Parker. "Materials Data Book for Engineers and Scientists", McGraw-Hill Book Company, New York, 1970.

116. B.V. Tryggvason, D. Surry, A.G. Davenport, "A Study of Wind Effects on an Aeroelastic Model of the Haj Terminal at Jeddah International Airport", The Boundary Layer Wind Tunnel Laboratory, Faculty of Engineering Science, The University of Western Ontario, London, Canada, BLWT-SS1-1979.

117. K.F. McNamara, "Characteristics of the Mean Wind Flow in the Planetary Boundary Layer and Its Effects on Tall Towers", Ph.D. Thesis, The University of Western Ontario, Oct. 1975.

118. S.O. Rice, "Mathematical Analysis of Random Noise", Bell System Technical Journal, Vol. 24, 1945, pp. 40-116.

119. E.H. Van Marcke, "On the Distribution of the First-Passage Time for Normal Stationary Random Processes", Journal of Applied Mechanics, March 1975.

120. M. Novak, "Galloping Oscillations of Prismatic Structures", Journal of Engineering Mechanics Division, ASCE, Feb. 1972.

121. M. Novak, H. Tanaka, "Effect of Turbulence on Galloping Instability", Journal of the Engineering Mechanics Division, ASCE, Feb. 1974.

122. M. Novak, L. El Hifnawy, "Effect of Soil-Structure Interaction on Damping", Boundary Layer Wind Tunnel Laboratory, The University of Western Ontario, London, Ontario, BLWT-4-1982, Oct. 1982.

123. H.P.A.H. Irwin, R.L. Wardlaw, K.N. Wood and K.W. Bateman, "A Wind Tunnel Investigation of The Montreal Olympic Stadium Roof", Laboratory Technical Report LTR-LA-228, National Research Council Canada, Ottawa, 31 May 1979.

124. W.F. Campbell, "The Added Mass of Some Rectangular and Circular Flat Plates and Diaphragms", Laboratory Technical Report LTR-LA-223, National Research Council Canada, Ottawa, July 1982.

125. World Congress on Shell and Spatial Structures, "Madrid Congress Proceedings - 20th Anniversary of the IASS", The International Association for Shell and Spatial Structures, Madrid, Spain, September 1979.

END

20030184

FIN

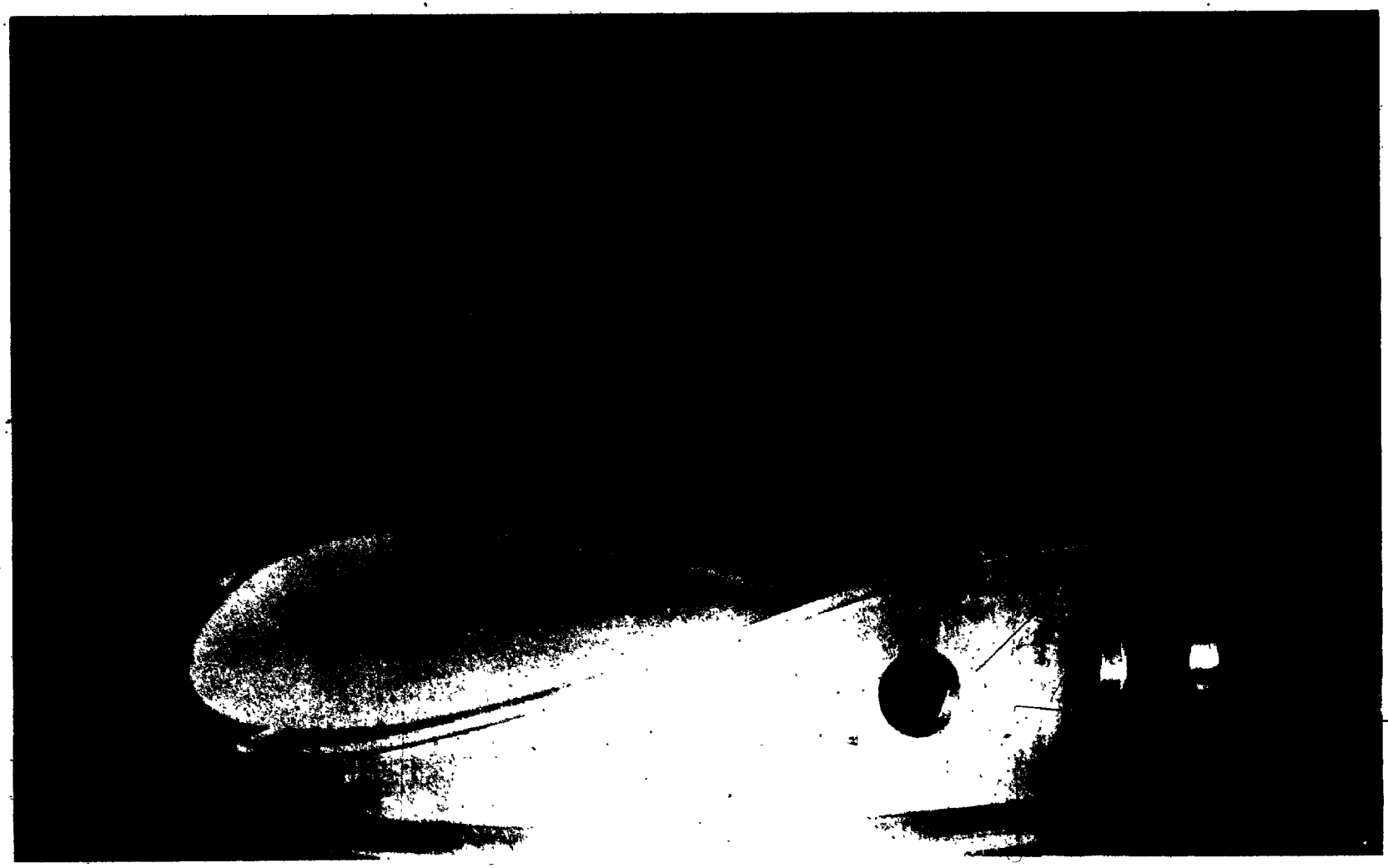

PLATE (6.1) Aeroelastic Model of the Calgary Olympic Coliseum (λ:- 1:384)

of this simplification is that the approximate model is more amenable to the theoretical analysis, conducted in Chapters 4 and 5.

The numerical values of parameters for this simplified model and the averaged prototype geometrical scaling are given in Table 6.3. The same pressure chamber was used in both models. Plan and elevation views of this simplified model are shown in Figures 6.3 and 6.4. Furthermore, in order to simulate the existence of openings in the prototype (doors and windows), nine circular holes of 3/4 inch (≃ 19 mm) diameter each are drilled in the walls of the simplified model, Plate 6.2.* This allowed study of the effect of air movement through the openings on the frequency characteristics of the roof and the total damping ratio of the system.

6.5.2 Sensing Devices Used in Experiment

The sensing devices used to measure the vertical displacements were Kaman non-contact reactance sensors of the displacement type. These devices measure change in reactance of the air gap between the vibrating surface and the probe plate. To improve the conductivity of the TFE membrane, a small piece of metal aluminum foil is attached to the internal surface of the membrane at the

* For the Calgary coliseum the estimated leakage rate corresponds to the wall area parameter of about 5 to 8%.

TABLE 6.3 SIMPLIFIED AEROELASTIC MODEL SCALING

No.	Parameter	Full Scale		Simplified Aeroelastic Model	
		Quantity	Dimension	Quantity	Dimension
1	Roof diameter (average)	416	ft	13	inch
2	Height (average)	80	ft	2.50	inch
3	Equivalent Roof Thickness	4	inch	0.01	inch
4	Modulus of Elasticity	1.5×10^6	psi	0.6×10^5	psi
5	Weight per Square Foot	46	lb/sq.ft	0.12	lb/sq.ft
6	Mass Per Square Foot	1.428	slug/sq.ft	0.0037	slug/sq.ft
7	Gradient Velocity	100	MPH	29.22	ft/sec
8	Fundamental Frequency	0.3458	Hz (cps)	26.556	Hz (cps)
9	Enclosure Volume	9.0×10^7	cu.ft	6.86×10^3	cu.inch

(1 ft = 0.3048 m ; psi = 6895 N/m^2 ; lbf = 4.448 N ; slug = 0.4536 kg)

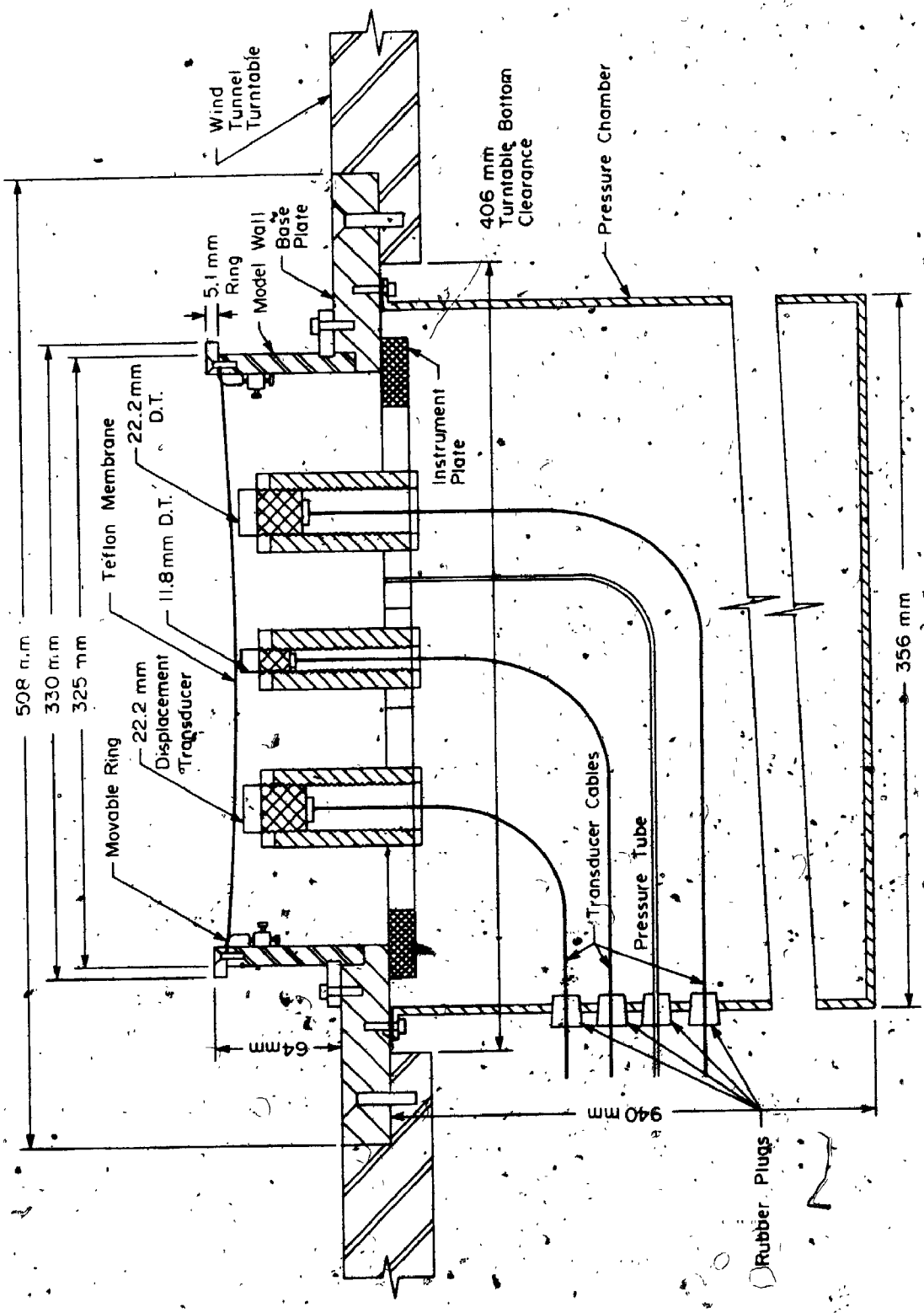

FIGURE 6.4 CROSS SECTION OF SHALLOW CIRCULAR GABLE ROOF MODEL

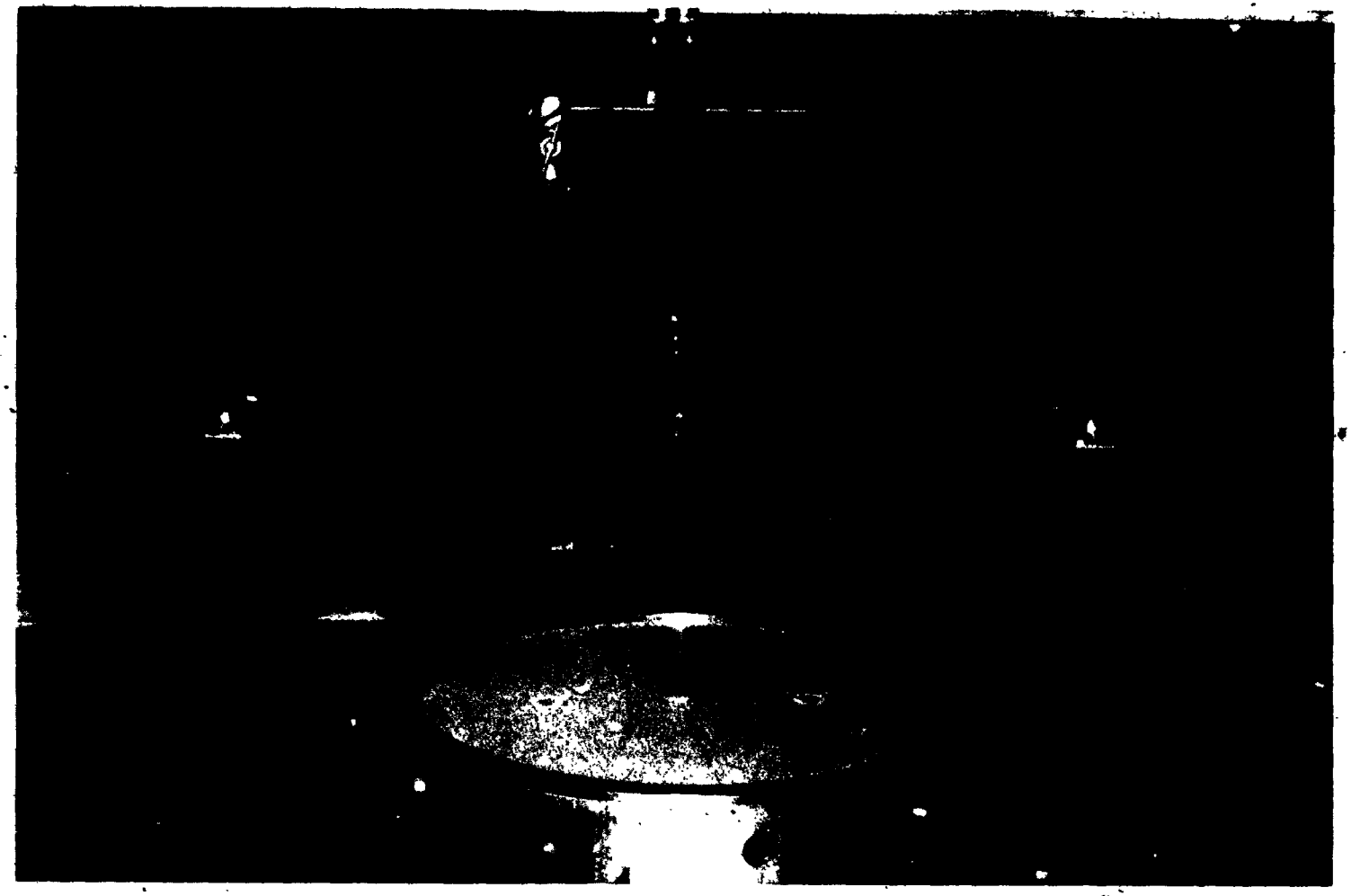

Plate (6.2) Simplified Aeroelastic Model

location of each Kaman probe. The Kaman sensors are calibrated each time they are used. The probes were located at the centre of the model and at an intermediate specific point of the base radius at distance r = 0.436a, Figure 6.5. The probe at the centre eliminated the asymmetrical modes f_{11} and f_{21} and the one at r/a = 0.436, eliminated mode f_{02}. Using the turntable in the wind tunnel floor, the latter position was related to $\theta = 0°, 45°, 90°$ with wind direction. This arrangement was done to separate the symmetric modes of vibration from the antisymmetric ones and to measure simultaneously the response at two points for cross-correlation analysis.

Due to instrumentation difficulties, the attempt to measure two records simultaneously failed and the response was measured separately.

6.6 EXPERIMENTAL TESTS

6.6.1 Simplified Aeroelastic Model

6.6.1.1 Experiments in Still Air

The model was first excited in still air by means of a loudspeaker, Figure 6.6 and Plates 6.3 and 6.4. It was observed that the first symmetric mode f_{01}, being the volume-displacing mode, is strongly dependent on the number of wall openings. It was found that the frequency of mode f_{01} is increased by increasing the number of

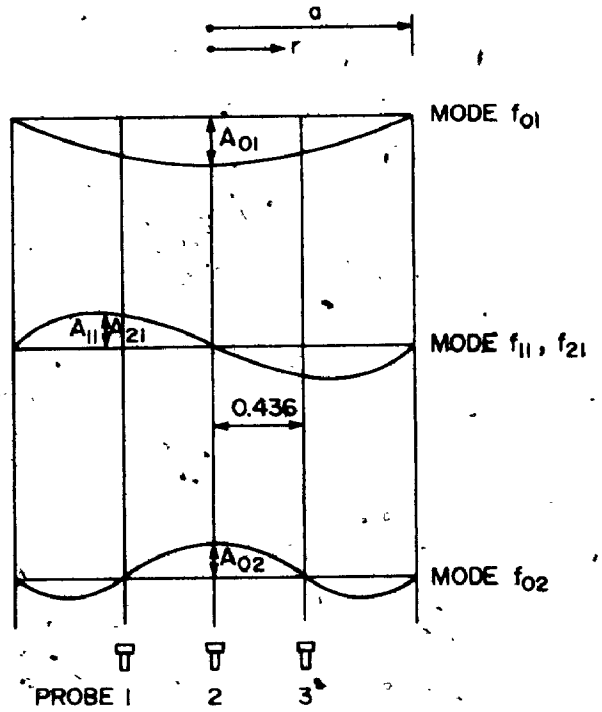

FIGURE 6.5. KAMAN DISPLACEMENT SENSORS ARRANGEMENT.

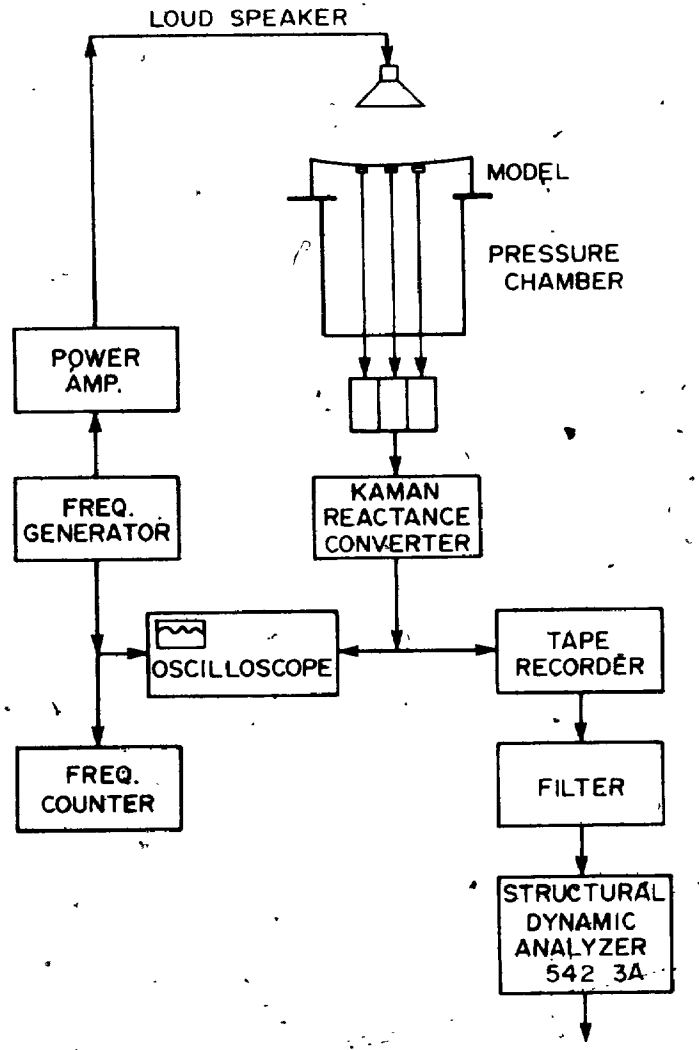

FIGURE 6.6. FREE VIBRATION EXPERIMENTAL SET-UP.

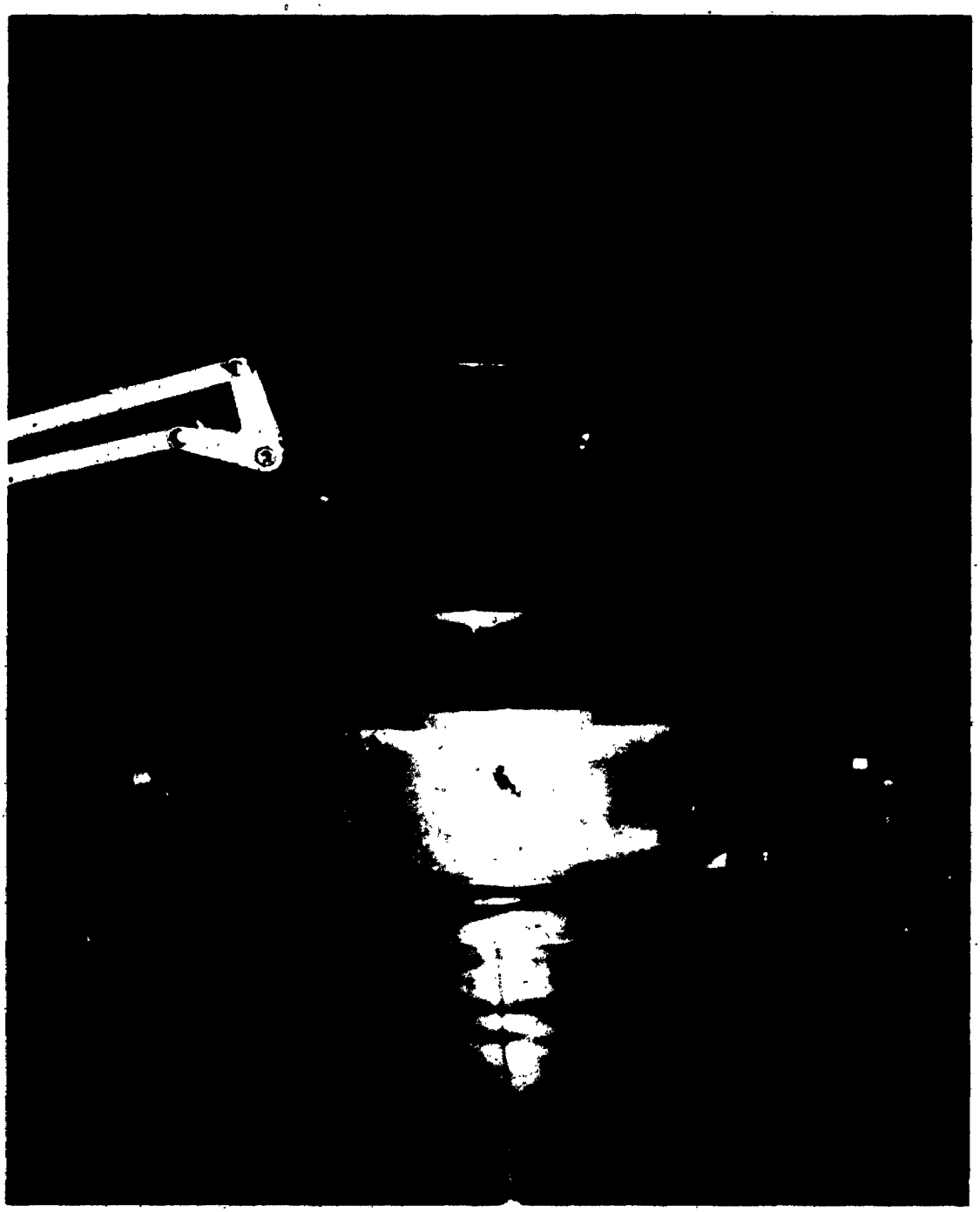

PLATE (6.3) Aeroelastic Model in Free Vibration Tests

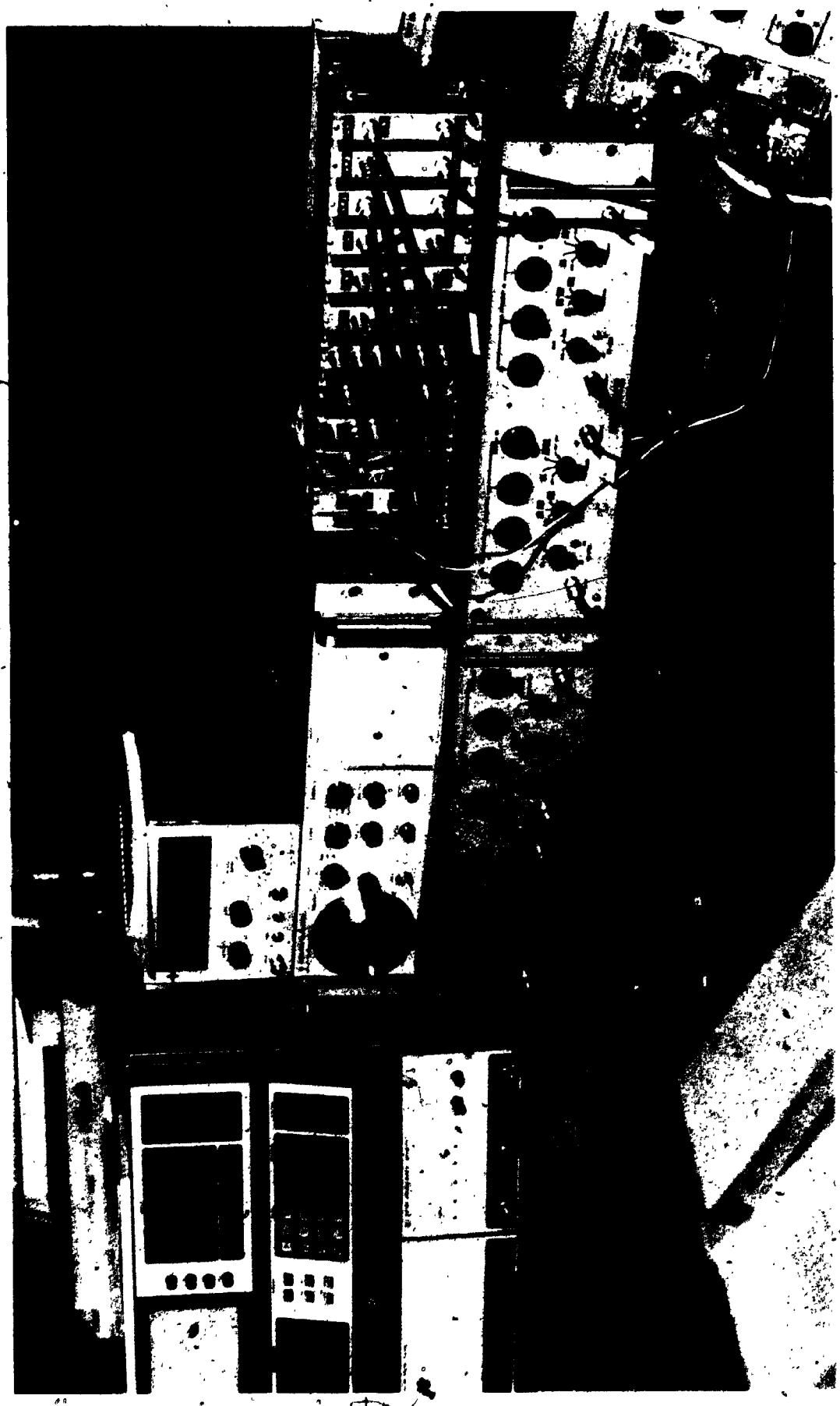

PLATE (6.4) Instrument Arrangement in Free Vibration Tests

openings while the other modes f_{11}, f_{21} and f_{02} were only slightly affected. The variation of the natural frequencies with the total area of openings is shown in Figure 6.7. The frequencies are plotted against the area parameter $\beta_a = (NA_o/A_c)x100$ in which N = number of openings, A_o = the area of one opening and A_c = the wall area. The natural frequencies were established from the spectra of the response to harmonic excitation for different openings and modes, Figure 6.7a. The spectra were obtained using the Structural Dynamics Analyzer 5423A of the Hewlett-Packard Co.

This analyzer also gives the total damping D_{nm}. The damping ratios found at different openings are presented in Table 6.4. This damping comprises all the material, structural and acoustical damping.

The acoustical damping is due to the movement of the membrane and is proportional to its velocity. As the frequency of mode f_{01} is decreased with the decrease of the area parameter β_a, the acoustic damping is decreased accordingly. The damping ratios of modes f_{11}, f_{21} and f_{02} are only slightly affected.

6.6.1.2 Wind Tunnel Tests

Flow Properties and Experimental Set-Up

The experiments were conducted in the Boundary Layer

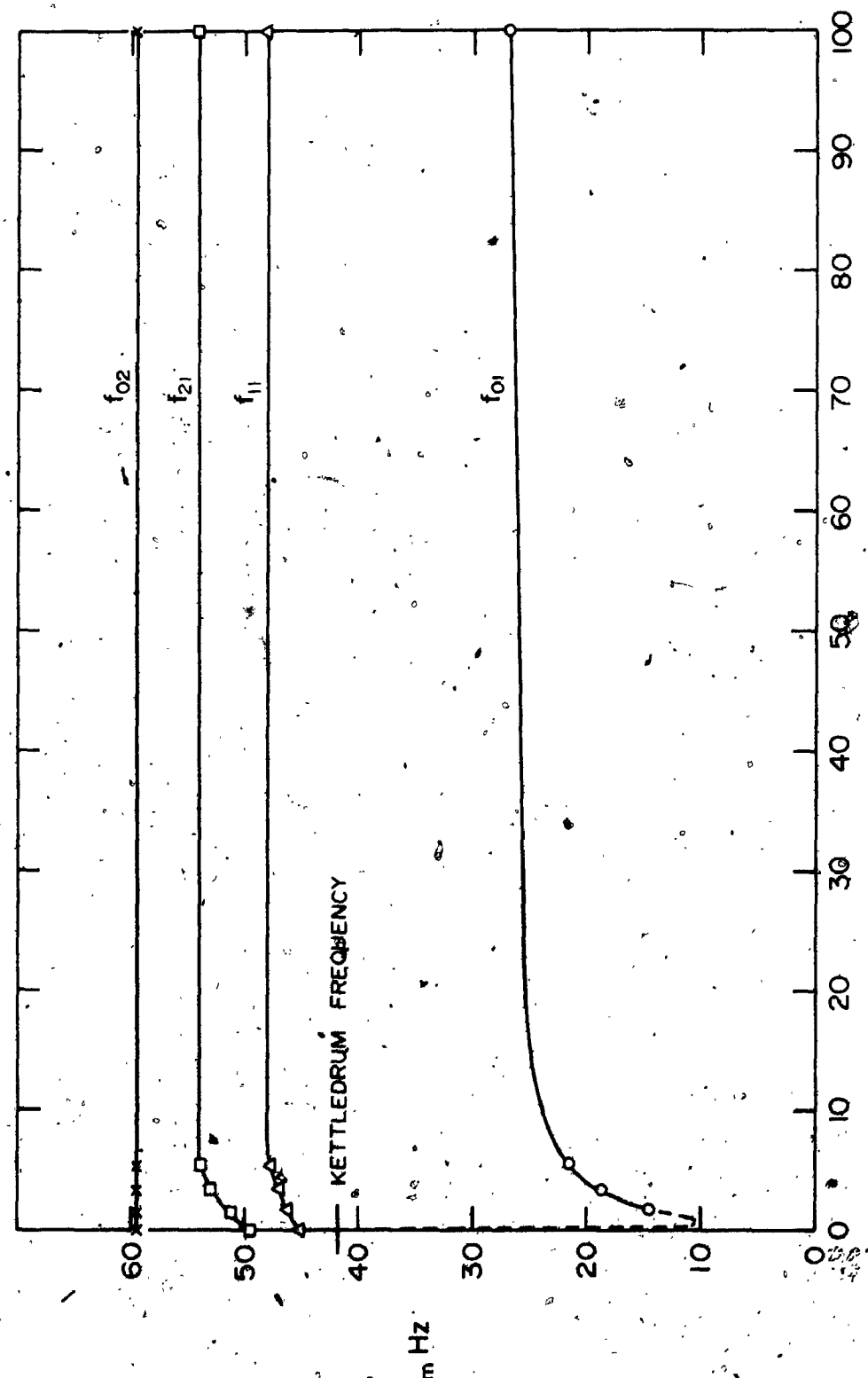

FIGURE 6.7 FREQUENCY OF MODES VERSUS AREA PARAMETER, IN FREE VIBRATION

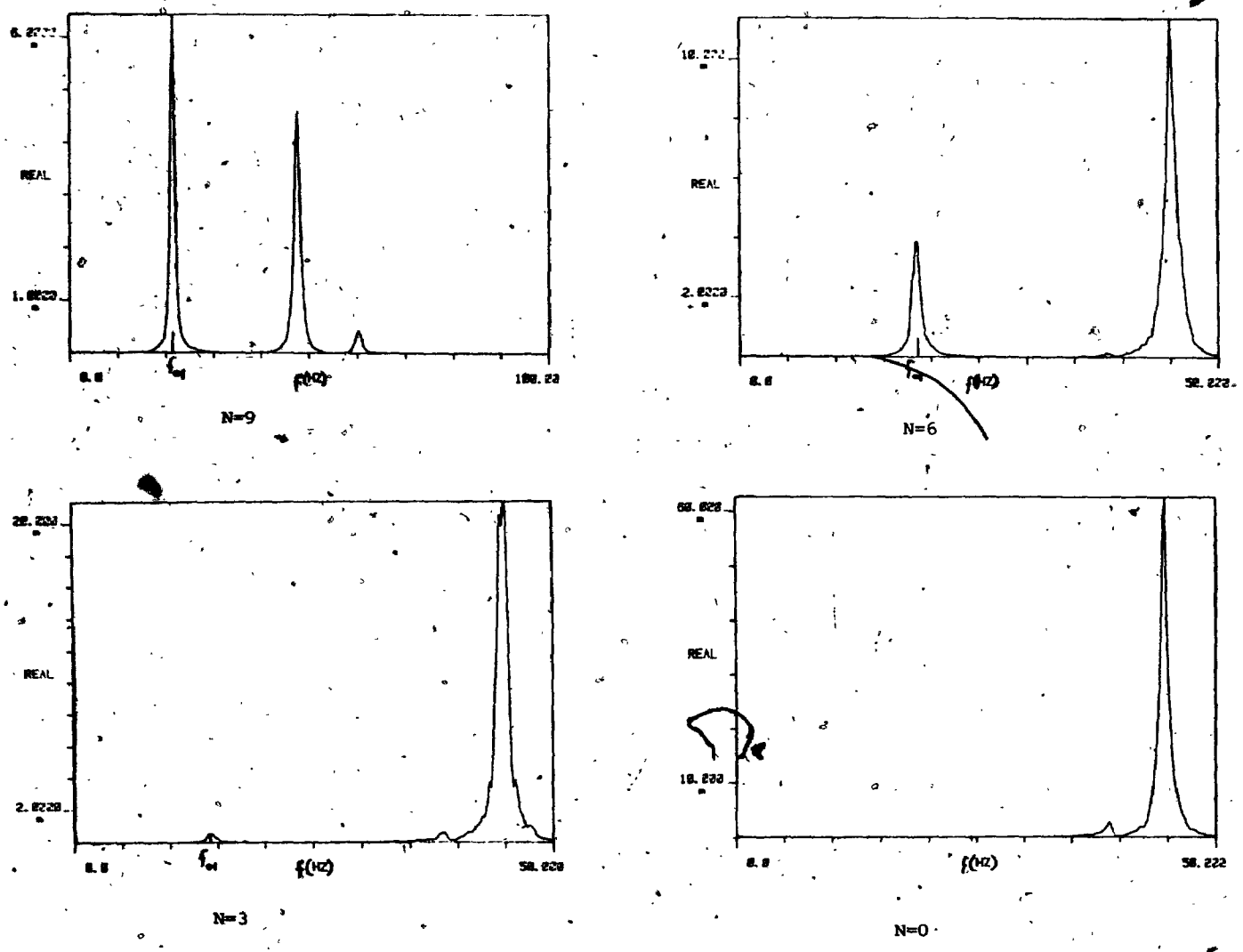

FIGURE 6.7a Spectra of Response to Harmonic Excitation for Different Openings (N)

TABLE 6.4 MODAL DAMPING RATIO AT DIFFERENT AREA PARAMETER β_a IN FREE VIBRATION TESTS

Number	Mode f_{nm}	Resonant Frequency Hz	Area Parameter $\beta_a = \frac{NA_o}{A_c} \times 100\%$	Damping Ratio D_{nm} %
1	f_{01}	26.556	Base open	3.110
2	f_{01}	21.402	5.30	2.565
3	f_{01}	18.931	3.54	2.616
4	f_{01}	14.523	1.78	2.22
5	f_{11}	48	Base open	-
6	f_{11}	47.586	5.30	1.389
7	f_{11}	46.922	3.54	1.343
8	f_{11}	46.075	1.78	1.466
9	f_{11}	44.914	0	1.053
10	f_{12}	52	Base open	0.668
11	f_{02}	54.766	5.3	1.306

Wind Tunnel Laboratory at The University of Western Ontario.

Two exposures were simulated at the wind tunnel floor. First, the tunnel floor was covered with randomly placed blocks of heights varying from 1/2 inch (= 12.7 mm) to 3 inches (= 76.2 mm) approximately, Plate 6.2.

The properties of the flow at the test section are shown in Figure 6.8, which shows the variation of mean wind speed velocity, $\bar{V}(z)$, and the standard deviation of the wind velocity fluctuation with height, $\sigma_v(z)$, at the test section. This velocity profile corresponds to the boundary layer of a built-up area [44], and its turbulence intensity is about 12% for V_G = 28.50 ft/sec (= 8.687 m/s) at the model height.

In the second phase of the experiments, the tunnel floor was covered with rough carpet. The properties of the flow at the test section for this exposure are shown in Figure 6.9, which also shows the variation of the mean wind velocity, $\bar{V}(z)$, and standard deviation of the wind velocity fluctuations with height, $\sigma_v(z)$, at the test section. This velocity profile corresponds to the boundary layer of open country area [44], and its turbulence intensity at the model height is about 8% for V_G = 31.30 ft/sec (= 9.54 m/s).

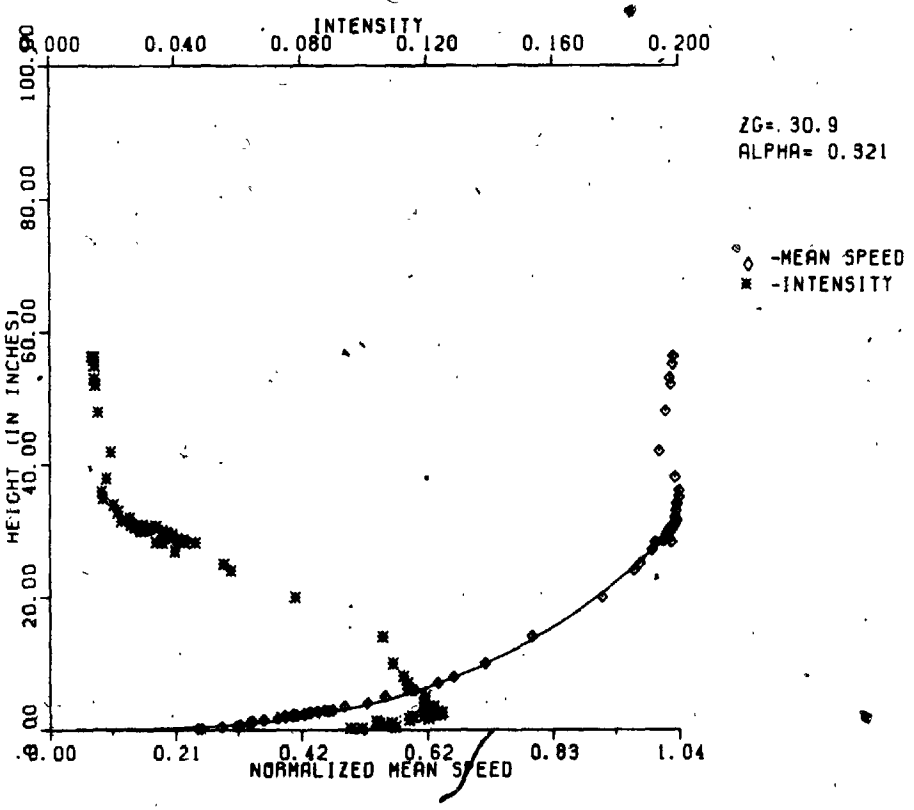

FIGURE 6.8 Wind Velocity Profile and Turbulence Intensity at Test Section (Built-Up Area, $\bar{V}_G$ = 28.5 ft/sec)

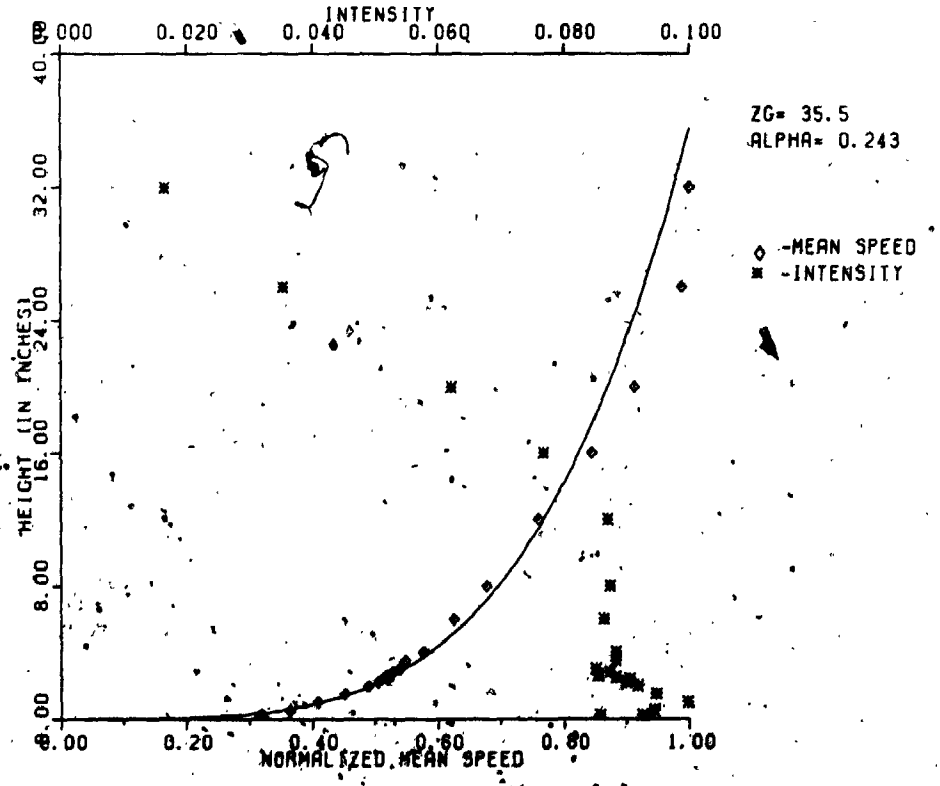

FIGURE 6.9 Wind Velocity Profile and Turbulence Intensity at Test Section (Open Country Exposure, $\bar{V}_G$ = 31.30 ft/sec)

The wind velocity was measured using a hot wire device. The spectrum of wind velocity at model height is presented in Figures 6.10 and 6.11 corresponding to built-up area and open country exposures respectively. The length scales calculated from the power spectrums were about 1 foot for built-up area and about 3.0 feet for open country exposure.

Measurements of membrane vertical displacement were made at the three different locations shown in Figure 6.5 using the Kaman probes. The output from the Kaman probes system was analyzed to determine the mean and the standard deviation of the response using a digital data acquisition system. The arrangement of the testing instruments is shown in Figure 6.12.

The HP 5423 A analyzer was employed for the computation of the autocorrelation functions. The number of correlation points sampled was 512 with a lag time interval of 0.60 milliseconds. The power spectrum of the membrane model response was obtained from the autocorrelation function by direct Fourier transformation. The mean response and the standard deviation were obtained after passing the total response signal into a digital acquisition system (PDP 11/60 computer).

To study the fluctuating internal pressure within

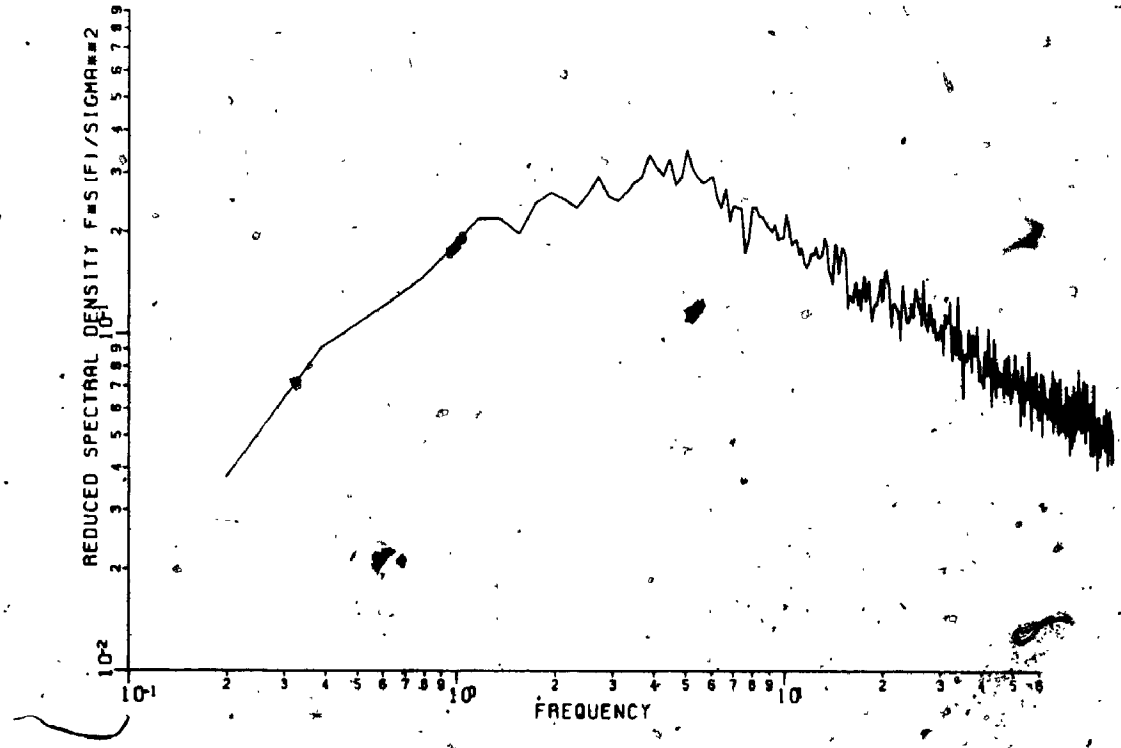

FIGURE 6.10 Power Spectrum of Velocity at Roof Height Level (Built-Up Area, $\bar{V}_G$ = 28.5 ft/sec)

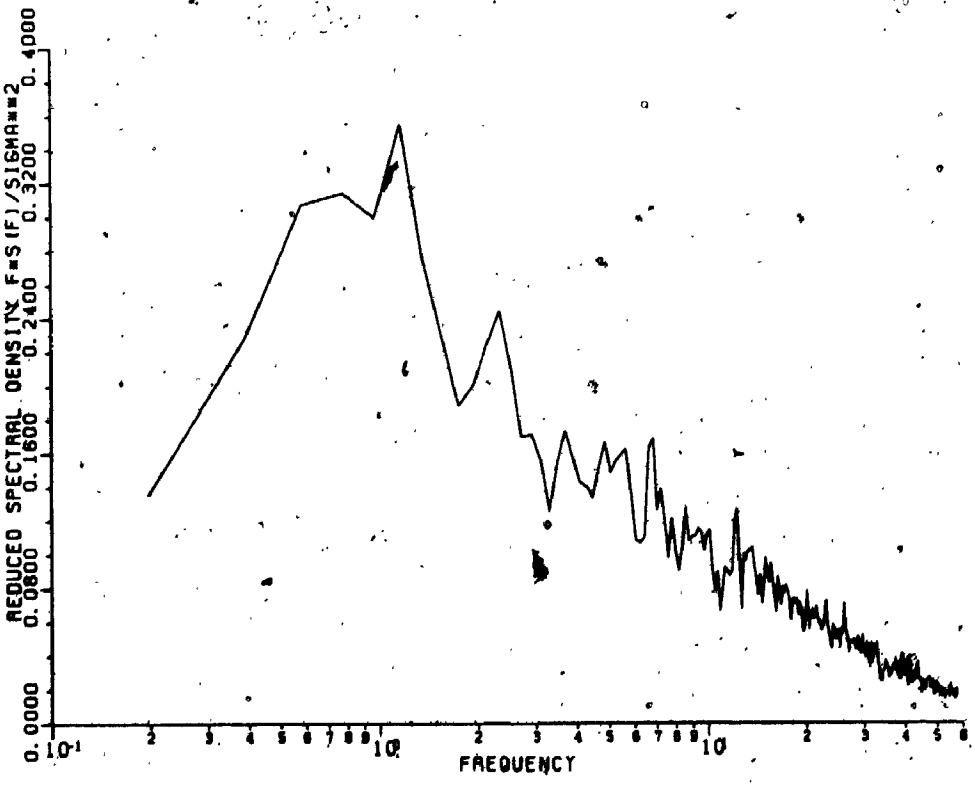

FIGURE 6.11 Power Spectrum of Velocity at Roof Height Level (Open Country Exposure, $\bar{V}_G$ = 31.3 ft/sec)

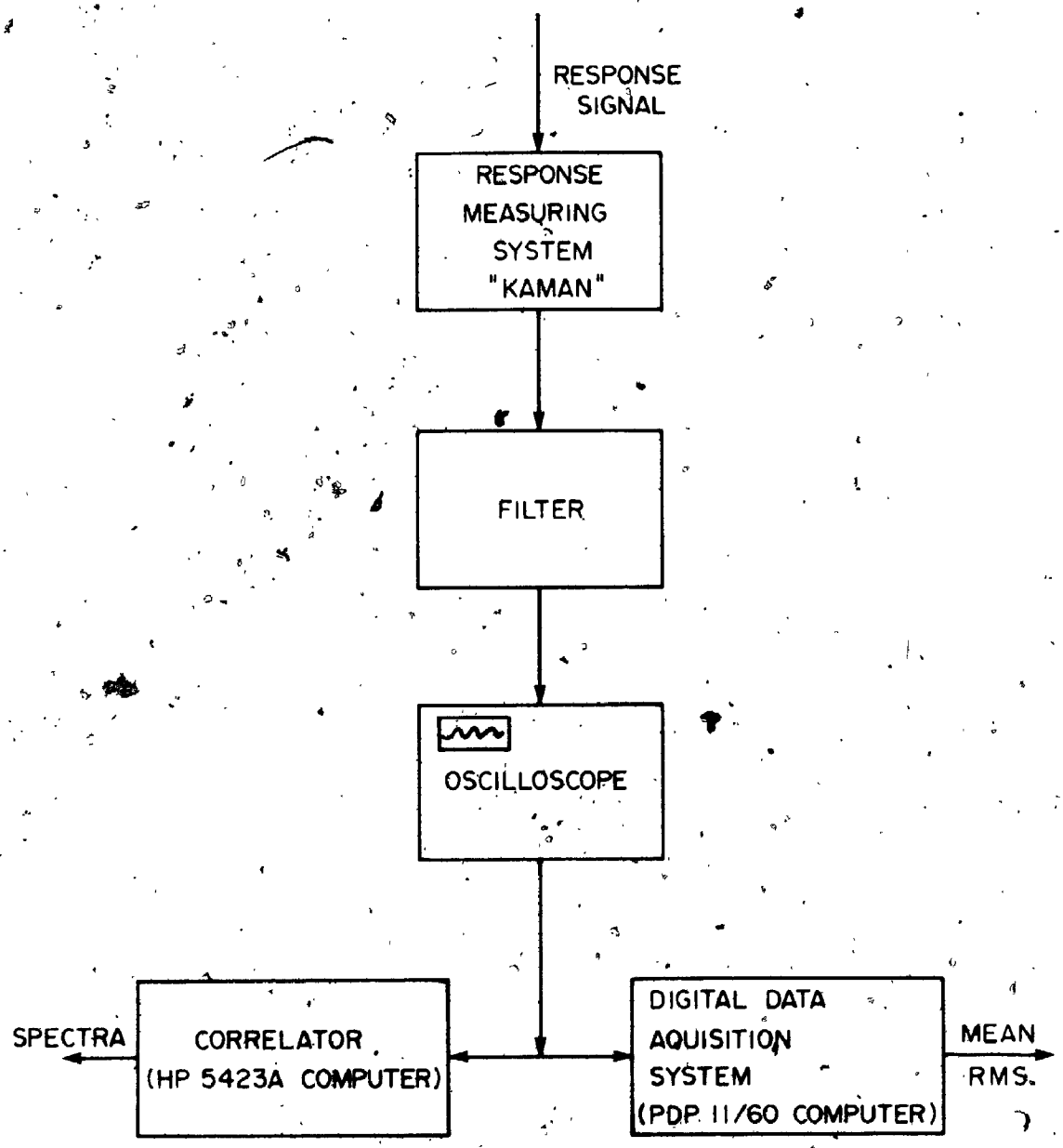

FIGURE 6.12. WIND TUNNEL EXPERIMENTAL SETUP

the enclosure due to the movement of the membrane under the turbulent wind, assuming that the internal pressure is homogeneous, a pitot tube was inserted at the instrument plate (see Figures 6.3 and 6.4).

Model Response

Several tests were conducted to assess the modal contributions and the effects of openings, terrain and wind velocity.

The mean and rms vertical deflection at r/a = 0 and $\pm$ 0.436 at angles θ = 0°, 45°, 90° with the wind direction were measured and are presented in Table 6.5. The spectra of response at centre and at r/a = 0.436 locations, for different area parameters (β_a = 5.3, 1.53, 0%) are presented in Figures 6.13 to 6.20.

When the Kaman probe is at the centre, modes f_{01} and f_{02} appear dominant. Mode f_{01} corresponds to internal volume changes while f_{02} is independent of these. Although the frequency of mode f_{01} decreases with smaller openings, and therefore response is likely to increase, the internal pressure builds up and the square of frequency response modulus decreases resulting in the virtual disappearance of resonance in mode f_{01}, Figure 6.15.

At r/a = 0.436, at which mode f_{02} is eliminated,

both the symmetric and antisymmetric components of mode f_{11} response are important in addition to the contribution of mode f_{01}, Figures 6.16 and 6.17.

When the model openings are completely closed, the only modes observed are modes f_{11}, f_{21} and f_{02} because the contribution of mode f_{01} has vanished.

The largest total mean response occurred at the angle of incidence $\theta = 0°$ at wind velocity 31.2 ft/sec (= 9.51 m/s) when the normal openings were completely closed. The largest total rms response was observed at r/a = 0.436 with $\theta = 0°$ to 90° and wind velocity 11.63 ft/sec (= 3.55 m/s) when the area parameter β_a was equal to 3.54% and 0%. This response is the largest of all points on the roof and was up to 250% larger than the response at the centre, Table 6.5.

With smaller openings (N = 0) and virtual disappearance of mode f_{01}, modes f_{11}, f_{21} and f_{02}, which are not affected by openings, remained the only main source of response.

Internal Pressure

The mean and the standard deviation for the internal pressure fluctuations were established and presented in Table 6.6 for different wind velocity and wall openings.

TABLE 6.5 VERTICAL TOTAL RESPONSE OF SIMPLIFIED MODEL

Probe Position r/a (no.)	Wind Velocity ft/sec	Wind Direction θ°	Mean Response $\bar{w}$ (inchx10^{-3}) Area Parameter B_a				RMS σ_w (inchx10^{-3}) Area Parameter B_a			
			5.3%	3.54%	1.78%	0%	5.3%	3.54%	1.78%	0%
0 (2)	11.63	0	0.30	0.70	0.20	3.50	5.20	5.70	4.40	5.50
0 (2)	11.60	45	0.30	0.50	0.30	3.10	3.70	5.60	4.60	4.50
0 (2)	11.63	90	0.20	0.70	0.30	2.30	4.60	6.40	5.00	4.00
0 (2)	19.91	0	0.0	0.0	-1.10	6.00	1.20	1.90	2.10	3.40
0 (2)	19.97	45	-0.20	-0.40	-0.80	6.20	1.20	1.80	2.10	2.00
0 (2)	19.95	90	-0.30	0.10	-0.20	4.10	1.20	1.80	1.90	1.7
0 (2)	31.21	0	-0.60	-0.50	-2.80	16.0	2.50	2.70	3.70	3.40
0 (2)	29.93	45	-1.10	-1.30	-2.20	6.30	2.20	5.50	3.30	3.10
0 (2)	29.96	90	-1.20	-0.30	-0.40	6.40	2.20	3.50	2.90	3.20
0 (2)	40.91	0	-1.90	-2.10	-6.90	11.50	4.00	4.50	5.40	5.50
0 (2)	40.79	45	-2.50	-3.30	-4.10	13.00	3.80	3.90	5.00	4.90
0 (2)	40.78	90	-3.00	-0.70	-0.80	9.40	4.20	4.10	4.90	5.40
0.436(1)	11.63	0	0.0	0.20	-0.20	2.20	6.20	8.60	8.20	12.80
0.436(1)	11.60	45	0.0	0.0	0.0	2.00	5.60	9.00	8.20	10.60
0.436(1)	11.63	90	0.0	0.20	0.20	1.20	7.20	10.80	11.60	9.40
0.436(1)	19.91	0	0.0	-0.20	-0.80	4.00	1.40	2.00	2.80	7.60
0.436(1)	19.97	45	-0.40	-0.40	-0.60	4.00	1.40	1.80	2.80	2.20
0.436(1)	19.95	90	-0.40	0.0	-0.10	2.60	1.40	2.0	2.40	2.40
0.436(1)	31.21	0	-0.20	-0.40	-1.80	11.20	2.00	4.60	5.60	4.60
0.436(1)	29.93	45	-0.60	-0.80	-1.40	4.40	1.80	10.00	4.00	3.60
0.436(1)	29.96	90	-1.00	-0.40	-0.40	4.20	2.00	4.0	3.20	3.80
0.436(1)	40.91	0	-0.60	-1.00	-3.80	8.60	3.00	3.20	5.20	10.80
0.436(1)	40.79	45	-1.40	-1.80	-2.20	9.60	2.80	2.80	5.00	7.00
0.436(1)	40.78	90	-2.20	-0.60	-0.40	6.40	3.20	3.40	5.20	11.80

TABLE 6.5 (cont'd)

0.436(3)	11.63	0	1.80	2.40	1.80	4.80	10.20	13.20	12.20	14.60
0.436(3)	11.60	45	1.20	2.00	2.00	4.40	8.00	11.80	12.60	13.20
0.436(3)	11.63	90	1.40	2.40	1.60	4.00	9.20	14.80	13.40	14.20
0.436(3)	19.91	0	0.60	0.40	0.00	6.20	3.00	4.40	6.40	6.00
0.436(3)	19.97	45	0.20	0.20	-0.40	6.20	3.20	4.40	4.80	5.20
0.436(3)	19.95	90	0.40	0.80	0.10	4.40	3.20	4.20	3.60	4.40
0.436(3)	31.21	0	0.00	0.40	-1.40	15.60	3.80	5.60	6.60	6.00
0.436(3)	29.93	45	-0.60	-0.20	-1.20	6.60	3.60	6.40	6.80	4.20
0.436(3)	29.96	90	-0.20	+0.60	0.0	6.80	3.60	4.20	4.20	4.80
0.436(3)	40.91	0	-1.40	-1.60	-5.80	10.60	5.20	6.20	8.20	9.00
0.436(3)	40.79	45	-2.00	-2.60	-3.40	12.00	4.80	6.00	7.00	6.20
0.436(3)	40.78	90	-2.00	0.0	+0.60	9.40	5.20	6.20	9.00	9.60

(1 inch = 0.0254 m ; ft/sec = 0.3048 m/s)

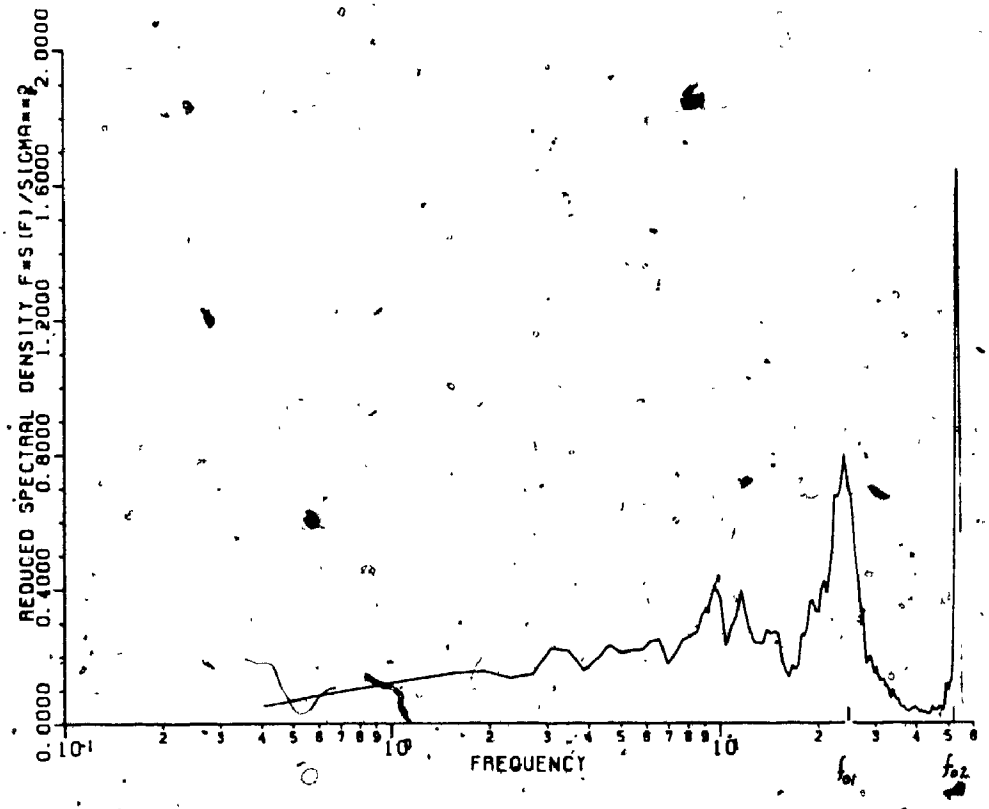

FIGURE 6.13 Power Spectrum of Response at r/a = 0, β_a = 5.31%, $\underline{\theta = 0°}$, $\bar{V}_G$ = 28 ft/sec (Built-Up Area)

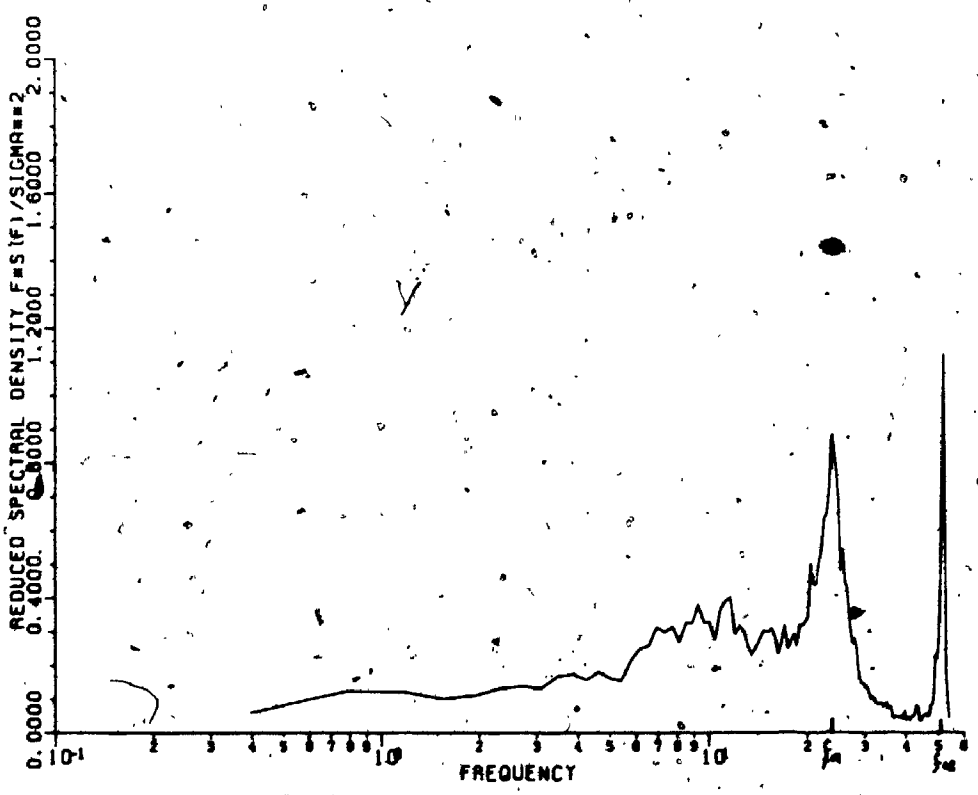

FIGURE 6.14 Power Spectra of Response at r/a = 0, β_a = 5.31%, $\underline{\theta = 90°}$, $\bar{V}_G$ = 28 ft/sec (Built-Up Area)

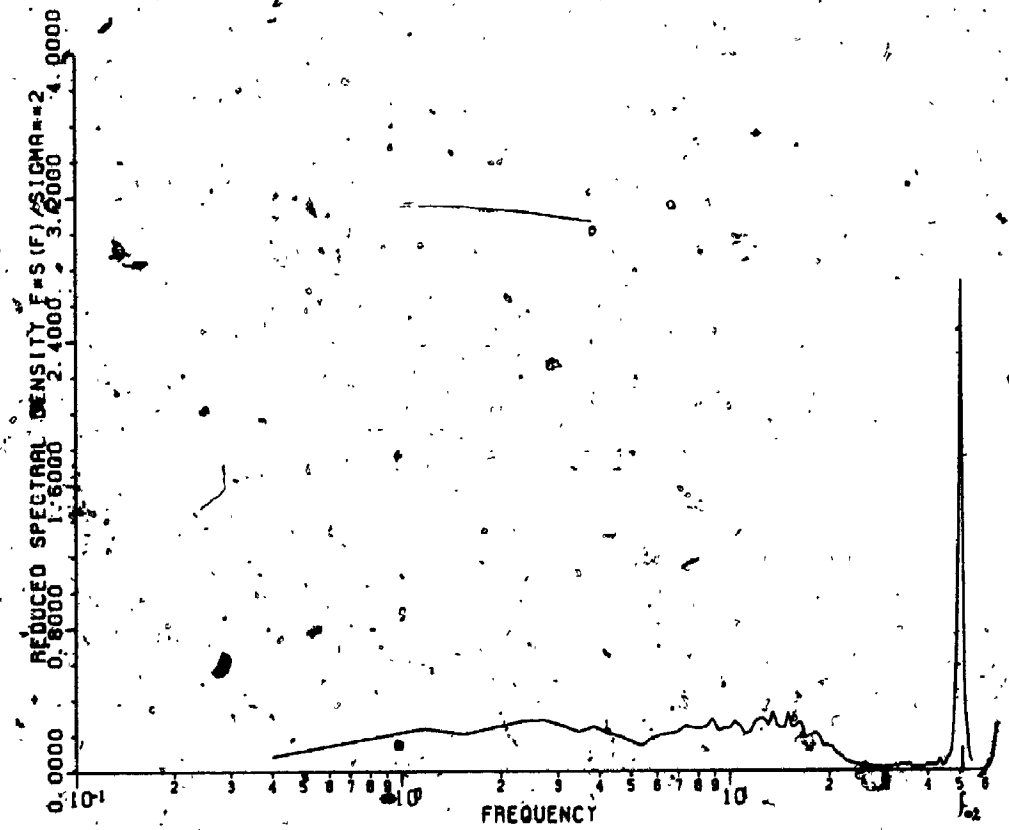

FIGURE 6.15 Power Spectrum of Response at r/a = 0, β_c = 1.78%, θ = 0°, $\bar{V}_G$ = 28 ft/sec (Built-Up Area)

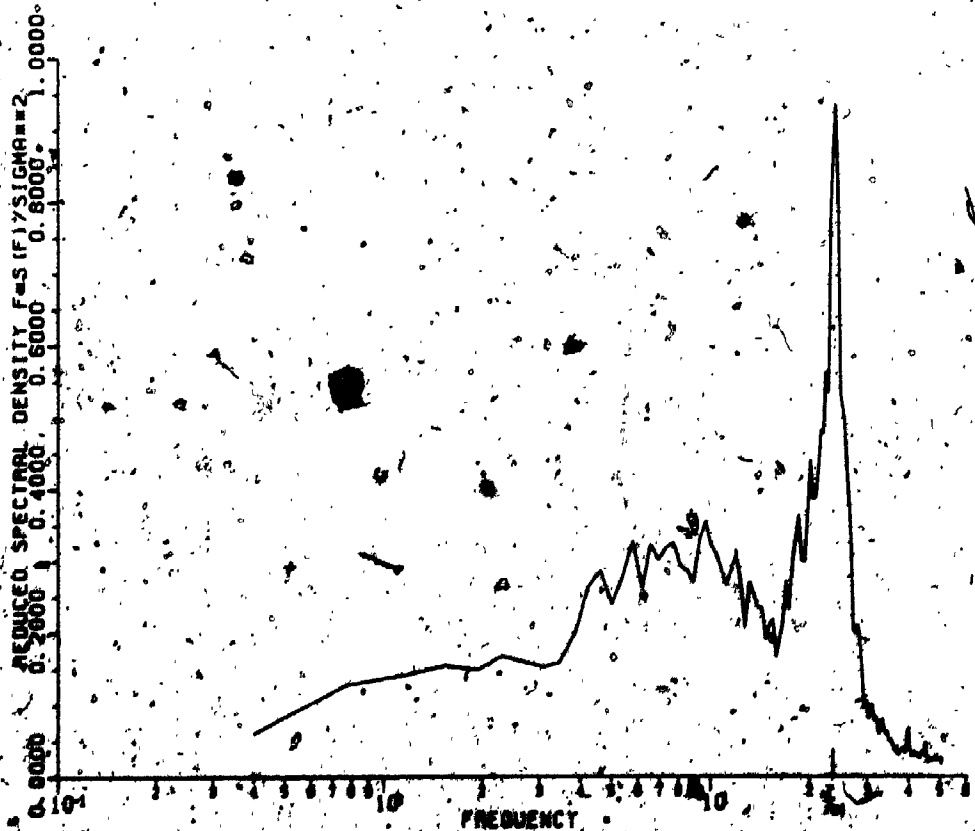

FIGURE 6.16 Power Spectrum of Response at r/a = 0.426, β_c = 5.3%, θ = 0°, $\bar{V}_G$ = 28 ft/sec (Built-Up Area)

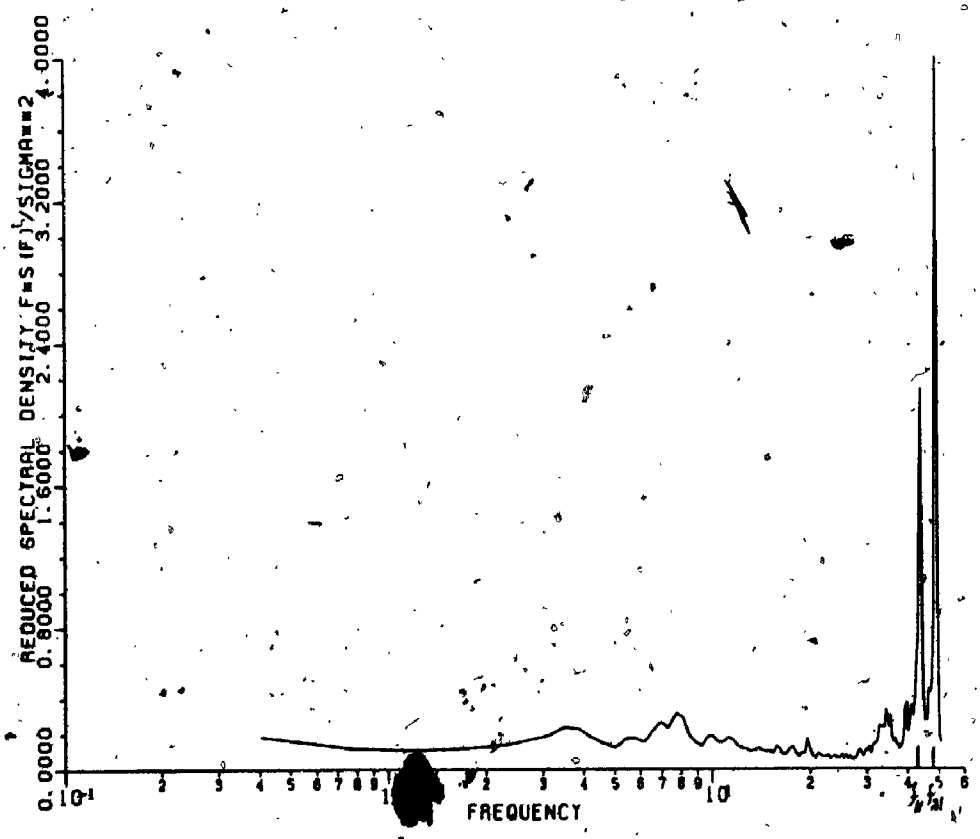

FIGURE 6.17 Power Spectrum of Response at r/a = 0.436, β_a = 0%, θ = 90°, $\bar{V}_G$ = 28 ft/sec (Built-Up Area)

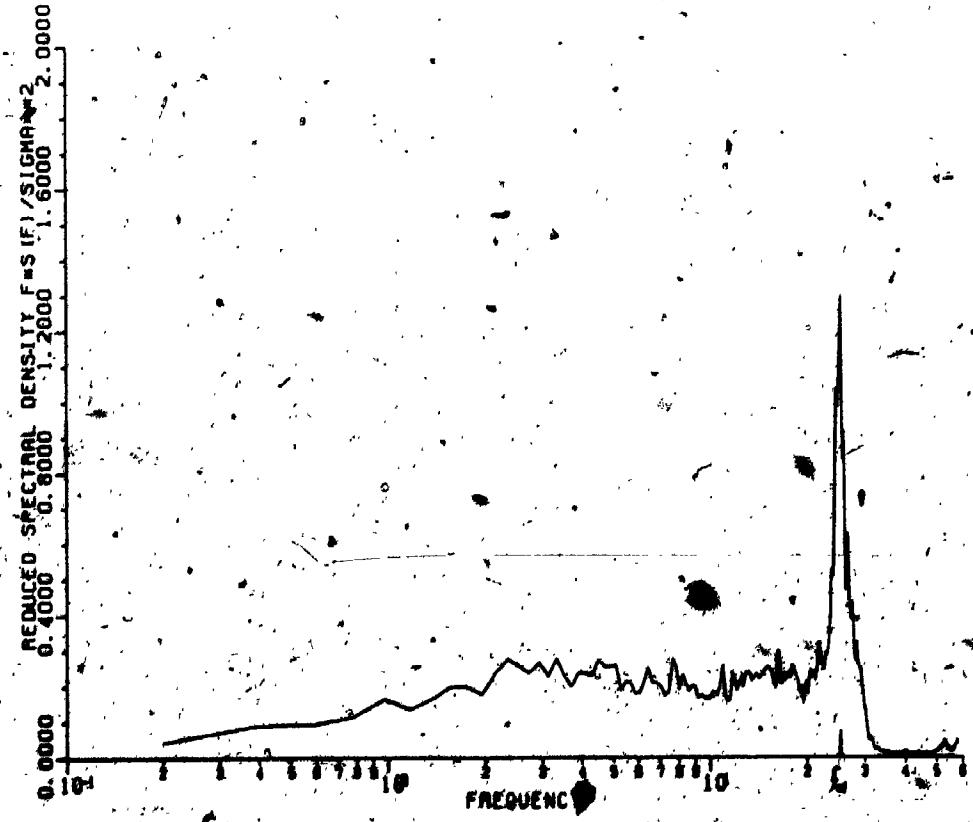

FIGURE 6.18 Power Spectrum of Response at r/a = 0, β_a = 5.30%, θ = 90° $\bar{V}_G$ = 20 ft/sec (Open Country Exposure)

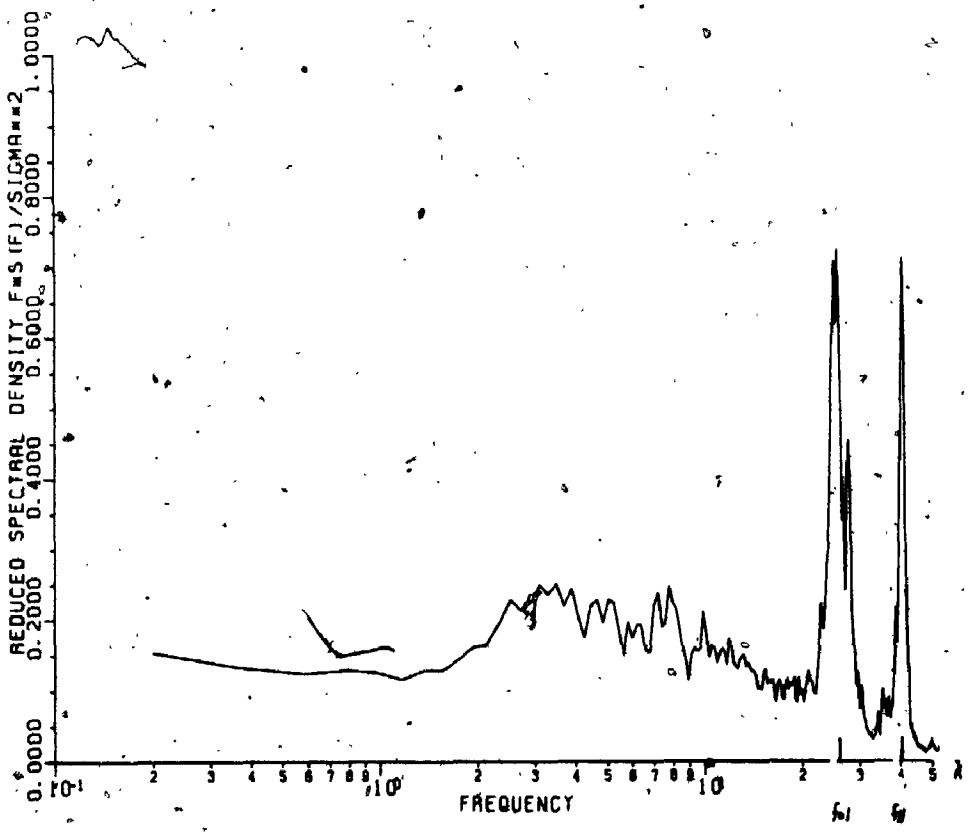

FIGURE 6.19 Power Spectrum of Response at $r/a = 0.436, \beta_a = 5.31\%$, $\theta = 45°$, $\bar{V}_G = 20$ ft/sec (Open Country Exposure)

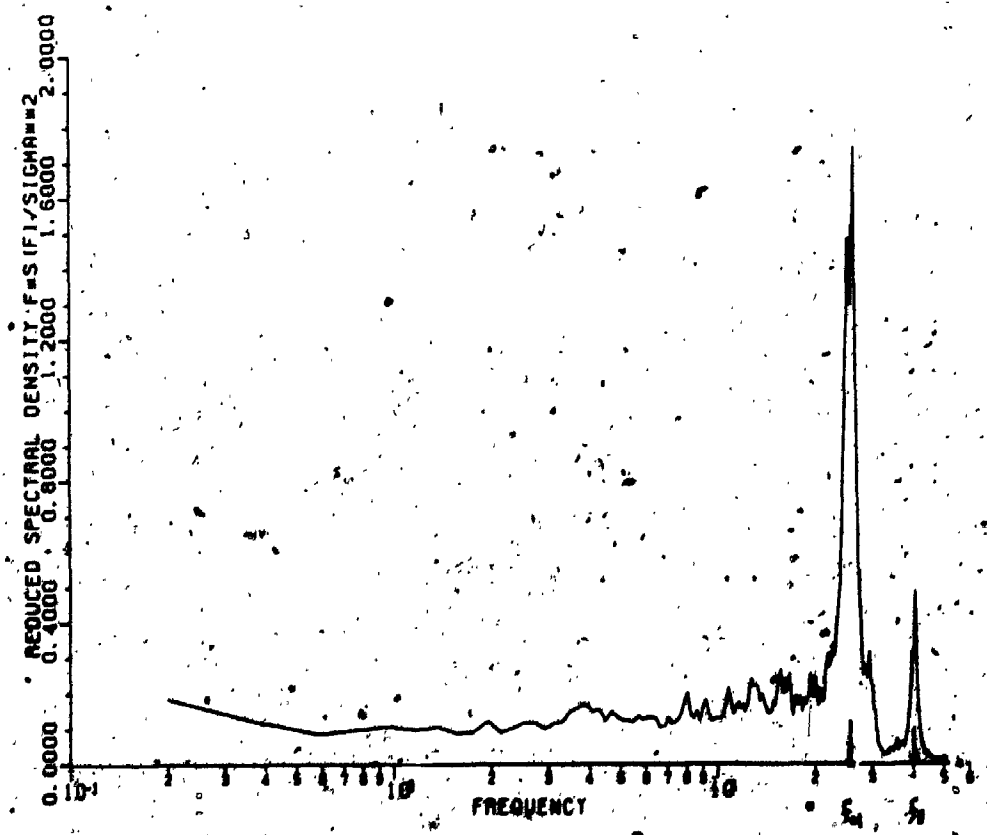

FIGURE 6.20 Power Spectrum of Response at $r/a = 0.436, \beta_a = 5.31\%$, $\theta = 0°$, $\bar{V}_G = 20$ ft/sec (Open Country Exposure)

TABLE 6.6 INTERNAL PRESSURE COEFFICIENT FOR DIFFERENT WIND VELOCITIES AND AREA PARAMETER ($\beta_a = NA_o/A_c \times 100$)

Wind Direction $\theta°$	Area Parameter β_a	Gradient Wind Speed $\overline{V}_G$ (ft/sec)	Pressure Coefficient $C_{\bar{q}}$ (mean)	Pressure Coefficient C_{q_σ} (RMS)
0°	5.30	38.0	-0.60	0.13
45°	5.30	38.0	-0.61	0.13
90°	5.30	38.0	-0.63	0.13
0°	5.30	28.0	-0.40	0.080
45°	5.30	28.0	-0.43	0.085
90°	5.30	28.0	-0.43	0.090
0°	3.54	28.0	-0.37	0.07
45°	3.54	28.0	-0.40	0.10
90°	3.54	28.0	-0.45	0.06
0°	0	28.0	-0.20	0.04
45°	0	28.0	-0.18	0.05
90°	0	28.0	-0.19	0.06

(1 ft/sec = 0.3048 m/s)

For a velocity of approaching flow $\bar{V}_G$ = 28 ft/sec (= 8.534 m/s) and with openings fairly uniformly distributed (N = 9) with area parameter β_a = 5.30% ($\beta = \frac{NA_o}{A_c}$ %), it was found that the mean pressure coefficient $C_{\bar{q}_\ell}$ = -0.43 and the rms pressure coefficient $C_{q_{\sigma_\ell}}$ = 0.085. For the same area parameter but with wind velocity $\bar{V}_G$ = 38 ft/sec (= 11.58 m/s) both coefficients increased to $C_{\bar{q}_\ell}$ = -0.63 and $C_{q_{\sigma_\ell}}$ = 0.13.

For a wind velocity of $\bar{V}_G$ = 28 ft/sec (= 8.534 m/s), but the area parameter β_a = 3.54%, the coefficients dropped to $C_{\bar{q}_\ell}$ = -0.37 and $C_{q_{\sigma_\ell}}$ = 0.07.

Cross-Spectra of Wind Fluctuations Over Model Roof Surface

To understand the correlation between the fluctuating flow velocities over the roof model, the cross-spectra of the longitudinal fluctuating component of turbulent wind were measured at different locations just above the surface of the roof. These measurements showed almost no correlation of wind fluctuations along and across the roof model when the velocity of the approaching flow $\bar{V}_G$ = 8 ft/sec (= 2.438 m/s), Figures 6.21 to 6.24, and a small correlation over the roof surface along wind, when $\bar{V}_G$ = 31 ft/sec (= 9.45 m/s), Figures 6.25, 6.26.

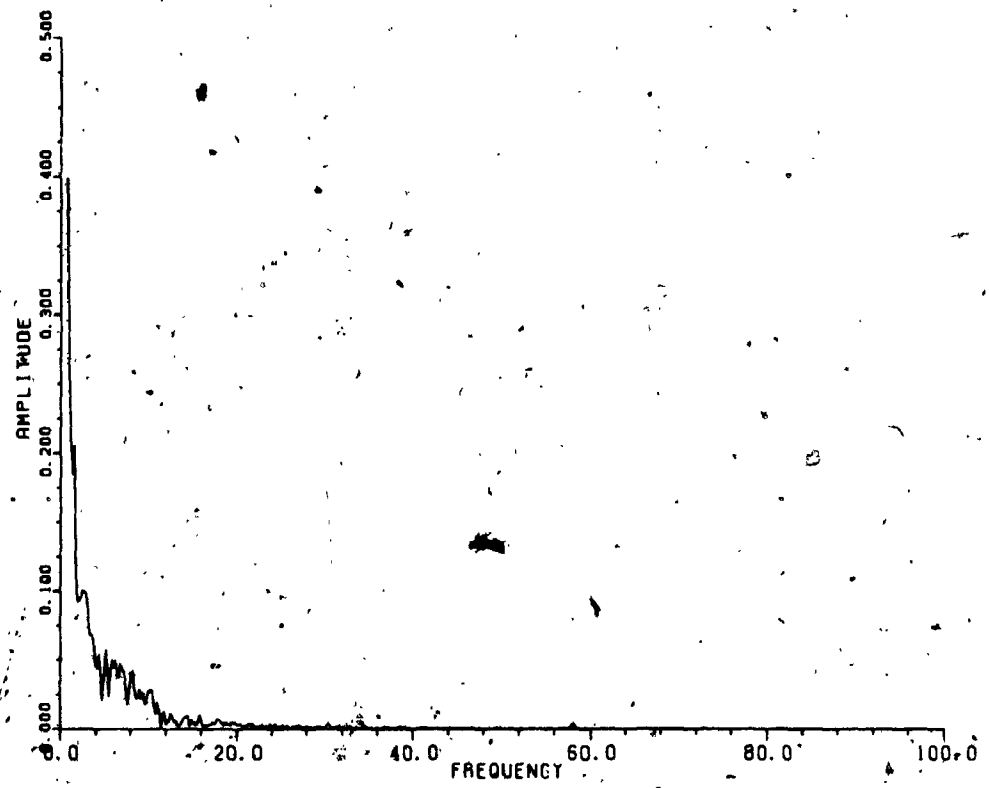

FIGURE 6.21 Cross-Correlation Coefficient (Coherence Function) of Wind Velocity, 8.0 ft/sec, at r/a = 0.436, 0.0 Along Wind

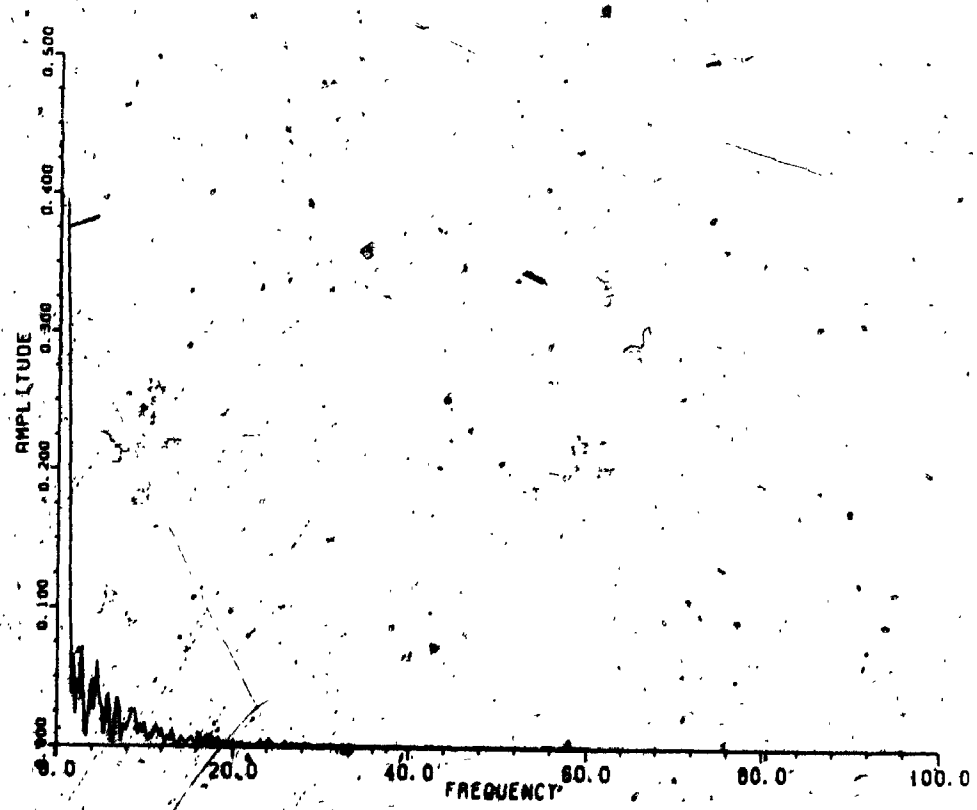

FIGURE 6.22 Cross-Correlation Coefficient (Coherence Function) of Wind Velocity, 8 ft/sec, at r/a = +0.436, -0.436 Along Wind

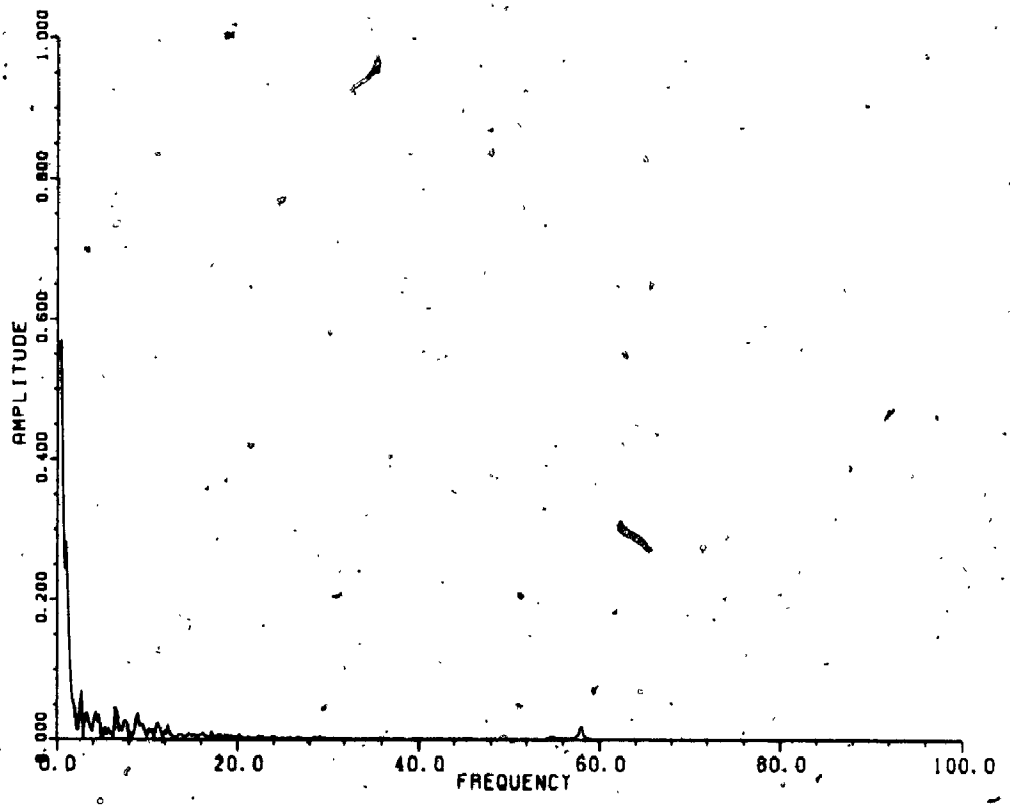

FIGURE 6.23 Cross-Correlation Coefficient (Coherence Function) of Wind Velocity, 8 ft/sec, at r/a = 0.0, +0.436 Across Wind

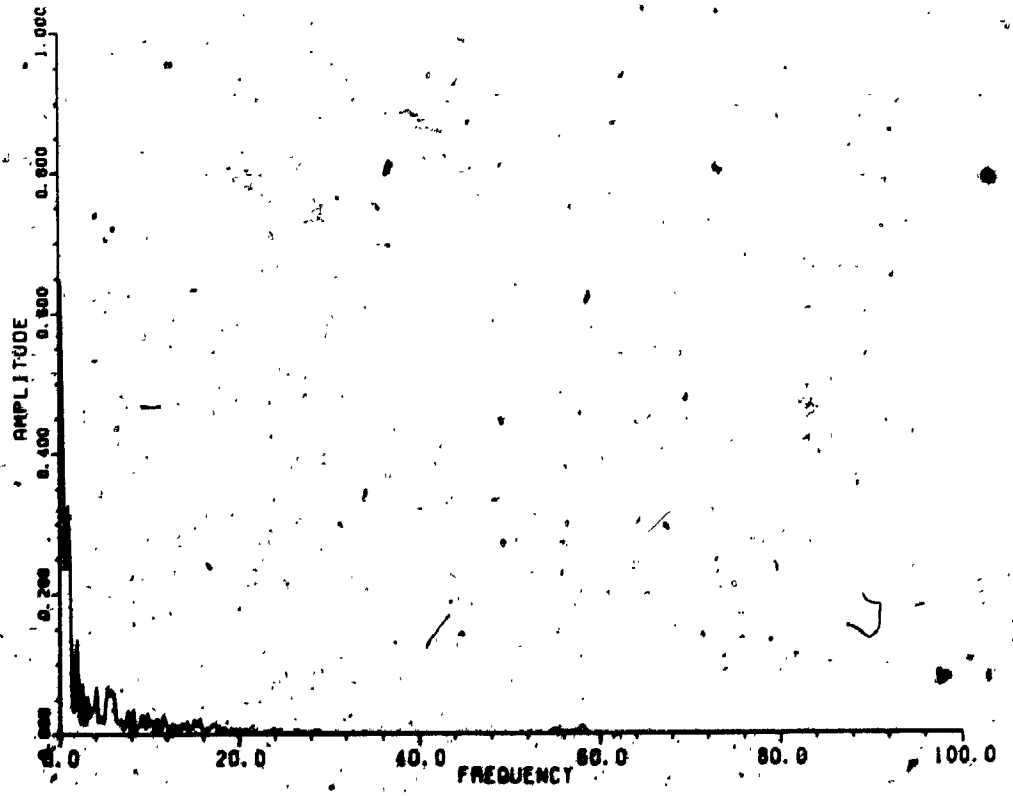

FIGURE 6.24 Cross-Correlation Coefficient (Coherence Function) of Wind Velocity, 8 ft/sec, at r = +0.436, -0.436, Across Wind

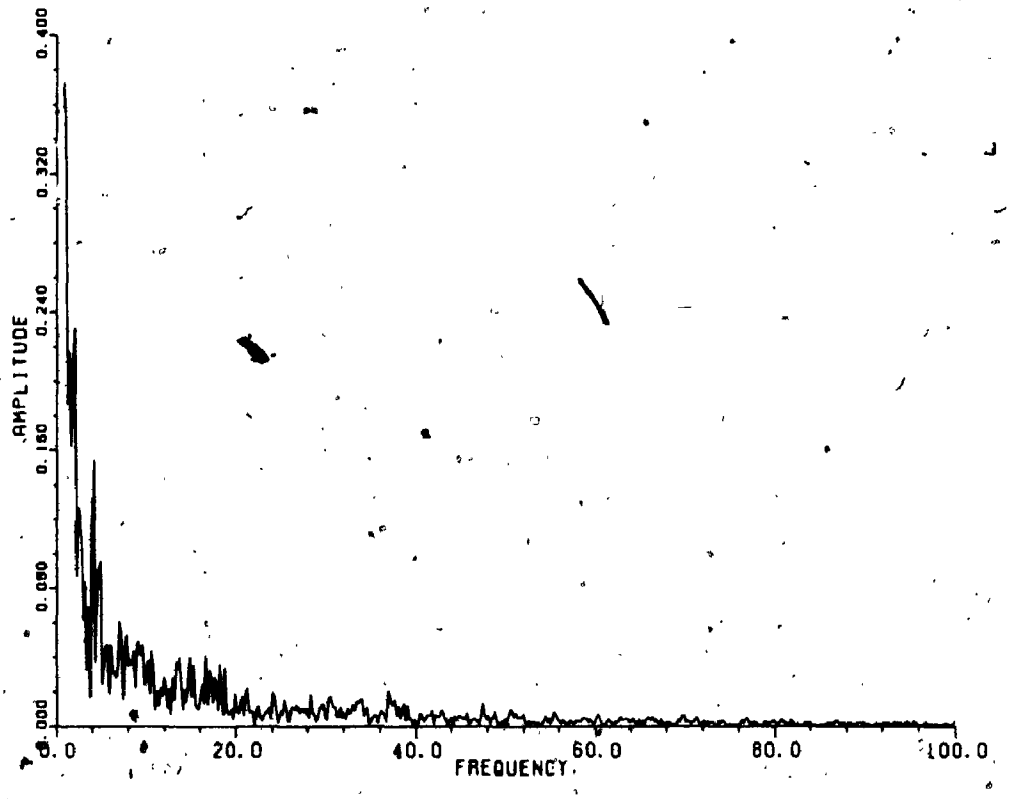

FIGURE 6.25 Cross-Correlation Coefficient (Coherence Function) of Wind Velocity, 31 ft/sec, at r/a = +0.436, -0.436 Across Wind

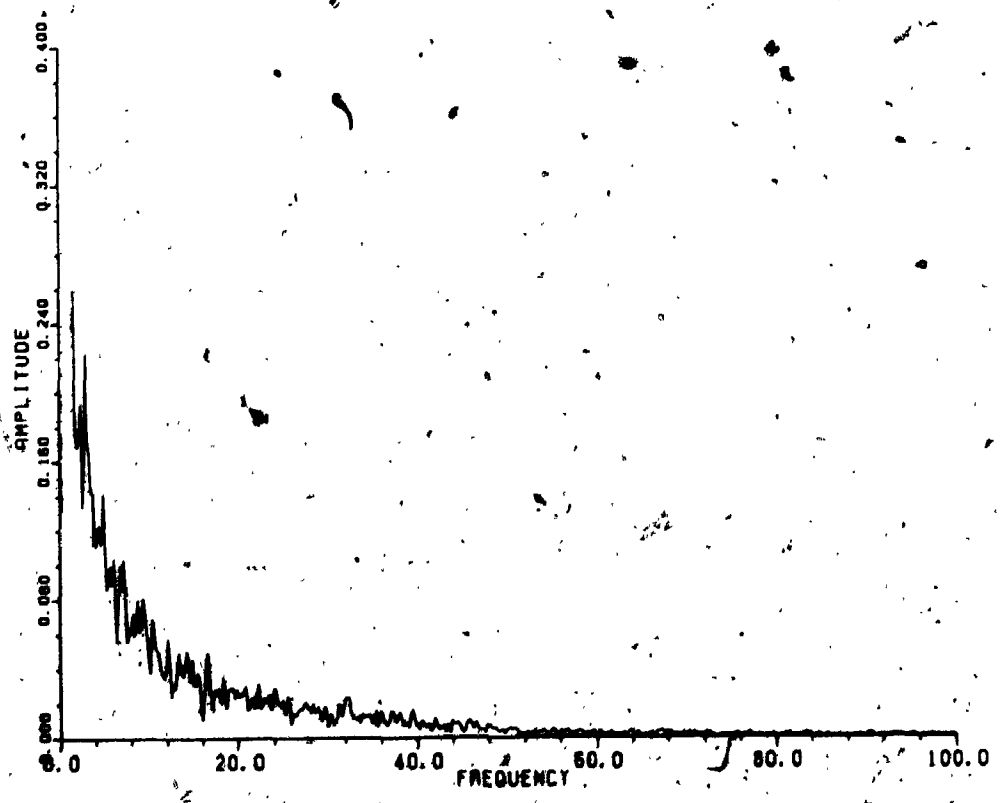

FIGURE 6.26 Cross-Correlation Coefficient (Coherence Function) of Wind Velocity, 31 ft/sec, at r/a = 0.436, 0.0 Along Wind

6.6.1.3 Effect of Cavity Openings on the Frequency Character

The variation of the model natural frequencies with total area parameter $\beta_a = \frac{NA_o}{A_c} \times 100$ is shown in Figure 6.7. Figure 6.7 indicates that the natural frequency of the first symmetrical mode is strongly dependent on the area parameter β_a, decreasing with the decrease of the total area of openings within the cavity wall, while the natural frequencies of the other modes are slightly affected.

For the first symmetrical mode, the variation of natural frequency with the cavity parameter $\beta_c = \ell' \frac{\rho a^2}{m\ Na_o}$ is shown in Figure 4.16 (Chapter 4). Figure 4.16 indicates that the natural frequency of this mode decreases due to the increase in the additional mass effect represented by the cavity parameter β_c.

For the light, highly taut roof tested, the natural frequencies increase with increasing area of openings indicating a behaviour similar to that of a Helmholtz resonator. The trends observed in Figures 4.16 and 6.7 are in agreement with the theory formulated in Chapter 4.

6.6.1.4 Effect of Wind Velocity and Cavity on Response

Figures 6.27 to 6.29 and Figures 6.30 to 6.32 show the variation of the dimensionless total mean and standard

deviation response respectively at different locations on the roof, for different wind velocities and area parameter β_a. In these figures it appears that the greatest response (a positive maximum, i.e. downwards) is attained when the model is completely closed; it occurs at the leeward position of r/a = 0.436 of the roof.

Figures 6.33 to 6.35 and Figures 6.36 to 6.38 show the dimensionless total mean and standard deviation response respectively at different locations on the roof, for different area parameter β_a at different wind velocities.

In these figures, a significant phenomenon is observed. When the gust size $(\frac{\overline{V}_G}{f})$ is about 0.33 of the structure size D, (i.e. $\frac{\overline{V}_G}{fD} \approx 0.33$), a peak response exists at all area parameters and everywhere on the roof.

6.6.1.5 Effect of Cavity and Wind Velocity on Damping

For free vibration tests, the total structural and acoustical damping ratio D_{nm} for each mode of vibration f_{nm} at different area parameter β_a is presented in Table 6.4.

The acoustical damping is due to the movement of the roof and is proportional to its vibration velocity. As

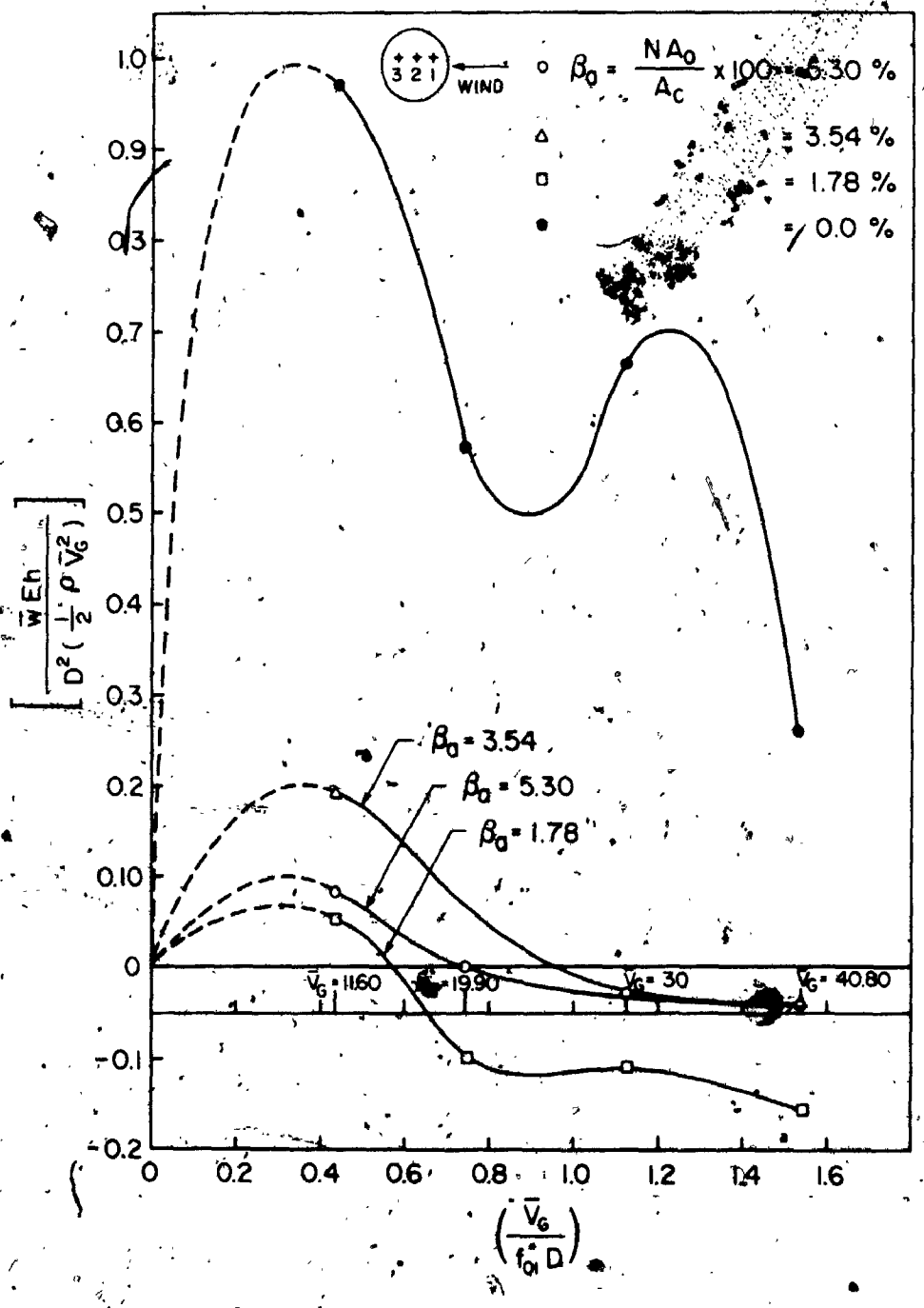

FIGURE 6.27 NON DIMENSIONAL MEAN RESPONSE AT CENTRE, r/a = 0.0 WITH WIND VELOCITIES AT DIFFERENT AREA PARAMETERS (PROBE NO. 2).

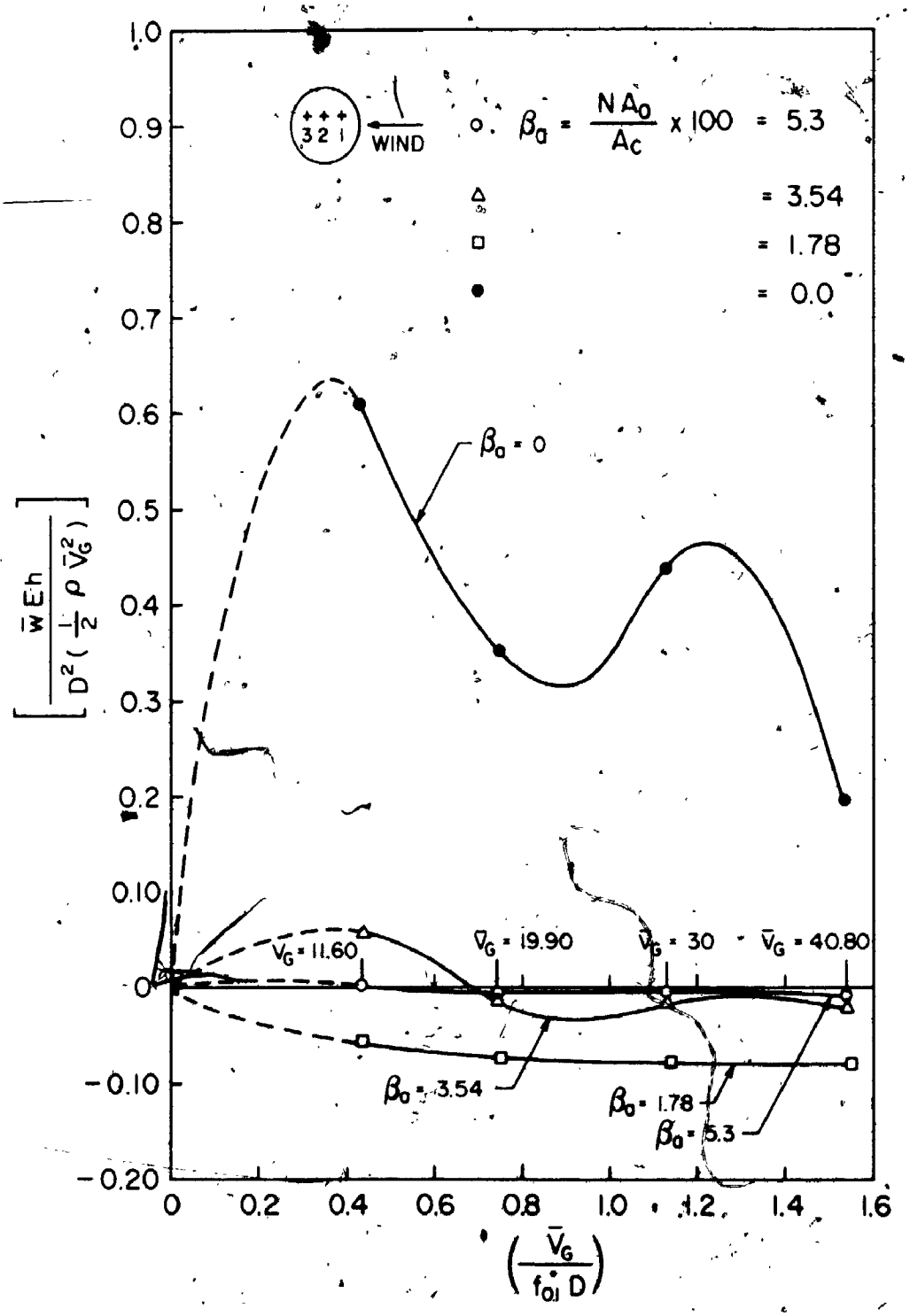

FIGURE 6.28 NON DIMENSIONAL MEAN RESPONSE AT $r/a = 0.436$ WITH WIND VELOCITIES AT DIFFERENT AREA PARAMETERS. (PROBE NO. 1)

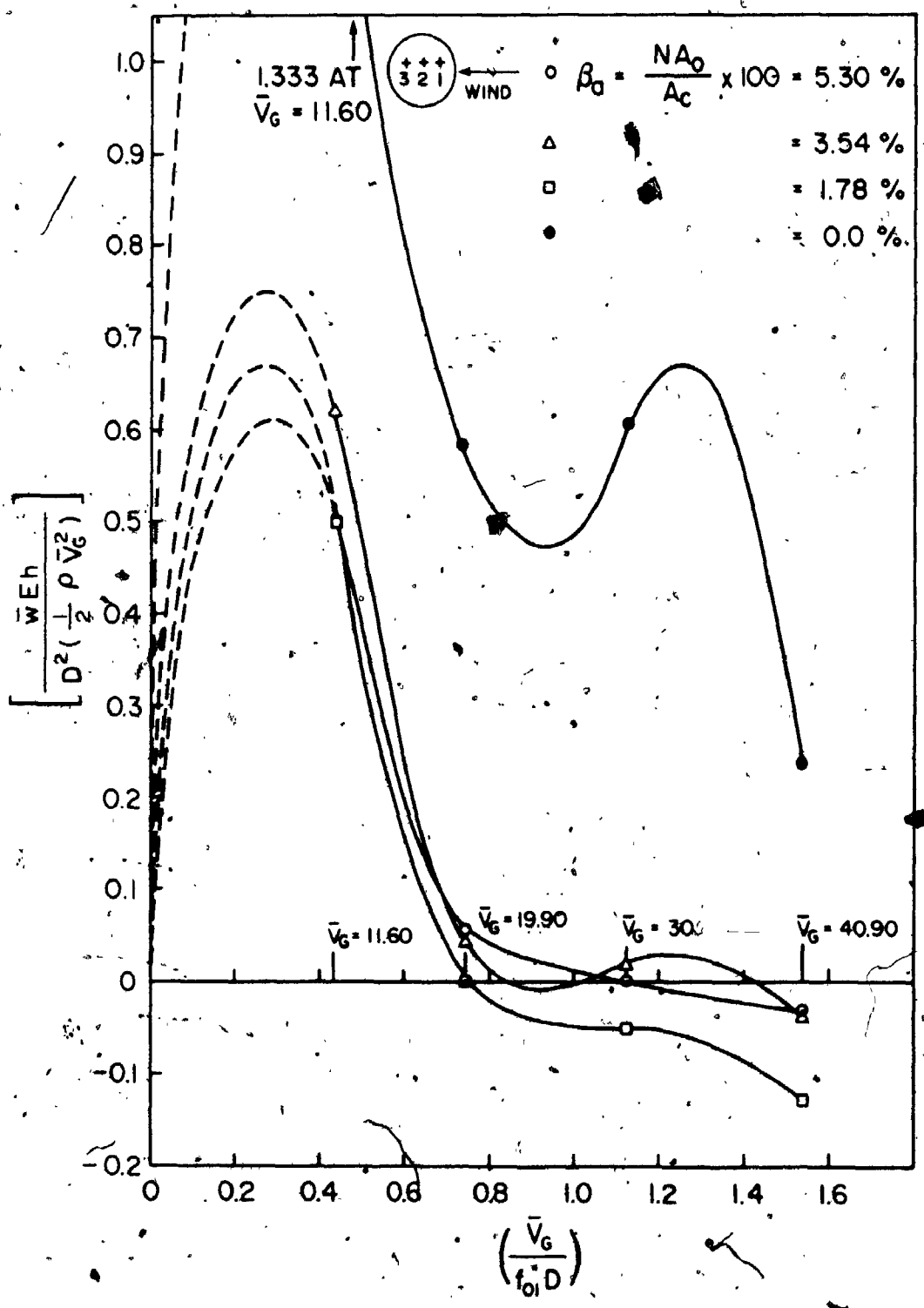

FIGURE 6.29 NON DIMENSIONAL MEAN RESPONSE AT r/a = 0.436 WITH WIND VELOCITIES AT DIFFERENT AREA PARAMETERS (PROBE NO. 3)

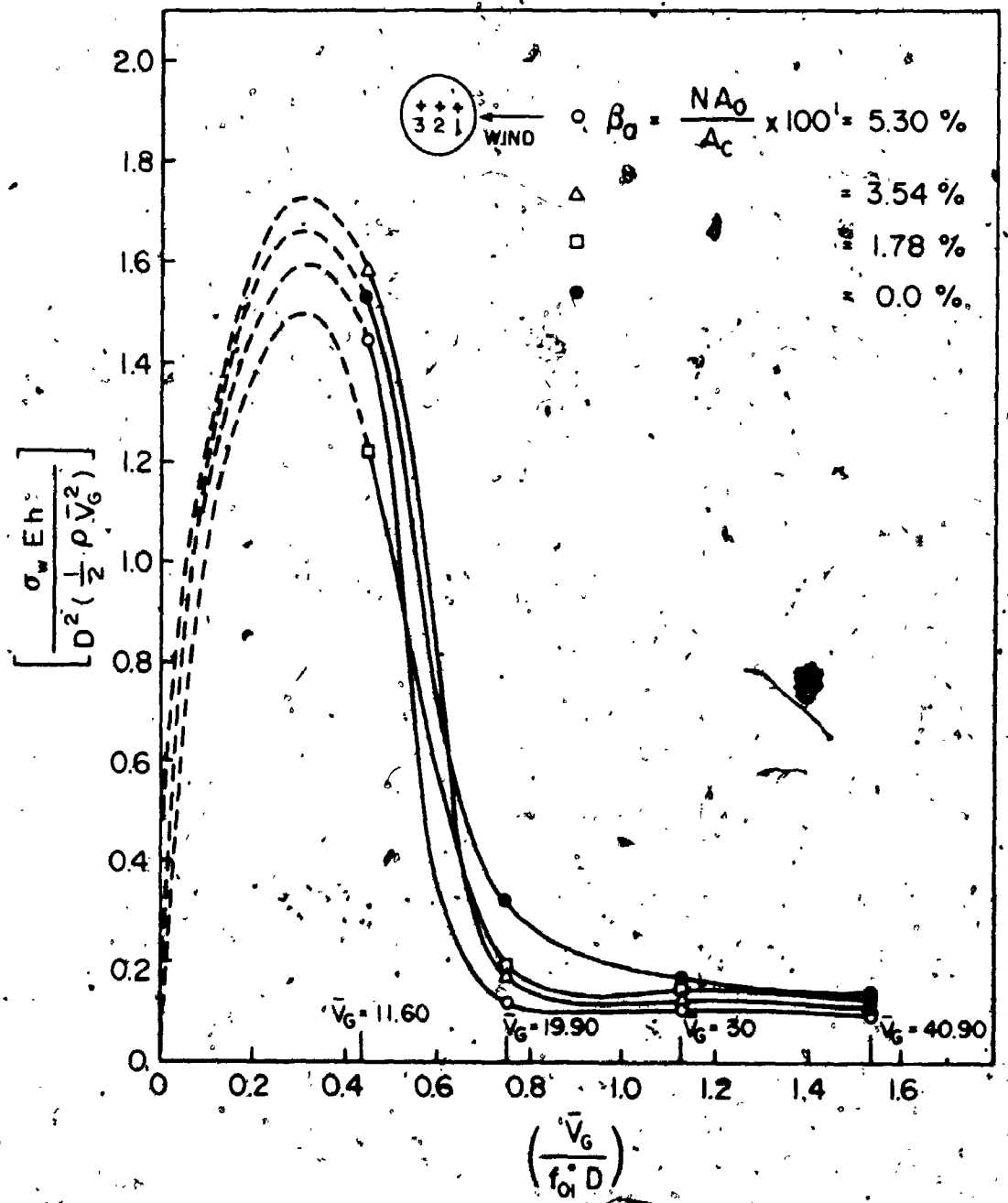

FIGURE 6.30 NON DIMENSIONAL RMS RESPONSE AT CENTRE WITH WIND VELOCITIES AT DIFFERENT AREA PARAMETERS (PROBE NO. 2)